Thesis submitted for the degree of
Master of Philosophy (Physics and Astronomy)

Probing the Gamma-ray Emission from HESS Source RX J1713.7-3946

Andrew Curzons

May 2019

Supervisors:
A/Prof. Gavin Rowell
Prof. Bruce Dawson

Faculty of Sciences
School of Physical Sciences
Department of Physics
The University of Adelaide

Principal Superviso:	A/Prof. Gavin Rowell
Co-Supervisor:	Prof. Bruce Dawson
Date of Submission:	21st May 2019

Abstract

The origin of Cosmic Rays (CRs) from our the galaxy remains a major mystery in high energy astrophysics. Astronomy techniques, such as γ-ray astronomy, have assisted us in coming closer to solving the problem, but many questions still remain unsolved. CRs are believed to produce γ-rays via interactions with the interstellar medium (ISM) in high energy situations. For this reason γ-rays are often used as a tracer for the parent CRs. The hadronic (pp interactions) and leptonic processes (IC scattering, synchrotron processes and relativistic Bremsstrahlung) involved in the production of the γ-rays are complex and at times intertwined. Hadronic processes are often favoured as the dominant production channel when there is spatially correlated ISM gas surrounding a source. RX J1713.7-3946 is a bright source of γ-rays, but is also visible in the radio and X-ray regime. The morphology of the radiation seen from this source is shell like, which leads us to believe that it resembles a supernova remnant (SNR). The high energy environment provided by SNRs is believed to be a great way to accelerate CRs to the energies we observe.

In this study we attempt to determine whether the γ-ray production is dominated by hadronic and/or leptonic processes towards RX J1713.7-3946. Using the latest high resolution γ-ray observations from the High Energy Stereoscopic System (HESS) along with X-ray and radio observations from *Suzaku* and the Southern Galactic Plane Survey (SGPS) respectively, we are able to model the broadband spectra from 29 distinct regions across the SNR. We investigate the resultant parameter space and begin to gain an idea of how the γ-rays are produced in some of these regions. Additionally, using the latest high resolution Mopra CO data we are able to estimate the density of the ISM in each region. This allows us to more accurately model the pp spectra and to uncover some regions where the often-negligible Bremsstrahlung emission is of significance. In addition to this spectral study, we use the high resolution γ-ray and CO data to perform a 2D correlation study between the γ-rays and ISM. Spatial correlation is found in 7 regions, suggesting the γ-rays are produced predominantly by hadronic processes. On the other hand, 5 regions display anti-correlation, leading us to favour the leptonic scenario for the γ-ray production. We also find observable and modeled differences between the correlated regions and anti-correlated regions, e.g. the radio synchrotron emission. These differences are investigated and discussed within the scope of the literature.

Declaration of Originality

I certify that this work contains no material which has been accepted for the award of any other degree or diploma in my name in any university or other tertiary institution and, to the best of my knowledge and belief, contains no material previously published or written by another person, except where due reference has been made in the text. In addition, I certify that no part of this work will, in the future, be used in a submission in my name for any other degree or diploma in any university or other tertiary institution without the prior approval of the University of Adelaide and where applicable, any partner institution responsible for the joint award of this degree.

I give consent to this copy of my thesis, when deposited in the University Library, being made available for loan and photocopying, subject to the provisions of the Copyright Act 1968.

I also give permission for the digital version of my thesis to be made available on the web, via the University's digital research repository, the Library Search and also through web search engines, unless permission has been granted by the University to restrict access for a period of time.

I acknowledge the support I have received for my research through the provision of an Australian Government Research Training Program Scholarship.

Date

Signature

Acknowledgment

First and foremost, I would like to thank my supervisor, Gavin, for all his guidance and expertise over the past two years. His mentorship and the time he has given me has been of the utmost importance to the completion of my thesis. Through him I have learned a great deal, not only about high energy astrophysics but more importantly, how to be a researcher.

Next, I would like to thank my co-supervisor, Bruce, and also Gary, Jose and Roger who have all played leadership roles throughout the astrophysics group. I am also thankful to Fabien, who has played a supervisor type role at times. The help he has provided me with any computational or astrophysical issues has been immensely appreciated. A special thanks also goes to Sabrina, who has also played a supervisor type role at times. I was fortunate enough to have her aid me in formulating the 'bootstrapping' method in chapter 5. Otherwise, she has been a great motivator and has taught me mostly everything I know about Python; I especially appreciate all the workshops.

I would also like to thank the other members of the gamma-ray astronomy group; Cameron, James, Kirsty, Rami and Rebecca. Having others to discuss issues with in the office has been a great help. I am also thankful to all other members of the high energy astrophysics department, who have provided me with a platform to develop my presentation skills.

My colleagues in Nagoya, Japan, Hidetoshi and Professor Fukui also deserve a thank you. A portion of this thesis is built upon the excellent work they have published and I have extensively made use of their resources and results. They also kindly welcomed me into their University for a period of time, of which I am grateful for the experience.

Lastly, I am deeply thankful to my family, friends and partner, Terri, who have all supported me and kept me grounded over the last two years. I wouldn't have been able to do it without you.

Contents

1 Introduction

1.1 Are Supernova Remnants the Source of Galactic CRs?

Cosmic Rays are particles, usually protons, but also heavier nuclei (Helium etc) that hit the Earth's atmosphere. They are characterized by their relativistic nature, with some being observed to reach energies above 10^{20} eV, see Figure 1.1.

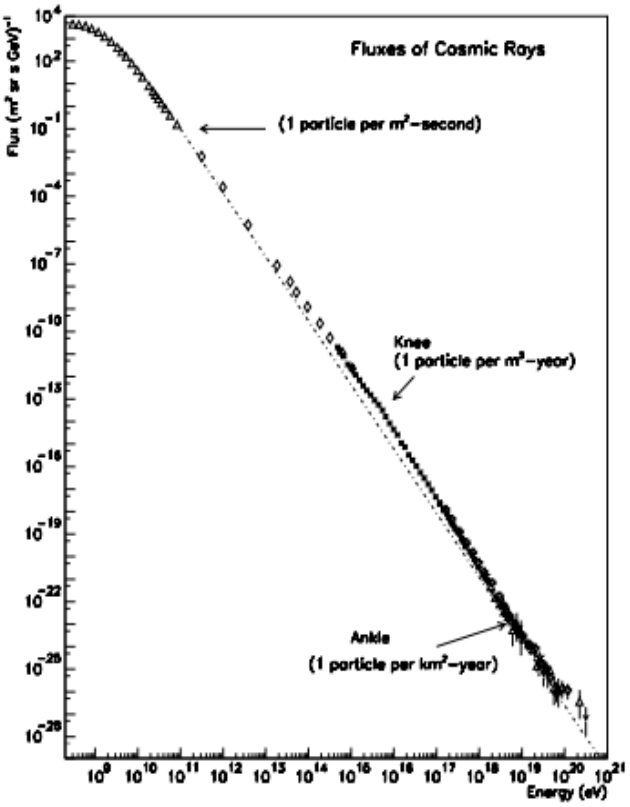

Figure 1.1: Entire observed CR spectrum (Swordy, 2001).

The long standing questions surrounding CRs are:

1. What is their origin?
2. How do that attain such high energies?

Answering the first of these questions is difficult. The direction we observe CRs here on Earth is not necessarily the direction they originated from. CRs are charged particles, so as they travel through the galaxy (or universe) magnetic fields alter their direction

of travel. The majority of the lowest energy CRs we detect are believed to be produced in our solar system; high energy solar events appear to coincide with the detection of these CRs. On the other hand, the highest energy CRs are believed to be extra-galactic, i.e. originate beyond our galaxy. These high energy CRs will have large momenta and hence large gyro-radii, r_g (Equation 1.1).

$$r_g = \frac{\gamma m v}{qB} \tag{1.1}$$

where γ is the relativistic Lorentz factor, B is the magnetic field strength and m, v and q are the mass, velocity and charge of the particle, respectively. The gyro-radii of these CRs are larger than the size of the galaxy, leading us to believe they should be extra-galactic (Gaisser, 1990). Extra-galactic CRs are believed to originate in objects such as Active Galactic Nuclei (AGN). CRs up to energies of 100 TeV - 10 PeV are believed to originate within the galaxy. As can be seen in Figure 1.2 there is a change in the spectral shape of the CRs at around this energy, the so called CR 'knee'. This is where the observed CRs are believed to transition from galactic to extra-galactic (Swordy, 2001). Supernovae (SNe), originally proposed by Baade and Zwicky (1934) as objects capable of accelerating particles to the high energies we see, are now commonly regarded as galactic CR sources. The huge amount of energy, 10^{51} erg, produced in these events has led to their increased interest from the community. It is currently believed that particles are accelerated to high energies in the expanding shells of supernova remnants (SNRs) via diffusive shock acceleration (DSA). Where the outer shell meets the ISM there is a shock front, the particles accelerate back and forth over the shock and in doing so attain their high energies. This is based on Fermi's original theory of CR acceleration (Fermi, 1949), which is also required to explain extra-galactic CR acceleration. We have observed similar behavior at the bow shock of the Earth and the solar system, where particles are accelerated to energies of keV-MeV (Gosling et al., 1978).

Shock acceleration is the leading theory in response to the second question, however, we need evidence to support the theory that CRs originate in objects like SNRs. Since the direction of origin of CRs, up to the highest energies ($\leq 10^6$ TeV), is distorted, other techniques were developed. One of the leading methods to detect CRs is γ-ray astronomy and is usually tightly linked to radio and X-ray astronomy, for reasons that will become clear later. The highest energy electro-magnetic radiation is called γ-ray radiation. One way in which this radiation can be produced is via CR interactions. If these interactions occur near the accelerating environments the γ-rays can act as tracers for the CRs, as they travel in straight lines. The dominant CR interaction producing γ-rays is termed π^0 decay, or alternatively, proton-proton (pp) interactions. CR protons, or nuclei, will collide with stationary protons, usually in the form of gas clouds, to produce neutral and charged pions. Due to their unstable nature, the neutral pions subsequently decay into 2 γ-rays. These processes are listed below (Equation 1.2):

$$\begin{aligned} p + p \rightarrow & \pi^0 + p + p \\ & \pi^0 \rightarrow \gamma + \gamma \end{aligned} \tag{1.2}$$

To make things more problematic, pion decay is not the only process capable of producing

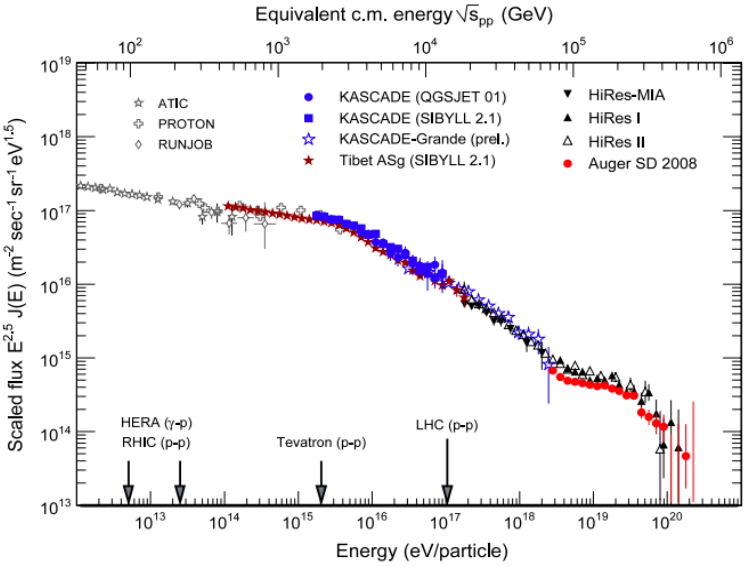

Figure 1.2: High energy tail of the CR spectrum, highlighting the spectral change above $\sim$ 10 PeV (Blümer et al., 2009).

γ-ray radiation at SNR sites. The discovery of non-thermal X-rays from SNRs is proof of that High energy electrons are also accelerated to high energies at their shock fronts. The same population of high energy electrons can produce γ-rays via inverse Compton (IC) scattering of lower energy photons. Additionally, the accelerated electrons may emit non-thermal Bremsstrahlung radiation if they interact with nuclei.

1.2 The Origin of Gamma-rays Produced at SNRs

The central problem within γ-ray astronomy is determining whether the γ-rays are produced via hadronic processes (*pp* interactions) or leptonic processes (electron interactions) in any given SNR environment. It is more than likely a combination of both, depending on the environment, but quantifying each contribution remains a problematic task. There are direct and indirect methods one can use to identify whether a certain processes is occurring. Firstly, a characteristic pion bump may be observed between 100 MeV and 1 GeV if hadronic processes are dominating the γ-ray production (Stecker, 1971). However, this feature may be disturbed by the γ-ray emission of secondary electrons (Yang et al., 2018), or if the spectral index of the parent protons is less than 2 (see Figure 1.3). The spectral index describes the shape of a particle distribution. Nonetheless, this direct evidence for proton acceleration has been observed by the *Fermi* Large Area Telescope (*Fermi*-LAT) at multiple SNRs (IC 443, W44, W49B, W51C) (Ackermann et al., 2013; Jogler and Funk, 2016; H.E.S.S. Collaboration et al., 2018). These SNRs are all quite old $\geq$ 10000 years (Lee et al., 2008; Wolszczan et al., 1991); except for W49B, which has an age estimate of $\sim 2000 - 4000$ years (Zhou et al., 2011; Hwang et al., 2000). Alternatively, because of the Klein-Nishina effect, the IC component should be suppressed at γ-ray energies above

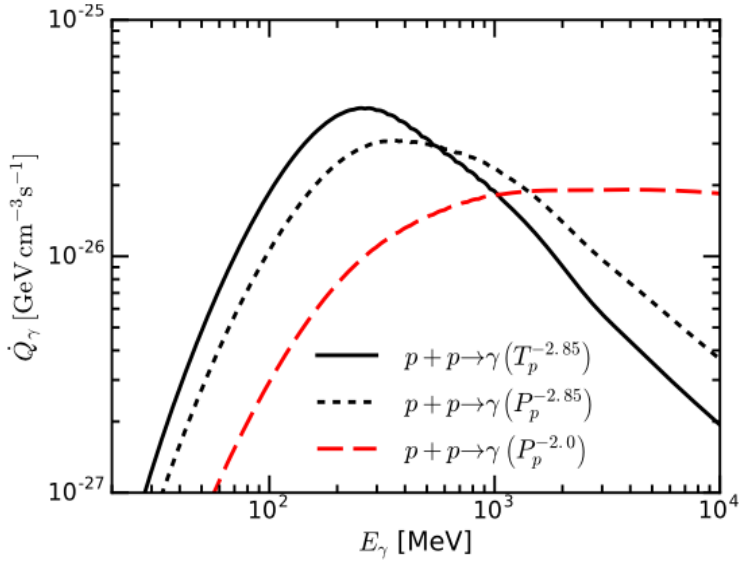

Figure 1.3: Example of the pion bump and how it disappears when the spectral index decreases below 2 (Yang et al., 2018). The spectral index basically describes the shape of the CR proton distribution, see section 3.1 for further discussion. Here T_p and P_p represent the proton kinetic energy and momentum respectively.

$\sim$ 10 TeV (Bykov et al., 2018). If γ-rays are observed at energies up to 100 TeV, then this would be firm evidence that CR protons are accelerated at the observation site (Aharonian, 2013). The detection of neutrinos towards an SNR would also imply the acceleration of protons to high energies. In Equation 1.2 it was illustrated how γ-rays were produced, however, in addition to the neutral pion, charged pions are also produced. The products of the decay of these charged pions include neutrinos:

$$\begin{aligned} \pi^+ &\rightarrow \mu^+ + \nu_\mu \\ \mu^+ &\rightarrow e^+ + \nu_e + \bar{\nu}_\mu \\ \pi^- &\rightarrow \mu^- + \bar{\nu}_\mu \\ \mu^- &\rightarrow e^- + \bar{\nu}_e + \nu_\mu \end{aligned} \tag{1.3}$$

Currently, no neutrinos have been detected towards an SNR source; such an observation would be groundbreaking. Finally, the presence of gas clouds/clumps, coincident with the γ-ray emission, is suggestive of a hadronic dominated scenario (Aharonian et al., 2008; Fukui et al., 2012).

Synchrotron radiation has been detected towards multiple SNRs (Cassiopeia A, RX J1713.7-3946, SN 1006 and Tycho, for example) (Mezger et al., 1986; Koyama et al., 1997; Koyama et al., 1995; Ammosov et al., 1994). This implies the presence of electrons, meaning that IC scattering should also be producing γ-rays, at least to some extent. Electrons will suffer synchrotron losses, resulting in a reduced amount of energy available for IC scattering. Moreover, Bremsstrahlung radiation is often disregarded as a dominant source of γ-rays. Unless a large amount of electrons are accelerated at an SNR, the pion decay process will

provide a more significant amount of γ-rays for a given target density (Abdo et al., 2010). Otherwise, it has been suggested that non-thermal Bremsstrahlung is responsible for a tail feature in the X-ray spectrum of some SNRs (RCW 86, Cassiopeia A and W49B for example) (Vink et al., 2002; Vink, 2008; Tanaka et al., 2018). Regardless, both hadronic (pp) and leptonic (IC) dominated scenarios have been shown to fit γ-ray observations towards SNRs. RX J1713.7-3946 is a prime case of this. The origin of the γ-ray emission has been under debate since the γ-rays were first detected (Muraishi et al., 2000). Currently, the problem is still unresolved. Both hadronic and leptonic models appear to recreate the broadband observations (see Figure 1.4), with no clear indication of which model is superior. We discuss this source in more detail below.

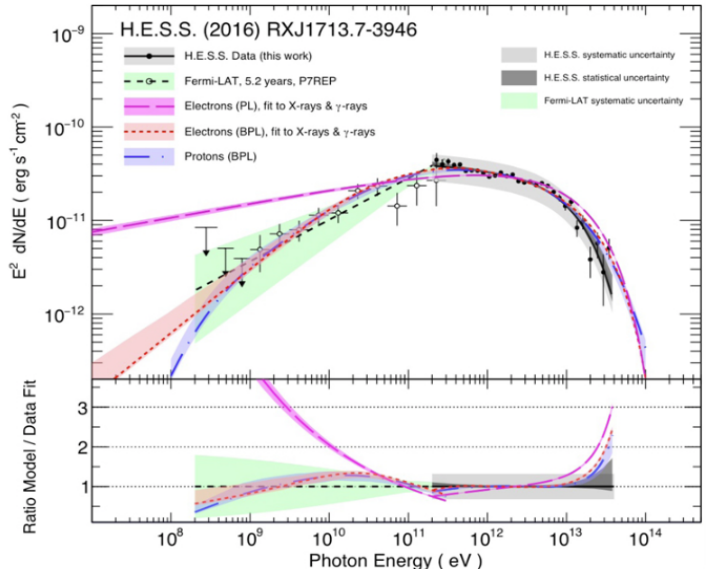

Figure 1.4: *Fermi*-LAT and HESS observations of RX J1713.7-3946 at γ-ray energies, fitted with both hadronic and leptonic models (H. E. S. S. Collaboration et al., 2018).

1.3 Overview of the Extensively Studied SNR RX J1713.7-3946

RX J1713.7-3946 (or G347.3-0.5) is a galactic SNR first observed by the ROSAT all-sky survey at X-ray wavelengths (Pfeffermann and Aschenbach, 1996). With an age of $\sim$ 1600 years (Wang et al., 1997), it is now one of the most extensively studied SNRs with strong TeV γ-ray emission as seen by HESS (Aharonian et al., 2004; H. E. S. S. Collaboration et al., 2018). Evidence from molecular gas surveys has associated RX J1713.7-3946 with many dense gas clumps in the velocity range of -20 to 0 km s^{-1} (Fukui et al., 2003; Moriguchi et al., 2005; Sano et al., 2010; Maxted et al., 2013). This velocity range corresponds to a distance of 1 kpc, favoured over the opposing 6 kpc distance suggested by Slane et al. (1999). Moriguchi et al. (2005) illustrates the features present at both these distances along with the super shell, SG 347.3-0.0-21 (Figure 1.5). The precise particle origin of the γ-rays seen at the location of RX J1713.7-3946 is still unclear and remains a big question.

Evidence supporting the acceleration of both hadronic and leptonic particles has been presented, yet the extent of each contribution is not accurately constrained. We discuss the history of the source in more detail below.

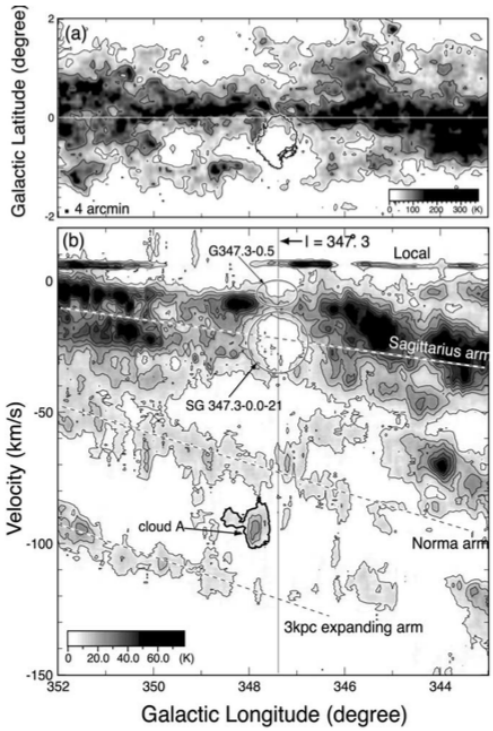

Figure 1.5: (a) The large scale ^{12}CO distribution surrounding RX J1713.7-3946 as seen by Nanten. The black outlines indicates the X-ray boundary of RX J1713.7-3946 as seen by Pfeffermann and Aschenbach (1996). (b) Galactic longitude-velocity map for the same region as (a), integrated over a latitude range of -1^o to 1^o. The accepted location of RX J1713.7-3946 is indicated by the arrow pointing towards G347.3-0.5, while cloud A has also been argued to be the location of the SNR (Slane et al., 1999). Image taken from (Moriguchi et al., 2005).

After an initial detection by the ROSAT all-sky survey at energies between 0.1-2.4 keV, many follow up observations and analyses were made (Koyama et al., 1997; Uchiyama et al., 2003), revealing the presence of 'hot spots' or filaments. These filaments are small regions with heightened X-ray emission. X-rays of a thermal nature were initially ruled out due to the lack of line emission, later confirmed by Slane et al. (1999) and Uchiyama et al. (2003). However, Katsuda et al. (2015) have recently detected the presence of line emission, confirming previous work by Hiraga et al. (2005). Nonetheless, the emission mechanism for the bulk remainder of the X-rays was attributed to non-thermal synchrotron radiation from high energy electrons. The presence of these electrons suggested that IC scattering should be occurring too, producing radiation at γ-ray energies. Observations at these energies then became an essential feature of understanding RX J1713.7-3946. Muraishi et al. (2000) obtained the first TeV observations of RX J1713.7-3946 using the CANGAROO telescope. Their results displayed an extended γ-ray emission shell coincidental with that

of the synchrotron X-ray shell, later confirmed by many studies (Aharonian et al., 2006; Aharonian et al., 2007; Tanaka et al., 2008; Acero et al., 2009; H. E. S. S. Collaboration et al., 2018). See Figure 1.6 for the latest γ-ray map from HESS. These results then led to the debate as to what process was responsible for producing these γ-rays, IC scattering or pp interactions.

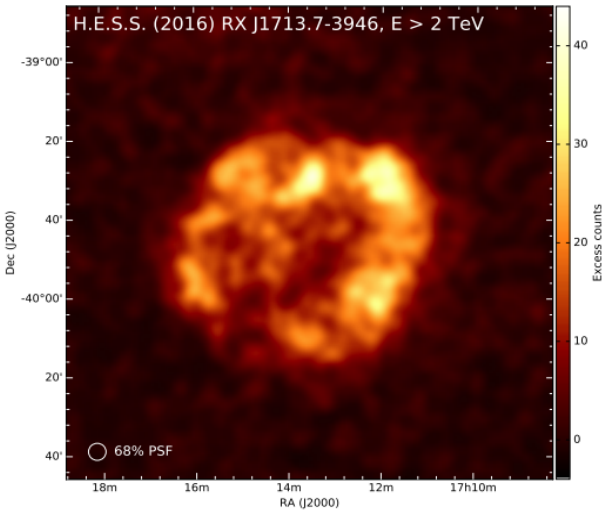

Figure 1.6: HESS γ-ray map of RX J1713.7-3946, with an applied energy threshold of 2 TeV (H. E. S. S. Collaboration et al., 2018).

Many studies successfully modeled the broadband emission from RX J1713.7-3946 using only leptonic mechanisms (Ellison et al., 2001; Lazendic et al., 2004; Yuan et al., 2011; Ohira and Yamazaki, 2017). Most of these models required a low magnetic field strength, Lazendic et al. (2004) suggested that the average intensity over the entire remnant should be less than 1 μG. A remarkable discovery by Uchiyama et al. (2007) found that particular X-ray hot spots brightened and dimmed again on timescales of one year (see Figure 1.7). Then considering the radiative cooling time for electrons:

$$t_{\rm sync} \sim 1.5 \left(\frac{B}{\rm mG}\right)^{-1.5} \left(\frac{\epsilon}{\rm keV}\right)^{-0.5} \tag{1.4}$$

where ϵ is the synchrotron photon energy, they were able to show that the average magnetic field over 0.1 pc sized regions could reach above 1 mG. Depending on the total extent of these hot spots, the global magnetic fields could average out to the order of μG. Finke and Dermer (2012) found that the leptonic scenario was better modeled with compact knots or hot spots (multi-zone model) with increased magnetic field strength. On the other hand, studies also failed to reproduce the broadband emission with a pure leptonic model. Uchiyama et al. (2003), Aharonian et al. (2006), and Yuan et al. (2011) illustrated how their IC models could not recreate the total observed spectrum. Moreover, relativistic Bremsstrahlung may also emit at γ-ray energies. This component is often disregarded due to the assumed low ISM gas density towards RX J1713.7-3946 (Ellison et al., 2010). Finke

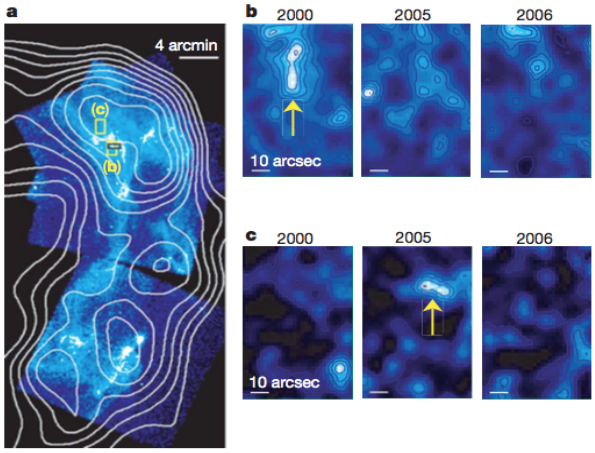

Figure 1.7: Chandra X-ray images of the western side of RX J1713.7-3946 (Uchiyama et al., 2007). (a) Chandra image taken in 2000, the yellow boxes labeled (b) and (c) represent the location of the zoomed images on the right. (b) and (c) illustrate how the X-ray morphology rapidly evolves over time scales of years.

and Dermer (2012) included a Bremsstrahlung component in their leptonic model but found an insignificant impact using an ISM density of $n_H = 0.2$ cm^{-3}. However, Fukui et al. (2012) use observations of molecular and atomic hydrogen to show that the average ISM gas density over the entire RX J1713.7-3946 region is $n_H \sim 130$ cm^{-3}. This value may increase significantly for smaller, denser regions. The Bremsstrahlung contribution to the total γ-ray emission needs further attention with updated ISM data.

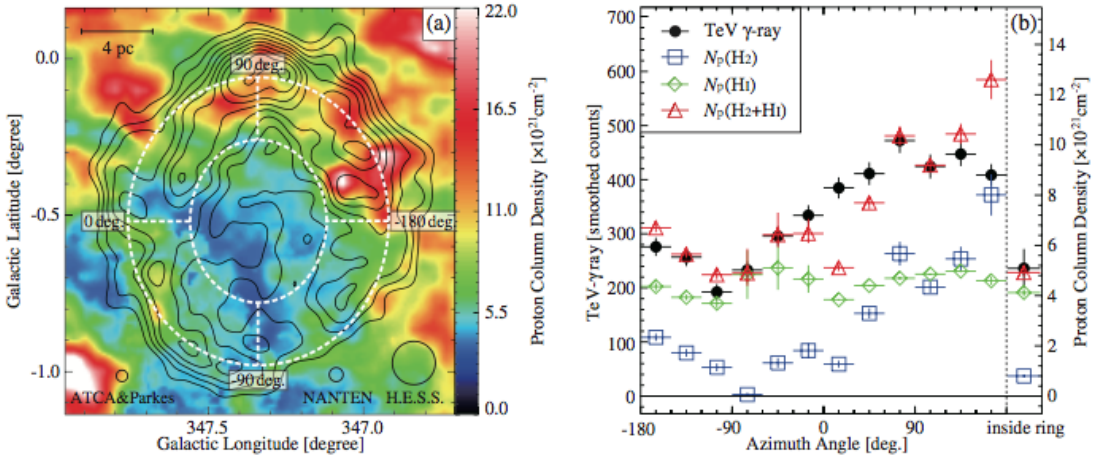

Figure 1.8: (a) The distribution of total ISM protons, using combined data from Nanten and the SGPS, in a velocity range of -20 to 0 km s^{-1}, overlaid with the HESS TeV γ-ray contours in black. The white ellipses indicate the regions used for the correlation analysis in (b). (b) illustrates the azimuthal distributions of the TeV γ-rays, total ISM column density, total atomic hydrogen and total molecular hydrogen. Both images taken from Fukui et al. (2012)

On the other hand, evidence for the hadronic scenario has also been presented. Fukui et al. (2012) reveal an azimuthal correlation between the gas and the TeV γ-ray distribution (Figure 1.8), implying that the gas is strongly connected to the production of the γ-rays. If CR protons are indeed accelerated at this SNR site, then it's hard to avoid the idea that the observed gas clumps are acting as a target for them. Broadband models assuming the γ-ray emission is dominated by the hadronic mechanism often come with downfalls too. We introduce 3 such problems below.

1. Normalising the synchrotron spectrum to the X-ray observations while reducing the contribution from IC scattering at TeV energies, requires extremely intense magnetic fields ($B > 100\mu$G (Tanaka et al., 2008)). This is much higher than the expected average, unless we assume a large amount of X-ray hot spots.

2. Hadronic models require a large target gas density (at least 1 cm^{-3}) to explain the intense γ-ray spectrum. However, the lack of thermal X-ray emission implies that the gas density should be < 0.01 cm^{-3} (Ellison et al., 2010).

3. It has been shown that hadronic models fail to explain the hard / steep GeV spectrum observed by *Fermi*-LAT (see Figure 1.9) (Abdo et al., 2011).

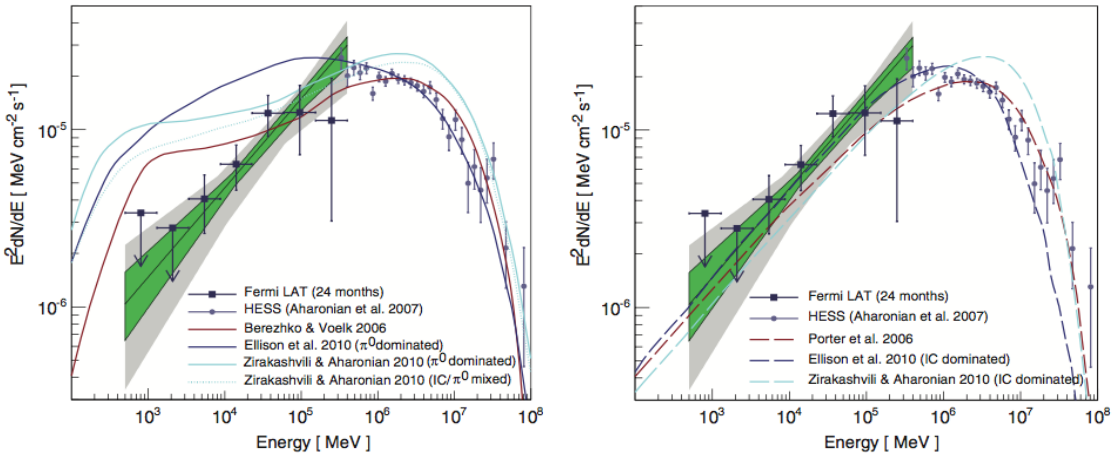

Figure 1.9: Left. Hadronic γ-ray models plotted against *Fermi*-LAT and HESS observations. Right. Leptonic γ-ray models plotted against the same observations. Both images taken from Abdo et al. (2011)

Two-zone hadronic models have been shown to be consistent with the hard *Fermi*-LAT spectrum, wherein an outer-zone consists of escaping, diffusive protons and an inner zone consists of the shock-confined protons (Zhang and Chen, 2016). This also explains why the γ-ray emission extends beyond that of the synchrotron emission (see Acero et al. (2009) etc as referenced earlier). High energy protons escaping the shock propagate further outwards than the confined electrons. If these protons interact with the ISM gas then we should see this extended γ-ray emission. Otherwise, the above setbacks can be made irrelevant if shock-gas interaction models are invoked. These models have been used to

show that dense clumps of gas, $n_H > 10^3$ cm^{-3}, can survive the progenitor stars stellar wind (Inoue et al., 2012; Gabici and Aharonian, 2014; Celli et al., 2018). These clumps go relatively un-shocked by the subsequent SNR shock front and hence wont heat up to produce thermal X-rays. Higher energy protons are more likely to penetrate within the clumps, which also explains the hard GeV spectrum observed (see Figure 1.10).

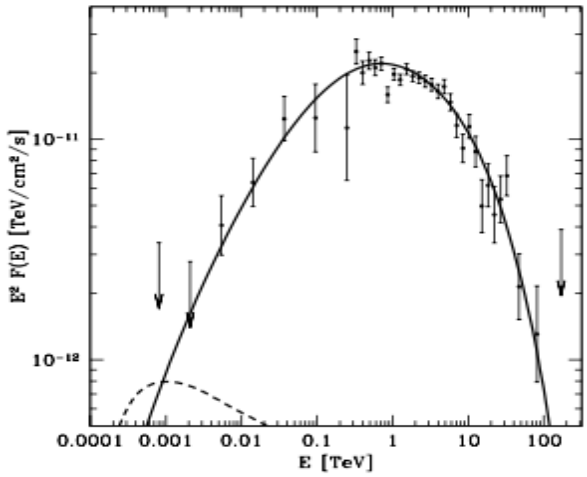

Figure 1.10: The hadronic SED of RX J1713.7-3946, assuming the emission originates from dense clumps (solid line) and diffuse gas in the SNR shell (dashed line) (Gabici and Aharonian, 2014).

Furthermore, at the boundary of the shock-gas interaction sites the magnetic field intensity can reach values above 100 μG (Inoue et al., 2012; Celli et al., 2018), explaining the observations made by Uchiyama et al. (2007). Inoue et al. (2012) and Sano et al. (2013) explain how the X-ray emission should correlate with the gas distribution on a broad scale due to these amplified magnetic fields. However, on much smaller scales, they should anti-correlate due to the amplification occurring at the boundary of the gas clumps and the lack of penetration by the electrons. This correlation/anti-correlation effect is supported by observations of synchrotron emission around cloud cores at different scales (Sano et al., 2010; Sano et al., 2013; Sano et al., 2015). Another consequence of the heightened B field in such locations is the increased synchrotron losses. Electrons will thus have less energy available for IC scattering of photons to γ-ray energies. Identifying the location of such phenomena aids in understanding the γ-ray emission mechanism.

HESS has provided the highest resolution TeV data to date (Figure 1.11) (H18). Using the latest spectral observations from HESS, 29 regions across the SNR are modeled with both a pure hadronic and pure leptonic scenario. The present age particle spectra are derived in each case, as opposed to the initial conditions. Recreating the initial parameter conditions becomes complicated, as they evolve over time. This study also assumed an ISM gas density of 1 cm^{-3} for each region, these values should be updated with actual observations (Mopra or Nanten + SGPS). A focus of this study is to incorporate the latest ISM gas density calculations into the SED models, taking the H18 work a step further.

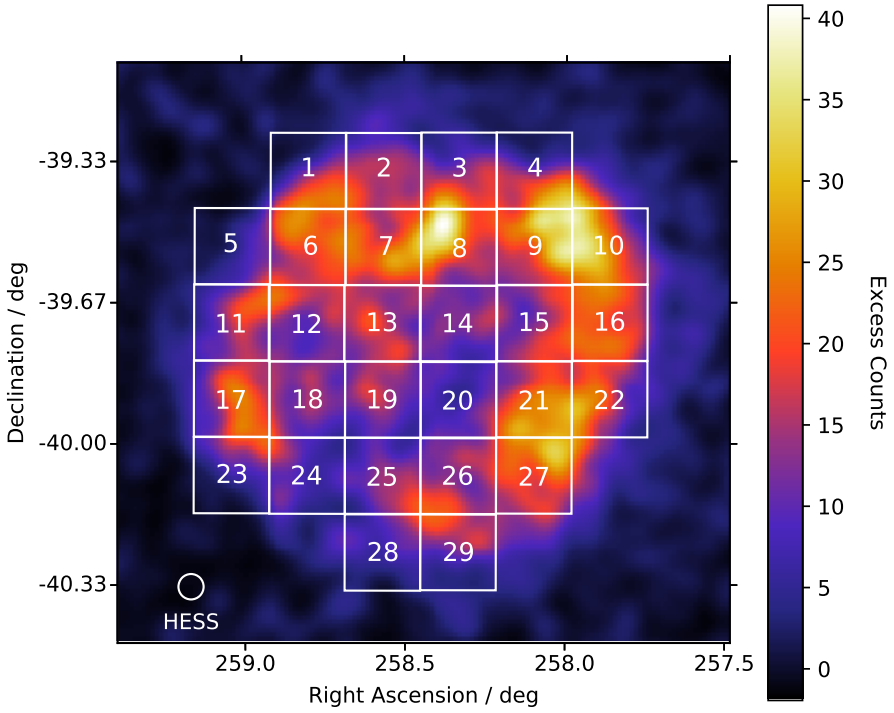

Figure 1.11: HESS γ-ray image of RX J1713.7-3946 for energies greater than 2 TeV. The overlaid white squares represent the 29 sub regions, while the white circle represents the point spread function of the HESS telescope.

2 RX J1713.7-3946 - A Closer Look at the TeV Bright SNR

The main focus of this paper is to determine the origin of the γ-ray emission from RX J1713.7-3946. Whether it be from hadronic or leptonic processes it is important to understand not only the γ-ray morphology, but also the morphology in other energy bands. In this section we present the relavent observations at TeV and GeV γ-ray energies along with those in the X-ray and radio regime. X-ray observations are useful for identifying the emission of synchrotron radiation via accelerated electrons. Regions where this emission is strong should subsequently experience reduced IC emission, due to synchrotron energy losses, hence assisting us in understanding the TeV emission. At lower energies, radio observations are vital for revealing the presence of the ISM gas. Gas clouds, or clumps, act as targets for CRs, with such interactions producing γ-rays. Investigating the spatial correlation between the ISM gas and TeV γ-rays is crucial for understanding this production channel. In this chapter the multi-wavelength observations of RX J1713.7-3946, relevant for this work, are presented.

2.1 HESS TeV Gamma-ray Observations

The High Energy Stereoscopic System (HESS) was originally an array of 4 identical Imaging Atmospheric Cherenkov Telescopes (IACTs) located in Namibia. More recently a 5th telescope has been added. IACTs detect the Cherenkov light emitted by γ-ray air showers and distinguish such events from particle air showers (Funk et al., 2004). Each of the detectors has a diameter of 13 m and a focal length of 15 m (Hinton and the HESS Collaboration, 2004). Each camera consists of 960 pixels of 0.16^{o} angular size, resulting in a field of view of 5^{o}. The original energy threshold was $E_{\gamma} \sim 100$ GeV, but with the more recent addition of a 5th telescope this has decreased to a few tens of GeV (Krayzel et al., 2013).

This work utilizes the latest observations made by HESS across a broad range of γ-ray energies (H18). The observations are compiled from two separate viewing campaigns. The first was run from 2003-2005 and the second from 2011-2012. The first campaign involved a total of 91.3 live hours of data collection (Aharonian et al., 2007). The second campaign involved a total of 78.7 live hours of data collection (H18). Figure 2.1 displays the morphological image for the HESS γ-ray excess counts above the threshold energy of 2 TeV. The energy threshold was applied to improve the angular resolution from 0.048^{o} for the entire data set to 0.036^{o}. The data were originally smoothed with a 2-dimensional Gaussian of width 0.03^{o} and then integrated over a circle of the same radius by H18. The contours were plotted at significance levels of 5, 15 and 25 σ, where σ is the standard deviation of the observations. We use the distribution of pixels from the image to deduce that $1\sigma = 1$ excess count. Thicker lines indicate more intense emission. Our maps are presented in equatorial coordinates to be consistent with H18, however, we refer to regions

in galactic coordinates to be consistent with gas studies like Fukui et al. (2012). There is an obvious shell-like structure, characteristic of an SNR object. In chapter 5 we perform gas correlation studies with this data and further investigate the shell-like features. We

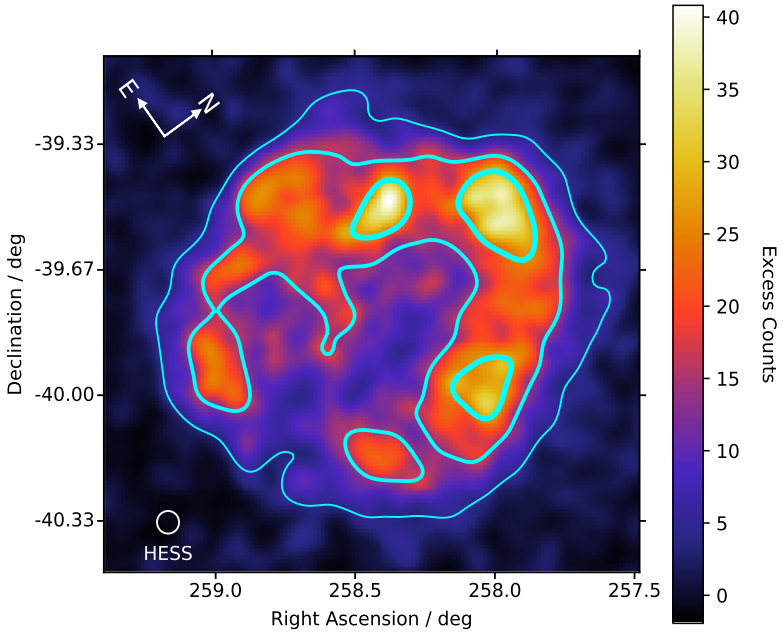

Figure 2.1: Smoothed excess counts of the HESS γ-rays above 2 TeV towards RX J1713.7-3946 overlaid with blue contours. The arrows indicating north and east correspond to galactic coordinates. The white circle indicates the angular resolution of the HESS point spread function.

also obtain the latest spectral data from HESS, see Figure 1.4 for a plot of this. These data have a high resolution enabling us to break the SNR down into 29 separate regions for analysis, following H18. These data will be used in the multi-wavelength SED modeling in chapter 3 and chapter 4.

2.2 Suzaku X-Ray Observations

The *Suzaku* X-ray in-orbit observatory was launched from Japan in 2005. With multiple instruments, the system can detect events in the energy range of 0.2 to 600 keV (Mitsuda et al., 2007). The low energy (0.3-12 keV) instrument, the X-ray Telescope (XRT), has an angular resolution of 2′. On the other hand, the high energy instrument, the Hard X-ray Detector (HXD), is non-imaging.

The *Suzaku* X-ray observations are used for our multi-wavelength spectral energy distribution study (chapter 3 and chapter 4) but can also be applied to our morphological studies (chapter 5). Tanaka et al. (2008) analysed an initial 11 pointings with this telescope and the HESS collaboration performed an additional 4 pointings in 2010 to complete the data set. The high resolution (2′) of *Suzaku* enables us to resolve the spectral data into

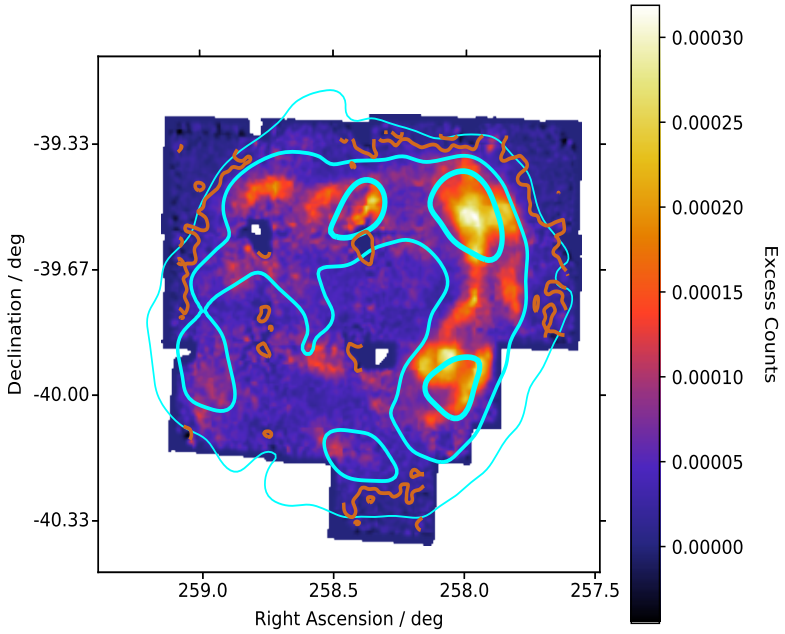

Figure 2.2: *Suzaku* X-ray image towards RX J1713.7-3946 at 5-10 keV with the HESS (> 2 TeV) contours overlaid in blue and the 5σ X-ray contour in brown.

the 29 regions of interest with coverage between 1-60 keV. For an extensive outline of the data analysis method see Tanaka et al. (2008). Figure 2.2 displays the X-ray excess counts map at 5-10 keV. There is an obvious shell-like structure much like that of the γ-ray shell. Additionally, the X-ray peaks appear to coincide with the TeV peaks as already established by Sano et al. (2013). H18 performed a radial analysis of five azimuthal regions in RX J1713.7-3946 with the latest HESS γ-ray data and $XMM - Newton$ X-ray data and found that the radial extent of the γ-ray shell was greater than that of the X-ray shell in four of the regions. In one region in particular, the γ-ray radial extent was $\sim 0.2^{o}$ larger than the synchrotron radial extent. This was interesting as it is the first time such an effect is seen in an SNR shell. H18 interpreted this finding as multi-TeV CRs escaping the main shock region, which is assumed to be located at the peak of the shell emission, or particles being accelerated in the shock precursor. There appears to be a similar trend in some regions with the *Suzaku* X-ray data if we compare both 5σ contours (X-ray contours are in brown).

2.3 Fermi-LAT Observations

The *Fermi* γ-ray space telescope consists of a primary instrument named the Large Area Telescope (*Fermi*-LAT). *Fermi*-LAT covers an energy range from below 20 MeV to more than 300 GeV (Atwood et al., 2009). Because of the overlap with the HESS energy range, observations from these two instruments complement each other. The angular resolution of *Fermi*-LAT is poor at MeV energies (3.5^{o}), but improves to 0.1^{o} at GeV energies.

We use *Fermi*-LAT observations of RX J1713.7-3946 (again, see Figure 1.4) in our multi-

wavelength SED study (Abdo et al., 2011). This data set covers an energy range from 200 MeV to 300 GeV. Unfortunately the *Fermi*-LAT data, even with a resolution of 0.1°, cannot resolve the smaller 29 regions with angular size 0.18° by 0.18°. However, an upper limit can be placed on the 29 regions and we can compare the total combined flux from all regions to this limit.

2.4 Radio Continuum and ISM Gas Observations

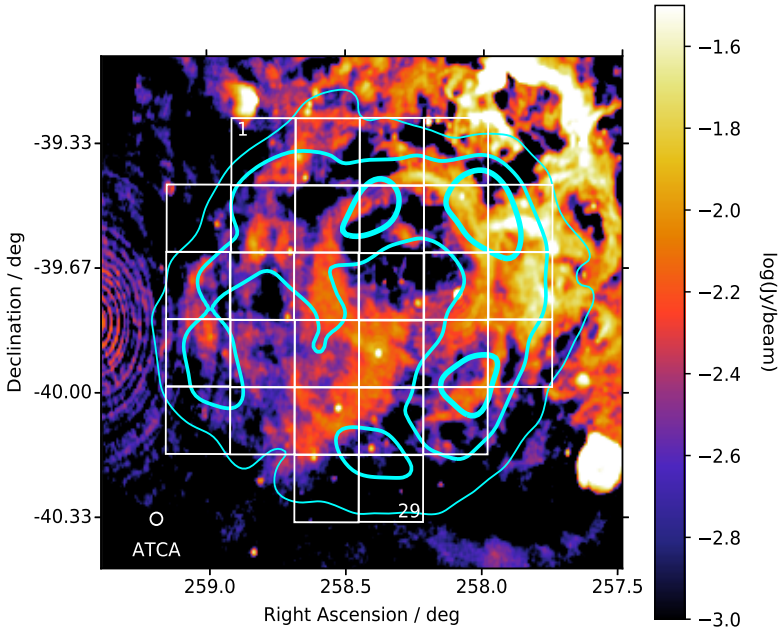

Figure 2.3: ATCA radio image towards RX J1713.7-3946 overlaid with the HESS γ-ray ($>$ 2TeV) contours and the 29 sub-regions. The white circle indicates the beamsize of the ATCA telescope.

The radio continuum ranges from millimetre to kilometre wavelengths requiring large telescopes to achieve high resolution imaging. Radio astronomy is complementary to γ-ray astronomy in that it can be used to reveal the presence of molecular clouds acting as targets for accelerated CRs. Not only this, but radio observations assist with the broadband modeling, as the continuum can reveal the presence of synchrotron X-rays. Below, multiple radio telescopes are discussed along with their observations of RX J1713.7-3946.

2.4.1 ATCA

The Australian Compact Telescope Array (ATCA) surveys HI gas at 21 cm with a high resolution of 2′ (McClure-Griffiths et al., 2005). ATCA spectral data was obtained at 1.4 and 2.5 GHz ($\approx$ 6 and 10 μeV respectively) from Lazendic et al. (2004). Additionally, the

high resolution 1.4 GHz image was used to obtain spectral data for each of the 29 smaller regions.

Reg.	Flux (erg s^{-1} cm^{-2}) $\times 10^{-15}$	Reg.	Flux (erg s^{-1} cm^{-2}) $\times 10^{-15}$	Reg.	Flux (erg s^{-1} cm^{-2}) $\times 10^{-15}$
1	2.32	11	2.15	21	4.54
2	3.81	12	2.82	22	7.03
3	3.91	13	5.66	23	1.13
4	9.26	14	2.29	24	2.52
5	0.33	15	6.07	25	5.87
6	3.44	16	15.07	26	2.76
7	2.18	17	2.66	27	3.51
8	2.19	18	3.21	28	0.81
9	8.50	19	5.12	29	-0.13
10	18.31	20	7.06		

Table 2.1: The observed total radio energy flux at 1.4 GHz for each region within RX J1713.7-3946.

Figure 2.3 displays the radio image, in units of log(Jy/beam) to emphasize the weaker features. Overlaid in blue are the HESS contours and in white are the 29 regions of interest. Again we observed shell-like features, this time in the form of arcs along the west side of the source. The total energy flux for each region can be calculated with a conversion to cgs units (Equation 2.1).

$$\begin{aligned} 1\ \mathrm{Jy} &= 1 \times 10^{-23}\,\mathrm{erg\,s^{-1}\ cm^{-2}\ Hz^{-1}} \\ 1\ \mathrm{Jy\,beam^{-1}} &= \frac{\nu_o \times 10^{-23}}{P}\ \mathrm{erg\,s^{-1}\ cm^{-2}} \end{aligned} \tag{2.1}$$

where P is the number of pixels within a beam area and ν_o is the frequency at which the observations were made. The beam size is 4.059×10^{-4} squared degrees (Lazendic et al., 2004), whilst the area of a pixel is 4.406×10^{-6} squared degrees, hence P = 92, pixels fit within 1 beam. The observed energy flux for each region is presented in Table 2.1. We note that region 29 is dominated by noise, hence a negative flux is not surprising. In the remaining regions the flux varies considerably, by more than a factor of 50 in the most extreme cases. We investigate this variability in **??**.

2.4.2 The Southern Galactic Plane Survey

The Southern Galactic Plane Survey (SGPS) combines data from the ATCA (mentioned above) and the Parkes Radio Telecope. Like the ATCA, the Parkes telescope surveys the sky for HI gas with a 21 cm beam receiver. It makes up the low-resolution (2′) portion of the Southern Galactic Plane Survey (SGPS) and is used to uncover large scale HI structure (McClure-Griffiths et al., 2005). Hence, this combined data set represents the

total intensity, or brightness temperature, of HI gas, the less major component making up the total number of ISM protons.

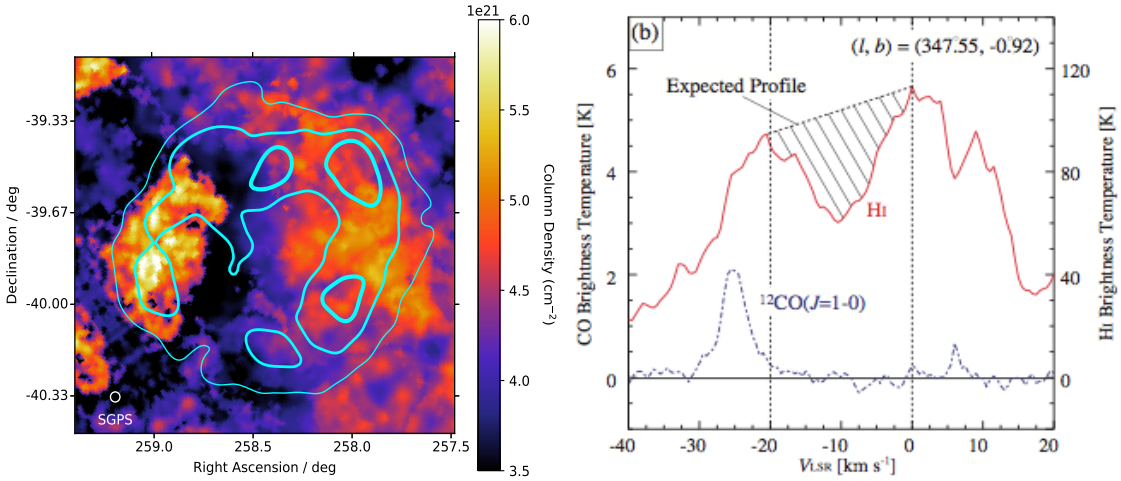

Figure 2.4: Left: The HI column density from the SGPS; made up of data from ATCA and the Parkes radio telescope. A velocity range of -20 to 0 km s^{-1} is integrated over and the HESS contours are overlaid in blue. The image has also been corrected for HI self-absorption. The beamsize of the survey is indicated with a white circle. **Right:** The HI (red) and ^{12}CO (blue) brightness temperature as a function of velocity in the direction of (RA,Dec) = (259.03°,-39.85°). A large dip is seen at -10 km s^{-1} due to the self-absorption of cool HI gas, the expected profile is shaded. Both images are taken from (Fukui et al., 2012).

The HI image of RX J1713.7-3946 is originally from McClure-Griffiths et al. (2005), we obtain the adjusted image from Fukui et al. (2012), which is presented in Figure 2.4 (Left). The data were integrated from -20 to 0 km s^{-1} with a velocity resolution and rms noise fluctuations of $\Delta v = 0.82$ km/s and $T_{rms} = 1.9$ K, respectively. The final angular resolution of the data is approximately 2.2′. The units of brightness temperature, $T(v)$, have been converted to that of column density (cm^{-2}) according to Equation 2.2 from Dickey and Lockman (1990):

$$N_{\rm HI} = 1.823 \times 10^{18} \int T(v) dv \ {\rm cm}^{-2} \tag{2.2}$$

where T is the brightness temperature and v is the velocity. This formula is valid for regions where the HI doesn't appear to suffer from self-absorption. Self-absorption of HI gas within a gas cloud is evident by a dip in the spectrum. Figure 2.4 (right) shows an example of one such dip for the dense cloud seen on the south-east side of RX J1713.7-3946. Other clouds are also analysed in Fukui et al. (2012). It is believed that the self-absorption of cold HI gas occurs within CO gas, so generally, these dips are associated with peaks in the CO spectrum. No CO peak is seen for the eastern cloud, as is evident in Figure 2.4 (Right). It is suggested that this cloud doesn't have the required density for collisional excitation of the CO and as a result has a higher spin temperature, T_S. The spin temperature is used

to calculate the column density, $N_{\rm HI}$ of the missing, or 'dark' HI gas, according to the following:

$$N_{\rm HI} = 1.823 \times 10^{18} \times T_S \times \Delta v \times \bar{\tau}\ {\rm cm}^{-2} \tag{2.3}$$

where $\Delta v = 10$ km s^{-1} is the half-power line width, since we are integrating over a velocity range of 20, and $\bar{\tau}$ is the HI optical depth. Fukui et al. (2012) adopt $T_S = 40$ K for the eastern cloud, which gives an optical depth of $\bar{\tau} = 1.1$. A similar analysis was performed on other regions with self-absorption dips giving us the corrected HI image presented in this study Figure 2.4 (Left).

The shell-like features of the HI gas stand out around the the central-east and west side of the source. We interpret this as the SNRs progenitor star's wind, driving the HI gas outwards and into clumps around the shell. In particular, the dense HI gas observed on the east side of the remnant delineates the γ-ray contours very closely. This gas could be responsible for the γ-ray emission on this side of the remnant. Much of the gas is also contained within the γ-ray shell. This could be an indication that the gas is located in the foreground/background of the spherical SNR shell. These data are combined with molecular hydrogen (H_2) data to obtain a total ISM proton number and provide the basis for the latest ISM gas density calculations. The ISM gas density is used as a spectral parameter (chapter 3 and chapter 4) and also for γ-ray and gas correlations (section chapter 5).

2.4.3 Nanten

The Nanten survey is aimed at mapping the distribution of the 2.6 mm wavelength Carbon Monoxide, specifically, ^{12}CO, throughout the galaxy. The importance of mapping this gas resides in the fact that it is a direct tracer of molecular hydrogen, H_2, the major component of ISM protons. H_2 is not as excitable as CO gas and is near impossible to detect. The angular resolution of the Nanten telescope is 2.6′ (Fukui et al., 2012). This means it can detect gas clumps down to a size of ~ 0.8 pc. Although Nanten observations will be unable to reveal the high resolution detail of the gas morphology, they are still useful for identifying the location of molecular gas clouds.

The Nanten data were obtained from Fukui et al. (2012) but have also been used by Moriguchi et al. (2005) in the past. The data were integrated from -20 km/s to 0 km/s with a velocity resolution and rms noise fluctuations of $\Delta v = 0.65$ km/s and $T_{rms} = 0.3$ K, respectively. Figure 2.5 presents the Nanten image with the HESS contours overlaid in blue. The units of intensity are integrated brightness temperature (K km/s), i.e. integrated over the specified velocity range. The contours are organised such that the thicker lines indicate more intense emission. There appears to be overlap between a γ-ray peak and some bright gas clouds on the west and north side of the SNR. These clouds may represent environments where the bulk of the γ-rays are being produced by pp interactions. The Nanten dataset is used in chapter 5 for our gas correlation study.

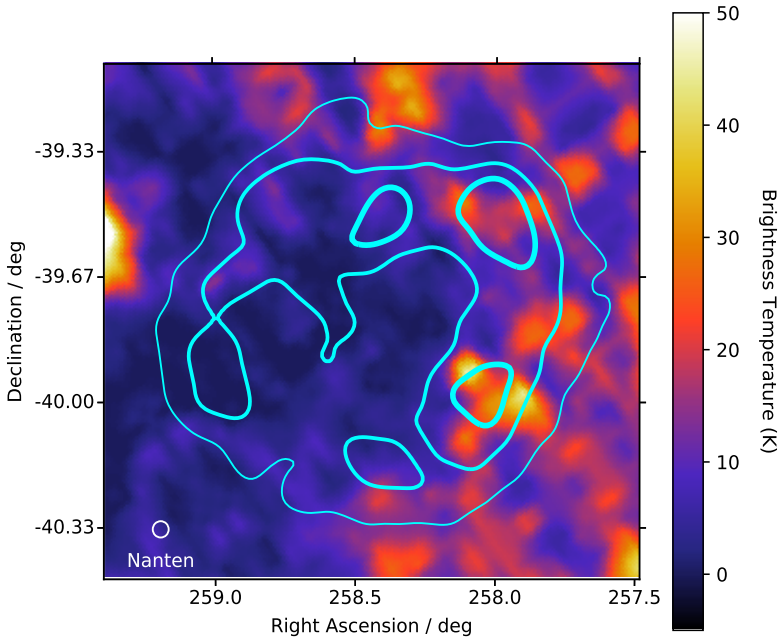

Figure 2.5: Nanten ^{12}CO image towards RX J1713.7-3946 integrated over the velocity range -20-0 km/s and overlaid with the blue HESS contours at levels of 5, 10 and 15 σ. The white circle indicates the beamsize of the Nanten telescope.

2.4.4 Mopra

Just like the Nanten telescope, the Mopra telescope also observes ^{12}CO; however the angular resolution is somewhat better (33″) (Ladd et al., 2005). This enables Mopra to detect small molecular clouds of size 0.16 pc. Additionally the spectral resolution of Mopra is 0.1 km s^{-1} (Burton et al., 2013). It is expected that Mopra and Nanten should yield similar results regardless of their differences. We investigate this with a correlation study in Appendix A.

The Mopra ^{12}CO image of RX J1713.7-3946 is obtained from Braiding et al. (2018). Again the data were integrated from -20 km/s to 0 km/s with rms noise fluctuations of $T_{rms} = 1.5$ K. The units of intensity are brightness temperature (K km/s). After data reduction the final spatial resolution is $0.6'$. Figure 2.6 presents the Mopra image overlaid with the blue HESS TeV contours. There are regions with dense gas along the west side of the remnant and in the south, there also appears to be a gas void around the centre of the SNR creating a shell-like structure. The white arrows point towards clouds of dense gas that also coincide with intense TeV emission. Each cloud is labeled consistently with Moriguchi et al. (2005). An association with synchrotron X-rays has been found for clouds A and C (Sano et al., 2010). It is also argued that cloud C has survived the progenitor stars stellar wind and the SNR shock blast (along with a number of other clouds in other regions) (Sano et al., 2013).

Figure 2.7 illustrates a zoom in of each of the clouds, A, B and C, along with a zoomed image of the region surrounding all three. The TeV γ-ray morphology appears to peak

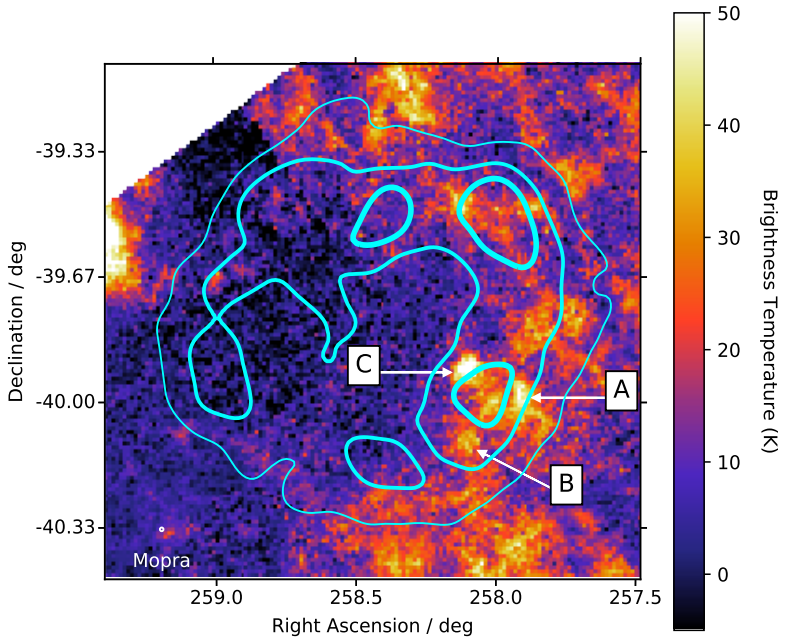

Figure 2.6: The ^{12}CO brightness temperature map from Mopra, integrated in the velocity range of -20 to 0 km s^{-1} and overlaid with the HESS contours in blue. The white circle indicates the beamsize of the Mopra telescope. The three clouds that are discussed in the text are indicated with and arrow and labels.

in the region between the three clouds. Dense gas is still observed here, however, the TeV peak doesn't coincide with any of the cloud cores. Intense TeV emission is still seen towards the clouds, especially A and C, it could be that the shock front and the bulk of the CRs are located in between the two clouds. Otherwise, this could be a result of the HESS point spread function or leptonic process. The Mopra data make up the molecular component of the total ISM protons, which is used to calculate the gas density in each of our regions of interest (chapter 4). Additionally, the morphology of the ISM protons is compared with the γ-ray morphology (chapter 5) to help understand whether γ-rays are accelerated from dense clouds like these.

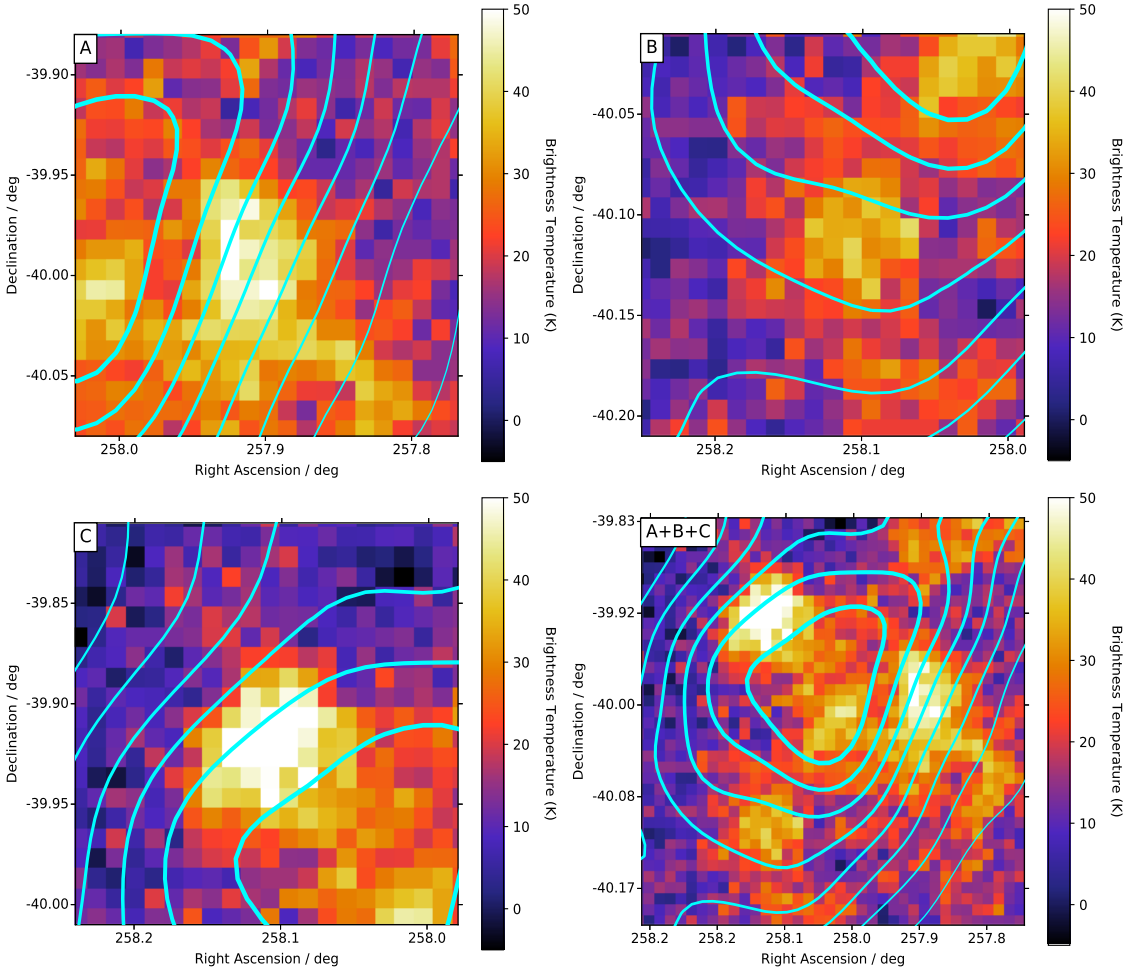

Figure 2.7: Zoomed in images towards the Mopra ^{12}CO map towards three different dense molecular clouds (A,B and C), including a zoomed image of the region surrounding the three clouds.

3 SED Modeling of RX J1713.7-3946 - Whole SNR

This chapter begins by outlining some of the framework relevant to the high energy processes that occur at SNR. Specifically, we introduce the theory behind how the accelerated CRs and electrons are distributed at the shock front. Then we continue on to detail how the γ-ray emission (and other non-thermal emission) is produced via hadronic and leptonic processes. This leads us into applying this theory to a model (either hadronic, leptonic or both) in order to account for the broadband observations of the entire SNR, RX J1713.7-3946. Our models are similar to that of H18, however, we incorporate a more recent measurement of the ISM gas density, required for our hadronic model and also the Bremsstrahlung model. The motivation for this chapter is to introduce this theory and to clarify the success of the code (sedprodv2.c) we use to model the theory.

3.1 Accelerated Particle Population from DSA

Each of the γ-ray producing processes depend on their parent particle population, i.e. the population of particles supplying their energy to the process. This population of particles, whether it be protons or electrons, can be represented first order Fermi acceleration - diffuse shock acceleration (DSA). This theory not only successfully predicts that the particle population should follow a power-law (PL) distribution (Equation 3.1), but also predicts the spectral index, $\alpha = 2$ (Gaisser, 1990). This is quite remarkable considering the observed CR spectrum is believed to be a PL with $\alpha \sim 2.1$ at its source.

$$\frac{dN}{dE} = AE^{-\alpha} \tag{3.1}$$

where A is a normalisation constant, E is the particle's kinetic energy and N is the number of particles, observed over some time and area.

Usually the particle accelerator has been working for a period of time before it is observed. This means some particles have had the opportunity to escape the environment. The time it takes for a particle to escape is called its escape time, τ_{esc}. This escape time is largely dependent on the particles energy; higher energy particles are more likely to escape after a shorter time period. Because of this, the higher energy particles are often suppressed with an exponential cut-off (Equation 3.2), governed by some cut-off energy, E_c.

$$\frac{dN}{dE} = AE^{-\alpha}e^{-E/E_c} \tag{3.2}$$

Additionally, an exponential cut-off may be employed to account for synchrotron losses. High energy electrons will lose their energy via synchrotron losses more readily than their low energy counterparts. As a result, these high energy electrons need to be suppressed.

There are other spectral features one needs to be wary of when modeling an SNR particle distribution. Firstly, Inoue et al. (2012) and Gabici and Aharonian (2014) showed that lower energy CRs cannot successfully penetrate into dense gas clumps unlike their higher energy counterparts. This means when modelling the CR distribution, there may be need to suppress the lower energy CRs. To steepen the CR distribution at low energies an energy-break can be applied, where the spectral index above and below this energy can be different. The spectral index for the low energy CRs can then be chosen such that this part of distribution is steep. The energy at which this break occurs depends on the density of the clumps and the time at which they interact with the shock (Gabici and Aharonian, 2014). Energy breaks are also important in leptonic scenarios, it provides us with another approach to compensate for synchrotron losses. The spectral index of higher energy electrons can be altered, subsequently steeping the spectrum and allowing less high energy electrons into the distribution. The break energy, E_b, can be calculated as the energy at which the SNR age, t_0, and the synchrotron loss time are the same (Equation 3.3).

$$E_b = 1.25 \left(\frac{B}{100\ \mu\mathrm{G}} \right)^{-2} \left(\frac{t_0}{10^3\ \mathrm{yr}} \right)^{-1} \mathrm{TeV} \tag{3.3}$$

The resulting particle distribution then takes on the form of Equation 3.4.

$$\begin{aligned} \frac{dN}{dE} &= A \left(\frac{E}{E_b} \right)^{-\alpha} && \text{if E} < \text{E}_b \\ \frac{dN}{dE} &= A \left(\frac{E}{E_b} \right)^{-\beta} && \text{if E} > \text{E}_b \end{aligned} \tag{3.4}$$

where α and β represent the spectral indices for the low and high energy particles respectively.

Lastly, all the above features can be applied in combination:

$$\begin{aligned} \frac{dN}{dE} &= A \left(\frac{E}{E_b} \right)^{-\alpha} e^{-E/E_c} && \text{if E} < \text{E}_b \\ \frac{dN}{dE} &= A \left(\frac{E}{E_b} \right)^{-\beta} e^{-E/E_c} && \text{if E} > \text{E}_b \end{aligned} \tag{3.5}$$

In Appendix C we illustrate some examples of how these PL distributions differ.

The normalisation, A, in all 4 cases, is controlled by the energy budget, W, of the particles, which is supplied by the SNR explosion (Equation 3.6). The energy budget is the amount of energy distributed to the entire particle population. In the case of a SN, it is some factor, η, of the 10^{51} erg budget. This factor is defined as the CR efficiency of the SNR.

$$W = \eta \times 10^{51} = 1.602 \int_{E_{min}}^{E_{max}} E \frac{dN}{dE} dE\ \mathrm{erg} \tag{3.6}$$

For any of the given PLs Equation 3.6 can be solved to obtain A.

3.2 Gamma-Rays from Cosmic Rays

Here, we describe each γ-ray production process in more detail and how each can be modeled. We begin by introducing the hadronic model, which consists of pp interactions. This framework is described in detail by Kafexhiu et al. (2014). Basically, pp interactions involve a CR proton colliding elastically with a stationary proton (gas cloud) to produce a neutral pion that subsequently decays into two γ-rays. The overall resulting γ-ray flux, Φ_γ depends on the initial proton distribution, the differential cross section of the interaction, and the amount of target protons (or their number density) as per Equation 3.7.

$$\Phi_\gamma = 4\pi c n_H \int \frac{d\sigma}{dE_\gamma} \frac{dN_p}{dE_p} dE_p \tag{3.7}$$

where E_p is the proton energy, n_H is the density of hydrogen (protons) in the target gas, $\frac{dN_p}{dE_p}$ is the CR proton number distribution and $\frac{d\sigma}{dE_\gamma}$ is the differential cross section, which will be discussed now.

The cross section can be expressed as:

$$\frac{d\sigma}{dE_\gamma}(E_p, E_\gamma) = A_{max}(E_p) \times F(E_p, E_\gamma) \tag{3.8}$$

where A_{max} is the max value of $\frac{d\sigma}{dE_\gamma}$ and depends on the proton energy. $F(E_p, E_\gamma)$ describes the shape of the function and depends on both proton and γ-ray energy. Both functions involve extensive parametrisations, which are omitted here but can be found as Eq. 9-12 in Kafexhiu et al. (2014).

CR protons must have a certain threshold energy in order to produce pions. One can use 4-vector analysis and the invariance of the product of the 4-momentum, $p^\mu = (E/c, \vec{p})$, with itself to find the threshold energy, $E_{p,\mathrm{thres}} \sim 1.218$ GeV. A derivation of this can be found in Appendix B. Consequently, we account for this by integrating Equation 3.7 from $E_{p,\mathrm{thres}}$ up to some maximum energy. Hillas (1972) suggested that the maximum energy for a CR proton accelerated in an SNR is 10 PeV, whereas a maximum of 100 TeV is suggested by Lagage and Cesarsky (1983). The difference between these two extremes is minimal once am exponential cut-off is applied to the proton distribution.

3.3 Gamma-Rays and Low Energy Radiation from Leptons

There are two processes that can produce γ-rays via interactions with leptonic particles in SNRs. However one must also understand the origin of the synchrotron radiation as this process competes for the same electron energy. Additionally, fitting the synchrotron spectrum to radio and X-ray observations is helpful in constraining the electron distribution, as we will see later.

3.3.1 Inverse Compton Scattering

We begin by outlining the inverse Compton (IC) process, where a low-energy photon is up-scattered by an electron. Consider a single electron of a particular energy, E_e, interacting with a photon field (CMB or other), the resultant γ-ray spectrum per electron is then

$$\frac{dN_\gamma}{dtd\epsilon}(E_e, \epsilon, \epsilon_i) = \frac{3}{4}\sigma_T c\left(\frac{m_e}{E_e}\right)^2 \int \frac{B(\epsilon_i) f_{IC}(E_e, \epsilon, \epsilon_i)}{\epsilon_i} d\epsilon_i \tag{3.9}$$

where ϵ is the excited γ-ray energy, ϵ_i is the initial photon energy, σ_T is the Thomson cross section, $B(\epsilon_i)$ is the black body distribution of the target photon field and f_{IC} is the IC distribution function (Meyer et al., 2010; Blumenthal and Gould, 1970; Manolakou et al., 2007). The subscript i simply denotes a property of the initial conditions.

The black body distribution function assumes that the photon field is a perfect black body and follows Planck's law (Equation 3.10).

$$B(\epsilon_i) = \frac{8\pi}{(hc)^3} \frac{\epsilon_i^2}{(e^{\epsilon_i/k_B T}) - 1} \tag{3.10}$$

where T is the temperature of the photon field, h is Planck's constant and k_B is the Stefan-Boltzmann constant. Planck's law can also be rewritten in terms of the energy density of the photon field, U_{rad}, which is approximated as:

$$U_{rad} = \frac{8\pi^5 (k_B T)^4}{15(hc)^3} \,. \tag{3.11}$$

The blackbody distribution function then becomes:

$$B(\epsilon_i) = \frac{15 U_{rad}}{(\pi k_B T)^4} \frac{\epsilon_i^2}{(e^{\epsilon_i/k_B T}) - 1} \,. \tag{3.12}$$

There are three main radiation sources that compose the interstellar radiation field (ISRF); the CMB, stellar radiation and radiation from dust. The CMB is commonly taken to be the most dominant source in terms of the γ-ray emission (Aharonian et al., 1997). However, the energy density of the other two fields does change throughout the galaxy, so often it is necessary to consider them.

The IC distribution function, f_{IC}, is the result of applying the Klein-Nishina limit to the IC cross section. This limit applies when the photon energy, ϵ_i, in the electron rest frame, before scattering is much greater than $m_e c^2$. It is most simple to express this function in terms of p and q where:

$$p = \frac{4\epsilon_i E_e}{m_e^2} \,, \tag{3.13}$$

$$q = \frac{\epsilon m_e^2}{4\epsilon_i E_e (E_e - \epsilon)} \,, \tag{3.14}$$

so that:

$$f_{IC} = 2q \ln q + (1 + 2q)(1 - q) + \frac{1}{2} p^2 q^2 \frac{1 - q}{1 + pq} \,. \tag{3.15}$$

Alternatively, the last term in this expression vanishes when in the Thomson limit. This limit is the opposing case to the Klein-Nishina limit, i.e. when $\epsilon_i \ll m_e c^2$.

If we then integrate Equation 3.9 and the particle distribution over all particle energies, we will obtain the total emitted γ-ray flux due to IC scattering:

$$\Phi_{IC} = \int \frac{dN_\gamma}{dtd\epsilon} \frac{dN_e}{dE_e} dE_e \, . \tag{3.16}$$

3.3.2 Synchrotron Radiation

Synchrotron radiation is the other important leptonic process to consider when attempting to model the γ-ray emission from an SNR. The magnetic field conditions, which can range from 5 μG to 1 mG at the shock front (Inoue et al., 2012), result in synchrotron emission in the radio to X-ray regime. Although it doesn't necessarily emit in the γ-ray regime, it aids in constraining the parameters used in the IC modeling. Synchrotron radiation is emitted by electrons that are accelerated by magnetic fields. Since it is the only dominant form of radiation expected in the radio to X-ray spectrum around SNRs, its detection demands the presence of electrons. However, the same electron population provides its energy to both synchrotron processes and IC scattering, meaning that whatever energy is consumed by synchrotron processes will not be available for IC scatterings.

The synchrotron emission due to a population of electrons in a magnetic field depends on the magnetic field strength, B, and the pitch angle α, e.g. the direction of the electron with respect to the magnetic field. As described by Blumenthal and Gould (1970), Manolakou et al. (2007), and Meyer et al. (2010) the power emitted by a single electron per unit frequency is:

$$P_\alpha(\nu) = \frac{\sqrt{3} e^3 B c}{4\pi\epsilon_0 m_e h} \frac{1}{\epsilon} \sin\alpha K_T \tag{3.17}$$

where e is the charge of the electron, B is the magnetic field strength, ϵ is the energy of the final photon, h is Planck's constant and K_T is the integrated form of the modified Bessel function of order $5/3$:

$$K_T = \int x K_{5/3}(x) dx \tag{3.18}$$

where $x = \nu/\nu_c$, ν being the photon's frequency and ν_c being a critical frequency with form:

$$\nu_c = \frac{3eBc^2}{4\pi m_e} \left(\frac{E_e}{m_e} \right)^2 \sin\alpha. \tag{3.19}$$

To obtain the power over all directions we must integrate over all α:

$$P(\nu) = \int P_\alpha(\nu) \sin\alpha d\alpha. \tag{3.20}$$

This can then be used to calculate the total synchrotron flux emitted from the electron population:

$$\Phi_{Synch} = \int P(\nu) \frac{dN_e}{dE_e} dE_e. \tag{3.21}$$

The key dependence of synchrotron radiation lies in the B field; for large B fields, the electron population will suffer large synchrotron losses, leaving less energy available for IC scattering.

Additionally, we can approximate the electron energy, E_e, associated with synchrotron photons radiated at energy E_γ (Slane et al., 1999) as:

$$E_e = \frac{300}{B_{\mu\mathrm{G}}^{0.5}} \left(\frac{E_\gamma}{1\ \mathrm{keV}} \right)^{0.5} \mathrm{TeV} \tag{3.22}$$

where $B_{\mu\mathrm{G}}$ is the magnetic field strength in units of μG.

3.3.3 Relativistic Bremsstrahlung

The final relevant leptonic process that will be discussed is relativistic Bremsstrahlung radiation. An electron is scattered by the Coulomb field of another charged particle and a photon is emitted. This process involves a proper treatment of quantum electrodynamics; second-order perturbation theory is needed to explain the effect so we will just quote the most basic result for the cross section, $d\sigma_B$, of the interaction between an electron and a nucleus, as in Blumenthal and Gould (1970):

$$d\sigma_B = 4Z^2 \alpha r_0^2 \frac{d\omega}{\omega} \frac{1}{E_i^2} (E_i^2 + E_f^2 - \frac{2}{3} E_i E_f) \left(\ln \frac{2E_i E_f}{mc^2 \hbar\omega} - \frac{1}{2} \right) \tag{3.23}$$

Z is the atomic number of the charged particle/nucleus, α is the fine structure constant (not to be confused with the spectral index), r_0 is the classical electron radius, $\hbar\omega$ is the energy of the radiated photon, E_i is the electron's initial energy and E_f is the electron's final energy. The cross section formula becomes more complicated when one begins to include nuclei with bound electrons, but extensive analyses can be found in Gould (1969) and Koch and Motz (1959). We can also highlight the fact that Bremsstrahlung radiation depends on a target of charged nuclei and hence the emission of such radiation will depend on the density of the target material, whether it be ISM gas or something else providing the interaction. The resulting Bremsstrahlung spectrum (Equation 3.24) will then be similar to that of the PP spectrum (Equation 3.7) except it will depend on a different cross-section (Equation 3.23) and a population of electrons.

$$\Phi_{Brems} = 4\pi n_H \int \frac{d\sigma}{dE_\gamma} \frac{dN_e}{dE_e} dE_e \tag{3.24}$$

3.4 Energy Conversion and Cooling Times

The aforementioned emission processes all take time to radiate their energy away as photons. Because the three leptonic processes will be competing over the same electron population, it is important to determine which process will radiate energy away the quickest. The time it takes for a population of particles to radiate all their energy away via a particular process is called the cooling time. A process with a short cooling time will

initially dominate the energy consumption over a process with a long cooling time. The cooling times for each of the four process can be derived by re-arranging the energy loss rate, $\dot{E} = dE/dt$, for that process:

$$t_{cool} = \frac{E}{\dot{E}} \,. \tag{3.25}$$

The energy loss rate expressions for each process are listed in Equation 3.26.

$$\begin{aligned} \dot{E}_{PP} =& n_H \sigma_{pp} f c E_p \\ \dot{E}_{IC} =& \frac{4}{3} \sigma_T c U_{\text{rad}} \left(\frac{E_e}{m_e c^2} \right)^2 \\ \dot{E}_{sync} =& \frac{4}{3} \sigma_T c U_B \left(\frac{E_e}{m_e c^2} \right)^2 \\ \dot{E}_{brems} =& \frac{9}{7} \sigma_o c n_H E_e \end{aligned} \tag{3.26}$$

where c is the speed of light, n_H is the ISM gas density, $f \sim 0.5$ is the in-elasticity for a single PP interaction (Gaisser, 1990), σ_{pp} is the PP cross-section, E_p is the proton energy, $\sigma_T = 6.65 \times 10^{-25}$ cm^2 is the Thomson cross-section, E_e is the electron energy, m_e is the electron mass, U_{rad} is the energy density of the photon field, $U_B = B^2/8\pi$ is the energy density of the magnetic field and lastly, σ_o is the pair production cross-section. Hence the cooling time for pion decay becomes:

$$\begin{aligned} t_{pp} &= (n_H \sigma_{pp} f c)^{-1} \\ t_{pp} &\approx 5.3 \times 10^7 (n_H/\text{cm}^3)^{-1} \text{ years} \end{aligned} \tag{3.27}$$

and only depends on the ISM gas density. Similarly, for the other three processes we can derive the following cooling times

$$\begin{aligned} t_{IC} &\approx 3 \times 10^5 (U_{\text{rad}}/\text{eV/cm}^3)^{-1} (E_e/\text{TeV})^{-1} \text{ years} \\ t_{sync} &\approx 1.2 \times 10^7 (B/\mu\text{G})^{-2} (E_e/\text{TeV})^{-1} \text{ years} \\ t_{brems} &\approx 4 \times 10^7 (n_H/\text{cm}^3)^{-1} \text{ years} \end{aligned} \tag{3.28}$$

Since the latter three processes are those competing for the electron's energy, it makes sense to consider their cooling times. At first glance it might seem as if IC scattering generally has the shortest cooling time, however the B^{-2} dependence of the synchrotron cooling time decreases it drastically. This will become more clear later when we establish appropriate values for all these parameters. The Bremsstrahlung cooling time only depends on the ISM gas density and is generally quite large considering the galactic average is about 1 hydrogen atom per cm^3 (Gordon and Burton, 1976). However, for situations where the gas density is larger than this, RX J1713.7-3946 for example ($n_H = 130$ cm^{-3} as predicted by Fukui et al. (2012)), Bremsstrahlung processes may become more significant. For now we consider consider the cooling times for a typical diffuse magnetic field strength, $B = 5$ μG, the results are shown as a function of electron energy on Figure 3.1. Clearly, we can see that Bremsstrahlung radiation is not of importance unless the gas density is

~ 130 cm^{-3}, even then still, only at low electron energies. The synchrotron channel seems dominant, even for the diffuse magnetic field strength.

Additionally, we have incorporated the IC cooling time from both the Thompson and Klein-Nishina cross section assumptions. Equation 3.28 displays the equation for the Thompson cross section cooling time, while the equation for the Klein-Nishina cooling time, $t_{\mathrm{IC,KN}}$, is show in Equation 3.29 (Manolakou et al., 2007).

$$t_{\mathrm{IC,KN}} = 1.6 \times 10^{13} \left(\frac{U_{\mathrm{rad}}}{\mathrm{eV\ cm^{-3}}} \right)^{-1} \frac{m_e c^2}{E_e} \left(1 + 4E_e \frac{2.8kT}{(m_e c^2)^2} \right) \text{ years} \tag{3.29}$$

where k is the Boltzmann constant, T is the temperature of the photon field and m_e is the mass of the electron. As can be seen from Figure 3.1, the Klein-Nishina cross section begins to affect the cooling time at energies above ~ 10 TeV. Not until the electron energy reaches above ~ 100 TeV is their a remarkable difference. The Bremsstrahlung cooling time would need to be a factor of ~ 10 smaller in order for it to be similar to this Klein-Nishina cooling time. Since the Bremsstrahlung cooling time is directly proportional to the ISM density, this would require $n_H \sim 10^3$ cm^{-3}. Our study will most likely be relevant to electrons with energy less than 100 TeV and an ISM gas density of less than 10^3 cm^{-3}. For this reason we assume the Thompson cross section regime when analysing the cooling times throughout this work.

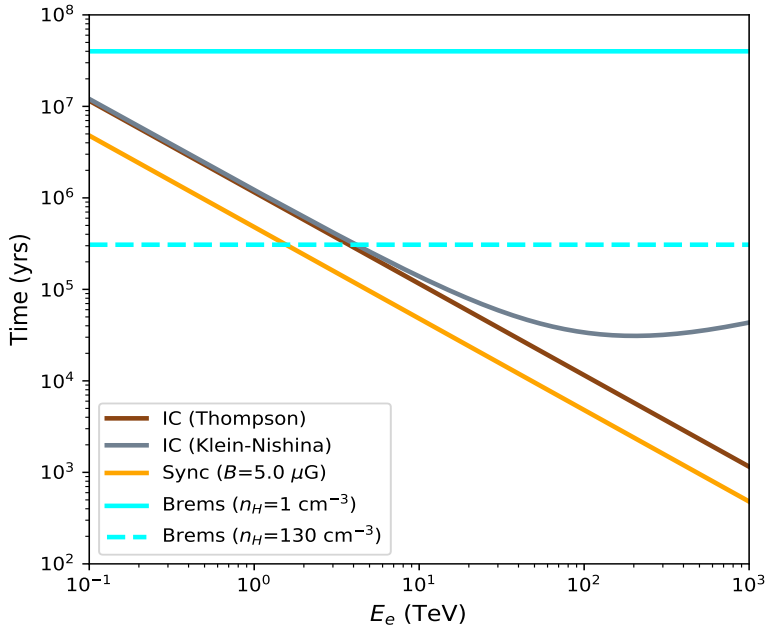

Figure 3.1: The cooling times vs electron energy for the three leptonic processes. The synchrotron cooling time assumes a magnetic field strength of 5 μG, whereas two different values of ISM density are assumed for Bremsstrahlung (see legend). Additionally, the IC cooling time is calculated assuming both the Thompson and Klein-Nishina cross section.

3.5 sedv2.c and Spectral Energy Distributions

Above, we have introduced the theory behind each spectral emission process along with other SNR-related astrophysics. The sedv2.c code integrates the necessary features of this theory, allowing us to successfully model the expected spectral emission from SNRs. The code allows an extensive list of input parameters: energy budget, proton energy fraction, source distance, source size, source age, ISM gas density, magnetic field strength, choice of particle distribution along with all defining spectral parameters, photon field parameters (energy density and temperature) and whether or not the source evolves with time. Applying the evolution option was beyond the scope of this work, hence we refrain from specifying the intricate details. The code also allows an option for simulating pulsar wind nebulae (PWNe), which are accelerating environments similar to SNRs. The distinguishing feature is that PWNe experience a continuous source of injected particles, while SNRs are better approximated by an impulsive injection. The resulting spectral flux is often displayed as a spectral energy distribution (SED). A SED is a plot of photon flux as a function of photon energy, where the flux is commonly multiplied by E^2 to emphasise the energy contained in each bin.

3.6 Simulated Particle Distributions of RX J1713.7-3946

H18 used the Monte Carlo fitting techniques of *naima* (Zabalza, 2015) to derive the best-fit parameters of both particle distributions for the entire SNR. The broadband observations were best fit with a broken power law with a cut-off (Equation 3.5) in both cases. The parameters describing each distribution are presented in Table 3.1. We attempt to model our particle distributions with these parameters. Only the low energy spectral index, α, for the electron distribution required adjusting (see Table 3.1). This final value was obtained by eye, by matching the spectrum to the observations.

Parameters	Proton	Electron
α	1.53	1.85 (1.78)
β	1.94	2.93
E_b (TeV)	1.4	2.5
E_c (TeV)	93	88
B (μG)	-	14.3

Table 3.1: The RX J1713.7-3946 proton and electron distribution parameters as modeled by H18. In both cases a PL with a combined exponential cut-off and energy-break has been applied Equation 3.5. The brackets indicate parameters that are used in this study, if different from H18.

The energy budget for the proton population, with an ISM gas cloud density of n_H, is specified to be $W_p(> 1\text{TeV}) = 5.80 \times 10^{49}(1\text{cm}^{-3}/n_H)$ erg (H18). We expect this value to decrease once we apply the average ISM gas density over the entire SNR. Fukui et al. (2012) calculate the average gas density over the entire SNR region to be $n_H = 130$ cm^{-3}.

This value is used for our modeling, as opposed to $n_H = 1$ cm^{-3} in H18. Meanwhile, the H18 electron population only required an energy budget of $W_e(> 1\text{TeV}) = 1.19 \times 10^{47}$ erg.

Our code requires a particle energy budget over the entire energy range, whereas H18 quoted their energy budgets only from particles with energy greater than 1 TeV (i.e. W_p(>1 TeV) and W_e(>1 TeV)). We re-normalise their values to an energy budget for the whole energy spectrum, (W_p and W_e) to check if our model is consistent with theirs. The re-normalisation uses the following idea of rearranging for the normalisation constant A in Equation 3.6,

$$W_{p/e}(> 1\text{TeV}) = A \int_{1\text{TeV}}^{\infty} E^{-\alpha+1} dE$$
$$A = \frac{W_{p/e}(> 1\text{TeV})}{\int_{1\text{TeV}}^{\infty} E^{-\alpha+1} dE}.$$

Hence the total particle energy budget becomes

$$\begin{aligned} W_{p/e} &= A \int_{\text{E}_0}^{\infty} E^{-\alpha+1} dE \\ W_{p/e} &= \frac{W_{p/e}(> 1\text{TeV})}{\int_{1\text{TeV}}^{\infty} E^{-\alpha+1} dE} \int_{\text{E}_0}^{\infty} E^{-\alpha+1} dE \,. \end{aligned} \tag{3.30}$$

Depending on the case, E_0 is either the proton threshold energy (1.218 GeV) or the electron threshold energy, which for simplicity we take to be the rest-mass energy of the electron (0.511 MeV). The above was done assuming a simple power law, but it is easily adapted for the functional form we used. Table 3.2 displays the H18 values for the total energy budget, e.g. after applying this normalisation and assuming an ISM gas density of $n_H = 130$ cm^{-3}, and also our derived values for our model after matching to the data. Our values are consistent with their work.

	H18	This work
$W_p(\times 10^{47})$ erg	6.50	6.50
$W_e(\times 10^{47})$ erg	5.05	4.30

Table 3.2: Both the proton and electron energy budgets required for our model to match the data and for comparison, those used in H18.

A comparison of our parent particle distributions is made with those of H18. As can be seen in Figure 3.2, the proton distributions are very consistent with each other. Meanwhile our electron distribution deviates slightly due to the altered parameters (W_e and α). The consistencies confirm that the particle distributions are being modeled correctly when using an impulsive scenario (SNR).

Thus far we have introduced how the particle distributions have been modeled, such that they produce γ-ray spectra that matches the broadband observations. In the next

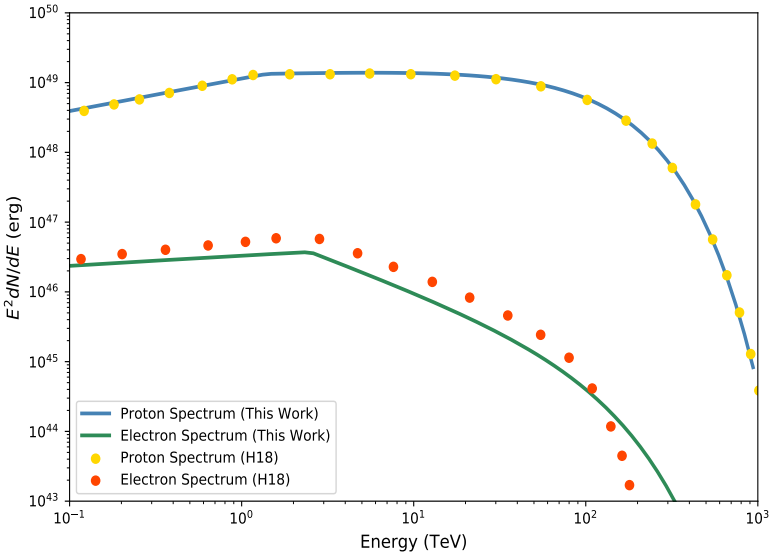

Figure 3.2: The proton and primary electron distributions derived for this work compared with those from H18.

two sections we present the spectra from both the hadronic and leptonic scenarios. We know from H18 that both these scenarios can explain the γ-ray spectrum over the entire remnant, however, for completeness we present the models and provide some brief discussion. Importantly, we extend the H18 leptonic model by including the Bremsstrahlung component produced by the same population of electrons. This will help us understand whether the contribution from Bremsstrahlung radiation is significant at any energies over the entire remnant. Because we are matching to the current observations, the derived parameters (from this section and the following) represent the current situation, not the initial conditions. For the following section we assume the SNR is located at the favoured distance of 1 kpc, with a radius of 10.5 pc.

3.7 Simulated Hadronic Gamma-Ray Emission from RX J1713.7-3946

The hadronic model was computed using the latest ISM gas density value averaged over the SNR, $n_H = 130$ cm^{-3} (Fukui et al., 2012), the proton distribution parameters from Table 3.1 and the proton energy budget from Table 3.2 (W_p). The model was matched to both the H18 and Fermi-LAT observations. The synchrotron spectrum is not included in this model so no B field parameter is required. Figure 3.3 displays the hadronic model including the comparison with the H18 model along with the broadband observations. The two models have a slight discrepancy. At energies lower than ~ 10 GeV our model over-predicts the flux output compared to H18, whereas the opposite occurs at higher energies. Despite this small inconsistency, our models agree with the observations.

As mentioned above, the synchrotron spectrum is not included; in the case that it was, we might expect to require a large magnetic field in order to suppress the IC component.

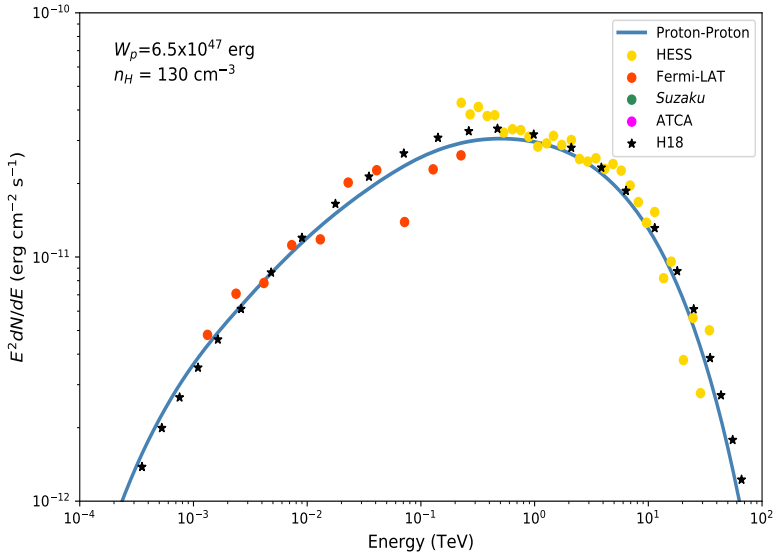

Figure 3.3: SED of the Hadronic model of γ-ray flux for source RX J1713.7-3946. A proton energy budget of 6.5×10^{47} was used.

(Tanaka et al., 2008) showed that an average magnetic field of 200 mG was required for their hadronic scenario. Magnetic fields of this strength may be feasible in sub-parsec scale regions considering the results from Uchiyama et al. (2007). However, not for the average magnetic field strength over the entire SNR. It is also worthwhile to consider the affect of secondary electrons on the synchrotron spectrum; recall the secondary particles produced in pp interactions (Equation 1.3):

$$\begin{aligned} \pi^+ &\rightarrow \mu^+ + \nu_\mu \\ \mu^+ &\rightarrow e^+ + \nu_e + \bar{\nu}_\mu \\ \pi^- &\rightarrow \mu^- + \bar{\nu}_\mu \\ \mu^- &\rightarrow e^- + \bar{\nu}_e + \nu_\mu \end{aligned}$$

The bulk of these secondary electrons will be produced within gas clumps, where the pp interactions are occurring. Huang et al. (2018) showed that only when a magnetic field of 2 mG is experienced, a significant contribution to the radio-synchrotron spectrum is seen from the secondary electrons. The magnetic field amplification occurs around the gas clumps, not within, so it seems unlikely that such a scenario would occur within them. However, the secondary electrons can penetrate out of the clouds before radiating their energy away via synchrotron radiation. Gabici et al. (2009) discuss how secondary electrons between the energies of 100 MeV and a few hundred TeV should escape the clumps quickly. Consequently, these electrons may in fact experience the amplified magnetic fields required to have an affect on the radio spectrum. We do not address this issue further in this work but it is still something of importance to consider. In the next section we model the leptonic broadband model assuming the synchrotron flux is strictly produced by primary electrons.

3.8 Simulated Leptonic Broadband Emission from RX J1713.7-3946

As discussed previously (section 3.3) the leptonic model combines the spectra from IC scattering, synchrotron radiation and bremsstrahlung radiation. The IC model was calculated using the CMB ($T = 2.7$ K and $U_{rad} = 0.26$ eV cm^{-3}) and a far-infrared photon field ($T = 26.5$ K and $U_{rad} = 0.415$ eV cm^{-3}), as per H18. This model was matched to the H18 and Fermi-LAT spectrum for the whole SNR by using the electron distribution parameters from Table 3.1 and the electron energy budget from Table 3.2 (W_e). The synchrotron model was matched to the *Suzaku* and ATCA observations, assuming the same population of electrons and by altering the magnetic field until the model was normalised correctly against the IC component. The magnetic field was found to be $B = 14.3$ μG. Lastly, the Bremsstrahlung component was computed with a target gas density of $n_H = 130$ cm^{-3}. This component was included to test whether it made a significant contribution to the entire leptonic spectrum at any energies.

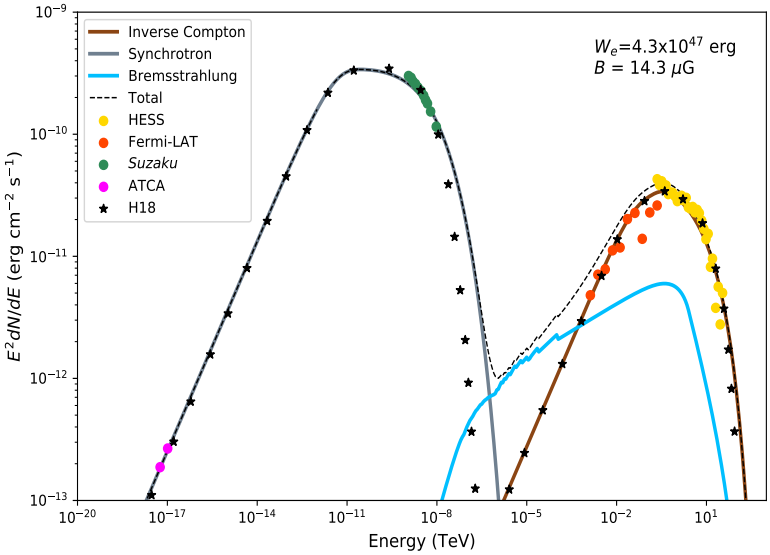

Figure 3.4: SED of the Leptonic model of γ-ray flux for source RX J1713.7-3946. See the legend for a depiction of each model. An electron energy budget of 4.3×10^{47} erg and an average magnetic field strength of 14.3 μG were used.

Figure 3.4 displays the leptonic model including the comparison with the H18 model and the Bremsstrahlung contribution. There appears to be some discrepancy between our model and that of H18 at X-ray energies, otherwise the 2 models are well matched. This may be a result of the different low-energy spectral index, α. The Bremsstrahlung contribution is a factor of $\sim 3 - 4$ smaller than the IC peak at TeV energies. It appears to affect the combined γ-ray spectrum only slightly. This effect becomes slightly stronger at GeV energies where the IC spectrum is hard. Bremsstrahlung is also dominant around the MeV range, where unfortunately, observational data are not available. Fermi-LAT observations aren't resolvable at these energies. This component is heavily dependent on the ISM gas density, since we have used an average value over the entire SNR it is

not representative of smaller regions where the gas might be more dense. At the same time though, regions with dense gas clumps will be surrounded by intense magnetic fields, amplifying the synchrotron spectrum. The electrons will suffer synchrotron losses, which will subsequently affect the bremsstrahlung spectrum (and the IC spectrum). We investigate this issue from a regional perspective in the next chapter.

3.9 Simulated Combined (Leptonic + Hadronic) Emission from RX J1713.7-3946

A combined hadronic-leptonic model of the entire SNR source is presented in this section. To match the combined model to the data we began with the H18 parameters from Table 3.1. We also needed some way to quantify the energy budget of both protons and electron distributions. Schlickeiser (2002) and Merten et al. (2017) derive an expression for the luminosity ratio of electrons to protons by assuming that the same total number of electrons and protons are accelerated at the SNR and that they share the same spectral index:

$$K_{ep} = \left(\frac{m_e}{m_p}\right)^{\alpha-1/2} \tag{3.31}$$

where α is the spectral index of the distribution of particles at the source and m_p and m_e are the rest mass of the proton and electron respectively. Taking $\alpha = 2.1$ (Gaisser, 1990), yields $K_{ep} \sim 0.016$. This corresponds to a proton fraction of ~ 0.98, as required by sedv2.c; this is the fraction of energy allocated to the proton distribution, while the remainder is allocated to the electron distribution. To match the final combined hadronic-leptonic spectrum to the observations we leave this proton fraction and the magnetic field as free variables. To maintain such a high proton fraction, extremely intense magnetic fields were required ($\sim$ mG). It is known that over small sub-pc regions, where the shock front interacts with gas clumps, the magnetic field can be amplified to strengths of $\sim$ mG (Uchiyama et al., 2007). However, it is unlikely that the average magnetic field over the entire SNR could attain such a value. By hand, we lower the proton fraction to $K_{ep} = 0.60$ to obtain a suitable average magnetic field ($B = 21.3$ μG). What is suitable for our scenario will become more clear in subsection 4.3.2. The particle distribution parameters were also altered in order to make a better match to the data, see Table 3.3.

Parameters	Proton	Electron
$W(\times 10^{47})$ (erg)	3.41	2.28
α	1.30	1.86
β	1.94	2.93
E_b (TeV)	1.4	2.5
E_c (TeV)	93	60

Table 3.3: Combined model proton and electron distribution parameters

Figure 3.5 displays the final combined model including all the individual contributions

for $K_{ep} = 0.60$. The combined model, assuming the proton possess slightly more energy, is successful in explaining the observed broadband spectra of RX J1713.7-3946. A scenario like this may be inherent within some regions of the SNR. We do know that electrons are accelerated at the shock front via X-ray observations, it is just a matter of determining how much of the γ-ray emission is due to hadronic or leptonic processes. The problem becomes difficult to solve in this combined scenario. The large parameter space (proton and electron energy budget, B field and particle distribution parameters) actually becomes degenerate, so unless we explicitly constrain the energy fraction, K_{ep}, and or the B field; the combined model has restrictions. We could apply it in the case where we have an explicit hadronic model and assume the proton energy fraction is greater than 0.9, this would be supported by CR observations where less than $\sim 1\%$ of their observed composition is electrons (Hillas, 1972). However we can't know for sure that this corresponds to the source composition. There may be some diffusion/propagation affects that are inhibiting the electrons/protons from reaching Earth. The low mass of the electron causes it to have a low gyro-radius Equation 1.1, hence their propagation through the galaxy is hindered.

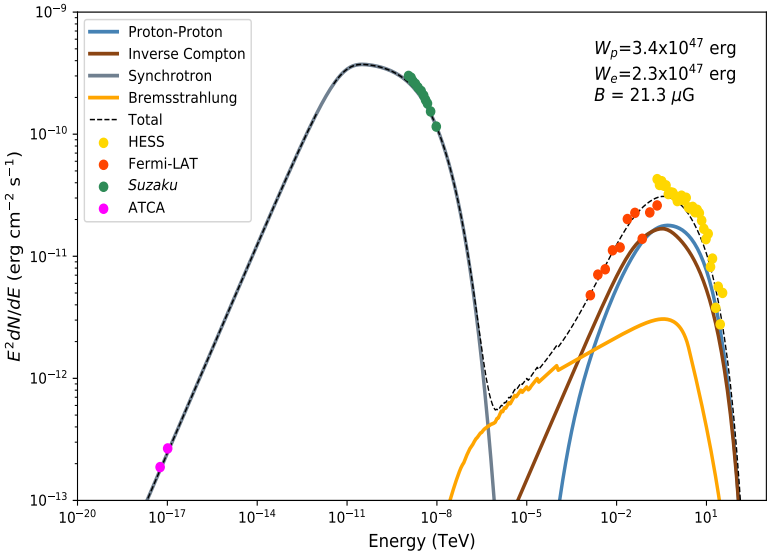

Figure 3.5: Broadband SED of the combined hadronic-leptonic model for RX J1713.7-3946 for $K_{ep} = 0.60$.

The models presented in this section are applied over the entire SNR. In the next chapter we apply the same models to the 29 smaller regions across the source. This will provide us with a way to quantify the fraction of hadronic and leptonic γ-ray emission and give us some idea about the fraction of energy allocated to both protons and electrons.

4 SED Modeling of RX J1713.7-3946 - Regional

The key aim of this chapter is to interpret both the pure hadronic and pure leptonic γ-ray emission scenarios. As mentioned earlier, H18 also investigated 29 smaller regions, originally proposed by Tanaka et al. (2008) when they examined the *Suzaku* X-ray data. Because we have such resolved images of RX J1713.7-3946 it makes sense to investigate the nature of these smaller regions. In this chapter we attempt to separately explain the spectral energy distribution of these regions with pure hadronic and pure leptonic models. In doing so the success of each scenario should be revealed. To test the validity of the hadronic SED model we compare the derived parameter space with what we would expect from an independent approach. A discussion surrounding the physical meaning associated with the derived parameter space for both hadronic and leptonic models is also presented. The contribution of Bremsstrahlung radiation to the leptonic spectrum within each region is examined. We discuss whether or not this γ-ray production channel should be neglected as a source of TeV γ-rays.

The highlighting features of this study were the addition of the latest ISM gas density measurements for each region. The molecular hydrogen component was traced by the Mopra CO survey (Braiding et al., 2018). Additionally, the radio energy fluxes unique to each region, as observed by ATCA, were used to model the synchrotron component of the leptonic model. As defined in Tanaka et al. (2008), each square region has a size of 10.8′ x 10.8′ = 0.18^o x 0.18^o. Assuming a distance of 1 kpc for the SNR (Fukui et al., 2003), this corresponds to a width and height of approximately 3.1 pc. This value will was assumed throughout the work for any analysis involving the regions, unless specified.

4.1 Regional ISM Gas Density Calculations

Fukui et al. (2012) performed an analysis on the SGPS HI gas data and the Nanten ^{12}CO data to calculate the total (atomic + molecular) ISM gas density, n_H, towards RX J1713.7-3946 for the entire SNR source. We performed a similar analysis to obtain the total ISM gas density for our 29 regions of interest. However, we use the Mopra ^{12}CO data set (Braiding et al., 2018) instead of the Nanten data set due to the former's better resolution of $0.6'$. The ISM gas density is an important parameter as both pp interactions and Bremsstrahlung processes have an explicit dependence on it. We outline our calculations below.

We assume that the ISM gas density is dominated by protons in the form of atomic (HI) and molecular hydrogen (H_2). The total number of protons per unit area, or proton column density, N_H, is calculated by summing the observed H_2 and HI components. The H_2 component was derived from the Mopra ^{12}CO gas map, while the HI gas map was taken from the SGPS at 21 cm (chapter 2). A conversion from HI brightness temperature,

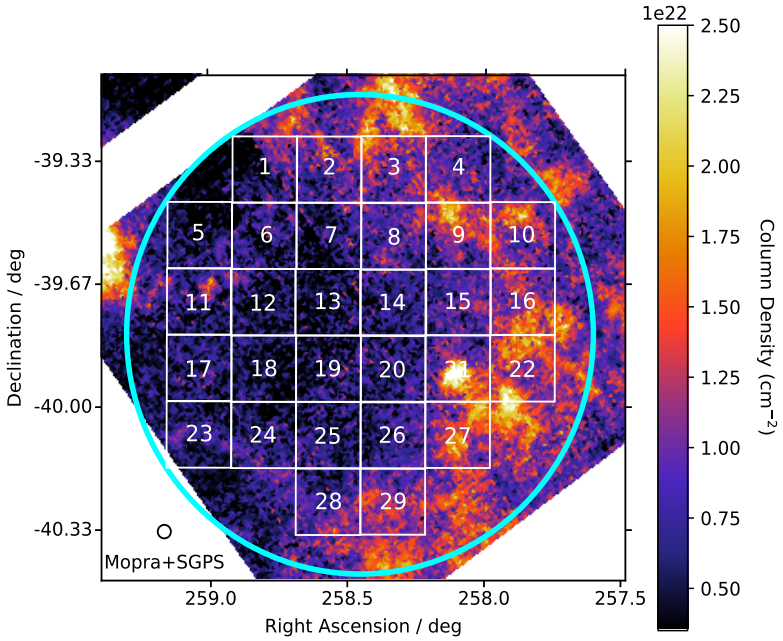

Figure 4.1: The total proton column density map consisting of the combined SGPS and Mopra contributions. Overlaid in white are the 29 regions of interest and in blue is the spherical shell used to approximate the depth of each region.

T, to HI column density is required, as per Equation 2.2:

$$N_{\rm HI} = 1.823 \times 10^{18} \int T(v) dv \ \ {\rm cm}^{-2}$$

where the integration is performed over the velocity range of -20 to 0 km s^{-1}. Additionally, the HI gas map obtained from Fukui et al. (2012) is corrected for self-absorption. This issue is discussed in chapter 2. To obtain the column density (cm^{-2}) for the molecular (H_2) counterpart we applied an X factor to the ^{12}CO brightness temperature, $W(^{12}{\rm CO})$:

$$N_{\rm H_2} = X \times W(^{12}{\rm CO}) \ \ {\rm cm}^{-2} \ . \tag{4.1}$$

In being consistent with Fukui et al. (2012) we adopted an X factor of 2.0×10^{20} cm^{-2} (K km s^{-1})$^{-1}$ (Bertsch et al., 1993). The H_2 column density needed an extra multiplicative factor of 2 to convert it into a proton column density before it was combined with the HI column density map. The average column density was then found for each of our 29 regions. To obtain the average proton volume density, n_H, for each region the column density was divided by the approximate depth of the SNR in that region. We assumed the SNR to be spherical, where each region makes up a slice of this sphere. Regions in the center were taken to have a depth of about 22.4 pc, which corresponds to a depth of 7 regions (see Figure 4.1). Regions on the rim of the SNR were taken to have a depth of 12.8 pc, corresponding to a depth of 4 regions. The remaining regions were taken to have a depth somewhere within these two extremities corresponding to their spherical geometry.

The average ISM gas density calculated for each region can be found in Table 4.1, along with their associated total proton mass.

Region	n_H (cm^{-3})	M$_\odot$	Region	n_H (cm^{-3})	M$_\odot$
1	151	488	16	240	968
2	189	761	17	116	468
3	226	909	18	76	367
4	228	735	19	72	408
5	112	360	20	90	508
6	116	468	21	209	1009
7	95	457	22	277	1116
8	146	705	23	147	473
9	238	959	24	113	453
10	284	914	25	97	467
11	137	554	26	114	553
12	88	426	27	256	1030
13	66	373	28	161	647
14	92	518	29	216	871
15	140	677			

Table 4.1: The average ISM gas density and total proton mass in units of solar masses for each region of RX J1713.7-3946. These quantities are calculated using Mopra CO and the SGPS HI data.

Not surprisingly, there is considerable variation in the gas density across the regions, ranging from 66 to 284 cm^{-3}. Figure 4.2 illustrates this with a colour-coded map. The morphology of the column density illustrates dense gas in the outer regions, likely due to the progenitor stars stellar wind bubble (Fukui et al., 2003). This morphology is still present in the volume density. Additionally, the spherical geometry of the outer regions requires that the observed ISM protons are spread over a smaller volume compared to the inner regions, yielding a higher volume density. As a result, the outer regions contain a large quantity of gas, while the inner regions are more sparse. The weighted average gas density value over all the regions is calculated to be $n_H = 148$ cm^{-3}. This weighted average is calculated by assuming each region makes up a column of volume within the sphere. The ISM gas density in each region is then weighted by the fraction of this volume to the entire volume of all columns within the sphere. This average value is slightly higher compared to that calculated by Fukui et al. (2012) ($n_H = 130$ cm^{-3}). This isn't surprising due to the resolution and sensitivity differences between Mopra and Nanten. Recall chapter 2; the Mopra telescope has a spatial resolution of $33''$, while the Nanten telscope has a resolution of $2.6'$. Additionally, the total proton mass within each region was found to range from 360 M$_\odot$ to 1116 M$_\odot$. These findings are consistent with other work. Moriguchi et al. (2005) found that dense gas clouds, with radii ranging from 1.8 pc to 4.2 pc, had a total proton mass of 38 M$_\odot$ to 686 M$_\odot$. This of course depended on

their size. The combined proton mass from each of our regions is found to be 1.9×10^4 $M_\odot$. This is consistent with the proton mass over the entire remnant (2×10^4 $M_\odot$), as calculated by Fukui et al. (2012)

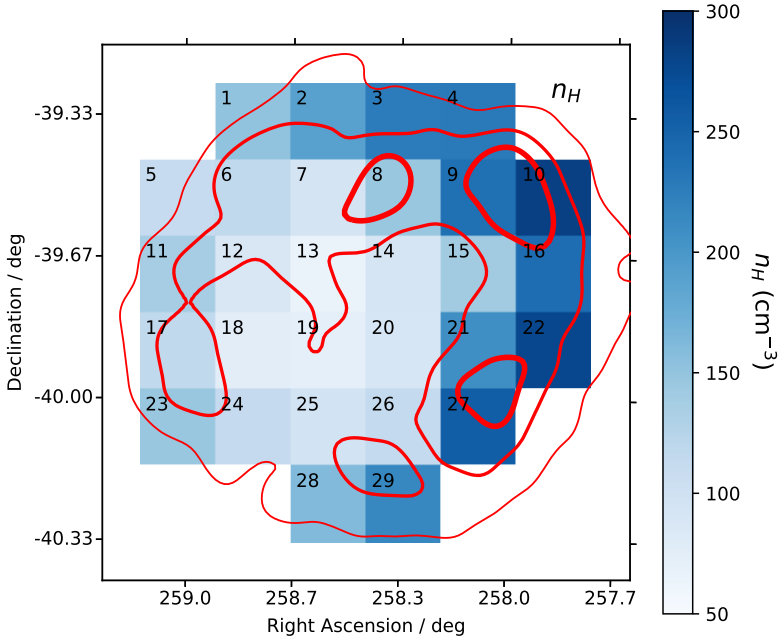

Figure 4.2: The average ISM gas density for each region (number labeled) displayed as a colour-coded map. The density ranges from 66 cm^{-3} in region 13 to 284 cm^{-3} in region 10. Overlaid in red are the HESS γ-ray contours at 5, 10 and 15σ, as per chapter 2.

4.2 Simulated Pure Hadronic Gamma-Ray Emission from 29 Regions

In this section we investigate a pure hadronic production scenario in each region. We begin by outlining the SED modeling process, which is adapted from H18, but also includes a new feature. This feature being the varying ISM gas density across each of the regions. We examine the reliability of our resultant SED CR proton energy budgets, $W_{p,\mathrm{SED}}$, for each region, by comparing against two other independent predictions. Here the subscript p denotes reference to the CR proton distribution and the subscript SED symbolises the parameter is used for the SED modeling. We also investigate whether the resulting spectra are consistent with the previous literature on RX J1713.7-3946, specifically work done by Inoue et al. (2012), Gabici and Aharonian (2014), and Celli et al. (2018).

4.2.1 Injected Proton Spectra

Similarly to H18, a power law with a cut-off was used to model the proton distributions within each region. Their cut-off energy, E_c, was not constrained when matching the spectra to only the HESS observations for each region (H18). For this reason H18 did

not vary the cut-off energy, instead they used the value required to model the entire remnant ($E_c = 93$ TeV). To match the pp spectra to the data, the energy budget, $W_{p,\mathrm{SED}}$, was adjusted by eye. The Fermi-LAT instrument has an angular resolution of 0.1^{o} at GeV energies, hence these observations are unable to resolve the 29 regions of size 0.18^{o} by 0.18^{o}. We resort to using the GeV observations for the entire SNR as upper limits.

H18 specified their proton energy budget for each region, W_p (>1TeV) (erg cm^{-3}), only for protons above an energy of 1 TeV and in terms of the ISM gas density, for which they assume a value of 1 cm^{-3}. So, in order to cross check our results with those of H18, firstly, we must re-normalise their results to the entire proton energy range:

$$W_{p,\mathrm{H18},n_H} = \frac{W_p(>1\mathrm{TeV})}{\int_{1\mathrm{TeV}}^{\infty} E^{-\alpha+1} dE} \int_{\mathrm{E_0}}^{\infty} E^{-\alpha+1} dE \ \ \mathrm{erg\ cm^{-3}}$$

where $W_{p,\mathrm{H18},n_H}$ is the total energy budget (still normalised in terms of the gas density) required by the H18 model and the proton energy ranges from the threshold proton energy (Appendix B) to the maximum CR proton energy. For simplicity we assume this approaches an infinite limit. Secondly, to account for the new region-specific gas density values we calculated, we simply divide $W_{p,\mathrm{H18}}$ by n_H, such that:

$$W_{p,\mathrm{H18}} = \frac{W_{p,\mathrm{H18},n_H}}{n_H} \ \ \mathrm{erg}. \tag{4.2}$$

Figure 4.3 illustrates six resultant SEDs of particular regions. The remainder can be found in Appendix D. We find that in all regions the hadronic spectra can be made to match the HESS observations comfortably. As a cross check, a cumulative sum of all the modeled spectra should be compared with the Fermi-LAT upper limits along with the HESS spectra for the entire SNR. Figure 4.4 illustrates the cumulative sum of the spectra from each region. Firstly, we note that the cumulative sum model matches the HESS data well. However, it can clearly be seen that in the GeV energy range (up to about 200 GeV) this cumulative sum over-predicts the Fermi-LAT observations. Previously, hadronic models have failed to reproduce the hard Fermi-LAT spectrum (Abdo et al., 2011) and leptonic models have been favoured (Ellison et al., 2012). This hard spectrum is explained by the lack of penetration into gas clumps from low energy protons (Inoue et al., 2012; Gabici and Aharonian, 2014; Celli et al., 2018). In our case, the GeV inconsistency arises mainly due to the lack of GeV observations.

Nonetheless, in some regions the TeV observations begin to indicate what is occurring at GeV energies. In particular, there are noticeable differences in the SEDs of regions 15 and 22 compared to region 1. Both region 15 and 22 have a soft spectral index, whereas the spectral index for region 1 is hard. The spectra for regions 15 and 22 are almost reaching the GeV upper limit imposed by the Fermi-LAT observations. These soft spectra are an indication that we are over-predicting the amount of low-energy protons that are interacting with the ISM. This explains why the cumulative sum over-predicts the GeV observations. The spectrum from many regions are likely over-predicting this GeV flux, however, we have no way of identifying this currently.

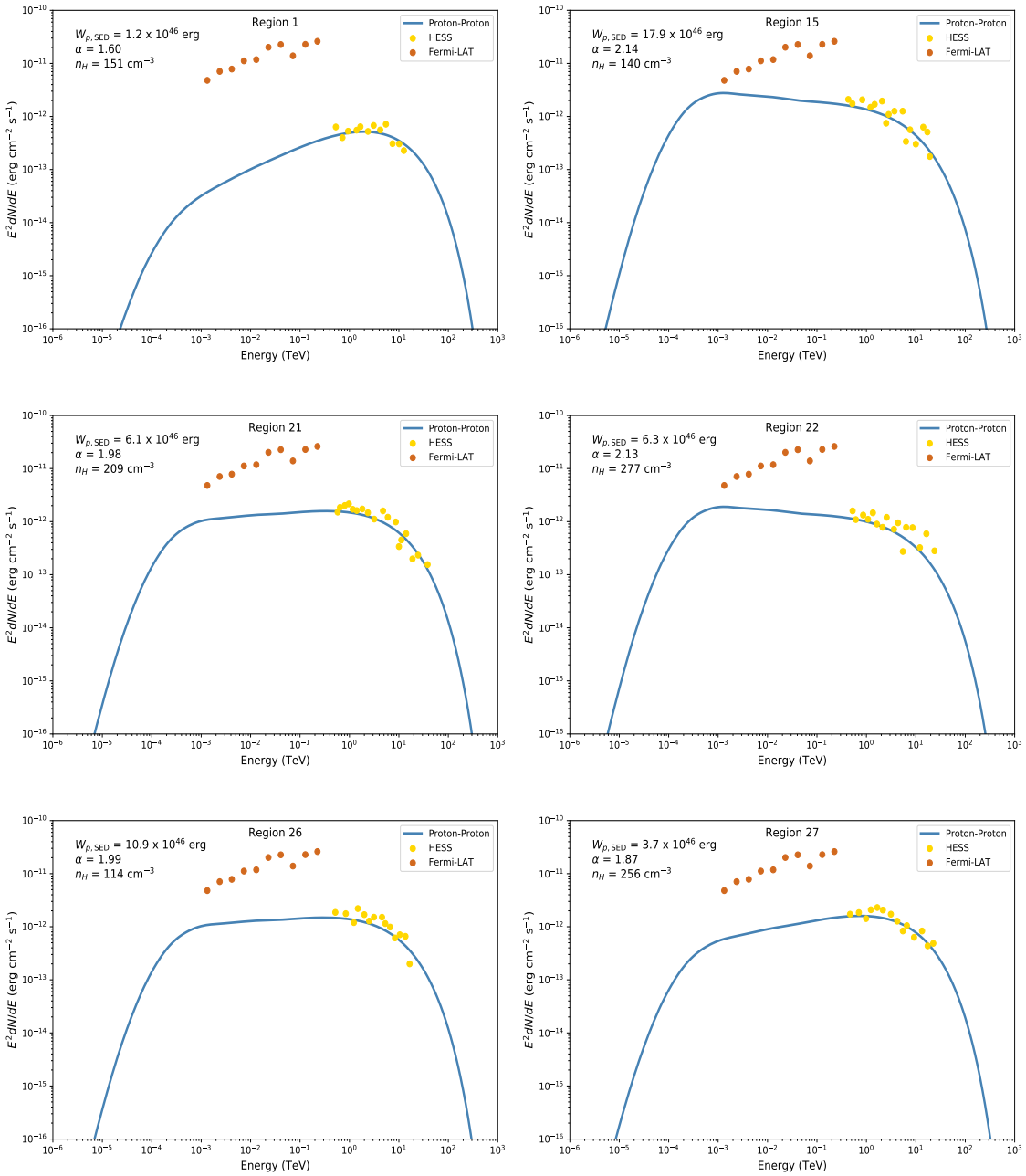

Figure 4.3: Hadronic SEDs for 6 regions within RX J1713.7-3946. In the legend we have specified the proton energy budget, $W_{p,\mathrm{SED}}$, the proton spectral index, α, and the ISM density, n_H.

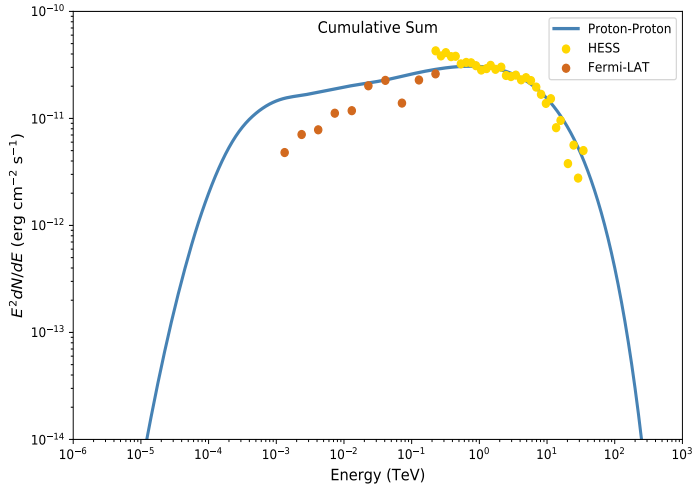

Figure 4.4: Cumulative sum of the hadronic spectra from each region with the Fermi-LAT and HESS data points for the entire SNR region.

The proton energy budget used for each region ($W_{p,\mathrm{SED}}$), the comparison H18 values ($W_{p,\mathrm{H18}}$) and other SED parameters can be found in Table 4.2. We portray both the proton energy budget, $W_{p,\mathrm{SED}}$, and the proton spectral index, α, on a color-scale map in Figure 4.5. The energy budget is generally larger in the central regions, ranging from $\sim 1 \times 10^{46}$ erg to $\sim 18 \times 10^{46}$ erg across the entire SNR. Most notably, the central regions 15 and 26 required significantly larger energy budgets. The proton spectral index varies from 1.60 in region 1 to 2.14 in region 15. The weighted average of the spectral index is 1.85, slightly below the expected DSA value. This weighted average was calculated by assuming that each region has a different volume filling factor within the SNR region. The volume filling factor is based on the depths of each region discussed in section 4.1. This is also discussed in more detail in subsection 4.2.2. Similarly, a weighted sum for the total proton energy budget was found to be 1.46×10^{48} erg. This is comparable to the proton energy budget for the entire SNR, 6.5×10^{47}, found in section 3.6.

To investigate the accuracy of the proton energy budgets found in this section we compared the SED model against two different theoretical calculations. The first of which takes into consideration the total amount of kinetic energy allocated to CRs from the SN explosion and also assumes that high energy CRs have escaped. Ginzburg and Syrovatskij (1967) and Drury (1996) provide simple calculations to show that SNe expel about 10% of their kinetic energy into CRs. The energy required to sustain the galactic CR population is $\sim 10^{41}$ erg s^{-1}. On the other hand, the total power output of SNe, assuming a rate of 1 every 30 years, is $\sim 10^{42}$ erg s^{-1} Hence, assuming that SNe are responsible for the galactic CR population, $\sim 10\%$ of their total energy must be supplied to CRs (10^{50} erg). In addition to this, Dorfi and Drury (1985) numerically investigate the problem to make the same conclusion. Secondly, we investigate how consistent our SED model is with a

Reg.	$W_{p,\mathrm{SED}}$ (erg) $\times 10^{46}$	$W_{p,\mathrm{H18}}$ (erg) $\times 10^{46}$	α	n_H (cm^{-3})
1	1.2	1.2	1.60	151
2	2.1	2.1	1.82	189
3	2.5	2.5	1.95	226
4	1.3	1.3	1.76	228
5	4.3	4.3	1.96	112
6	4.4	4.4	1.70	116
7	6.0	7.0	1.74	95
8	5.4	6.3	1.81	146
9	5.8	8.2	1.94	238
10	2.0	2.0	1.78	284
11	3.9	3.9	1.85	137
12	4.8	5.6	1.72	88
13	7.1	6.1	1.74	66
14	7.0	6.0	1.87	92
15	17.9	21.7	2.14	140
16	5.0	5.1	2.01	240
17	4.2	4.2	1.79	116
18	6.7	7.9	1.91	76
19	6.0	6.0	1.80	72
20	5.3	5.3	1.83	90
21	6.1	7.3	1.98	209
22	6.3	5.2	2.13	277
23	3.0	3.0	1.80	147
24	2.1	2.1	1.63	113
25	6.0	7.0	1.92	97
26	10.9	13.0	1.99	114
27	3.7	5.2	1.87	256
28	1.8	1.4	1.62	161
29	3.0	2.4	1.89	216
	145.5	157.8	1.85	148

Table 4.2: The proton energy budget results of our SED modeling compared to those from H18. The results from H18 have been re-normalised to the entire energy spectrum and have been adjusted to account for the new ISM gas density calculations (see text). We also indicate the required spectral index, α, for each region as per H18. The values along the bottom line represent the total sums (for the energy budget columns) or the weighted averages (for α and n_H). The weighted averages are calculated via the method described in the previous section (section 4.1).

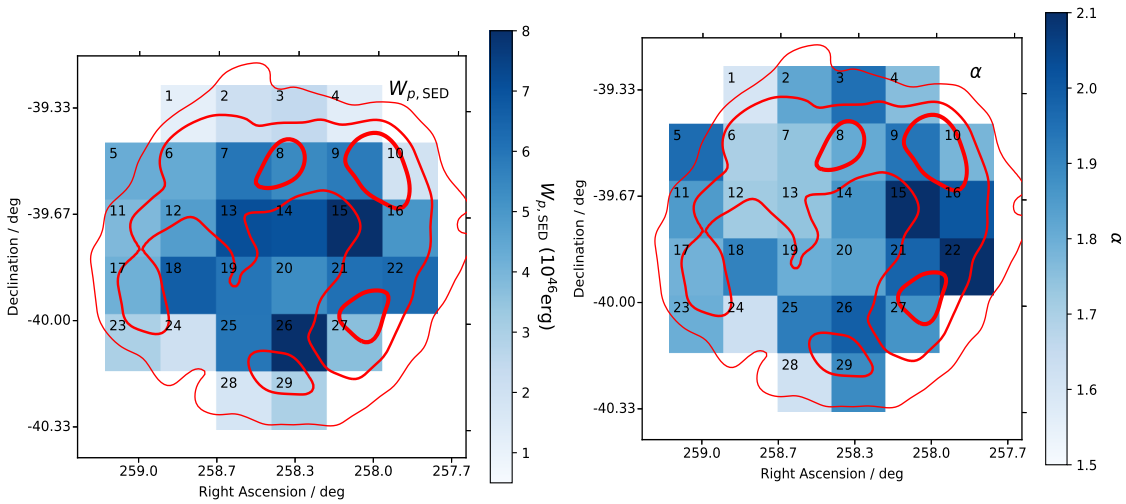

Figure 4.5: Left: All regions colour coded according to their proton SED energy budgets, $W_{p,\mathrm{SED}}$. **Right:** All regions colour coded according to their proton spectral index. Both images are overlaid in red with the HESS γ-ray contours at 5, 10 and 15σ, as per chapter 2.

simple cooling time (t_{pp}) approximation of the proton energy budget. This approximation is limited, in that it assumes all the CRs have lost their energy to pp processes, but it also directly incorporates the HESS observations for each region (H18), as we will see.

4.2.2 Comparison with 10^{50} erg Energy Budget Model

Our first theoretical model exploits the expected 10^{50} erg energy budget for CRs in SNRs (Ginzburg and Syrovatskij, 1967). This energy is geometrically distributed amongst the 29 regions. Assuming the CRs are isotropically distributed within a sphere the size of our entire SNR region (recall Figure 4.1), each region receives a slightly different fraction of the 10^{50} due to geometry. We should note that the geometry of the 29 regions doesn't fully extend to the edge of the SNR shell - along its circumference (Recall Figure 4.1). Consequently, some of the 10^{50} erg is provided to regions other than the 29 designated regions, hence the sum of energy injected into the 29 regions doesn't equate to 10^{50} erg. Nonetheless, the amount of energy injected into each region scales according to its volume filling factor (V_{ff}) within the SNR sphere. The V_{ff} depends on the region's position on the surface of the sphere and followed a similar analysis to that of section 4.1. Table 4.3 shows the depth and volume filling factor of each region, which were both used to calculate the total fractional energy budget, $W_{p,50,\mathrm{T}}$, for each region. Here the subscript '50' is used to denote the 10^{50} erg assumption, while the subscript 'T' denotes the fact that this energy budget is allocated to the entire proton energy range.

Next, we assume that escaped CRs carry a significant amount of energy and don't interact with the ISM. This missing energy is accounted for in the SED model as it matches the γ-ray emission. To account for it in this new model, we assume protons with energy greater than 150 TeV have escaped (Casanova et al., 2010). We re-normalised the fractional

Depth (pc)	V_{ff}	$W_{p,50,\mathrm{T}}$ ($\times 10^{48}$erg)	Regions
12.8	0.022	2.23	1, 4, 5, 10, 23
16.0	0.028	2.78	2, 3, 6, 9, 11, 16, 17, 22, 24, 27, 28, 29
19.2	0.033	3.34	7, 8, 12, 15, 18, 21, 25, 26
22.4	0.039	3.90	13, 14, 18, 19

Table 4.3: Column depth into the SNR, volume filling factor and fractional energy budget for each region based on a total 10^{50} erg budget for the SNR.

energy budget up to a proton energy of 150 TeV to find the theoretical proton energy budget $W_{p,50}$:

$$W_{p,50} = W_{p,50,\mathrm{T}}(<150\mathrm{TeV}) = \frac{W_{p,50,\mathrm{T}}}{\int_{\mathrm{E}_0}^{\infty} E^{-\alpha+1} dE} \int_{E_0}^{150\ \mathrm{TeV}} E^{-\alpha+1} dE \ \mathrm{erg} \tag{4.3}$$

where E_0 is the proton threshold energy required to produce a neutral pion. To ensure this model was completely independent from the SED model we invoke a simple power-law distribution, with $\alpha = 2$ (in being consistent with DSA theory), to represent the proton population in each region.

A comparison of $W_{p,50}$ with the SED energies, $W_{p,\mathrm{SED}}$ (Table 4.4), showed that the SED model energies are consistently less than $W_{p,50}$. For a visual comparison we display the ratio of $W_{p,50}$ to $W_{p,\mathrm{SED}}$ on a colour-scale map (Figure 4.6), this ratio, $R_{50/\mathrm{SED}}$, is also included in Table 4.4. In some of the outer regions this ratio is large, up to values of ~ 16, implying that the models are inconsistent with each other. Since these regions are located near the rim of the SNR the CRs within may not have had sufficient time to expel their energy into γ-ray production; recall the cooling time for pp interactions:

$$t_{pp} \approx 5.3 \times 10^7 (n_H/\mathrm{cm}^3)^{-1} \text{ years} .$$

The cooling time is dependent on gas density, so the CRs accelerated in these outer regions may not yet have interacted with all the observed gas. This would imply that a portion of the energy budget allocated in these regions is still retained by the protons, contrary to the assumption that all the available energy has been distributed to γ-ray production.

4.2.3 Comparison with HESS Flux Data and Cooling Time Model

An issue that the previous model failed to recognise, was that of the cooling time of the pp interactions. The cooling time represents the amount of time required for a population of particles to radiate away their energy. We now present a prediction of the energy budget that incorporates the pp cooling time. Additionally, we utilised the HESS γ-ray spectral observations for each region. These flux values were integrated to find the total flux and then converted into a luminosity and hence a total energy budget for each region. We outline the calculations below. The energy flux data points were integrated (Equation 4.4)

Reg.	$W_{p,\mathrm{SED}}$ (erg) $\times 10^{46}$	$W_{p,50}$ (erg) $\times 10^{46}$	$R_{50/\mathrm{SED}}$
1	1.2	18.2	15.7
2	2.1	22.7	10.8
3	2.5	22.7	9.2
4	1.3	18.2	14.2
5	4.3	18.2	4.2
6	4.4	22.7	5.2
7	6.0	27.3	4.6
8	5.4	27.3	5.0
9	5.8	22.7	3.9
10	2.0	18.2	9.3
11	3.9	22.7	5.8
12	4.8	27.3	5.7
13	7.1	31.8	4.5
14	7.0	31.8	4.6
15	17.9	27.3	1.5
16	5.0	22.7	4.5
17	4.2	22.7	5.4
18	6.7	27.3	4.1
19	6.0	31.8	5.3
20	5.3	31.8	6.0
21	6.1	27.3	4.4
22	6.3	22.7	3.6
23	3.0	18.2	6.1
24	2.1	22.7	10.9
25	6.0	27.3	4.6
26	10.9	27.3	2.5
27	3.7	22.7	6.2
28	1.8	22.7	12.9
29	3.0	22.7	7.6
	145.5	708.8	6.2

Table 4.4: The energy budget required by the SED model for each region ($W_{p,\mathrm{SED}}$) compared to the energy budget theorized by the 10^{50} erg model ($W_{p,50}$). Additionally, the ratio of both energy budgets has been included to highlight regions where the parameters are consistent, or inconsistent. The values along the bottom line represent the total sums (for the energy budget columns) or the weighted average (for $R_{50/\mathrm{SED}}$). The weighted averages are calculated via the method described in section 4.1.

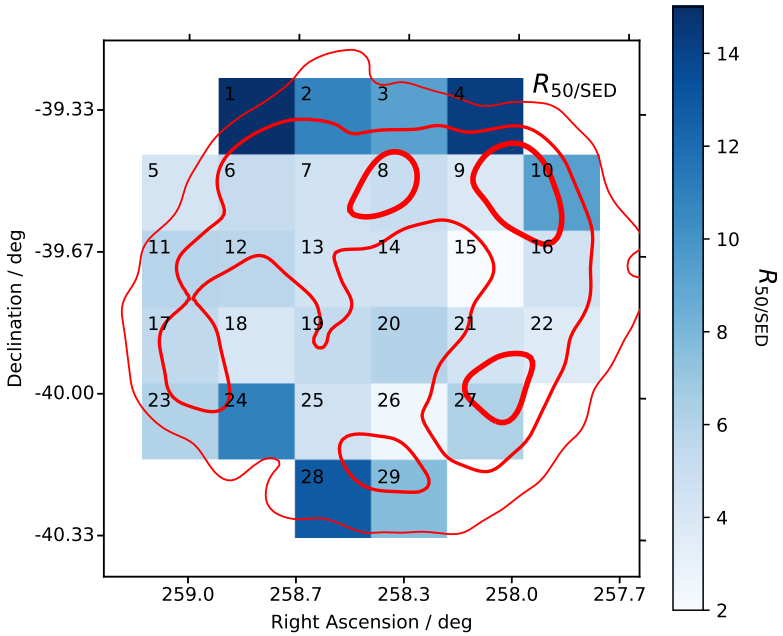

Figure 4.6: The the ratio of $W_{p,50}$ to $W_{p,\mathrm{SED}}$ (Table 4.4) for each region displayed as a colour-coded map. Overlaid in red are the HESS γ-ray contours at 5, 10 and 15σ, as per chapter 2.

to obtain the total γ-ray flux, F_γ, within the energy range imposed by the data (E_{min} and E_{max}).

$$F_\gamma = 1.6 \int_{E_{\mathrm{min}}}^{E_{\mathrm{max}}} F_{\gamma,i} \frac{1}{E_i} dE \ \ \mathrm{erg\ cm^{-2}\ s^{-1}} \tag{4.4}$$

where $F_{\gamma,i}$ and E_i are the γ-ray photon flux and energy, respectively, corresponding to the ith data point. The total γ-ray flux was then converted into a luminosity, L_γ, by projecting it onto a sphere of radius d, where d is the distance to our source. Since the total luminosity is just the amount of energy emitted per unit time, multiplying it by the density dependent cooling time, t_{pp} (Equation 3.27), provides us with our predicted energy budget, $W_{p,\mathrm{cool}}$. Here the subscript 'cool' simply refers to this model that incorporates the cooling time. These last 2 steps are summarised in Equation 4.5.

$$W_{p,\mathrm{cool}} = t_{pp} \times L_\gamma = t_{pp} \times 4\pi d^2 \times F_\gamma \ \ \mathrm{erg}. \tag{4.5}$$

Including the region-dependent calculations of t_{pp} ensures us that $W_{p,\mathrm{cool}}$ is a more accurate calculation than $W_{p,50}$. Both $W_{p,\mathrm{cool}}$ and t_{pp} can be found in Table 4.5.

The HESS data only covered a limited γ-ray energy range ($\sim$ 0.1 TeV to 30 TeV), so $W_{p,\mathrm{cool}}$ also only applies to this limited range. To compare the SED modeled energy budgets with $W_{p,\mathrm{cool}}$, we must re-normalise $W_{p,\mathrm{SED}}$ to match the appropriate γ-ray energy range. However, re-normalising $W_{p,\mathrm{SED}}$ requires integrating over proton energies, so we must convert the γ-ray energy range into a proton energy range. It is commonly accepted that

Reg.	$W_{p,\mathrm{SED,TeV}}$ (erg) $\times 10^{45}$	$W_{p,\mathrm{cool}}$ (erg) $\times 10^{45}$	$R_{\mathrm{SED,TeV/cool}}$	t_{pp} (years) $\times 10^{5}$
1	6.8	2.6	2.6	3.5
2	8.2	2.8	2.9	2.8
3	5.8	2.2	2.6	2.3
4	5.8	2.2	2.7	2.3
5	8.3	3.9	2.1	4.7
6	25.3	9.5	2.7	4.6
7	34.0	14.3	2.4	5.6
8	20.6	8.8	2.3	3.6
9	17.7	7.0	2.5	2.2
10	9.4	4.3	2.2	1.9
11	13.7	6.1	2.2	3.9
12	26.2	10.5	2.5	6.0
13	32.3	13.2	2.5	8.0
14	25.6	9.6	2.7	5.8
15	21.4	8.3	2.6	3.8
16	11.3	4.8	2.3	2.2
17	18.8	7.2	2.6	4.6
18	20.3	7.9	2.6	7.0
19	27.5	10.3	2.7	7.3
20	22.3	8.5	2.6	5.9
21	14.3	5.3	2.7	2.5
22	7.3	2.8	2.6	1.9
23	9.5	3.9	2.5	3.6
24	11.3	5.4	2.1	4.7
25	17.6	6.6	2.7	5.5
26	24.8	9.8	2.5	4.6
27	13.7	5.2	2.6	2.1
28	10.2	5.1	2.0	3.3
29	8.8	3.7	2.4	2.4
	478.5	191.7	2.5	4.3

Table 4.5: The theorized energy budgets using the HESS observations and cooling time calculations ($W_{p,\mathrm{cool}}$) are compared against the energy budgets required by the SED model, which have been re-normalised to the same energy range ($W_{p,\mathrm{SED,TeV}}$). Also presented are the ratios of the two energy budgets, $R_{\mathrm{SED,TeV/cool}}$, as described in the text, and the cooling time, t_{pp}. The values along the bottom line represent the total sums (for the energy budget columns) or the weighted averages (for $R_{\mathrm{SED,TeV/cool}}$ and t_{pp}). The weighted averages are calculated via the method described in section 4.1.

γ-rays of a given energy are produced (via pion decay) by protons with energies a factor of ~ 10 larger. So a γ-ray of energy 1 TeV was likely produced by a proton with energy 10 TeV. We make this assumption in the following calculations to re-normalise $W_{p,\mathrm{SED}}$:

$$W_{p,\mathrm{SED,TeV}} = \frac{W_{p,\mathrm{SED}}}{\int_{\mathrm{E_0}}^{\infty} E^{-\alpha+1} dE} \int_{E_{p,\mathrm{min}}}^{E_{p,\mathrm{max}}} E^{-\alpha+1} \ \mathrm{erg}. \tag{4.6}$$

where instead of assuming $\alpha = 2$ for all regions we have used the spectral results from the SED modeling. Since the spectral index, α, for each region was obtained by matching (or in the case of H18, fitting) the pp spectra to the HESS observations. So also using these α values shouldn't affect the independence of this model from the SED model, since we use the HESS observations again. Additionally, $E_{p,\mathrm{max}} \sim 1$ TeV and $E_{p,\mathrm{min}} \sim 300$ TeV, represent the maximum and minimum proton energies corresponding the photon energy range covered by HESS. The results, $W_{p,\mathrm{SED,TeV}}$, are also shown in Table 4.5.

The SED energy budget for all regions are larger than $W_{p,\mathrm{cool}}$. However, this should come as no surprise considering that our cooling-time calculations assume that the all of the CRs interact with all of the ISM gas. More realistically, some of the observed gas will be in the foreground and background of the SNR. Table 4.5 also shows the ratio, $R_{\mathrm{SED,TeV/cool}}$, of the SED energy budget $W_{p,\mathrm{SED,TeV}}$ to the cooling-time model energy budget, $W_{p,\mathrm{cool}}$. Figure 4.7 displays the variation of $R_{\mathrm{SED,TeV/cool}}$ across each region, where lower values imply more consistent results between the two hadronic models. $R_{\mathrm{SED,TeV/cool}}$ doesn't show much variation across the regions at all, ranging from 2 to 3. Region 2 stands out for having the largest ratio $R_{\mathrm{SED/cool}} = 2.9$, while region 28 has the lowest $R_{\mathrm{SED/cool}} = 2.0$.

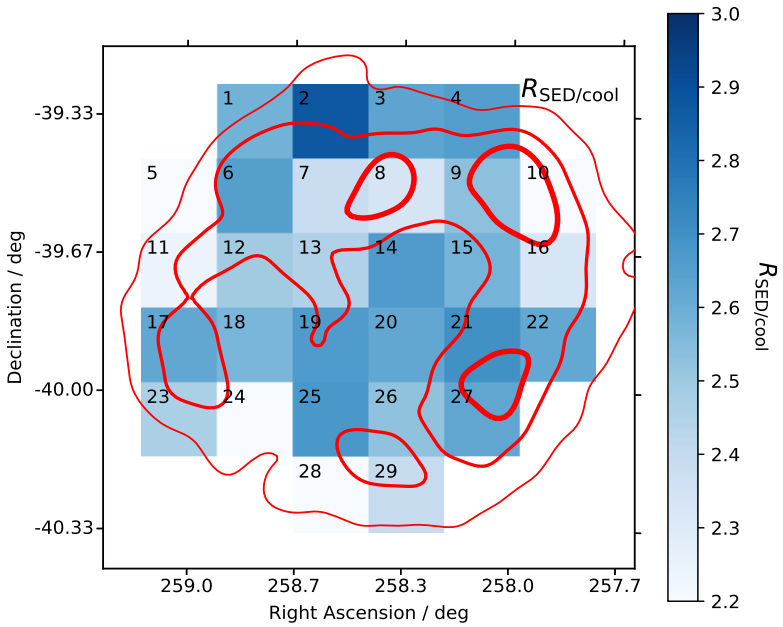

Figure 4.7: All regions colour coded according to their $R_{\mathrm{cool/SED}}$ values. Overlaid in red are the HESS γ-ray contours at 5, 10 and 15σ, as per chapter 2.

4.2.4 Discussion

Not surprisingly, the SED model is more consistent with the cooling-time model compared to the 10^{50} erg model. The cooling-time model was based upon assumptions and observations, whilst the calculations of $W_{p,50}$ were based solely on assumptions. Our main assumption in the latter model, that the CRs have an energy budget of 10^{50} erg, may be incorrect. It wouldn't be unrealistic if less energy was injected into the CRs. Leahy (2017) showed that SNe (both core-collapse and type Ia) in the Large Magellanic Cloud could expel as little as 0.04×10^{51} erg of kinetic energy into their explosions. Subsequently the CRs would only receive 10% of this energy, e.g. as little as 4×10^{48} erg. This is an order of magnitude less than what we assumed when calculating $W_{p,50}$. The cumulative sum of $W_{p,\mathrm{SED}}$ across all regions was calculated to be 1.46×10^{48} erg. Similarly, the total sum of $W_{p,50}$ across all regions was 7.09×10^{48} erg. Both of these are comparable to the lower limit result from Leahy (2017) (4×10^{48} erg in CRs). This suggests that the hadronic models are consistent on a broader scale. Recalling the H18 hadronic model of the entire SNR ($W_{p,\mathrm{H18}} = 6.50 \times 10^{47}$ erg over all protons energies and for $n_H = 130$ cm^{-3}), we are led to believe that our SNR may only convert a small amount of its explosion energy into CRs.

Moreover, we found that the proton spectral index was generally harder (lower) than the canonical value of 2. As mentioned in H18, this is not surprising if we consider shock-cloud interactions where the penetration depth of the accelerated protons depends on their energy. Inoue et al. (2012), Gabici and Aharonian (2014), and Celli et al. (2018) explain how lower energy CR protons would have limited interactions if a clumpy medium were present in the shock environment. These small (radius ~ 0.1 pc), dense ($n_H \geq 10^3$ cm^{-3}), clumpy regions stay intact after experiencing the stellar wind and SN shock and remain as target gas for the protons, while the remainder of the medium gets expelled outwards. The penetration depth of protons is energy dependent. Higher energy protons will be more likely to penetrate the dense clumps, so the bulk of the γ-ray production will come from these protons. The lower energy protons are responsible for producing the low energy γ-rays (around GeV energies), hence the spectrum towards the clumps becomes harder.

Furthermore, we found that the cumulative sum of the spectra from each region over-predicted the GeV upper limit. This arises due to the fact that we didn't have any GeV observations to match our individual spectra to. We can also consider the effect of modeling a region (3.1 pc by 3.1 pc) much larger than the typical clump size of 0.1 pc (Celli et al., 2018). Subsequently, we take the average density of the clumps and low density surrounding gas in these regions. This assumes that our entire population of CRs are interacting with most of the gas and hence will over-predict the γ-ray emission from the low-energy protons. An energy-break could be applied to the proton distributions for each region to decrease the amount of low energy protons interacting with the ISM gas. This would ultimately only affect the low energy (GeV) tail of the spectra, whilst maintaining the γ-ray emission from the higher energy protons. However, assigning a low energy spectral index would be ambiguous and have no physical meaning without any constraining observations. Because of this, our hadronic models are limited.

Nonetheless, we attempt to explain some of the results. The GeV spectrum for region 1 appears very hard ($\alpha = 1.60$). We interpret this result in the context of the region's location. Since it's located on the edge of the SNR, the γ-ray emission is likely dominated by high-energy protons as they escape the shock first (Gabici et al., 2009). The lower energy protons haven't had sufficient time to produce γ-rays or only a small fraction have. Similarly, we interpret the spectra of regions 24 and 28 in the same manner. They are located on the edge of the SNR and have hard GeV spectra.

Region 21 and 27 both contain the dense cloud cores C and B respectively (Moriguchi et al., 2005). Region 21 has a soft GeV spectra ($\alpha = 1.98$), while that of region 27 isn't as soft ($\alpha = 1.87$). Both regions were also found to have moderate energy budgets ($W_{p,\mathrm{SED}} \sim 5 \times 10^{46}$ erg) and large masses of proton gas $\geq 1000\,\mathrm{M}_{\odot}$. The soft spectral index in region 21 could be representative of the efficiency of both low and high energy protons interacting with the gas and producing γ-rays. This would demand the presence of sparse gas to ensure that both low and high energy protons are sufficiently interacting. The same scenario could be occurring in region 27, however, the effect may be less substantial, as suggested by the harder GeV index. The gas density in region 27 ($n_H = 256$ cm^{-3}) is in fact greater than in region 21 ($n_H = 209$ cm^{-3}), so we expect less penetration from the low energy protons in the former region if the ISM is more clumpy. Nonetheless, both region 21 and 27 are good candidates for hadronic dominated γ-ray emission.

We have shown that a pure hadronic model can reproduce the observed γ-ray emission from each region. However, a pure leptonic model should be investigated too. Direct evidence for the acceleration of electrons at RX J1713.7-3946 has been revealed through the observations of synchrotron X-rays, so we can expect that these same electrons might be responsible for some, if not all, of the γ-ray emission through IC scattering, or even Bremsstrahlung, in some of the 29 regions. The next section investigates whether a pure leptonic scenario is plausible within each region, as a next step towards understanding the level of hadronic vs leptonic emission in each region.

4.3 Simulated Pure Leptonic Broadband Emission from 29 Regions

In this section we model the broadband observations from each region assuming a pure leptonic particle distribution. The non-thermal radio and X-ray synchrotron emission from RX J1713.7-3946 indicates that electrons are accelerated up to multi-TeV energies inside this SNR. However, the relative amount of contribution to the TeV γ-rays from both leptonic and hadronic processes is still unclear. If electrons are responsible for part of the emission, then the leptonic models should at least recreate the broadband spectrum with physically sound parameters. However, this won't necessarily confirm the leptonic scenario as the dominant γ-ray producing process, nor quantify the contribution from leptonic and hadronic processes.

Electrons can IC scatter off the CMB to produce γ-rays. Alternatively, they can be decelerated by nuclei to produce relativistic Bremsstrahlung γ-rays. The latter depends on the density of the gas within the shock-front and surrounding the SNR. The methodology for this section is similar to H18, however there are two new aspects. Firstly, we incorporate

the radio energy flux from each region, as calculated in subsection 2.4.1. This assists us in matching the synchrotron spectrum by constraining the low energy spectral index for the electron population. Secondly, we incorporate our gas density calculations, as calculated earlier in section 4.1. This enables us to investigate the significance of the Bremsstrahlung component in comparison to the IC channel.

To provide initial insight into whether Bremsstrahlung plays a significant role vs IC scattering in any of the regions we look at the cooling times for the three leptonic processes. Here we assume the Thompson limit for the IC cross section, as discussed in section 3.4. This is a safe assumption up to electron energies of about 100 TeV and given the range of ISM density values being used (66 to 284 cm^{-3}). The Bremsstrahlung and synchrotron cooling times are region dependent. They depend on the ISM gas density and magnetic field strength respectively. However, as we have not derived the regional B field strength yet we assume the average value over the entire SNR ($B = 14.3$ μG, see section 3.8) for each region. We also only examine the most extreme cases of density from a minimum of 66 cm^{-3} in region 13 to a maximum of 284 cm^{-3} in region 10.

We present a plot of each cooling time as a function of electron energy in Figure 4.8. Increasing the density from the minimum to the maximum decreased the Bremsstrahlung cooling time by a factor of 4. Only when the density is near its maximum will Bremsstrahlung dominate both the synchrotron and IC emission. However, this is only the case for electrons with energy < 5 TeV. Bremsstrahlung will dominate only IC processes for electrons with energies less than 10 TeV; this energy limit decreases as the density decreases. Given the gas density in some regions approaches this maximum, we may expect to see some regions with significant Bremsstrahlung contributions at low γ-ray energies. Furthermore, the synchrotron cooling time is at least an order of magnitude shorter than that of IC at all energies due to its B^2 dependence (see section 3.4). This effect would only be intensified if the average B field in a region is greater than 14.3 μG. We increase B to 20 μG to show the effect of amplified magnetic fields. This is a rough upper limit. The amount of amplification will scale with the amount of dense gas clumps. In this upper limiting case, the synchrotron cooling time dominates at most electron energies. Hence, these electrons will lose a substantial amount of their energy to synchrotron processes leaving minimal remaining for the other two. This concept is important to address in order to understand the broadband leptonic emission.

4.3.1 Injected Electron Spectra

In accordance with H18, the electrons were assumed to up scatter the CMB and far-infrared photon fields described in section 3.8. To model each electron population we used a broken power-law with an exponential cut-off, E_c. The break energy was set to be $E_b = 2.5$ TeV, in accordance with the energy-break for the entire SNR. This reduced the parameter space to 5 variables (W_e, B, α_1, α_2 and E_c), where W_e is the electron energy budget required for each region and α_1 and α_2 are the low and high spectral index respectively. These five parameters, excluding the newly added α_1, should agree with those derived in H18, unless the Bremsstrahlung component significantly affects the total TeV emission. The final spectra for each region was obtained by simultaneously matching the IC and

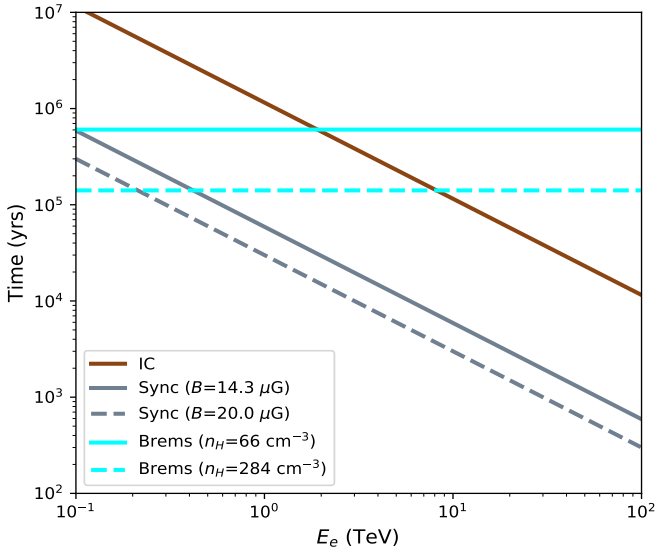

Figure 4.8: The cooling times (Equation 3.28) vs electron energy for each leptonic process. The Bremsstrahlung cooling time has been calculated for two different values of ISM gas density (see text). The solid cyan line represents the cooling time in the region with the lowest density, while the dashed cyan line represents the highest density case. Additionally, we look at the synchrotron scenario for the average B field over the entire remnant (grey-solid line) and an amplified scenario (grey-dashed line).

Bremsstrahlung emission to the HESS observations and the synchrotron emission to the *Suzaku* and ATCA observations. To control the ratio of the total TeV emission to the synchrotron spectra the B field was varied. Once the peak emission from each component matched the intensity of the observations, the shape of the spectra were obtained by varying the spectral index (high and low) and the exponential cut-off. Computational fitting techniques were beyond the scope of this work, so the parameters were chosen by eye. The shape of the low energy tail of the synchrotron spectra was controlled by the ATCA radio data - and more directly, the low energy spectral index.

Figure 4.9 displays the SEDs for regions 1, 4, 5, 16, 21 and 22, while the remainder can be found in Appendix D. Regions 16, 21 and 22 were chosen to highlight their substantial Bremsstrahlung peak (cyan line) at TeV energies. Subsequently, the total TeV emission (dashed line) is significantly affected in these regions. Regions 1, 4 and 10 were selected due to the strong Bremsstrahlung spectrum peaking at MeV energies. This phenomenon is not seen in any other regions. The total TeV emission is also substantially affected in regions 4 and 10. Otherwise, the SED for each region was found to match the observations comfortably. The GeV upper limit was not violated, nor approached in any case. Additionally, no other stand out features were found for the remaining regions.

Table 4.6 highlights the parameters required to model the broadband observations from each region. We find that they are equivalent to those derived in H18, except in cases where the Bremsstrahlung component has significantly affected the γ-ray spectrum. These

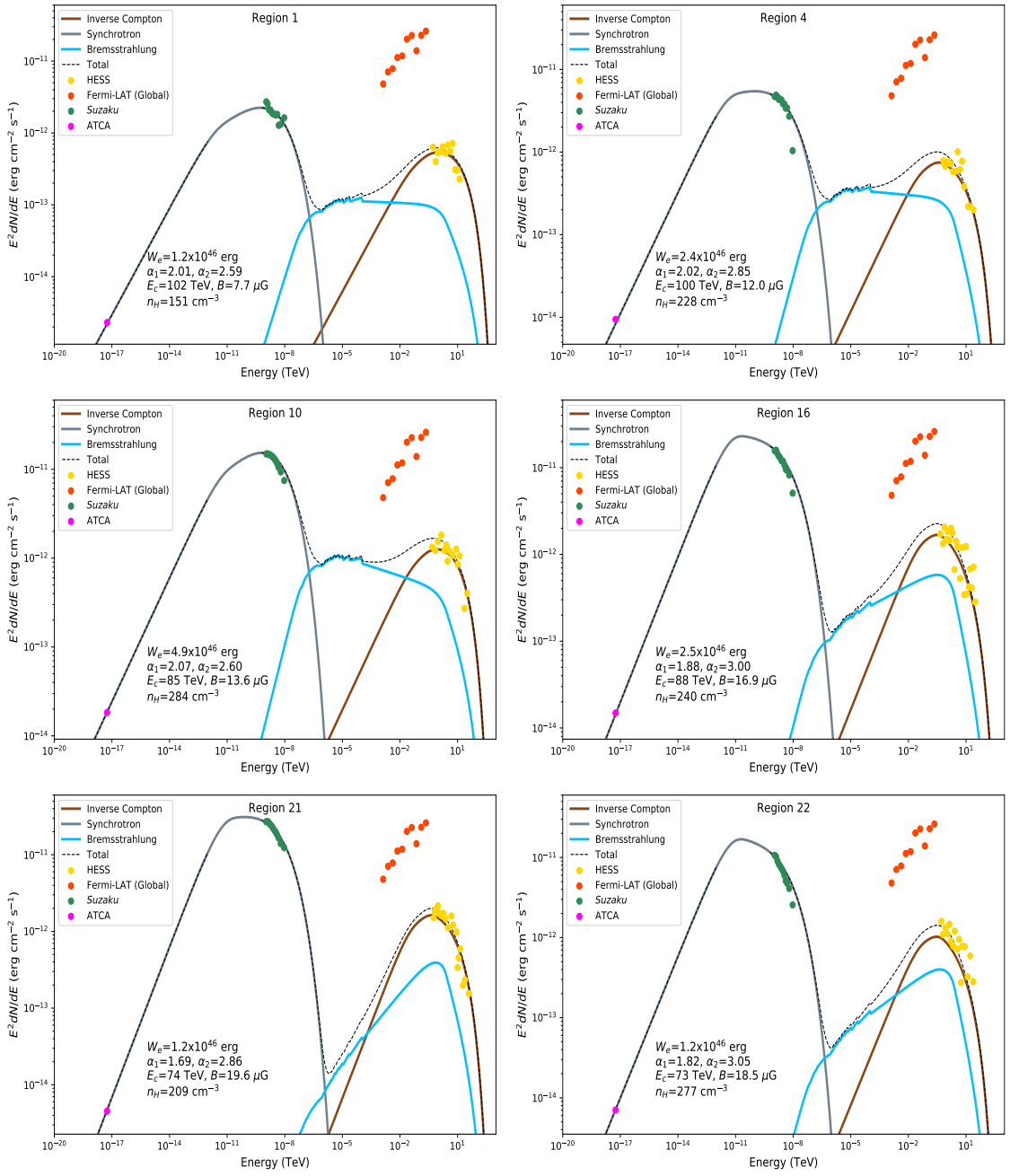

Figure 4.9: Leptonic SEDs for 6 regions within RX J1713.7-3946.

Region	$W_e(\times 10^{46}$ erg)	$B(\mu$G)	α_1	α_2	E_c(TeV)	n_H(cm^{-3})
1	1.25	7.7	2.01	2.59	102	151
2*	1.41	9.5	1.92	2.78	75	189
3*	1.27	10.6	1.89	2.84	59	226
4*	2.39	12.0	2.02	2.85	100	228
5	0.51	8.3	1.50	2.94	170	112
6	1.13	11.3	1.85	2.56	100	116
7	1.00	11.4	1.72	2.68	112	95
8	1.02	13.6	1.63	2.68	64	146
9*	2.07	15.5	1.81	2.73	70	238
10*	4.88	13.6	2.07	2.60	85	284
11*	1.05	10.0	1.76	2.85	100	137
12	1.16	10.2	1.83	2.74	137	88
13	1.72	11.4	1.90	2.59	54	66
14	0.95	14.1	1.67	2.74	50	92
15*	1.51	18.9	1.70	3.06	71	140
16*	2.50	16.9	1.88	3.00	88	240
17	1.25	9.3	1.80	2.80	110	116
18	1.12	10.8	1.82	2.91	144	76
19	1.49	11.7	1.91	2.72	106	72
20	1.79	12.4	1.90	2.89	89	90
21*	1.18	19.6	1.69	2.86	74	209
22*	1.22	16.4	1.82	3.05	73	277
23	0.72	18.5	1.65	2.80	121	147
24	0.90	9.8	1.88	2.64	108	113
25	1.28	15.2	1.80	2.91	62	97
26	1.57	14.5	1.57	2.99	55	114
27*	1.05	18.7	1.68	2.80	67	256
28	0.55	10.2	1.67	2.60	68	161
29	0.50	12.8	1.25	2.69	42	216
	4.32	13.0	1.78	2.79	87	148

Table 4.6: Parameters used to model the pure leptonic model for each region. W_e is the electron energy budget, B is the average magnetic field strength over the region, α_1 is the low-energy spectral index, α_2 is the high-energy spectral index, E_c is the exponential cut-off energy and n_H is the ISM gas density. The bottom row of quantities represents either the total sum (energy budget) or the weighted average values across the remnant (all other parameters). See section 4.1 for calculations of the weighted average. An asterisk (*) placed next to a region number indicates that at least one of the regions parameters were different from that of HESS.

11 regions are indicated with an asterisk. The H18 parameters can be found in Appendix D. There is some variation within each parameter but no stand out anomalies. The B field ranges from $7.7 - 19.6$ μG, with a weighted average of 13.0 μG. Recall section 4.1 for calculations of the weighted average. Our weighted average is consistent with the average B field for the entire remnant, $B = 14.3$ μG (H18). The total energy allocated to the electron population in each region ranged from $0.5{-}4.9\times10^{46}$ erg, with a total sum of 4.1×10^{47} erg. This is consistent with the energy budget of 4.3×10^{47} erg required for the entire remnant from H18. The low-energy spectral index, α_1, ranges from 1.25 to 2.07, with a weighted average of 1.78, which is compatible with the entire SNR value of 1.85 (H18). This is also consistent with what we would expect from DSA (~ 2), however it does suggest that some GeV hardening effects are occurring to the electron population. Similarly, the high-energy spectral index, α_2, ranges from 2.56 to 3.06 with an average of 2.79. The model for the entire SNR used an index of 2.93 (H18). Again there appears to be some hardening effects, this time to the high-energy part of the spectrum. This could be due to synchrotron losses. These results will be discussed in more detail below.

4.3.2 Magnetic Field Amplification

We have illustrated the variation of each parameter with a colour map in Figure 4.10. In general, the regions on the western side of the SNR (Regions 21, 22 and 27), where the gas is most dense, require large magnetic fields ($B \geq 16$ μG). In fact, there appears to be a gradient of decreasing B field as one progresses from the west of the SNR to the east. The large magnetic fields corresponding to regions of high density in the west is an expected result. When the shock-front reaches and interacts with a dense gas clump the surrounding B field should be amplified (Inoue et al., 2012; Celli et al., 2018). Recalling Equation 3.3, the electron break-energy depends on the magnetic field strength:

$$E_b = 1.25 \left(\frac{B}{100\ \mu\text{G}} \right)^{-2} \left(\frac{t_0}{10^3\ \text{yr}} \right)^{-1} \text{TeV} \tag{4.7}$$

We can calculate the break-energy for each region, using the derived B field strength, and compare this to the 2.5 TeV value we assumed. The break-energy ranges from 23 to 131 TeV across the 29 regions, with an average of 60 TeV. This is much larger than the expected 2.5 TeV. In order to recreate the average break-energy of 2.5 TeV, the B field needs to be increased by a factor of ~ 5 in each region, corresponding to an average B field of ~ 55 μG. To determine whether the average B field within a region can reach these intensities, we turn to the size of the X-ray hot spots observed by Uchiyama et al. (2007). The size of such hot spots were found to be ~ 10" by 10" and it was proposed that the B field could reach values of at least mG at these locations. We can calculate the amount of time-variable hot spots that are required in order to obtain an average B field of 55 μG in a region by assuming the post-shock B field, $B_{\mu\text{G}} \sim 10\mu$G, and calculating a weighted average:

$$B = \frac{B_\text{h} \times A_\text{h} + B_{\mu\text{G}} \times (A - A_\text{h})}{A} \tag{4.8}$$

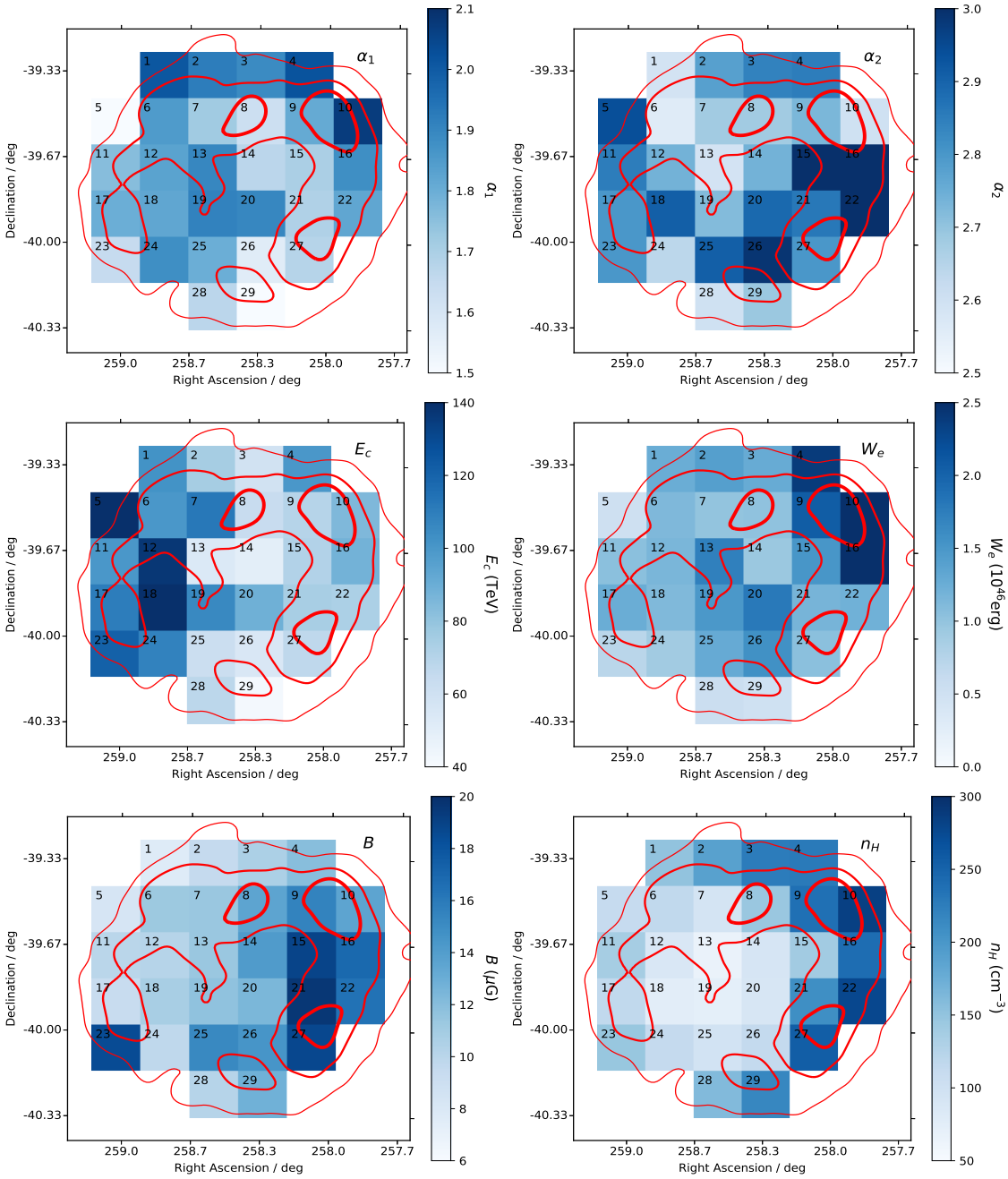

Figure 4.10: Colour maps portraying the variation of the low-energy spectral index **(top left)**, high-energy spectral index **(top right)**, energy cut-off **(middle left)**, energy budget **(middle right)**, the magnetic field strength **(bottom left)** and the ISM gas density **(bottom right)** across each region. All maps include the HESS γ-ray contours at 5, 10 and 15σ overlaid in red, as per chapter 2.

where B is the average B field strength for a region, $B_h = 1$ mG is the B field strength of the hot spots, $A_h = N_h \times (10'')^2$ is the total area of hot spots and $A = (648'')^2$ is the total area of a region. Rearranging for N_h gives:

$$N_h = A\frac{B - B_{\mu\mathrm{G}}}{(10'')^2(B_h - B_{\mu\mathrm{G}})} \sim 191\ . \tag{4.9}$$

So, a total number of 191 hot spots within a region are required to produce an average B field of 55 μG and, hence a break-energy of 2.5 TeV. Since hot spots, or regions of amplified B field, are produced around gas clumps, this doesn't seem too unreasonable. Basically, the number of hot spots we have calculated corresponds to the number of pc-scale clumps we require. The observation of such clumps is beyond the scope of this work as the Mopra telescope cannot resolve such detail. However, the Atacama Large Millimeter Array (ALMA) can resolve such hot spots and observations are underway. Finally, if we also consider the weighted average of the derived B fields across the regions (13.0 μG), we find that this corresponds to a total clump number of 13. This number is much more feasible than the that resulting from the 2.5 TeV break-energy assumption. An aim for the ALMA would be to resolve and quantify the pc-scale clumps around RX J1713.7-3946 in order to establish whether these parameters are realistic.

4.3.3 Variation of the Electron Distribution over the SNR

The exponential cut-off energy appears to be lower on the western side compared to the eastern side of the remnant. One would expect this inverse relationship between the B field and E_c, as the synchrotron losses should increase as B increases. Higher energy electrons suffer most from synchrotron losses and hence when the losses are greater the maximum electron energy is limited. The exponential cut-off is then controlled by the synchrotron losses and the amount of high-energy electrons remaining.

Moreover, Regions 15 and 22 stand out with a large high-energy electron index $\alpha_2 > 3$. Otherwise, there appears to be no trend corresponding to the geometry of the regions (Figure 4.10). As mentioned earlier, the large α_2 values (average of 2.81) are quite inconsistent with that expected from DSA (~ 2). H18 suggested that electrons with energies greater than 5 TeV (corresponding to the α_2 energies) are affected by modifications like synchrotron cooling. This seems reasonable considering high energy electrons are cooled quicker than their lower energy counterparts as discussed above. In other words, α_2 and E_c are basically controlled by the same phenomena; the amplification of the B field. We can see this in Figure 4.11, where we have plotted the average B field for each region against the corresponding exponential cut-energy and high-energy spectral index in the top left and right plots respectively. The correlation in both cases has a significance greater than 3σ, where the significance is equal to 1 minus the p-value. More on how this correlation coefficient is calculated is presented in chapter 5. Surprisingly, when we examine the relationship between the cut-off energy and the high-energy spectral index, no correlation is found ($\rho = 0.01$). This indicates that even though the cut-off energy and high-energy spectral index are dependent on the magnetic field, they are completely independent from each other.

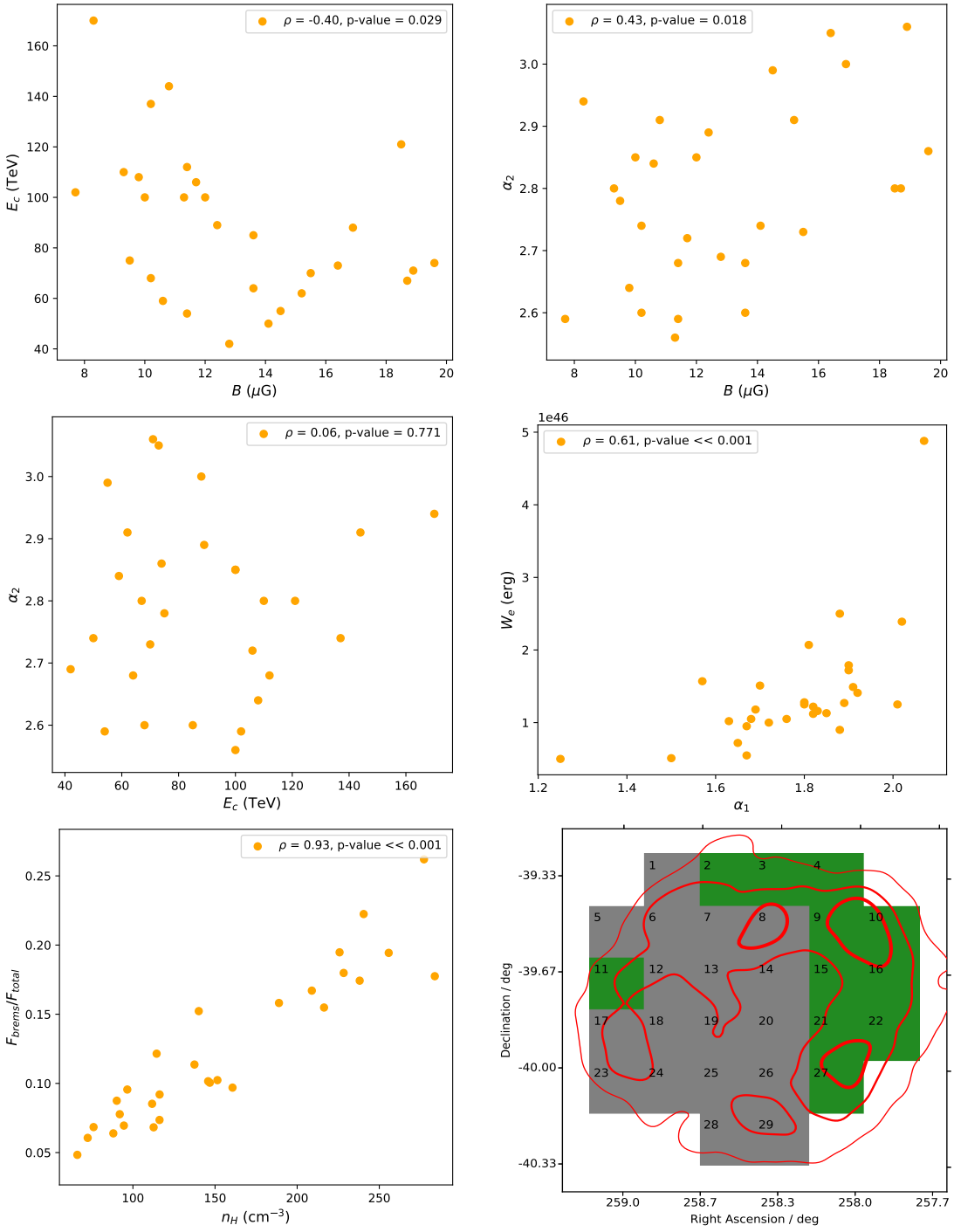

Figure 4.11: **Top Left:** Scatterplot of the average magnetic field, B, against the exponential cut-off energy, E_c. **Top Right:** Scatterplot of the average magnetic field, B, against the high-energy spectral index, α_2. **Middle Left:** Scatterplot of the high-energy spectral index, α_2 against the cut-off energy, E_c. **Middle Right:** Scatterplot of the electron energy budget, W_e, against the low-energy spectral index, α_1. **Bottom Left:** Scatterplot of the ratio of TeV Bremsstrahlung emission to total TeV emission (see text for a description) against the ISM volume density, n_H. **Bottom Right:** Colour map plot of the regions (green) with at least one different parameter from H18. The colour grey indicates regions with the same leptonic parameters. Overlaid in red are the HESS TeV contours.

Even more interesting is the change in relationship between the magnetic field and the cut-off energy at about 13 μG. The cut-off energy appears to level off at about 40 - 80 TeV as the magnetic field reaches this threshold value. This may be suggestive of a limit to the amount of synchrotron losses an electron distribution can experience. To interpret this finding we turn to a suggestion from H18. They suggested that the age of the remnant (1600 years) is not consistent with the theory of synchrotron losses, that the SNR is too young to have suffered from sufficient losses to affect the spectral index and cut-off energy. However, Figure 4.8 illustrates otherwise. Electrons with energy 5 TeV and 50 TeV have synchrotron cooling times of approximately 10000 years and 1000 years respectively (for a B field strength of 14.3μG). In fact, ~ 35 TeV electrons have a cooling time of ~ 1600 years, so any electrons with energy greater than this would've had sufficient time to expel their energy through synchrotron processes. Any electrons below this energy haven't had sufficient time to lose all their energy and this could be why we don't see the cut-off continually decrease below 40 - 80 TeV.

The electron energy budget appears to be greater in the north, specifically, regions 4, 10 and 16. Similarly, the low-energy spectral index peaks in these northern regions but also has some larger values in the south. We illustrate the correlation between these two parameters in Figure 4.11 (middle right). As indicated in the figure, the correlation coefficient is 0.61. What these results are suggesting is that in the regions where more energy is distributed to the electrons there are also more low energy electrons producing synchrotron and IC emission. It could be that this extra energy is not accounted for in the other regions because we don't see the emission from the low energy electrons. Considering that these low energy electrons should produce both synchrotron and IC emission, it could be indicative of some phenomena suppressing the acceleration of the low energy electrons, especially in regions 5, 23, 28 and 29, where both α_1 and W_e are low. Revealing the trigger of this suppression is a matter that should be investigated in future studies. Alternatively, a pure leptonic scenario may fail to capture the full picture of how the γ-rays are emitted in those regions with extreme parameters. The correlation study in chapter 5 may give some more insight into these regions.

4.3.4 The Role of Bremsstrahlung

As shown in Figure 4.9, regions 16, 21 and 22 all have substantial TeV Bremsstrahlung peaks. Regions 16, 21 and 22 all have dense gas located within, they also have unusually large synchrotron spectra (grey), with very steep X-ray spectra. The dense gas in these regions is not only providing a target for Bremsstrahlung processes but is also amplifying the local B field, producing the intense synchrotron spectra we see. The Bremsstrahlung peak at TeV energies in region 16 and 22 is quite large; we can see the total leptonic TeV emission (dashed) is significantly affected. As a result, the parameters for these region were quite distinct from those derived in H18. Regions 16 and 22 have the largest ratio of Bremsstrahlung TeV emission to total TeV emission we see from any of the regions; $\sim 22\%$ and $\sim 26\%$ respectively. To calculate this ratio we integrate both the Bremsstrahlung spectrum and the total leptonic spectrum over the energy range covered by HESS (~ 0.1 TeV to 50 TeV). The ratio of the TeV Bremsstrahlung emission to the total TeV emission in

other regions ranges from $\sim 5-22\%$. The significance of this contribution at TeV energies has a strong dependence on the ISM gas density as illustrated in Figure 4.11 (bottom left).

Regions 1, 4 and 10 have strong MeV Bremsstrahlung components. Both regions 4 and 10 required distinct parameters from H18. This is because they still have quite significant TeV Bremsstrahlung emission as opposed to region 1. Regardless, the synchrotron spectra is not so intense in regions 1 and 4, meaning electrons have more energy available for Bremsstrahlung (and IC) processes. This explains why the Bremsstrahlung spectrum peaks so strongly at MeV energies in these regions. All three of these regions have the largest low-energy electron index $\alpha_1 > 2$. This suggests that the low-energy electrons are responsible for these MeV peaks. As proposed above, there may be some phenomena suppressing the acceleration of the low-energy electrons in regions where the low-energy electron index is low. Identifying whether the MeV Bremsstrahlung peak actually exists would give us further confirmation of this mechanism.

Additionally, in Figure 4.11 (bottom right), we display what regions required different parameters to those derived in H18. The differences arise due to the effect Bremsstrahlung has on total TeV emission. As this figure displays, the regions with significant TeV Bremsstrahlung emission appear to be mostly situated on the north and west side of the SNR. The spatial location of these regions is coincident with the strongest TeV emission (see red contours). We must consider the Bremsstrahlung component in these regions when investigating the γ-ray emission in chapter 5.

4.4 Conclusions

We have shown that the hadronic model is sufficient in producing the TeV γ-ray emission seen towards RX J1713.7-3946. Generally, the parameters used in our models were physically reasonable. The proton spectral index for each region agreed with DSA theory and the hardening of GeV spectrum due to a clumpy ISM theory. Additionally, the energy budgets agreed with two other predictions, one of which was based on assumptions about the energy budget of SNe, the other was based upon reproducing the HESS γ-ray observations. Some regions were flagged for having either an abnormally soft spectral index and/or a large energy budget. The possible causes for these peculiar scenarios were discussed and either attributed to large amounts of gas or leptonic involvement.

Alternatively, we have shown that the leptonic model can reproduce the broadband observations seen towards RX J1713.7-3946. However, it does appear to have some trouble; the high-energy spectral index, α_2, required for each region was > 2.5. This deviates from the expected DSA prediction, but can be explained by synchrotron cooling effects. Also, we have estimated that the number of molecular clumps at and within the shock-front would need to exceed 191 in order to satisfy the assumed break-energy of 2.5 TeV. Otherwise, the number of expected clumps declines if we allow a much larger break-energy and a subsequent B field strength less than 20 μG. Either way, we have provided a technique to constrain the B field for future studies if the number of clumps can be observed. Furthermore, we have shown the presence of a strong Bremsstrahlung component at TeV energies in region 22 ($\sim 26\%$ of the total TeV emission), along with

its dependence on the gas density, which was expected. Additionally, the low-energy electrons in some regions appear more prevalent, as a result the Bremsstrahlung emission peaks at MeV energies. MeV observations are required to constrain this phenomena; which are currently unavailable at the resolution of the regions.

Some regions were found to be interesting due to the nature of the parameters required to model their hadronic or leptonic emission. From this, we can begin to form an understanding of the γ-ray emission in these regions. However, the hadronic vs leptonic nature of the γ-ray emission is still not clear from our SED models alone. We aim to unveil more on the issue with a correlation study between the ISM and the γ-rays in the next chapter (chapter 5).

5 2D ISM/Gamma-ray Correlation Study of RX J1713.7-3946

The SED modeling in the previous section was not able to quantify the relative contribution of hadronic vs leptonic γ-rays. We now turn to a complementary approach aiming to address this issue. This comes in the form of a 2D correlation study between the ISM gas and the γ-rays. Fukui et al. (2012) have shown that there is an azimuthal correlation between the ISM gas and the γ-rays; indicating some level of hadronic emission. In our study we utilise the latest ISM gas density data, as measured by the Mopra telescope and SGPS, and the latest high resolution HESS γ-ray flux observations to compare the morphology within each of the 29 regions. In doing so, we aim to study the correlation, or anti-correlation, between the two quantities on a more refined scale. We begin with an initial spatial comparison study that categorizes regions according to their average gas density and total γ-ray flux. Then we proceed to perform a more quantitative study that involves breaking each region down into smaller cells. The size of each cell are matched to the HESS TeV γ-ray resolution.

5.1 Initial ISM and Gamma-ray Spatial Comparison

Displayed in Figure 5.1 is the total ISM column density map calculated with the Mopra and SGPS data from section 2.4, overlaid with the γ-ray contours in blue. For now, we consider this map as a guide to see what regions are rich in gas and those that are not. It also gives us a first impression of the spatial coincidence between the ISM and the γ-ray intensity in each region. Regions along the north and following the γ-ray shell around the west to the south-west appear, at face value, to display some γ-ray and ISM coincidence. This is consistent with the results from Fukui et al. (2012).

Table 5.1 classifies all the regions according to their average ISM gas density, n_H, and total γ-ray flux. Regions are classified as being gas-poor if their average ISM density is below the threshold of $n_H = 120$ cm^{-3}. On the other hand, regions are classified as being gas-rich if their average ISM density is above this threshold. Choosing this threshold value ensures that the regions are divided equally into each category. Similarly, a region is classified as having a mild γ-ray flux if the total excess counts in that region are below 3500. If the total excess counts are above 5000 then the region is classified as having an intense γ-ray flux. Finally, regions with total excess counts between these two extremities are classified as having a moderate γ-ray flux. These threshold values were chosen to isolate those regions with extreme (low and high) total excess counts.

Firstly, note that regions 1, 23 and 28, located on the edge of the SNR are gas-rich and have a mild γ-ray flux. The gas observed in these regions may be beyond reach of the CRs. An intense γ-ray flux is mostly seen in gas-rich regions. This gives us reason to believe that

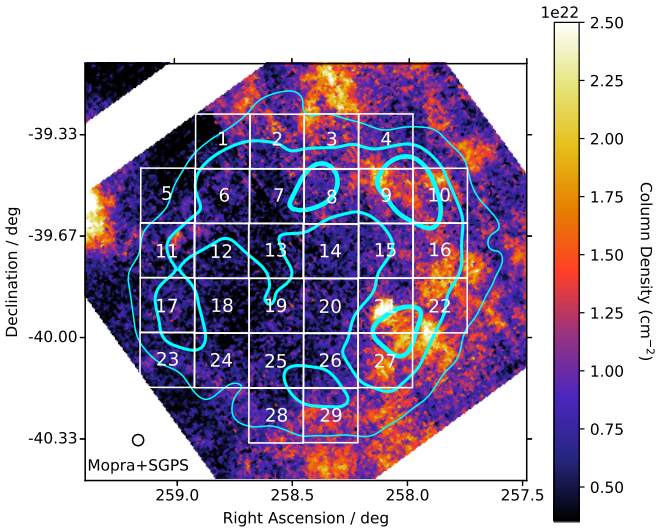

Figure 5.1: The total proton column density map consisting of the combined SGPS HI column density and the Mopra ^{12}CO(1-0) brightness temperature converted into H_2 column density. Overlaid in white are the 29 regions of interest and in cyan are the γ-ray contours (>2 TeV). The resolution of the image is that of the SGPS (2.2′).

the gas is influencing the production of these γ-rays. By itself, region 22 was shown to have a modeled GeV flux that almost violated the Fermi-LAT measurement for the entire SNR (section 4.2). It also falls in the category of intense γ-rays and being gas-rich. In this region a Bremsstrahlung component was found to be significant in a pure leptonic model (subsection 4.3.4). This suggests that the γ-ray emission has a substantial contribution from both leptonic and hadronic processes. Gas-poor regions generally appear to have a moderate γ-ray flux. It could be that all or most of the gas we observe in these regions is acting as a target for the CRs. Alternatively, the ISM could be influencing the particle acceleration conditions. To better understand the relationship a quantitative approach is applied in the next section.

	Mild Flux counts $<$ 3500	Moderate Flux 3500 $<$ counts $<$ 5000	Intense Flux counts $>$ 5000
Gas-poor ($n_H < 120$ cm^{-3})	5,24	12,13,14,18,19,20,25,26	6,7,17
Gas-rich ($n_H > 120$ cm^{-3})	1,23,28	2,3,4,11,15,29	8,9,10,16,21,22,27

Table 5.1: Regions classified according to their ISM gas density and γ-ray flux intensity (>2 TeV). For details on the classification see the text.

5.2 Quantitative ISM and Gamma-ray Flux Correlation Analysis

A quantitative correlation study was performed by calculating the Pearson Correlation coefficient between the ISM gas density and the γ-ray flux for all 29 regions. If we expect the hadronic scenario to be dominant then the spatial correlation between the γ-ray flux, Φ_γ, and the gas density, n_H, should be positive and approximately linear. Recall Equation 3.7:

$$\Phi_\gamma = 4\pi n_H \int \frac{d\sigma}{dE_\gamma} \frac{dN_p}{dE_p} dE_p \, .$$

As the contribution from the hadronic mechanism decreases, this positive-linear relationship is expected to diminish. This behaviour is expected since we anticipate some level of IC γ-ray emission. Since gas clumps amplify the B field, electrons will more readily lose their energy to synchrotron processes in these regions. Such energy losses will cause the IC emission to be suppressed in these regions resulting in IC γ-rays to be anti-correlated with the ISM gas. For this reason we may expect anti-correlation to represent regions where the IC mechanism is dominant.

We also consider the Bremsstrahlung process as its flux is also linearly dependent on the ISM gas density. Correlation between the γ-rays and ISM may also indicate the presence of this component. The Bremsstrahlung fraction results from subsection 4.3.4 will be used in conjunction with our 2D correlation study here to assess the fraction of Bremsstrahlung emission over the entire SNR.

5.2.1 Methodology

Re-binning the ISM Data

To correctly quantify the ISM gas density we required the total column density of both the atomic and molecular protons. The Mopra ^{12}CO data was used as a measure for the column density of molecular protons, N_{H_2}, by applying an X-factor, X, to the observed brightness temperature, T (Equation 5.1).

$$N_{H_2} = X \times T \, \mathrm{cm}^{-2} \tag{5.1}$$

Fukui et al. (2012) take X to be 2.0×10^{20} (cm^{-2} (K km s^{-1})$^{-1}$), which we also adopted. The atomic hydrogen column density was taken from the ATCA and the Parkes Radio Telescope (McClure-Griffiths et al., 2005). We obtained the HI column density map from Fukui et al. (2012), which was already converted from a brightness temperature to a column density as explained in subsection 2.4.2. As mentioned in chapter 2, the velocity range for all gas maps is from -20 to 0 km s^{-1}, as is the range considered to be associated with the SNR.

Similarly to Mopra above, we also used the Nanten ^{12}CO data as a tracer for the molecular protons. This H_2 component is also combined with the SGPS HI component to produce a map of the total ISM proton column density. The resulting map is used as an independent data set for our correlation study in order to validate the results obtained with the Mopra data set.

As mentioned previously, the Nanten telescope has a poorer angular resolution than that of the Mopra telescope. However, both yielded consistent results at the angular scales of Nanten (see Appendix A for a comparison of both data sets). The focus and discussion of our study centered on the results obtained with the Mopra data set due to its superior resolution. The majority of the Nanten correlation results can be found in Appendix E, however we do show some of these results later in this chapter.

The HESS γ-ray data were analysed in units of excess counts (as in section 5.1). Each 0.6′ x 0.6′ (0.01° by 0.01°) pixel in the HESS ($>$ 2 TeV) γ-ray image was smoothed and integrated over a circle of radius 0.03° to obtain the excess count number (H18). Since the pixel size was much smaller than the integration region, neighboring pixels contain overlapping information. Each of our 29 regions has size 0.18° by 0.18° and can be split up into 9 sub-regions with independent information (see Figure 5.2). We used these 9 sub-regions for our correlation study to ensure we obtained a data set of independent measurements; no more information would be provided by using any more sub-regions. We used the Miriad software (Sault et al., 1995) to re-bin the HESS γ-ray image into pixels with size 0.06° by 0.06° (3.6′ by 3.6′). This ensured that each region contains the required 9 independent pixels. The re-binning function took the average of the original, smaller pixels contained within the larger desired region and used this as the new pixel value. See Figure 5.3 (top left) for the final re-binned image.

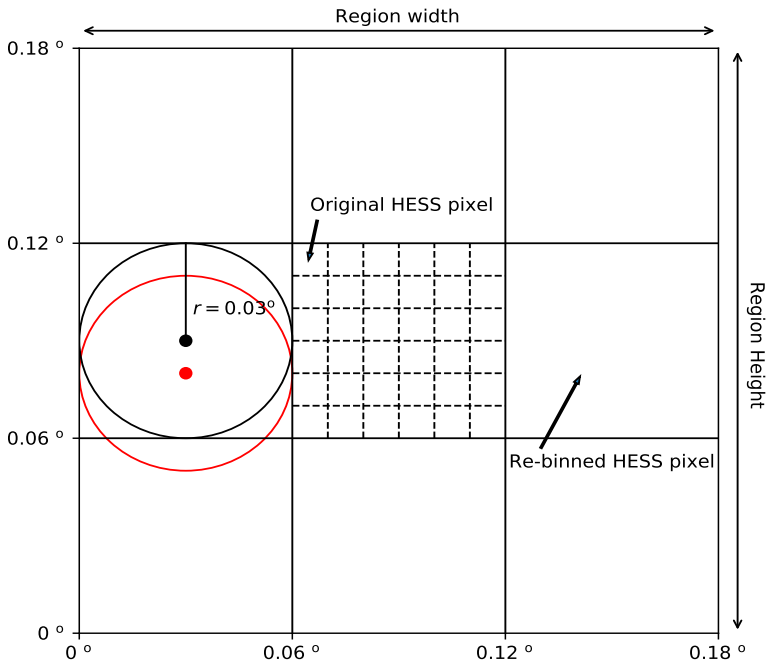

Figure 5.2: Depiction of the HESS re-binning process for one of our 29 regions. The dashed squares indicate the size of the original HESS pixels. The nine large-solid squares represent the size and location of the re-binned pixels. The circles represent the integration region for two of the original pixels. The red circle is clearly overlapping with the black circle and hence they do not contain independent information.

We then used Miriad again to re-grid and match the Mopra ^{12}CO image resolution to the HESS image resolution. This ensures the information in both images are spatially matched. In doing so, the original Mopra CO pixels of size 0.01° by 0.01° were re-gridded to a size of 0.06° by 0.06°. Similarly, the SGPS HI column density map was re-gridded from an original pixel size of 0.5′ by 0.5′. We then combined the two gas maps together to obtain a total proton column density value for each of the re-gridded pixels. The molecular column density was also multiplied by a factor of 2 to account for both protons within the H_2 molecule. The re-binned molecular, atomic and combined maps can be found in Figure 5.3.

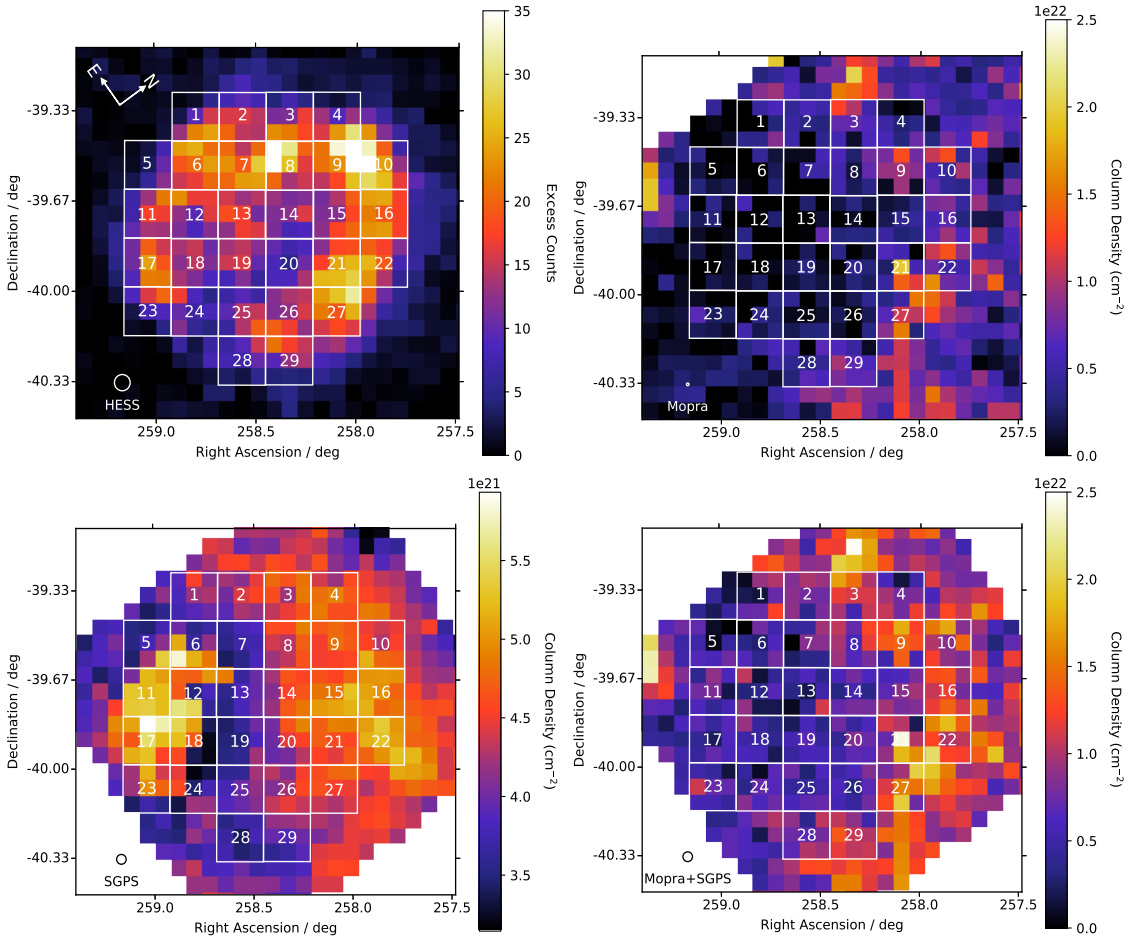

Figure 5.3: Top Left: HESS γ-ray excess counts for $E_\gamma > 2$ TeV, re-binned to fit 9 pixels in each 0.18° by 0.18° region as described in text. The arrows indicating north and east correspond to galactic coordinates. **Top Right:** Mopra ^{12}CO map, converted to proton column density (cm^{-2}) and re-gridded to match the re-binned HESS image. **Bottom Left:** Column density (cm^{-2}) of the HI emission derived from the ATCA and Parkes data, re-gridded to match the re-binned HESS image. This image has been corrected for HI self-absorption (Fukui et al., 2012). **Bottom Right:** The total proton column density, N_p, derived from the Mopra and SGPS data.

Applying Gamma-ray Threshold Cuts

The γ-ray emission declines radially and rapidly in the outer regions, while the gas pertains to its clumpy nature (see Figure 5.3). ISM gas may exist beyond the γ-ray shell that has been 'untouched' by the shock and the majority of the accelerated particles. In such a case, where there is more untouched gas beyond the shock front than there is within, we may expect some anti-correlation with the γ-rays. Since the radial gas density profile is likely more complex than a simple circular boundary, as shown by Moriguchi et al. (2005), this issue can be managed by removing pixels that correspond to γ-ray counts below a certain threshold. We therefore apply a threshold of 5σ to the HESS γ-ray counts (this corresponds to ~ 5 excess counts). This ensures that only pixels with a significant signal are being used and also allows us to define a γ-ray 'boundary'. This boundary encompasses the region where the bulk of the γ-rays are emitted. Figure 5.4 displays the HESS γ-ray map (left) and ISM gas density map (right) after this threshold has been applied. The pixels that appear white have been removed from their particular regions' data. Interestingly, some pixels have been removed from within the SNR. This only ensures us that pixels corresponding to significant γ-ray signal have been used, even for the inner regions.

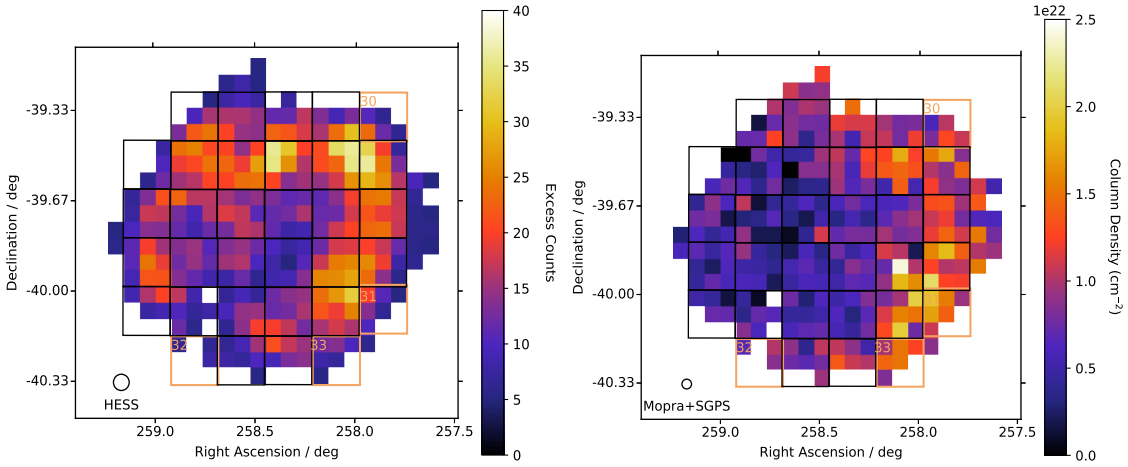

Figure 5.4: Left: The ISM gas column density map, calculated with the SGPS and Mopra datasets, with the 5σ threshold for the γ-ray pixels applied. **Right:** The HESS γ-ray map, with the same 5σ threshold applied. Both images have the original 29 regions outlined in black, while 4 extra regions, have been outlined in brown due to them containing sufficient γ-ray and ISM data.

After applying the threshold cuts there still remain many pixels beyond that of the 29 regions. We added four new regions, encompassing some of these pixels, to perform our correlation study. These regions can be seen in Figure 5.4, outlined in brown. We should take caution when interpreting the results for region 32 as it contains only 3 pixels and region 5 as it only contains 4 pixels.

Error Analysis

As performed in Fukui et al. (2012), the error in the γ-ray excess counts, σ_γ, was calculated as the square root of the number of counts in that pixel:

$$\sigma_\gamma = \sqrt{\text{number of counts}}\,. \tag{5.2}$$

A more correct way to quantify the significance of γ-ray counting experiments is presented in Li and Ma (1983); however, this method requires detailed information about the HESS observing process, e.g. the total 'ON-source' area, total 'OFF-source' area and the total number of 'OFF-source' counts. This information was not available for this study. However, Equation 5.2 assumes statistical errors in the Gaussian regime, which applies to the HESS excess counts since the ON and OFF events are large (>20).

To obtain the error measurement for the gas column density we calculated the errors in the Mopra, Nanten and HI data separately and combined them accordingly. The error in the Mopra brightness temperature data was derived from the root-mean-square (rms) noise fluctuations per velocity channel and the number of integrated channels. The rms brightness temperature value for each pixel within an observed velocity channel was $T_{rms} = 1.5$ K. Since we integrated over a velocity range of -20 km s^{-1} to 0 km s^{-1} and the velocity resolution is $\Delta v = 0.11$ km s^{-1}, we had $N_M = 20/0.11 \approx 182$ total velocity channels (Mopra observations). Using the principles of error propagation for integration (or summing), the error in the velocity-integrated brightness temperature map, σ_I, is calculated by Equation 5.3.

$$\sigma_I = T_{rms} \times \sqrt{N_M} \tag{5.3}$$

Additionally, the Mopra map was re-gridded to match the HESS pixelation. As a result, we lose resolution but we also decrease the error in the Mopra data since the re-griding is an averaging process. The re-griding process involved averaging over 38 independent Mopra pixels (beam size = 35′′) to obtain the larger pixel. The error in the re-gridded Mopra data, σ_R, can be again expressed with error propagation:

$$\sigma_R = \sigma_I \times \frac{1}{\sqrt{n}} \tag{5.4}$$

where $n = 38$ is the number of pixels averaged over. To convert this into a column density error we simply multiplied by the X factor, $X = 2.0 \times 10^{20}$, and the factor of 2 accounting for two protons per H_2 molecule. Hence the rms error in the proton column density due to the H_2 molecules traced by Mopra was found to be:

$$\begin{aligned} \Delta N_{p,\mathrm{M}} = T_{rms} \times \sqrt{N_M} \times \frac{1}{\sqrt{n}} \times 2.0 \times 10^{20} \times 2\ \mathrm{cm}^{-2} \\ \sim 1 \times 10^{21}\ \mathrm{cm}^{-2} \end{aligned} \tag{5.5}$$

A similar analysis was used to obtain the error in the Nanten and HI data. For the HI data we use the same velocity range as Mopra, which results in ~ 24 velocity channels due to the velocity resolution of $\Delta v = 0.82$ km s^{-1}. We take $T_{rms} = 1.9$ K and use the

SGPS beam size (2.2′) to find a total number of ~ 3 independent pixels averaged over in the re-griding process. We also include the conversion factor of 1.823×10^{18} from Equation 2.2. The calculated error in the proton column density due to the observed atomic hydrogen was found to be:

$$\Delta N_{p,\mathrm{HI}} \sim 0.01 \times 10^{21} \ \mathrm{cm}^{-2} \ . \tag{5.6}$$

The error in the proton column density due to the H_2 molecules traced by Nanten was calculated to be:

$$\Delta N_{p,\mathrm{N}} \sim 0.4 \times 10^{21} \ \mathrm{cm}^{-2} \ . \tag{5.7}$$

Here we have used $T_{rms} = 0.3$ K per velocity channel, ~ 31 velocity channels due to $\Delta v = 0.65$ km s^{-1} and ~ 2 independent pixels averaged over in the re-griding process. Additionally, we have accounted for the molecular to atomic conversion with a multiplicative factor of 2 and also the X factor conversion. Table 5.2 presents the rms noise fluctuations, velocity resolution and beam size required to calculate the error for all three surveys along with the final uncertainty, $\Delta N_{p,i}\mathrm{cm}^{-2}$ (calculations shown above). In this case, the subscript i denotes the different gas surveys; Mopra, Nanten and SGPS (HI).

Telescope	T_{rms} (K)	Δv (km s^{-1})	Beam Size	$\Delta N_{p,i}\mathrm{cm}^{-2}$
Mopra	1.5	0.11	35′′	1×10^{21}
Nanten	0.3	0.65	2.6′	0.4×10^{21}
SGPS	1.9	0.82	2.2′	0.01×10^{21}

Table 5.2: The rms noise fluctuations, velocity resolution, beam size and the final calculated uncertainty for the Mopra, Nanten and SGPS (McClure-Griffiths et al., 2005) surveys, re-gridded to the HESS resolution.

Bootstrapping the Correlation Coefficient

To quantify the correlation between the gas density and the γ-ray flux we calculate the Pearson correlation coefficient, ρ, for the 9 pixels in each region. The Pearson correlation coefficient is a measure of the linear correlation between two variables and takes on a value between -1 and +1. A value of +1 indicates a perfect, positive-linear relationship, a value of 0 indicates no linear relationship and a value of -1 indicates a perfect, negative-linear relationship. The coefficient, ρ, is defined as:

$$\rho = \frac{\mathrm{cov}(x, y)}{\sigma_x \sigma_y} \tag{5.8}$$

where $\mathrm{cov}(x, y)$ is the covariance of both data sets and quantifies the variability of both variables. It is defined as:

$$\mathrm{Cov}(x, y) = \frac{1}{n_d} \sum_{i=1}^{n_d} (x_i - \bar{x})(y_i - \bar{y}) \ . \tag{5.9}$$

Its purpose is to measure the linearity of the two variables but needs to be normalised by the standard deviations of both x and y, σ_x and σ_y respectively, in order to interpret the magnitude. The standard deviation measures the amount of uncorrelated variation within each data set:

$$\sigma_x = \sqrt{\frac{\sum_{i=1}^{n_d}(x_i - \bar{x})^2}{n_d}} \tag{5.10}$$

where n_d is the number of measurements in the data set, x_i and y_i are the individual measurements and $\bar{x}$ and $\bar{y}$ are the means of each data set. In our case, we take x and y to be the ISM column density and γ-ray excess counts respectively.

Since ρ does not incorporate the individual error from each data point, we employ a bootstrapping technique. This enables us to calculate a significance related to ρ. We take the nine data points from a given region and randomly re-distribute them in both x and y directions assuming each data point follows its own normal distribution. The actual x-y values are taken as the means for the re-distribution, while the standard deviations are taken to be the errors in each direction. An example of this randomisation is shown in Figure 5.5 (left). This new, randomised data set produces a new ρ value. Reiterating the process multiple times provides a distribution of ρ values. Figure 5.5 (right) shows the distribution obtained for region 1 after 100 000 iterations were performed. We highlight the location of the ρ value corresponding to the original data set with the red line along with the 3σ values (99.7%) of the distribution (dashed lines).

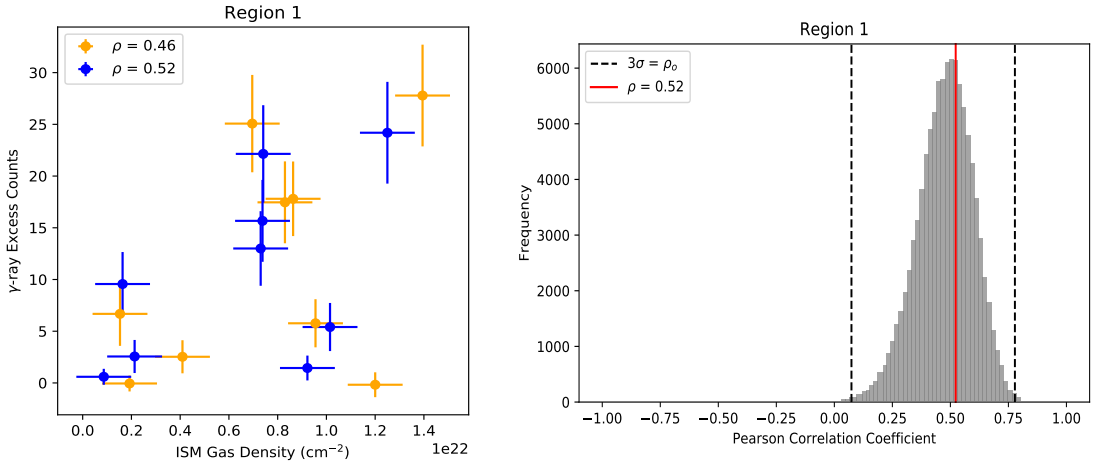

Figure 5.5: An example of bootstrapping the γ-ray counts and the ISM column density data sets for region 1. **Left:** The original nine data points (blue) plotted and compared against a single set of randomised data points (orange), as described in text. The same error bars are used on both data sets and the new ρ value is indicated in the legend. **Right:** The distribution of ρ values calculated from a total of 100 000 randomisations. The red line signifies the ρ value of the original data, while the dashed lines represent the 3σ significance band.

We take the original $\rho = 0.52$ to be our final value, but we wish to quote the significance of some optimistic value ρ_o. In this case, because ρ is positive, we take the optimistic

value to be the upper 3σ value from the distribution (right dashed line in Figure 5.5). If ρ was negative we would take the lower 3σ value to be the optimistic value. The choice of 3σ is arbitrary. In this case it encompasses 99.7% of the values within the distribution. This optimistic value, $\rho_{\mathrm{o}} = 0.78$ for region 1, is the correlation coefficient we might expect the data set to produce in the most extreme case. The optimistic correlation coefficients for the remaining regions can be found in Table 5.3. Additionally, the ρ distributions for all the remaining regions can be found in Appendix E.

Finally, the significance of ρ_{o}, and hence of ρ, is found by determining the probability that a randomly distributed data set will produce a Pearson correlation coefficient equal to or as extreme as ρ_{o}. This probability is what is known as the p-value. To determine this probability we need to make some assumptions about our data. We assume that each data set is distributed normally (e.g. with a Gaussian, $N(\mu_{x,y}, \sigma_{x,y})$). We randomly re-distribute the entire data set according to its normal distribution and hence find a new ρ value, see Figure 5.6 (Left). The mean and standard deviation for the Gaussian distribution are taken as the mean and standard deviation of the data set. Likewise to above, we then re-iterate this process 100 000 times in order to produce a distribution of correlation coefficients. This is the distribution of correlation coefficients we would expect from 100 000 random data sets. We analyse our distribution in terms of the absolute value, $|\rho|$, enabling us to deal with negative correlation coefficients (see Figure 5.6 Right). The distributions for the remaining regions can be found in Appendix E. If these random data sets can produce a ρ value, within the 3σ value, as extreme as ρ_{o} then clearly ρ_{o} is not special. We call this 3σ value, ρ_{thresh}. So if $\rho_{\mathrm{o}} > \rho_{\mathrm{thresh}}$ then we have a significant result. Figure 5.6 (Right) illustrates this process for region 1. Clearly, $\rho_{\mathrm{o}} < \rho_{\mathrm{thresh}}$, hence the result is not significant. In fact we can calculate the exact integer significance of ρ_{o} by

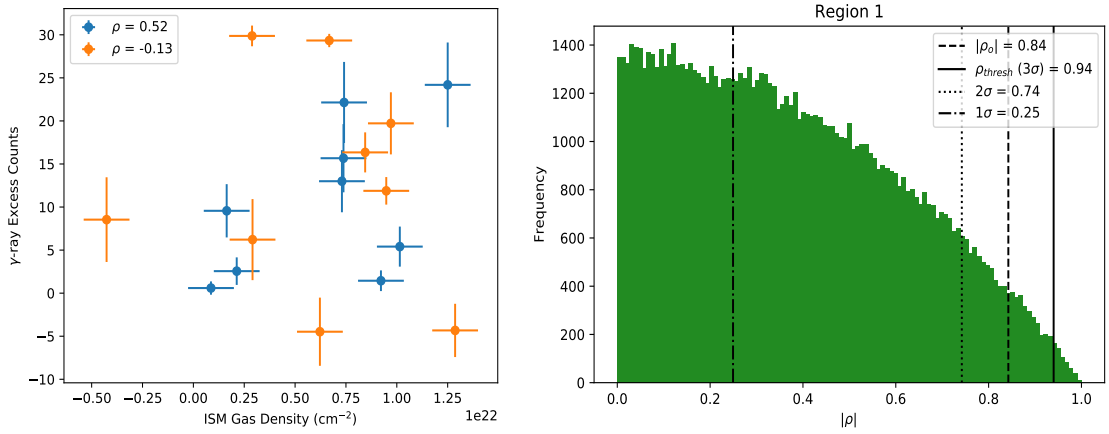

Figure 5.6: An example of how the significance of the ρ value for region 1 is calculated. **Left:** A depiction of how the original data (blue) is randomly re-distributed according to a normal distribution (orange). **Right:** The absolute values of our random distribution of ρ values. The 1σ, 2σ and 3σ values are illustrated with dot-dashed, dotted, and solid lines respectively. In being consistent with Figure 5.5, ρ_{o} is illustrated with a dashed line.

rounding it down to the nearest integer sigma. For example, $\rho_o = 0.78$ in region 1, which is above the 2σ threshold but below the 3σ threshold so we attribute it a significance of 2σ. This significance is what we quote for our original ρ value.

Summary of Methodology

Before preceding to present the results from this study we summarise the steps carried out above. The aim was to quantitatively compare the Mopra and Nanten ^{12}CO gas maps separately to the HESS γ-ray map by calculating the correlation coefficient within each region. The pixels within each region of each map were re-binned to match the HESS resolution in order to ensure each pixel contained independent information. Threshold cuts were applied to the HESS γ-ray map and the co-located pixels from the gas maps. This ensured only pixels with significant γ-ray counts were used. The uncertainty for each pixel was calculated within each map; these values aid in later significance analysis. The Pearson Correlation Coefficient was then calculated for each region twice, i.e. for each gas map. We then incorporate the individual pixel uncertainties by employing the bootstrapping technique to find an optimistic correlation coefficient for each region. The significance of this optimistic coefficient is calculated and used as the significance for the original correlation coefficient. Through doing this we hope to reveal regions where correlation/anti-correlation between the γ-rays and ISM gas exists.

5.2.2 Results

Table 5.3 presents ρ for the ISM column density and γ-ray counts in each region (original 29 plus the 4 new regions). Here we have performed our correlation analysis using both the Mopra and Nanten data sets separately. Additionally, the optimistic (3 σ) value, ρ_o, is specified along with its statistical significance rounded down to the nearest integer. A scatter plot for each region was also produced and is overlaid with a line of best fit, illustrating the relationship between the ISM column density and the HESS γ-ray emission. Figure 5.7 illustrates some example scatter plots. In these images the molecular component of the ISM column density is calculated using the Mopra data. The plots for these regions are chosen because the ρ value has a significance greater than 3σ, illustrating the most significant correlation. The remaining Mopra/γ-ray plots and also the Nanten/γ-ray plots can be found in Appendix E. The line of best fit (γ-ray excess counts vs ISM column density) is calculated using a least squares regression model. An associated reduced chi-squared value, χ^2/ν, is quoted, where the chi-squared value, χ^2, is a measure of the goodness of fit (Equation 5.11) and ν represents the degrees of freedom:

$$\chi^2 = \frac{(y_i - \hat{y})^2}{\hat{y}} \tag{5.11}$$

where y_i is observable data and $\hat{y}$ is the corresponding predicted value from the linear model. In our case, the degrees of freedom are simply the size of the data set, $n = 9$, minus the number of coefficients in the regression model (2 for linear regression), e.g. $\nu = 7$.

Reg.	Mopra(H_2) + SGPS(HI)			Nanten(H_2) + SGPS(HI)		
	ρ	ρ_o	Significance	ρ	ρ_o	Significance
1	0.40	0.84	2σ	-0.35	-0.88	2σ
2	-0.29	-0.86	3σ	-0.67	-0.94	3σ
3	-0.81	-0.98	3σ	-0.63	-0.95	3σ
4	0.58	0.97	3σ	0.00	0.75	1σ
5	0.44	1.00	2σ	0.87	1.00	3σ
6	-0.00	-0.82	2σ	0.01	0.78	2σ
7	0.01	0.79	2σ	-0.07	-0.81	2σ
8	0.02	0.64	1σ	0.10	0.69	2σ
9	0.38	0.82	2σ	0.56	0.89	3σ
10	0.11	0.63	1σ	0.06	0.56	1σ
11	-0.04	-0.74	2σ	0.57	0.91	3σ
12	0.54	0.90	3σ	0.77	0.95	3σ
13	-0.02	-0.82	2σ	-0.26	-0.88	3σ
14	-0.74	-0.93	3σ	0.21	0.86	2σ
15	0.34	0.88	3σ	0.75	0.94	3σ
16	0.80	0.93	3σ	0.15	0.82	2σ
17	-0.11	-0.80	2σ	0.27	0.87	2σ
18	0.56	0.91	3σ	0.63	0.92	3σ
19	0.13	0.83	2σ	-0.35	-0.88	3σ
20	0.02	0.80	2σ	0.53	0.91	3σ
21	0.49	0.87	3σ	0.73	0.95	3σ
22	0.44	0.86	3σ	0.40	0.83	2σ
23	-0.92	-1.00	3σ	-0.50	-0.97	2σ
24	-0.08	-0.86	2σ	-0.08	-0.84	2σ
25	0.12	0.78	2σ	-0.27	-0.83	2σ
26	-0.02	-0.83	2σ	0.42	0.89	3σ
27	0.24	0.80	2σ	0.46	0.88	3σ
28	0.24	0.89	2σ	-0.03	-0.84	2σ
29	-0.39	-0.96	3σ	-0.74	-0.98	3σ
30	-0.31	-0.94	2σ	-0.80	-0.99	3σ
31	0.85	0.99	3σ	0.61	0.96	3σ
32	0.08	1.00	3σ	0.65	1.00	3σ
33	0.22	0.93	2σ	-0.19	-0.91	2σ

Table 5.3: The calculated Pearson correlation coefficient, ρ, the optimistic Pearson coefficient, ρ_o, and the associated significance, for the ISM column density and the γ-ray counts for each region and for both Mopra + SGPS and Nanten + SGPS data sets. The regions shown in the top section represent our original 29 regions. The regions in the bottom section are the newly added regions that have sufficient pixels after applying the γ-ray threshold (see section 5.2.1).

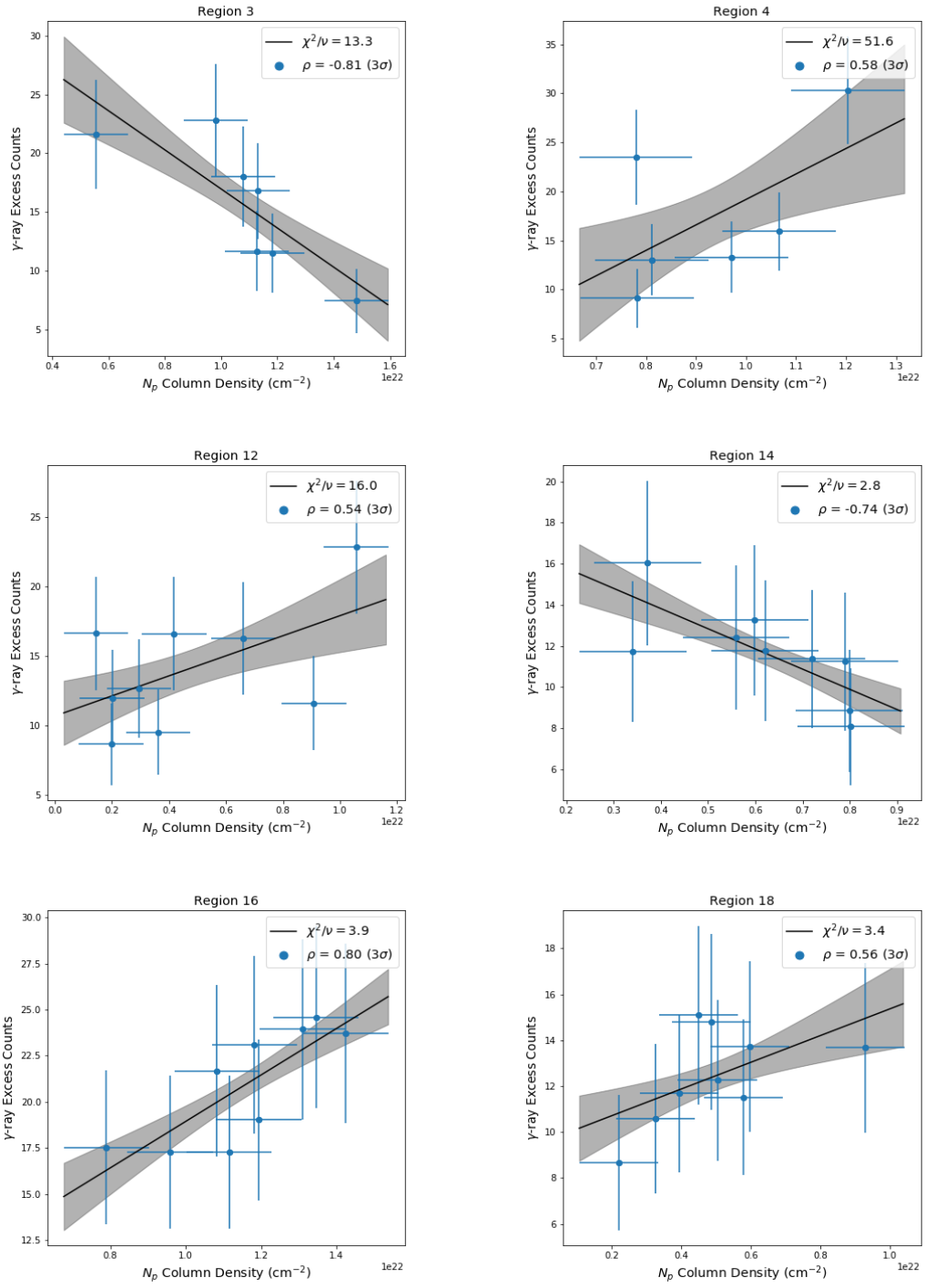

Figure 5.7: Scatter plots between the γ-ray excess counts and ISM gas (H_2 and HI) column density, N_p, where we have used the Mopra ^{12}CO data for the molecular component of the column density. The line of best fit for each data set is shown in black, while the grey area illustrates the 1σ confidence bands. The associated reduced chi-squared value for each fit is labeled along with the Pearson correlation coefficient. Regions with correlations that have at least a 3σ significance associated with their ρ value are displayed.

As can be seen in Table 5.3, the ρ value changes considerably across the 29 regions (plus the additional four). In Figure 5.8 we present a colour-coded map of the Pearson correlation coefficient for each region for both column density data sets (Mopra + SGPS and Nanten + SGPS). We see similar trends in both ISM data sets. Firstly, on the west to north-west side of the SNR there appears to be consistent positive correlation. There is also prominent positive correlation towards the south-east, more so for the Nanten data set. Regions 2 and 3 in the north-east have consistent negative ρ values across both data sets. Regions in the south-west also appear to have more negative correlation. Otherwise, there are mixed results across both the Mopra and Nanten data sets, e.g. in the central regions. A few regions show consistent statistical significance above 3σ across both data sets (regions 2, 3, 12, 14, 15, 18, 21 and 29). However, a large portion of the regions on the west to south-west show significance above 3σ in at least one of the ISM data sets. There are a total of 14 regions in the Mopra + SGPS data set that were found to have significant results, two of these being from the additional regions. The result from region 32 was significant, however, the sample size of 3 pixels and the neutral Pearson value ($\rho = 0.08$) does not tell us much. The lack of significant results in region 5 may be attributed to the small sample size (n=4).

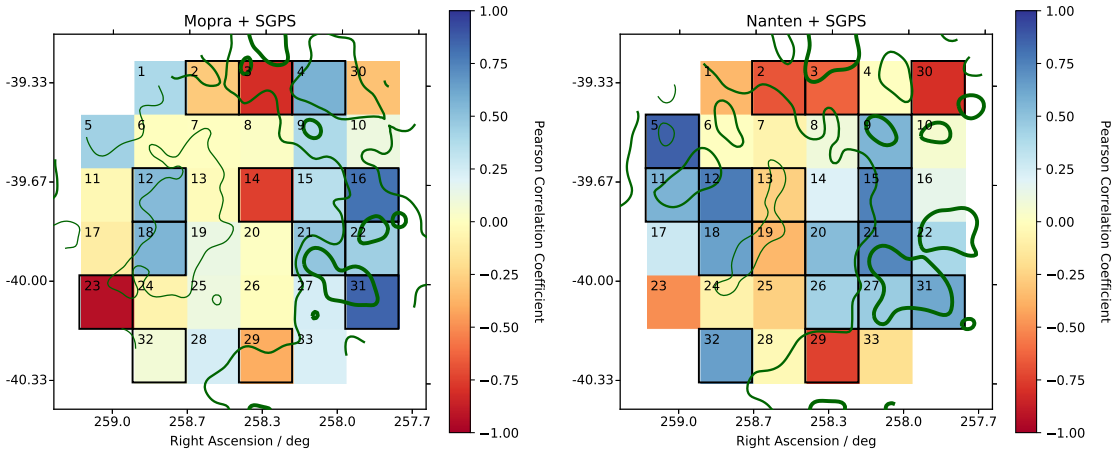

Figure 5.8: 2D colour maps portraying each region according to their Pearson correlation coefficient, ρ, using the Mopra + SGPS data set **(Left)** and the Nanten + SGPS data set **(Right)**. The regions bordered in black are those with significance $> 3\sigma$. The contours are taken from their respective column density maps (molecular plus atomic), before re-binning, at levels of 5, 10 and 15 σ.

We can now use our correlation study results to investigate the presence of any spectral differences between the correlated or anti-correlated regions. This may indicate whether either type of region has any special features, which will subsequently help us discuss the mechanisms behind the γ-ray emission. Specifically, we look at the 12 regions with a correlation coefficient significance larger than 3σ from the adjusted Mopra (+SGPS) data set. We do not include the extra regions (regions 30-33) in this analysis as we have no TeV γ-ray spectral information on them.

Figure 5.9 displays how some observed quantities vary with ρ, specifically the observed radio, X-ray and γ-ray energy fluxes and the ISM column and volume density. We distinguish between the correlated and anti-correlated regions with the blue and red data points, respectively. We use the γ-ray energy flux, F_γ, at TeV energies observed by HESS to represent the γ-ray flux in each region. The HESS observations covered an energy range of ~ 0.1 TeV to 30 TeV. We simply summed the energy flux seen from each energy bin to obtain F_γ. Assuming that the synchrotron flux is represented by X-ray (Tanaka et al., 2008) and radio observations (Lazendic et al., 2004), we can use both of these observations to investigate how the synchrotron flux varies across each region. Firstly, the synchrotron flux is represented by the X-ray energy flux, F_X, between 1-10keV. Similarly to F_γ, this is calculated by summing the *Suzaku* energy flux data from each energy bin for each region. See the pure leptonic SED modeling in section 4.3 for illustrations of these energy flux data. Secondly, we use the ATCA radio energy flux, F_R, at 1.4 GHz (see subsection 2.4.1 for calculations). Lastly, we use the observed ISM column and volume density as calculated by the Mopra and SGPS data sets. The uncertainties for each of the data points are shown, however, they do not contribute to further analysis. The uncertainty in each ρ value is taken as the 1σ value from the bootstrapping distributions.

From Figure 5.9, it appears that both the correlated regions (blue data points) and the anti-correlated regions (red data points) are not significantly different in terms of their γ-ray flux (top left panel). The average TeV γ-ray energy flux from the correlated regions was calculated to be $3.73 \pm 1.27 \times 10^{-11}$ erg cm^{-2} s^{-1} compared to $3.53 \pm 1.27 \times 10^{-11}$ erg cm^{-2} s^{-1} from the anti-correlated regions. To quantitatively check whether the two populations are different, a Welch's t-test is performed. Specifically, this tests whether the sample means for each population are significantly different. In our case, a sample simply refers to either the correlated regions or anti-correlated regions. In Figure 5.9, the sample means for all observed quantities for both the correlated and anti-correlated regions are indicated by the blue and red triangles respectively. The magnitude of the ρ value has no relevance in this test, so the x-axis position of the sample means is arbitrary. We place them on either side of the plot for best visibility. To perform the t-test we also need the sample variance, which is the square of the standard deviation (recall Equation 5.10). In Figure 5.9 we have indicated the sample standard deviation by the error bars around the sample means.

The t-statistic, t, is calculated to measure the difference between the two sample means:

$$t = \frac{\bar{x}_1 - \bar{x}_2}{\sqrt{\frac{s_1}{N_1} + \frac{s_2}{N_2}}} \tag{5.12}$$

where $\bar{x}_1$ and $\bar{x}_2$ are the sample means, s_1 and s_2 are the variances and N_1 and N_2 are the sample sizes. A larger t-statistic generally is an indication that the two means are significantly different. The t-statistic is then compared against a t-distribution with degrees of freedom, ν. The degrees of freedom describe the shape of the distribution and

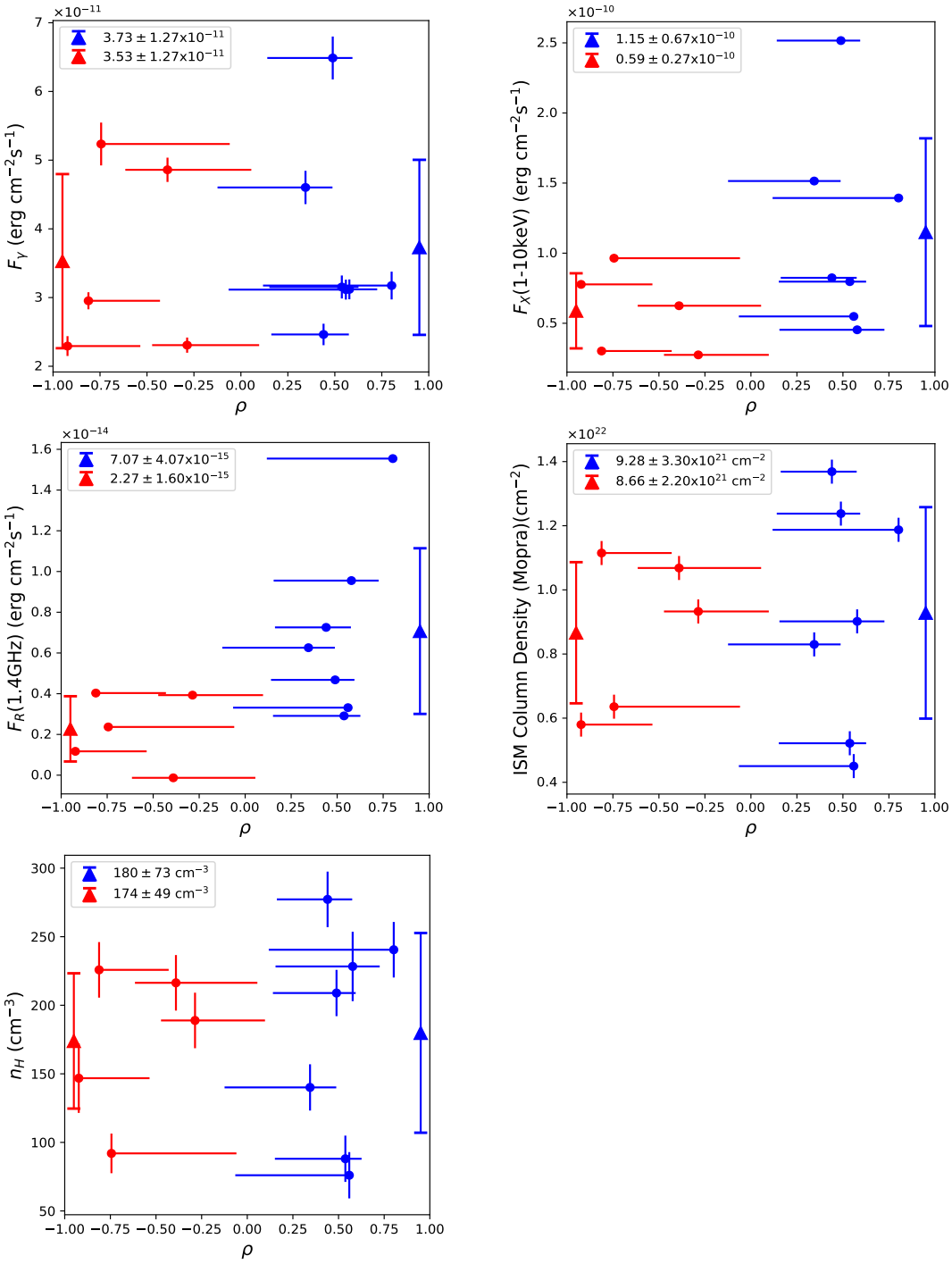

Figure 5.9: Scatter plots of some observed quantities vs correlation coefficient for regions with correlation significance, $|\sigma| > 3$. The blue data points represent correlated regions, while the red data points represent anti-correlated regions. The quantities in the legend, in units of erg cm^{-2} s^{-1} when no units are shown, represent the sample means for either type of region and their associated sample standard deviation. The triangles and their error bars on either side of the plot illustrate these averages and standard deviations. **Top Left:** The HESS γ-ray energy flux at TeV energies. **Top Right:** The *Suzaku* X-ray energy flux between 1-10 keV. **Middle Left:** The ATCA radio energy flux at 1.4GHz. **Middle Right:** The combined Mopra and SGPS representation of the ISM column density, N_H. **Bottom Left:** The total ISM gas density, n_H, as calculated by the Mopra and SGPS data sets.

are associated with the original samples via:

$$\nu = \frac{\left(\frac{s_1}{N_1} + \frac{s_2}{N_2}\right)^2}{\frac{s_1^2}{N_1^2 \nu_1} + \frac{s_2^2}{N_2^2 \nu_2}} \tag{5.13}$$

where $\nu_1 = N_1 - 1$ and $\nu_2 = N_2 - 1$ are the degrees of freedom associated with each sample. On comparison with the t-distribution, we can determine the probability of obtaining a more extreme value for t. This probability is called the p-value and can also be interpreted as the probability that two randomly sampled sets of data produce a t-statistic at least as extreme as the one in question. The shaded regions in Figure 5.10 indicate the extreme values of t and the total shaded area is equal to the p-value. In this figure we illustrate the t-distribution for the γ-ray energy flux and also the radio energy flux, which was found to have a significant result (see below).

If two randomly sampled sets of data have, at most, a 5% chance of producing the corresponding t-statistic then we consider there to be a significant difference between the two original sample means. This probability corresponds to a p-value of 0.05. For example, the t-statistic for the γ-ray energy flux (Figure 5.9: Top Left panel) is 0.25 and the p-value is 0.406, so there is 40.6% chance that the difference is attributed to randomness. This is larger than the threshold 5% so we cannot claim that the γ-ray energy flux differs for the correlated and anti-correlated regions. On the other hand, the p-value for the radio energy flux (Figure 5.9: Middle Left panel) is 0.015, which is below the threshold value. We consider the radio flux difference between the correlated and anti-correlated regions to be significant.

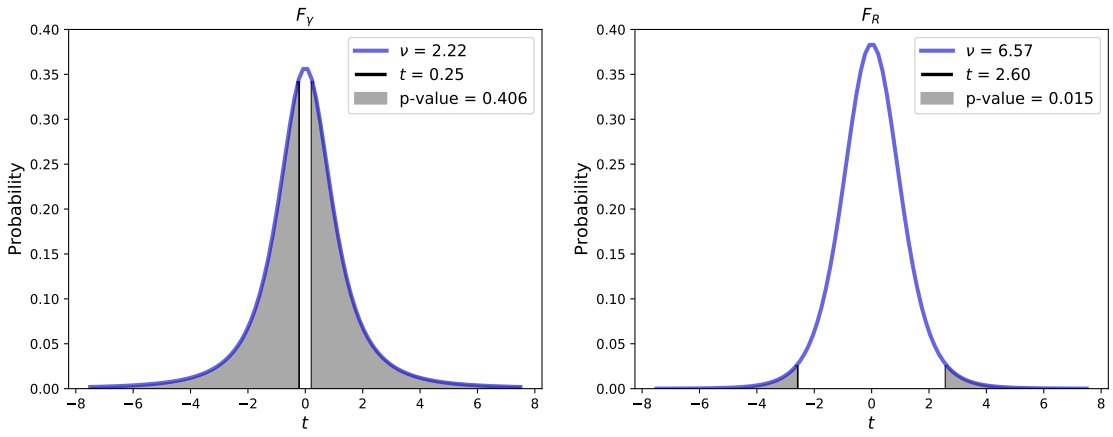

Figure 5.10: The estimated t-distributions for the observables, F_γ and F_R, from the Top Left and Middle Left panels of Figure 5.9 respectively. The legend indicates the relevant t-statistic and associated p-value, along with the degrees of freedom, ν, related to the original samples.

Similar plots for the X-ray energy flux and other observed quantities (the ISM column and volume density), can be found in Appendix F. We display the average results for the

observed quantities in the top section of Table 5.4 along with the associated t-distribution quantities, e.g. the t-statistic, the degrees of freedom and the p-value. We find a significant difference between the two populations for the radio energy flux. A borderline significant result is found for the X-ray energy flux (p-value = 0.050). The ISM density appears to be equivalent for both types of regions, regardless of the geometry (column or volume density). Region 12 and 18, which were found to have ISM gas correlated with TeV γ-rays, are the only two such regions on the south-eastern side of the SNR. Interestingly, these two regions also had the lowest ISM density (column or volume).

We now plot parameters from our SED modeling (pure hadronic and pure leptonic) against their corresponding correlation coefficient values. In doing so we hope to reveal, and subsequently investigate, some differences between the correlated and anti-correlated regions. The hadronic parameters are the proton energy budget, W_p, and spectral index, α (see section 4.2). These quantities are compared in terms of the correlated and anti-correlated regions in Figure 5.11. Additionally, we quantitatively test whether the correlated and anti-correlated regions have any differences between their sample means by calculating a t-statistic and associated p-value (as above). We find no significant difference between the two types or regions for the hadronic parameters. However, we do note that one of the correlated regions (region 15) is an outlier in the W_p data set. The removal of this point does not affect the comparison, as it only makes the means more similar. The middle section of Table 5.4 displays the relevant quantities used in this analysis.

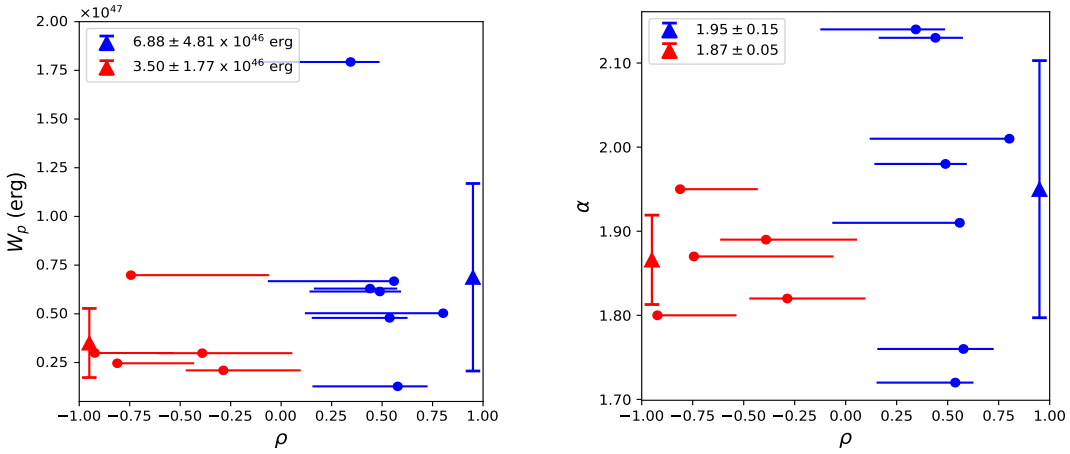

Figure 5.11: The same as Figure 5.9, except for the pure hadronic SED modeled parameters. **Left:** The proton energy budget, W_p. **Right:** The proton spectral index, α.

Lastly, we investigate the pure leptonic SED parameters that were modeled in section 4.3 for any differences across the correlated regions and anti-correlated regions. Specifically, we look at the electron energy budget, W_e, the magnetic field strength, B, the low and high electron spectral index, α_1 and α_2, respectively, the energy cut-off, E_c, and the ratio of the TeV Bremsstrahlung flux to the total TeV γ-ray flux. Recall that the last of these quantities was calculated in subsection 4.3.4, while the remainder were used in subsection 4.3.1. Figure 5.12 displays how these quantities vary for each kind of region. Similarly as above,

to determine whether the correlated regions required any leptonic SED parameters that were distinct from those of the anti-correlated regions, we performed a t-statistic analysis. The results of which can be found in the bottom section of Table 5.4. Appendix F displays the t-distributions for each of the SED modeled parameters (hadronic and leptonic).

A significant difference was found between the two types of regions for the electron energy budget, W_e, and the high-energy electron spectral index, α_2. The p-values were 0.028 and 0.007 respectively. Otherwise, no difference was found for the remaining observables. The low-energy electron spectral index, α_1, appears to have an outlier in the anti-correlated regions (region 29). Removal of this point would only increase the sample mean for the anti-correlated regions closer to that of the correlated regions. Also, region 23 appears to be somewhat of an outlier in terms of its energy cut-off, E_c. Removal of this point would create a significant difference between the averages of the correlated and anti-correlated regions, the energy cut-off being greater for the correlated regions on average. Interestingly, regions 12 and 18 (correlated regions) were both at the same extreme end of the range for all leptonic SED parameters except for the high and low electron spectral index. These regions are also the only correlated regions on the south-eastern side of the SNR.

5.2.3 Discussion

We draw upon our correlation results from the previous section and discuss the possible mechanisms behind the positive and negative correlation. Firstly, we briefly describe the physical scenario that applies to RX J1713.7-3946 and then we go on to describe how our observations fit with such a scenario.

Initially, the stellar wind of the progenitor star projected outwards, sweeping up most of the gas it encountered and creating a cavity. It is suggested that only highly dense gas clumps (~ 0.1 pc radius) survived the winds and remained within the cavity (Inoue et al., 2012; Gabici and Aharonian, 2014; Celli et al., 2018). About 1600 years ago the supernova occurred (Wang et al., 1997). A short time after this, the shock-front, responsible for the particle acceleration, then propagated outwards through the cavity. As it encountered any remaining gas clumps the accelerated protons penetrated and interacted with these clumps (Fukui et al., 2012), producing γ-rays. Hence the hadronic γ-ray emission we observe now should coincide with the location of the gas. Additionally, electrons are accelerated at the shock-front and experience amplified magnetic fields (due to turbulence in the clumps) when they reach the dense gas clumps. The magnetic fields may reach values of ~ 1 mG (Uchiyama et al., 2007) causing the electrons to emit intense synchrotron radiation (Tanaka et al., 2008), which peak around the dense gas clumps (Sano et al., 2010). These electrons will have less energy remaining for other leptonic processes, in comparison to electrons that are not experiencing amplified magnetic fields, i.e. those away from dense clumps. For this reason the IC emission may be stronger away from gas clumps. Bremsstrahlung radiation depends on the gas density, so as we look away from the dense clumps we should expect this emission component to decrease. However, the effect of increasing synchrotron losses towards the dense clumps will act to decrease the amount of Bremsstrahlung emission towards dense ISM. We attempt to draw some

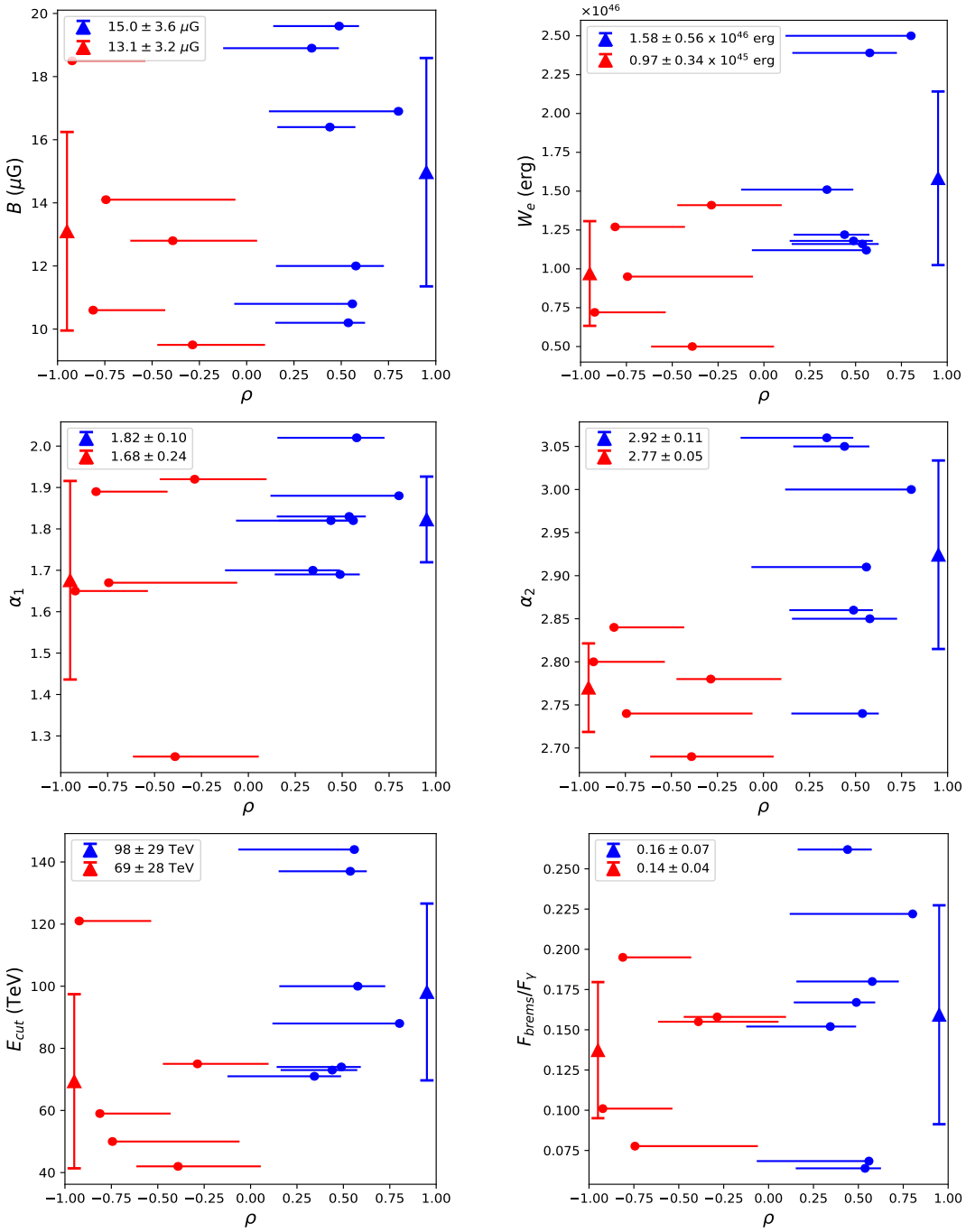

Figure 5.12: The same as Figure 5.9, except for the pure leptonic SED modeled parameters, as described in text. **Top Left:** The magnetic field strength, B. **Top Right:** The electron energy budget, W_e. **Middle Left:** The low-energy spectral index, α_1. **Middle Right:** The high-energy spectral index, α_2. **Bottom Left:** The energy-cut off, E_c. **Bottom Right:** The ratio of Bremsstrahlung TeV emission to total TeV emission.

	Average				
	Correlated Regions (4, 12, 15, 16, 18, 21 & 22)	Anti-Correlated Regions (2, 3, 14, 23 & 29)	t-statistic	ν	p-value
F_γ	$3.73 \pm 1.27 \times 10^{-11}$	$3.53 \pm 1.27 \times 10^{-11}$	0.25	2.22	0.406
F_X	$1.15 \pm 0.67 \times 10^{-10}$	$0.59 \pm 0.27 \times 10^{-10}$	1.84	6.53	0.050
F_R	$7.07 \pm 4.07 \times 10^{-15}$	$2.27 \pm 1.60 \times 10^{-15}$	2.60	6.57	**0.015**
N_H (cm^{-2})	$9.28 \pm 3.30 \times 10^{21}$	$8.66 \pm 2.20 \times 10^{21}$	0.36	4.04	0.365
N_H* (cm^{-2})	$11.05 \pm 2.05 \times 10^{21}$	$8.66 \pm 2.20 \times 10^{21}$	1.59	2.43	0.076
n_H (cm^{-3})	180 ± 73	174 ± 49	0.15	3.95	0.441
n_H* (cm^{-3})	219 ± 45	174 ± 49	1.34	2.38	0.108
W_p (erg)	$6.88 \pm 4.81 \times 10^{46}$	$3.50 \pm 1.77 \times 10^{46}$	1.57	6.69	0.078
α	1.95 ± 0.15	1.87 ± 0.05	1.24	6.75	0.125
B (μG)	15.0 ± 3.6	13.1 ± 3.2	0.87	2.70	0.204
W_e (erg)	$1.58 \pm 0.56 \times 10^{46}$	$0.97 \pm 0.34 \times 10^{46}$	2.16	4.64	**0.028**
E_{cut} (TeV)	98 ± 29	69 ± 28	1.58	2.25	0.075
α_1	1.82 ± 0.10	1.68 ± 0.24	1.16	1.02	0.150
α_2	2.92 ± 0.11	2.77 ± 0.51	2.99	5.99	**0.007**
$F_{\text{brems}}/F_\gamma$	0.16 ± 0.07	0.14 ± 0.04	0.63	4.46	0.271

Table 5.4: The average values of some observed quantities and SED modeled parameters for the significantly correlated and anti-correlated regions. The observed γ-ray, X-ray and radio energy flux are in units of erg cm^{-2} s^{-1}. For each quantity the derived t-statistic and associated degrees of freedom, ν, and p-value are quoted. The p-values printed in bold font are those that are below the significance threshold of 5%. See the text for a description of how these are calculated. The ISM density values labeled with an asterisk (*) indicate that regions 12 and 18 have been removed from the correlated regions data set, as described in subsection 5.2.3.

qualitative conclusions below.

Since the radio energy flux is a measure of the synchrotron flux (from GeV electrons), our results have shown that the synchrotron flux is greater in the correlated regions. Also, the X-ray energy flux was found to be marginally more intense in the correlated regions. This supports our argument that the synchrotron emission is more intense in regions with spatially correlated γ-rays and ISM gas. This is in accordance with our notion that the γ-rays in correlated regions are more likely hadronic in origin.

To understand this, consider the energy losses electrons would experience due to the more intense synchrotron output (synchrotron losses). These losses would leave electrons with less energy available for IC scattering. Hence, the IC γ-rays would be, to some extent, suppressed in the correlated regions. As a result the γ-rays must be predominantly produced by hadronic and Bremsstrahlung processes. On the other hand, the electrons in anti-correlated regions suffer minimal, or less, synchrotron losses and hence the IC

γ-rays are more prominent. Hence, a large portion of the γ-ray emission produced in these regions is anti-correlated with the ISM gas.

Our results also suggest that the high-energy electron spectral index is harder for the correlated regions. This is in agreement with the argument made in the paragraph above; specifically, that the synchrotron losses are more substantial in the correlated regions. High-energy electrons will radiate their energy away via synchrotron faster than low-energy electrons. A hard high-energy electron spectra steepens the high-energy tail of the electron spectrum, i.e. it acts to suppress the energy available to high-energy electrons.

The larger electron energy budget required by the correlated regions is no surprise considering the synchrotron losses are also greater. In such a case the IC γ-ray emission would decrease, as less energy is available for this process. Hence, our attempts at explaining the TeV observations, which are most likely hadronic in origin in these regions, with a pure leptonic model required more energy to be available for the electrons in order for them to produce the required IC emission.

Surprisingly, we found no difference between the magnetic field strength and electron cut-off energy for both types of region. We would expect the magnetic field to be more intense in the correlated regions as the synchrotron flux has a strong dependence on the B field intensity. Similarly to the high-energy electron spectral index, the electron cut-off energy acts to suppress the energy available to high-energy electrons. For the same reason we expected a soft high-energy electron spectra in the correlated regions, we expect a low cut-off energy in correlated regions, and vice versa for the anti-correlated regions. The reason why we observe no difference for these two parameters, B and E_c, may come down to the fact that we are attempting to use a leptonic SED model to represent a hadronic scenario. This is the case for the correlated regions. The leptonic parameters derived for the correlated regions are likely less representative of the real properties within those regions. A combined SED model would yield more accurate parameters. However, this is beyond the scope of the current study due to the degenerate parameter space required, as discussed in chapter 4.

Additionally, we found no evidence that the hadronic SED parameters, W_p and α_p, were significantly different for the correlated and anti-correlated regions. Similarly to the argument made for the magnetic field, this could come down to the fact that the parameters used for the anti-correlated regions are inaccurate. This is because we are attempting to fit a hadronic model to TeV observations that are leptonic in origin. Alternatively, our sample sizes for both the correlated and anti-correlated regions may not be large enough to accurately represent their populations. Subsequently, the resultant averages may not be accurate either.

We briefly mention some other study limitations. The methodology was limited by the resolution of the HESS observations (0.03°). We were unable to isolate potential TeV γ-ray emission from small gas clumps. Recall the size of each pixel was 0.06° by 0.06°, corresponding to 1 pc by 1pc, whereas the radius of gas clumps may be as small as 0.1 pc (Celli et al., 2018). On the other hand, the Mopra resolution should be fine enough to identify clumps as small as 0.17 pc. Clearly, we need to wait for the next generation of

Cherenkov telescope arrays to be able to resolve this detail. Additionally, it is not certain whether some of the observed ISM was in the foreground or background. ISM gas may experience local turbulence, resulting in velocity components that represent unreliable distance estimates.

Now we will discuss the results relating to the correlated and anti-correlated regions separately and in more detail.

Regions with Positively Correlated ISM gas and Gamma-rays

It is expected that regions with a positive correlation between their ISM gas and γ-ray emission (regions 4, 12, 15, 16, 18, 21 and 22) could be dominated by hadronic processes. But we must also consider Bremsstrahlung radiation as a source of γ-rays, especially if synchrotron losses are not too substantial. Our results indicate that the gas in regions on the west to north-west side of the SNR positively correlates with the γ-ray emission. Large amounts of gas are situated here (see contours in Figure 5.8), likely in the form of clumps. These are regions where we might expect hadronic processes to be dominant.

The dense core, 'core C', situated in region 21 has previously been shown to be associated with X-ray emission (Sano et al., 2010). Around this core, anti-correlation between the X-rays and ISM gas was seen on small sub-parsec scales. On more broader, parsec scales, correlation between these two quantities was found (Sano et al., 2013). Now we have quantitatively shown that the region surrounding this gas core is also associated with γ-rays. We can draw upon the TeV Bremsstrahlung fraction results from subsection 4.3.4 to estimate both the Bremsstrahlung and hadronic emission fractions in this region. In subsection 4.3.4 we found the fraction of TeV Bremsstrahlung emission was 17% of the pure leptonic TeV emission. If we assume that all of the TeV emission in this region is due to hadronic and Bremsstrahlung processes, i.e. the spatially correlated processes, then we can crudely take the total fraction of Bremsstrahlung emission to be 17%. This leads us to roughly estimate that the remaining 83% of the TeV emission in region 21 is hadronic.

We can perform the same procedure on the remaining correlated regions to determine their total fraction of Bremsstrahlung and hence hadronic TeV emission. Both these fractions are presented in Table 5.5. Region 22 encompasses the dense ISM core, 'core A' (Moriguchi et al., 2005). The Bremsstrahlung emission accounts for 26% of the total pure leptonic TeV emission in this region. The remaining 74% is attributed to hadronic processes. Previously, in section 4.2 we argued that the γ-ray emission was predominantly hadronic. Moreover, in section 4.2, region 15 was found to have a modeled hadronic GeV spectrum that almost violated the *Fermi*-LAT flux for the entire SNR. Recall that an upper limit was used as the *Fermi*-LAT resolution was poorer than the size of the regions (section 4.2). Due to the lack of constraints at GeV energies this was not deemed problematic. Our correlation results indicate that 85% of the γ-ray emission is hadronic (Table 5.5). This leads us to believe that the hadronic GeV spectrum for region 15 should be harder, as the SED modeling suggested. The hardening may arise due to the lack of dense ISM clump penetration by lower-energy (GeV) protons, as argued by Gabici and Aharonian (2014) and Inoue et al. (2012). Our SED modeling did not account for this.

Region	Bremsstrahlung TeV Fraction	Hadronic TeV Fraction
4	0.18	0.82
12	0.06	0.94
15	0.15	0.85
16	0.22	0.78
18	0.07	0.93
21	0.17	0.83
22	0.26	0.74
Fraction of total TeV emission (entire SNR)	0.04	0.20

Table 5.5: The total fraction of Bremsstrahlung TeV emission and hadronic TeV emission for the TeV γ-ray/ISM correlated regions (with $\rho > 0$ and $\sigma > 3$). We assume that these two processes make up the TeV emission in these regions. Additionally, the fraction of the total TeV flux for both hadronic and Bremsstrahlung across the entire SNR are shown in the bottom line.

Additionally, we estimate a lower limit for the total hadronic TeV emission from the entire SNR. To do this, we utilise the HESS TeV flux for each region (H18) and proceed as follows:

1. We apply the hadronic TeV fraction from each of the correlated regions (Table 5.5) to their corresponding HESS TeV flux. This gives us the total hadronic TeV emission from each of our 7 correlated regions.
2. Summing the total hadronic TeV emission from these 7 regions gives us the total hadronic TeV emission from all the correlated regions.
3. We then divide this by the total sum of HESS TeV flux from all 29 regions to find the total fraction of hadronic emission from the entire SNR.

We find the total fraction of hadronic emission over the SNR to be 20%. A similar process can be used to find that the total fraction of Bremsstrahlung TeV flux is 4%. These estimates are lower limits. We may still expect some fraction of hadronic and Bremsstrahlung emission from regions other than those with $\rho > 0$ and $|\sigma| > 3$. Additionally, we expect some contamination from IC emission due to the HESS resolution, potentially reducing the fraction of hadronic TeV emission. Our final HESS pixel size was ~ 1 pc by 1 pc, whereas gas clump radii can be as small as 0.1 pc (Sano et al., 2010; Celli et al., 2018). As a result, a single pixel may detect γ-ray emission that is both spatially correlated (hadronic and Bremsstrahlung) and anti-correlated (IC) with the ISM. Nonetheless, both values are presented in the bottom row of Table 5.5.

The γ-ray shell is observed to extend beyond the X-ray synchrotron shell (H18). This is due in part to the escape of both electrons and protons from the shock front and/or the shock precursor scattering protons upstream (H18). If the protons do indeed propagate further out from the SNR shock, then any γ-ray emission observed beyond this shock

boundary is likely due to accelerated protons. However, the emission should decline rapidly at the boundary as only $E_p > 150$ TeV protons are believed to have escaped thus far (Casanova et al., 2010). This escaping energy estimate is approximate, but it corresponds to a γ-ray energy of ~ 15 TeV (or 10% of E_p). We see indication for a decline in region 4 where the TeV emission matches the gas and there does not appear to be much gas beyond the γ-ray shell, e.g. see Figure 5.3 (Top Left). This gas-sparse region might allow CR protons to penetrate somewhat freely and potentially even escape the region.

To understand the lack of differences seen in the ISM density vs ρ (Figure 5.9: Middle Right panel), we consider the individual properties of some regions. Of most interest are regions 12 and 18. These regions were found to have positive correlation, required similar SED parameters and are located on the gas-poor side of the SNR. The HI emission is strong in these regions, with an average column density of 4.6×10^{21} cm^{-2} and 4.3×10^{21} cm^{-2} in regions 12 and 18 respectively (recall Figure 5.3). This ISM contribution greatly outweighs the molecular counterpart, which has an average column density of 0.1×10^{21} cm^{-2} and 0.7×10^{21} cm^{-2} in regions 12 and 18 respectively (again, recall Figure 5.3). It has previously been argued that the HI is responsible for the γ-ray emission on this side of the SNR (Fukui et al., 2012). Interestingly, removal of these regions in our analysis increases the average ISM column density for the correlated regions to $11.05 \pm 2.05 \times 10^{21}$ cm^{-2}, as shown in Table 5.4. This almost makes it significantly different from that of the anti-correlated regions, with a p-value of 0.076. A similar trend is seen for the ISM volume density (see Table 5.4). If the γ-rays are produced predominately by the HI gas on this side of the SNR then we should see similar correlation results in the other HI rich regions (regions 5, 6, 11, 17 and 23) that are adjacent, which we do not. However, these other HI rich regions are located closer to the SNR edge, so they may be different in terms of the amount of CRs 'touching' the gas.

Regions with Negatively Correlated ISM gas and Gamma-rays

The anti-correlation results suggest that the γ-ray emission in regions 2, 3, 14, 23 and 29 is dominated by IC emission. We note that none of the γ-ray emission in these regions was initially identified via our SED modeling (chapter 4) as being noticeably leptonic, i.e. none of the regions required extreme parameters with either a pure hadronic or pure leptonic model. Nonetheless, bringing our attention back to the results from our hadronic model, we find that the proton energy budget required for regions 2, 3, 23 and 29 was relatively low ($< 3 \times 10^{46}$ erg) in comparison to the remaining regions (average $\sim 5 \times 10^{46}$ erg). A low proton energy budget, relatively speaking, could be an indicator that a pure hadronic model is not sufficient at explaining the γ-rays. Alternatively, it could be an indication that the observed ISM gas is over-estimated, i.e. some is located in the foreground or background. If we assume that all regions should receive a similar amount of cosmic ray protons and some regions are found to have less, it may suggest that some of that proton energy is missing. The missing energy may arise due to the failure of the protons to radiate all their energy into γ-rays. This is perhaps due to the energy dependence of the CR penetration into ISM clumps (Gabici and Aharonian, 2014).

In chapter 4, we showed that the electron cut-off energy, E_c, was inversely proportional

to the magnetic field strength (recall Figure 4.11). However, we failed to acknowledge the regions with small cut-off energies. Among them were regions 3 and 14 with $E_c = 66$ TeV and 50 TeV respectively, which were also found to have ISM gas that anti-correlates with the TeV γ-rays. A low cut-off energy is often argued to be the result of intense synchrotron losses. The more energy electrons lose via synchrotron the less they have available to produce IC γ-rays. This becomes problematic as we have interpreted the main mechanism for γ-ray emission in the anti-correlated regions as being IC scattering. Nonetheless, the energy cut-off was found to be, on average, no different between the anti-correlated and correlation regions.

Regions 2, 3, 23 and 29 are all situated on the edge of the SNR. As stated previously, there is likely to be gas beyond the γ-ray shell, 'untouched' by CRs. We attempted to account for this by applying a γ-ray threshold to the data in section 5.2.1. However, in Figure 5.4 (Left) we can still see that in these four regions the γ-rays are radially declining. On the other hand, the ISM gas does not radially decline (Figure 5.4, Right). IC emission may indeed be dominating the γ-ray emission in these regions, but we must also consider the fact that some of the CR protons have not sufficiently penetrated these outer regions yet. In such a case, the hadronic γ-rays would anti-correlate with the ISM. This makes it more difficult to draw firm conclusions about these regions.

5.2.4 Conclusion

The main purpose of this chapter was to begin building a quantitative understanding of the γ-ray emission from RX J1713.7-3946 and to quantify the level of hadronic vs leptonic TeV emission. Throughout this chapter we have succeeded in identifying a number of regions within RX J1713.7-3946 that are possibly dominated by hadronic or leptonic emission, via a 2D correlation study. We have drawn upon statistical methods, such as calculating the Pearson Correlation Coefficient and the bootstrapping technique to derive our results. From this, we have performed subsequent analyses to illustrate or further investigate the results; these will be listed below.

1. Scatter plots of the ISM gas and the γ-ray counts were produced to illustrate any linear relationship that might exist between the two observables.

2. 2D colour maps portraying the correlation coefficient of each were produced to illustrate the correlation changes over the remnant.

3. Those regions that were found to have a significant positive correlation coefficient were then compared to those regions with a significant negative correlation coefficient to investigate whether there were any differences between the two types of regions. In particular, the following observables were compared; the γ-ray, X-ray and Radio flux and the ISM column and volume density. A t-test was performed for each of these comparisons to quantitatively compare each population. On top of these, the SED parameters derived in chapter 4 were also compared, with their own t-tests.

4. Those regions with significant positive correlation were further analysed to reveal their fraction of bremsstrahlung and hadronic emission.

The results from this correlation study enabled us to categorize certain regions as 'hadronic' (TeV/ISM correlation) or 'leptonic' (TeV/ISM anti-correlation) in reference to their γ-ray emission. Regions 4, 12, 15, 16, 18, 21, and 22 were found to be more hadronic, whereas regions 2, 3, 14, 23 and 29 were found to be more leptonic. Additionally, we were able to set some initial constraints on the total hadronic and Bremsstrahlung TeV γ-ray flux from RX J1713.7-3946. Assuming that the γ-ray emission from the correlated regions is predominantly from hadronic and Bremsstrahlung processes, we found lower limits of $\sim 20\%$ and $\sim 4\%$ respectively. This is a rough estimate; some of the γ-rays in these regions would still be leptonic in origin and we would still expect some hadronic/Bremsstrahlung contributions from the remaining regions. More specifically, we found that the TeV γ-rays in region 15 were predominantly hadronic (85%).

Lastly, we compared various parameters for both types of regions to determine whether either displayed any unusual differences. We found no difference between the TeV γ-ray emission of the two types of regions, but we did find a difference between their radio synchrotron emission. This provided observational evidence that the TeV γ-ray emission, in regions where the γ-rays are spatially correlated with the ISM gas, is predominantly produced by hadronic and, in part, by Bremsstrahlung processes. The lack of difference seen between the ISM observations of the correlated and anti-correlated regions were not consistent with this argument. The notion that the γ-rays in region 12 and 18 are produced from the less prevalent atomic gas may have consequences on this result.

6 Conclusions and Summary

6.1 Conclusions and Summary

In this chapter the work that has been presented throughout the thesis, 'Probing the Gamma-ray Emission from HESS Source RX J1713.7-3946', is summarised. RX J1713.7-3946 is a young SNR that emits brightly in the TeV and X-ray bands. The X-ray emission is well understood to be non-thermal synchrotron emission of high energy electrons. The origin of the γ-rays however is not so well understood. Theory suggests that both electrons and protons can be accelerated to high energies at the shock front and produce γ-rays via their own independent processes. This work aimed to reveal which of these processes are more dominant in RX J1713.7-3946 by splitting the entire SNR into 29 smaller regions, of size 0.18^{o} by 0.18^{o} (~ 3.1 pc by 3.1 pc). Within each region we then performed a separate broadband spectral study and 2D correlation study between the γ-rays and ISM gas. Determining the spatial correlation between the ISM gas and the γ-rays is important for locating where the hadronic/Bremsstrahlung γ-ray emission is.

1. In chapter 4 we used the latest high resolution HESS observations along with *Suzaku* X-ray and ATCA radio observations to fit spectra in our 29 regions of interest. The HESS observations were used to fit the hadronic models, whilst the lower energy observations were included in the broadband leptonic models. Additionally, we used the latest high-resolution CO observations from Mopra to trace the morphology of the molecular hydrogen, H_2. Combining this molecular component with the atomic component, taken from the SGPS, we were able to estimate the average ISM gas density, n_H, within each region. These values ranged from $n_H = 66$ cm^{-3} to $n_H = 284$ cm^{-3}. The new ISM gas density measurements were used to model the hadronic-*pp* interactions from a distribution of protons and also the leptonic-Bremsstrahlung from a distribution of electrons. Previously the highly resolved ATCA radio data had not been used in such models, the inclusion of such allowed us to derive a low-energy electron spectral index for each region.

2. We found that both the hadronic and leptonic spectra from each region successfully fitted the observations. The main issues arose when attempting to interpret some of the parameters required to fit the models. For instance, some required hadronic parameters were disproportionate in comparison to their regional counterparts. It was proposed that the unusually high proton energy budget and low gas density in regions 15 and 26 were due to the γ-ray emission being predominantly leptonic. While on the other hand the soft proton spectra required in region 22 was attributed to the rich amount of ISM gas. It was suggested that the ISM here was clumpy, but also contained some diffuse-low density gas that allowed the low-energy CRs to interact with.

In the case of the leptonic models, each electron distribution required a high-energy spectral index (average of 2.81) that was much steeper than that predicted by DSA (~ 2). This could be explained by taking into account synchrotron losses and hence the hardening of the spectra at high energies. With this in mind, most of the extreme parameters seemed to follow the trend set by the magnetic field. In regions where the average magnetic field was intense, the high-energy tail of the spectra was steep and the cut-off energy was small. Whereas, the converse was observed for less intense magnetic fields. Additionally, γ-rays from regions with either an extreme electron energy budget or low-energy electron spectral index were argued to be more hadronic in origin. Overall, the leptonic model was successful at predicting the affects of synchrotron losses.

We found that the Bremsstrahlung TeV emission within region 22 was $\sim 26\%$ of the total TeV emission. The gas density is high here, $n_H = 277$ cm^{-3}, as well as the magnetic field, $B = 16.4$ μG. We also found a few regions where the Bremsstrahlung emission peaked at MeV energies (regions 1, 4 and 10). We concluded that Bremsstrahlung shouldn't be ignored as a source of γ-rays and in fact the MeV emission may help constrain future models. The spectral fitting provided us with good insight into the hadronic and leptonic nature of the γ-rays in some regions.

3. We again drew upon the latest HESS observations and Mopra CO observations to perform a 2D correlation study between the TeV γ-rays and the total ISM column density in each region. This analysis allowed us to determine whether the TeV γ-rays in each region were more hadronic or leptonic. We discovered that the hadronic regions grouped together either on the north-west or the south-east. The bulk of north-western TeV γ-rays are believed to be produced by molecular gas, while the south-eastern γ-rays were argued to be produced predominantly by atomic gas. The TeV γ-ray emission in regions 4, 12, 15, 16, 18, 21 and 22 was found to be more hadronic, while in regions 2, 3, 14, 23 and 29 it was likely leptonic. This allowed us to set a lower limit of $\sim 20\%$ on the amount of observed TeV γ-ray flux from the SNR in total that is hadronic in origin. We also considered the total fraction of γ-ray emission Bremsstrahlung processes were responsible for; a lower limit was set at 4%.

4. Next we found that the radio synchrotron emission from hadronic regions was significantly stronger than that from the leptonic regions, while no difference was found for the γ-ray emission. It was concluded that synchrotron losses are stronger in the hadronic regions. Surprisingly, the derived magnetic field, from the spectral fitting, which the synchrotron emission depends on, was no larger for the hadronic regions. This discrepancy was likely due to attempting to apply an IC model to regions that are likely hadronically dominated. The ISM gas density (column and volume) in both types of regions was found to be similar, again creating a discrepancy with the observed synchrotron emission differences. The idea that the south-eastern γ-rays are produced by the less prevalent atomic gas may affect our interpretation of these results.

6.2 Limitations and Further Work

The spectral fitting we performed in chapter 3 and chapter 4 assumed pure hadronic or pure leptonic origins. More realistically, a combined leptonic and hadronic model should be applied to each region. Doing so would require some constraining assumptions about either the proton to electron energy ratio or the relationship between the magnetic field and electron break energy. Most importantly, we now have some quantitative results on the fraction of hadronic and/or leptonic γ-ray flux from each region. The 2D correlation coefficients could be used to crudely estimate the proton to electron energy ratio. Alternatively, the results of such a combined model can also be used to more accurately compare results from a correlation study. When we compared the derived magnetic field between the regions with more hadronic γ-rays to more leptonic γ-rays, the magnetic field was derived from a pure leptonic scenario. Deriving the magnetic field strength for a combined scenario will make these comparisons more meaningful.

Furthermore, we can add other complexities to the spectral models so they are more realistic and potentially provide more insight into the physics of RX J1713.7-3946 for example. The models used in this study had no time dependencies, i.e. none of the parameters evolved as the SNR aged. For future models, we aim to incorporate a time dependent magnetic field. This can either be done in a simple step-wise manner, where the magnetic field is incremented every few hundred years. Or we can force a continuous time-dependence upon the magnetic field, which will also require evolving the particle distributions over time. Reynolds et al. (2012) provide a thorough review of the magnetic field strength in SNRs, which includes an expression for synchrotron induced magnetic fields in terms of the shock front speed, a parameter which should evolve with time. This will allow us to determine whether the evolution of such a magnetic field significantly affects the output spectra.

Lastly, a correlation study should be performed on the γ-rays with the atomic gas and molecular gas separately to potentially identify regions that produce γ-rays predominantly from atomic gas. The reason being is that the atomic gas is less prevalent over the entire SNR and its morphology is lost in the molecular sea. Even in the south-east regions where the HI column density reaches its maximum ($\sim 5 \times 10^{21}$ cm^{-2}), it is still a fraction of the dense molecular bubble ($> 1 \times 10^{22}$ cm^{-2}) that is believed to be producing the γ-rays in the north-west. This is all assuming that the CRs/electrons are interacting differently with each ISM component. This behaviour is expected if their density distributions are distinct.

A Comparison Between the Mopra and Nanten Data Sets

The total column density of ISM protons is calculated by combining observations of atomic and molecular hydrogen. The atomic hydrogen, HI, can be observed directly, for example, with the Parkes telescope and the ATCA. Both these HI surveys are combined in the SGPS to provide a dataset of the total atomic hydrogen throughout the galaxy. The molecular hydrogen cannot be directly observed, but is instead detected by its tracer, ^{12}CO, which is detected by both the Mopra and Nanten telescopes. The resolution of the Mopra telescope is better than that of the Nanten telescope, however the Nanten data is included as a complementary feature. To ensure that both datasets are providing us with consistent information, a short correlation study is performed.

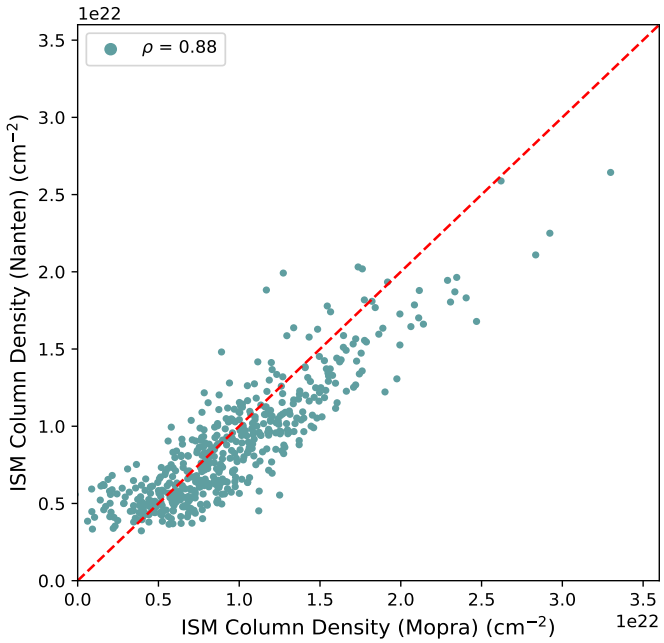

Figure A.1: A scatterplot of the Mopra column density data set against the Nanten column density data set. The red dashed line indicates a perfect linear relationship.

The correlation study compares the total column density of ISM protons calculated with the Mopra and SGPS datasets with that calculated with the Nanten and SGPS datasets. To ensure independent information is compared across each pixel, the required pixel size should be at least the resolution of the Nanten telescope. Since we re-gridded the pixels to a size of 3.6 arcmins in chapter 5, it is appropriate to re-use these datasets, especially since it is the data we used for the study. A comparison of the two datasets is shown in Figure A.1. There appears to be some scatter about the perfect linear relationship

(red dashed line), but overall the relationship is as expected. The calculated correlation coefficient, $\rho = 0.88$, is in agreement with this. Unsurprisingly, the Mopra dataset extends down to a column density of 0 cm^{-2}, whereas Nanten cannot detect anything below about 0.3×10^{21} cm^{-2}. This is due to poorer sensitivity of the Nanten telescope, failing to detect weaker signals.

Since our SED study (chapter 4) required the use of the average ISM gas density in each region, it makes sense to also compare the average column density values for each region across the Mopra (+ SGPS) and Nanten (+ SGPS) datasets. Figure A.2 shows such a comparison. We can see that the linear relationship between the two datasets is almost perfect ($\rho = 0.97$). The average Mopra values appear to be generally slightly larger than the Nanten values, this is not surprising considering the extra detail Mopra should detect.

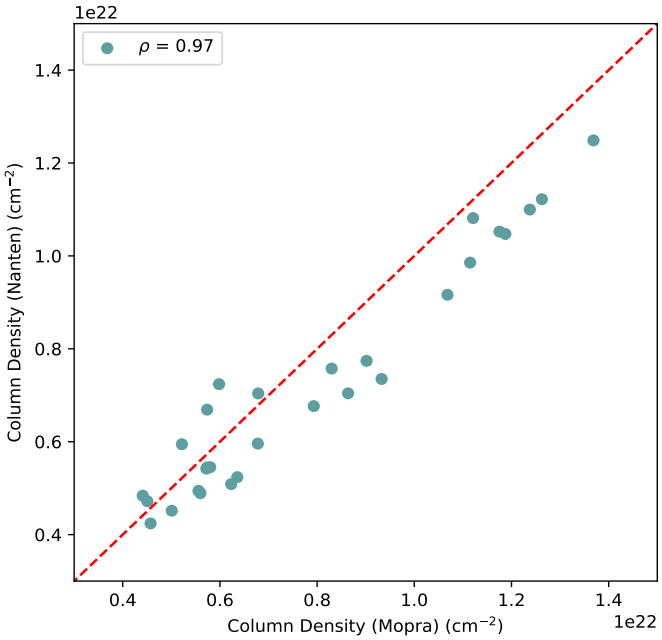

Figure A.2: A scatterplot of the average Mopra column density against the average Nanten column density for each region.

B Deriving the Threshold Proton Energy Required to Produce Pions

This study aims at determining whether the γ-ray emission from RX J1713.7-3946 is hadronic or leptonic. In order to determine the hadronic γ-ray emission from our SNR we must understand how pp interactions occur. An accelerated proton interacts with a stationary proton to produce a pion, which subsequently decays into two γ-rays. However, the accelerated proton must have sufficient energy in order to produce a pion. We call this energy the threshold proton energy for pp interactions and we derive it below.

To derive the threshold proton energy required to produce a pion we turn to 4-vector analysis. The 4-momentum of a particle/system is defined as:

$$p^{\mu} = \left(\frac{E}{c}, \vec{p}\right) \tag{B.1}$$

where E is the total energy of the particle/system, $\vec{p}$ is the total 3-dimensional momentum and c is the speed of light. If we consider a single pp interaction; a proton with energy E_p collides with a stationary proton with rest mass ($E = m_p c^2$) to produce a pion. The 4-momentum of our combined system before the collision can then be written as:

$$p_i^{\mu} = \left(\frac{E_p + m_p c^2}{c}, \vec{p_p}\right) \tag{B.2}$$

where $\vec{p_p}$ is simply the 3-momentum of the high energy proton. If we then examine the 4-momentum of the system after the interaction in the centre of momentum frame, the two protons and the pion will be at rest, giving us:

$$p_f^{\mu} = \left(\frac{2m_p c^2 + m_\pi c^2}{c}, \vec{0}\right) \tag{B.3}$$

where the total energy of this system is simply the sum of the three rest masses. We can now find the minimum E_p required to produce a pion by invoking the invariance principle, $p_{\mu,i} p_i^{\mu} = m^2 c^2 = p_{\mu,f} p_f^{\mu}$:

$$\left(\frac{E_p + m_p c^2}{c}\right)^2 - p_p^2 = \left(2m_p c + m_\pi c\right)^2 . \tag{B.4}$$

Making use of the Energy-momentum relation $E^2 = p^2 c^2 + m^2 c^4$ and rearranging for E_p gives us:

$$E_p = m_p c^2 + 2m_\pi c^2 + \frac{m_\pi^2 c^2}{2m_p} . \tag{B.5}$$

Finally, using $m_p = 938.27$ MeV/c^2 and $m_\pi = 134.98$ MeV/c^2, we find that $E_p \approx 1.218$ GeV and the Kinetic Energy, $K_p \approx 0.2797$ GeV.

C Visualising the Various Power Law Spectra

In chapter 3 we discuss the importance of the particle populations responsible for producing the γ-ray emission at SNRs. Additionally, we describe how some various PL distributions can be used to represent these populations. In Figure C.1 we illustrate how a PL with an exponential cut-off can vary for different cut-off energies, E_c. This cut-off energy controls the amount of high-energy particles are available in the distribution. Additionally, in Figure C.2 we illustrate how a broken PL can vary for various high and low energy spectral indices, α_1 and α_2 respectively. A broken PL can be exploited to suppress both high and low energy particles within the distribution.

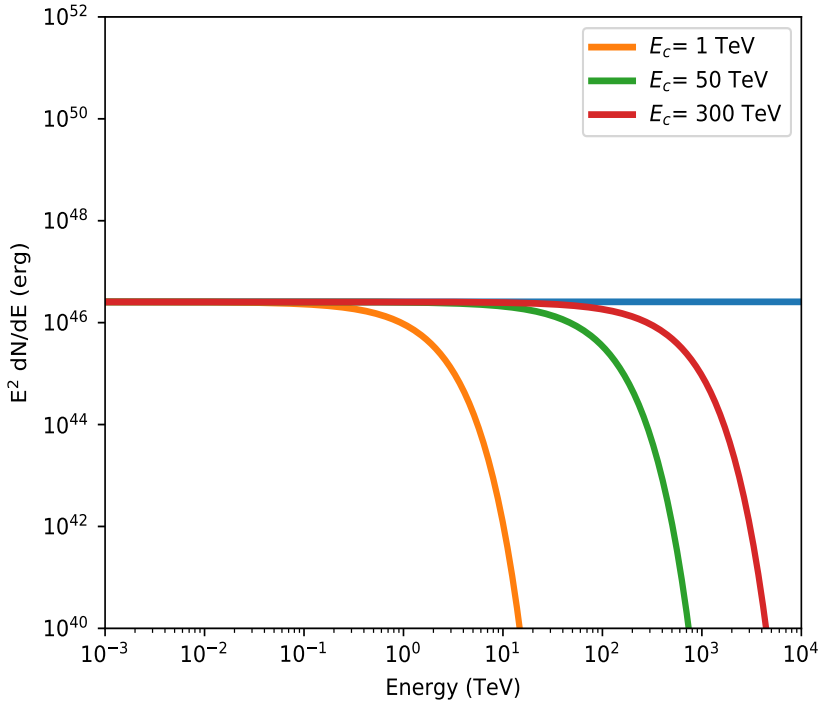

Figure C.1: The power-law spectra for various exponential cut-off energies (E_c). An injection energy of 1×10^{46} erg is assumed.

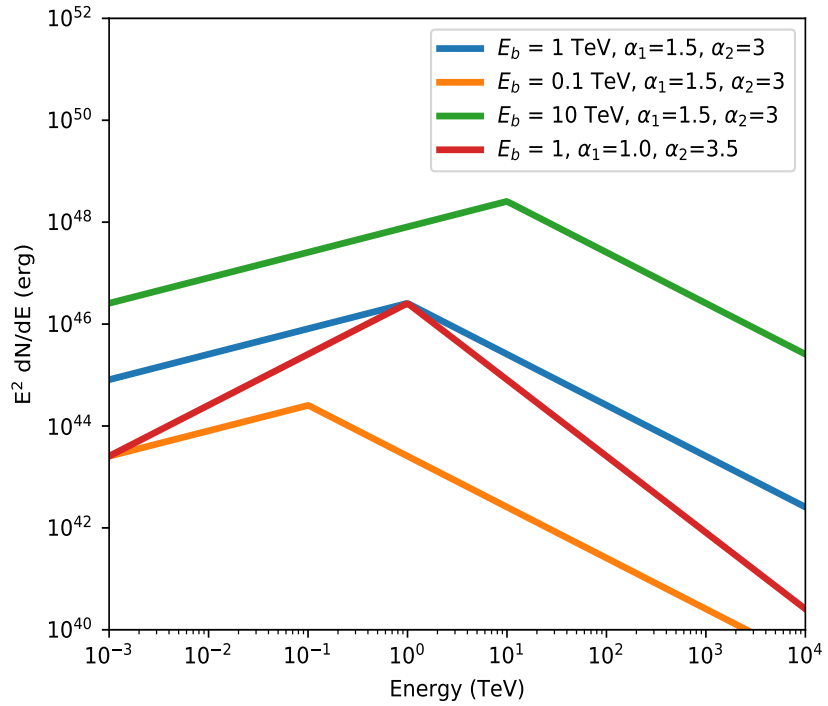

Figure C.2: The spectra for various broken power-laws. Either the energy break, E_b, or the high and low spectral indices, α_1 and α_2, are altered. An injection energy of 1×10^{46} erg is assumed.

D Hadronic and Leptonic SED Results of All 29 Regions

D.1 Hadronic SEDs

The SEDs presented in this section are based on a pure hadronic model as discussed in section 4.2. We display the SEDs for all 29 regions along with their corresponding proton energy budget, $W_{p,\mathrm{SED}}$, proton spectral index, α, and ISM volume density, n_H.

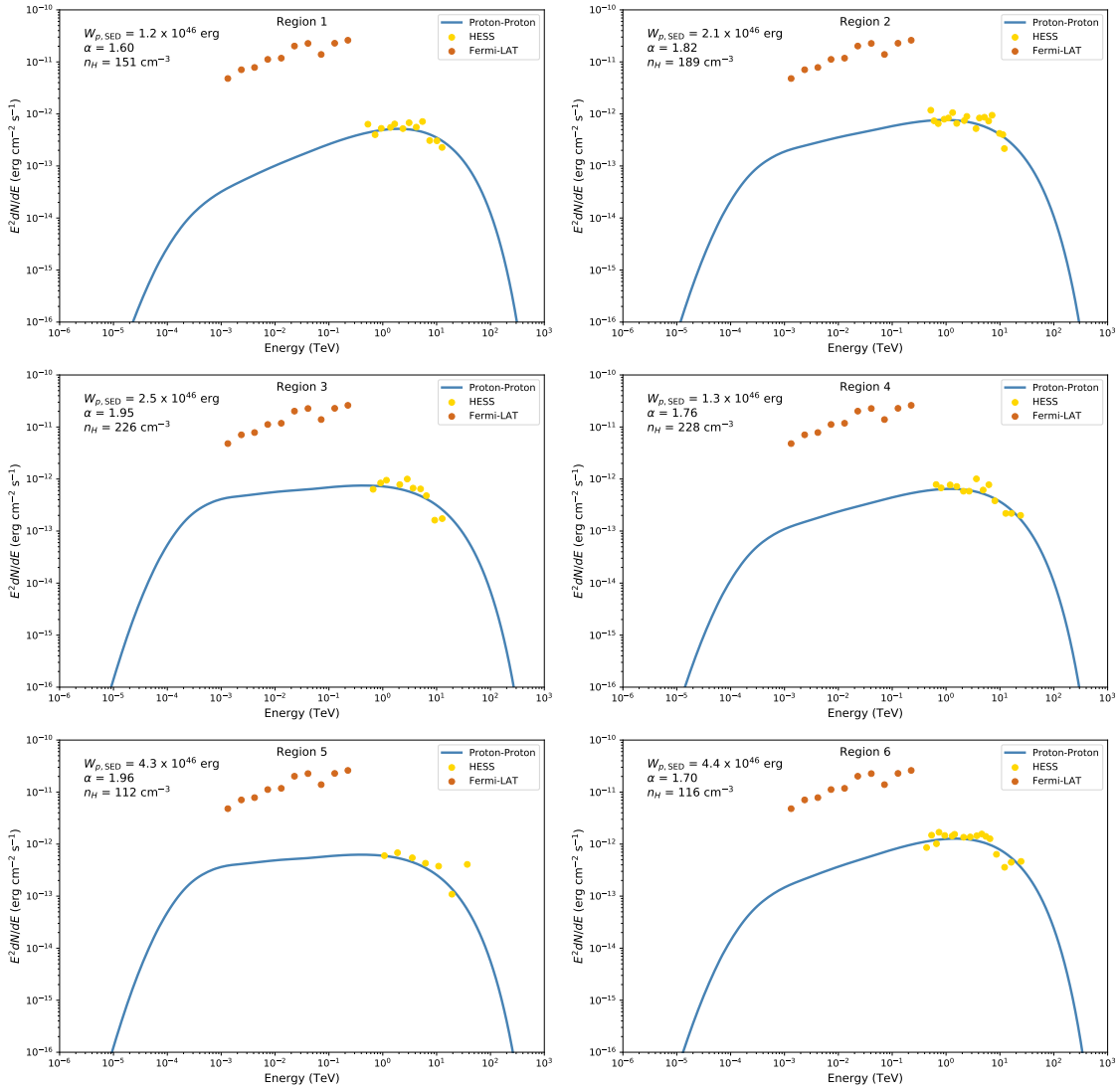

Figure D.1: Hadronic SEDs for regions 1 to 6 within RX J1713.7-3946

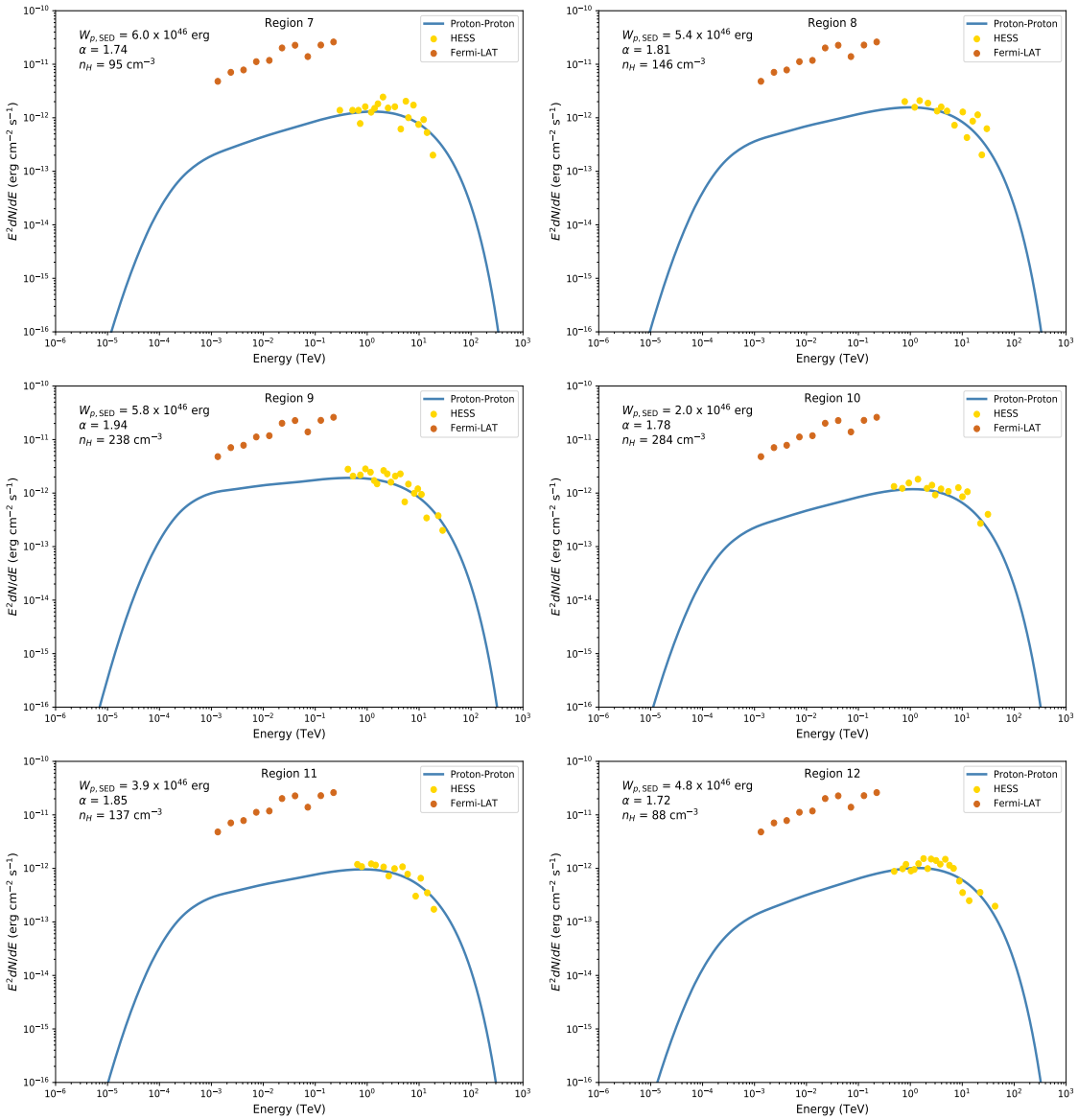

Figure D.2: Hadronic SEDs for regions 7 to 12 within RX J1713.7-3946

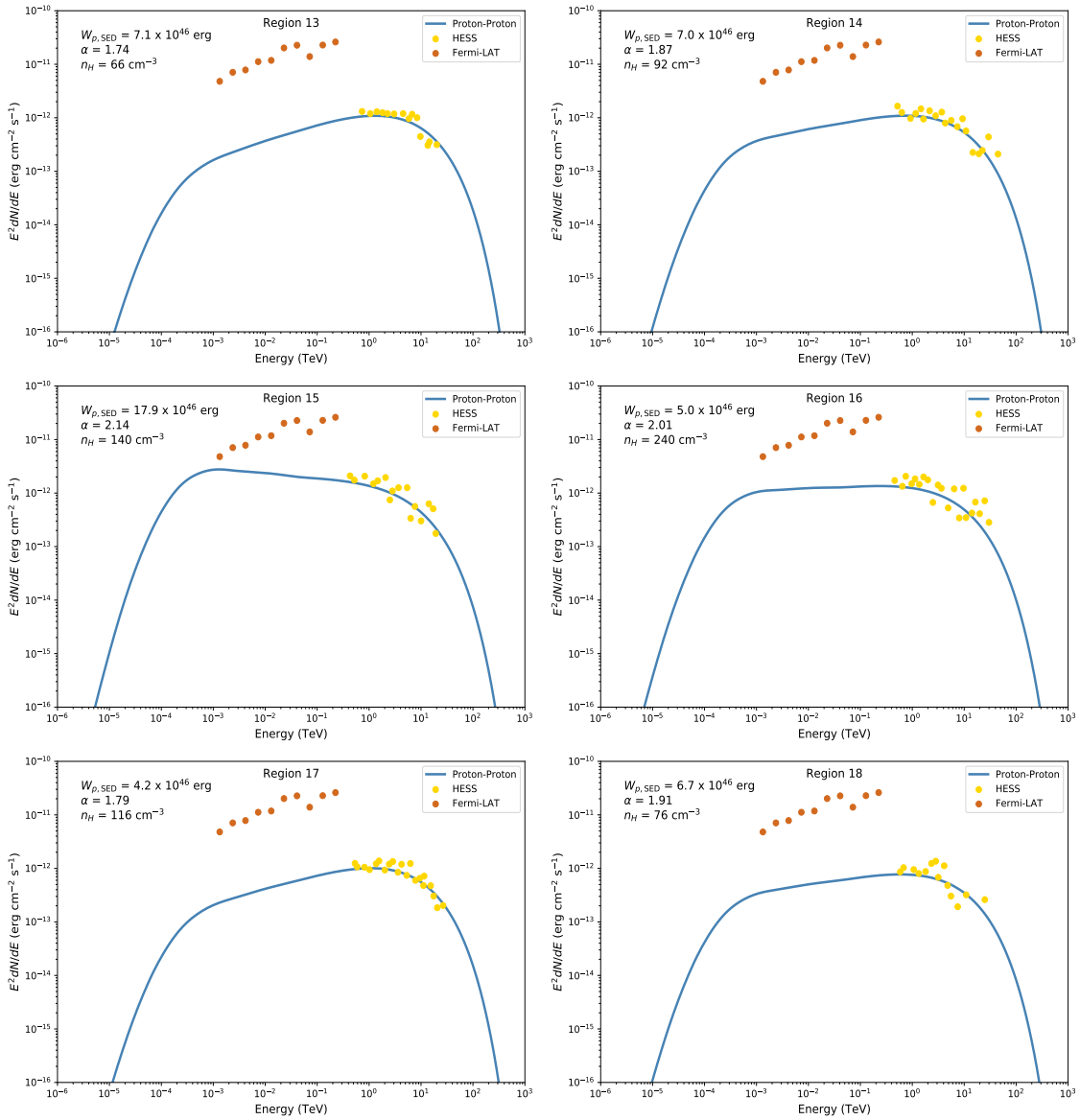

Figure D.3: Hadronic SEDs for regions 13 to 18 within RX J1713.7-3946

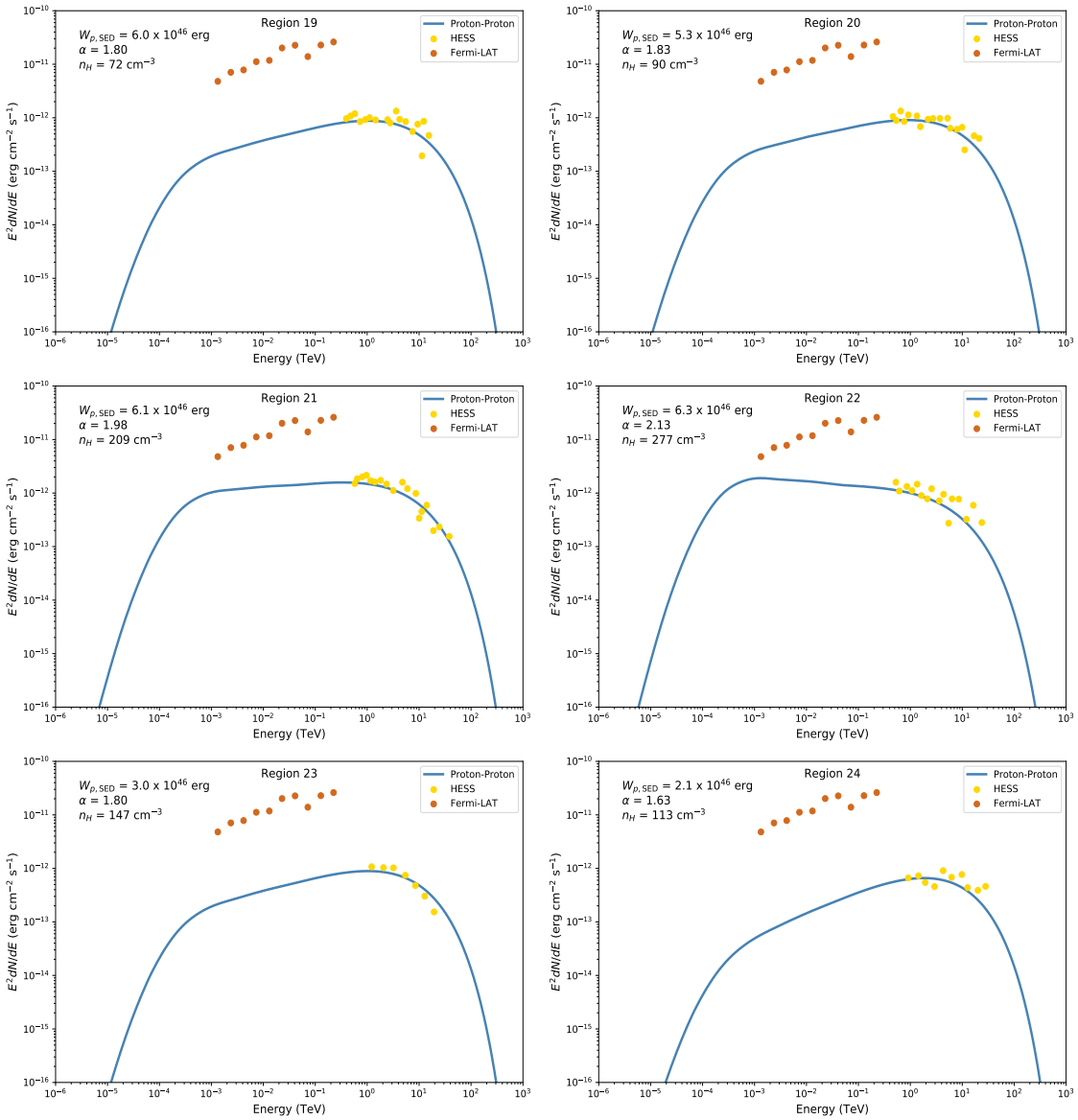

Figure D.4: Hadronic SEDs for regions 19 to 24 within RX J1713.7-3946

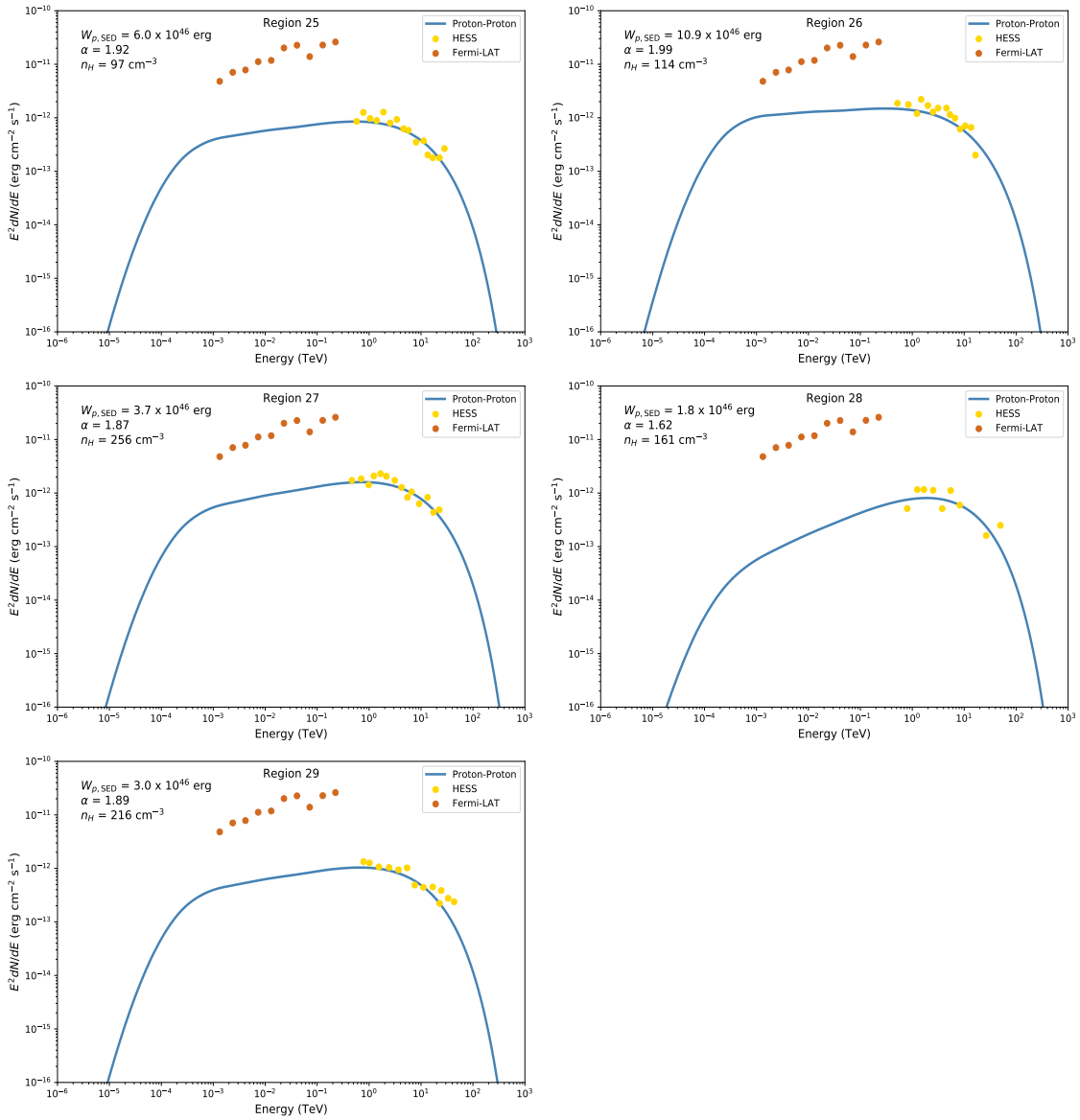

Figure D.5: Hadronic SEDs for regions 25 to 29 within RX J1713.7-3946

D.2 Leptonic SEDs

The SEDs presented in this section are based on a pure leptonic model as discussed in subsection 4.3.1. We display the SEDs for all 29 regions along with their corresponding electron energy budget, W_e, low energy spectral index, α_1, high energy spectral index, α_2, exponential cut-off energy, E_c, magnetic field strength, B, and ISM volume density, n_H. Additionally, a break-energy of 2.5 TeV is assumed for each region, in accordance with the average value of the entire SNR.

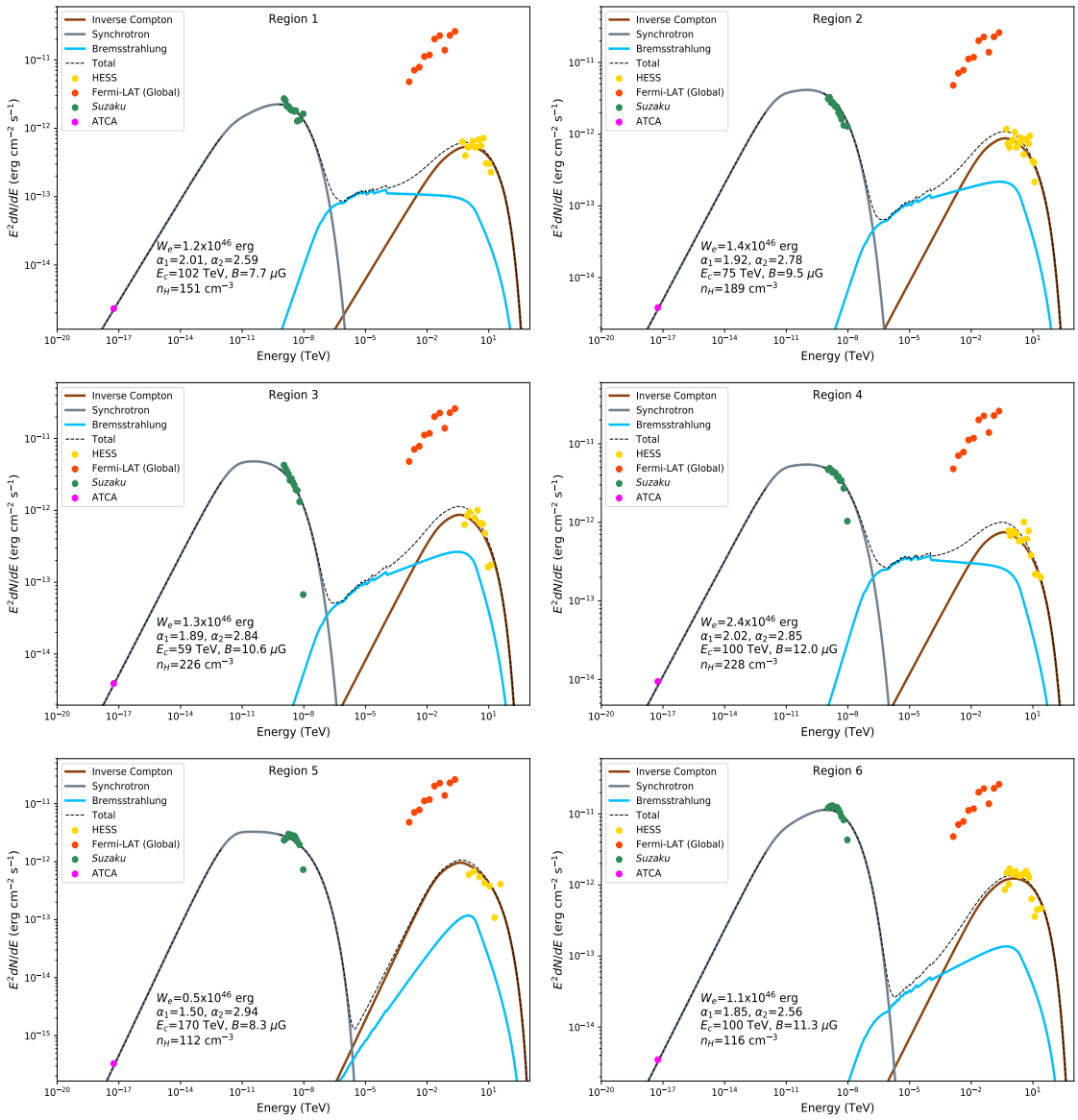

Figure D.6: Leptonic SEDs for regions 1 to 6 within RX J1713.7-3946

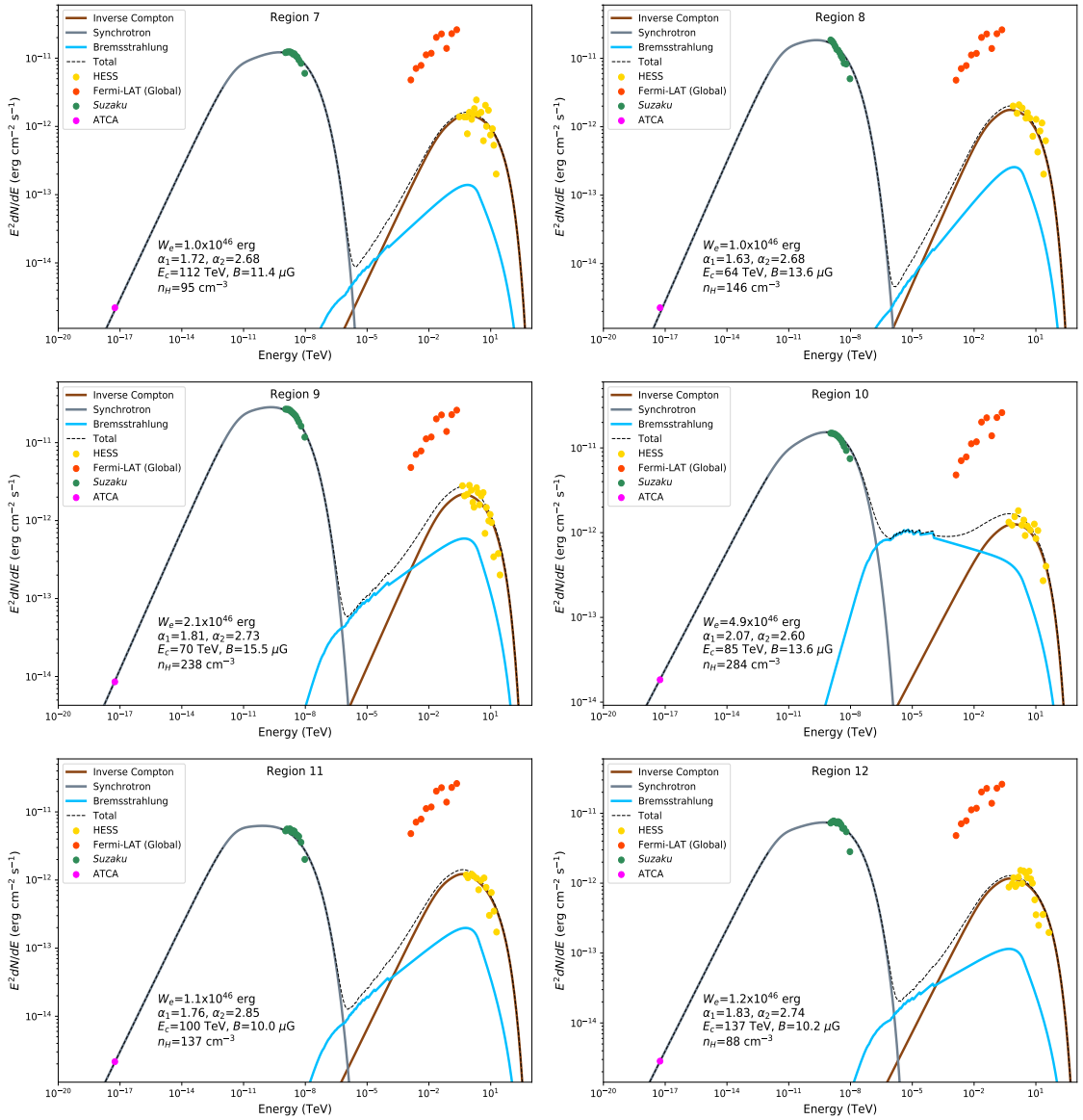

Figure D.7: Leptonic SEDs for regions 7 to 12 within RX J1713.7-3946

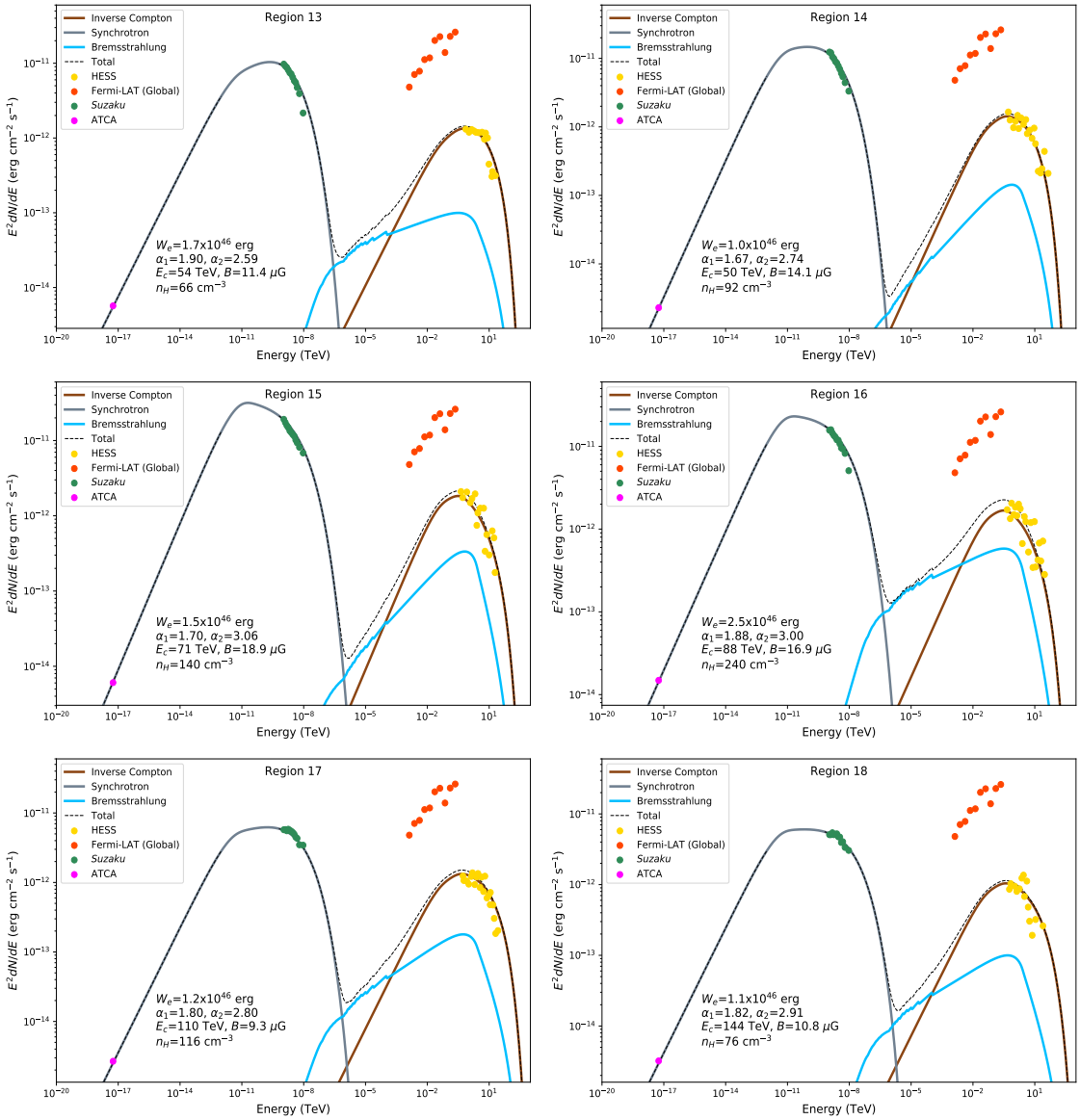

Figure D.8: Leptonic SEDs for regions 13 to 18 within RX J1713.7-3946

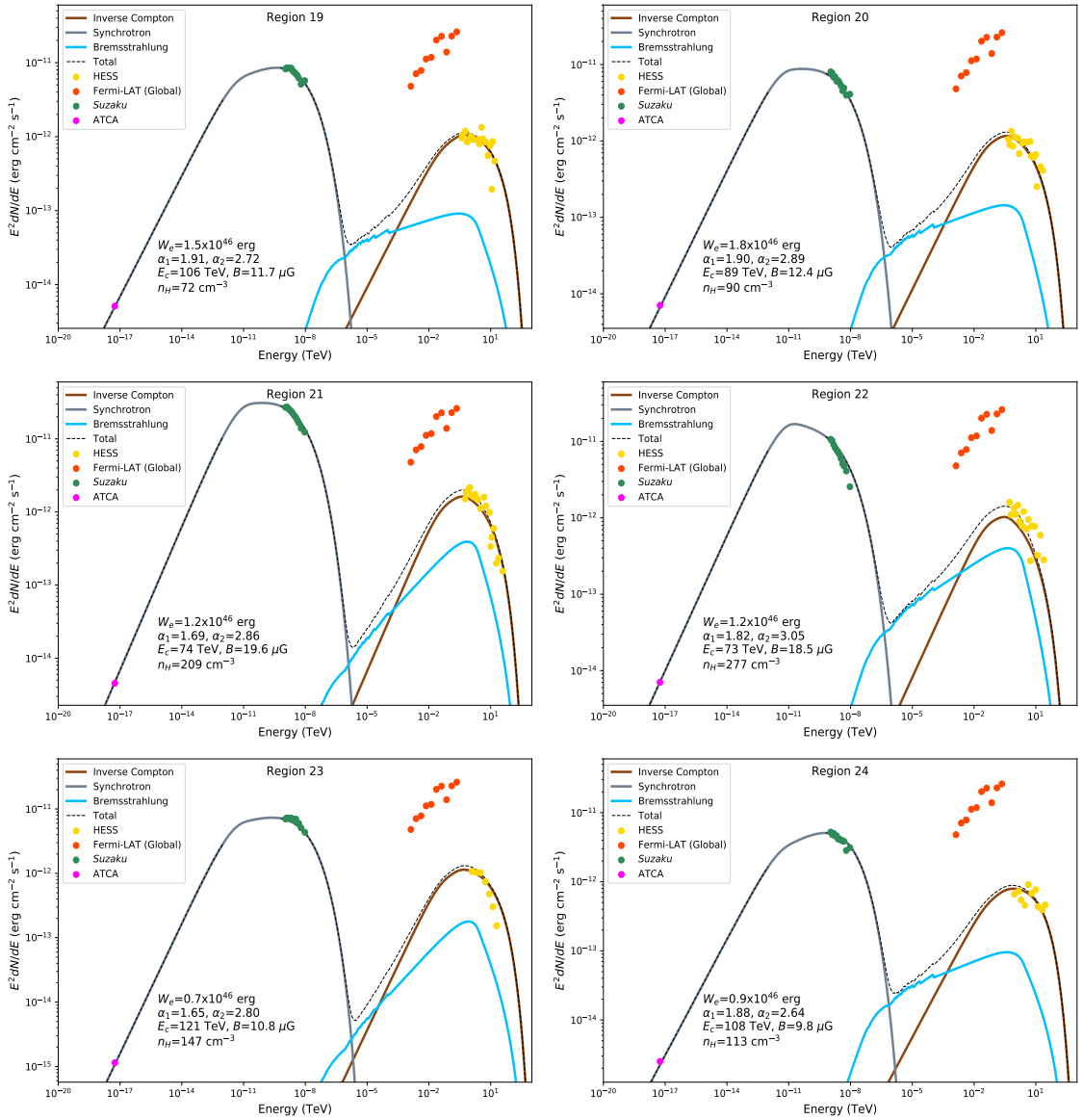

Figure D.9: Leptonic SEDs for regions 19 to 24 within RX J1713.7-3946

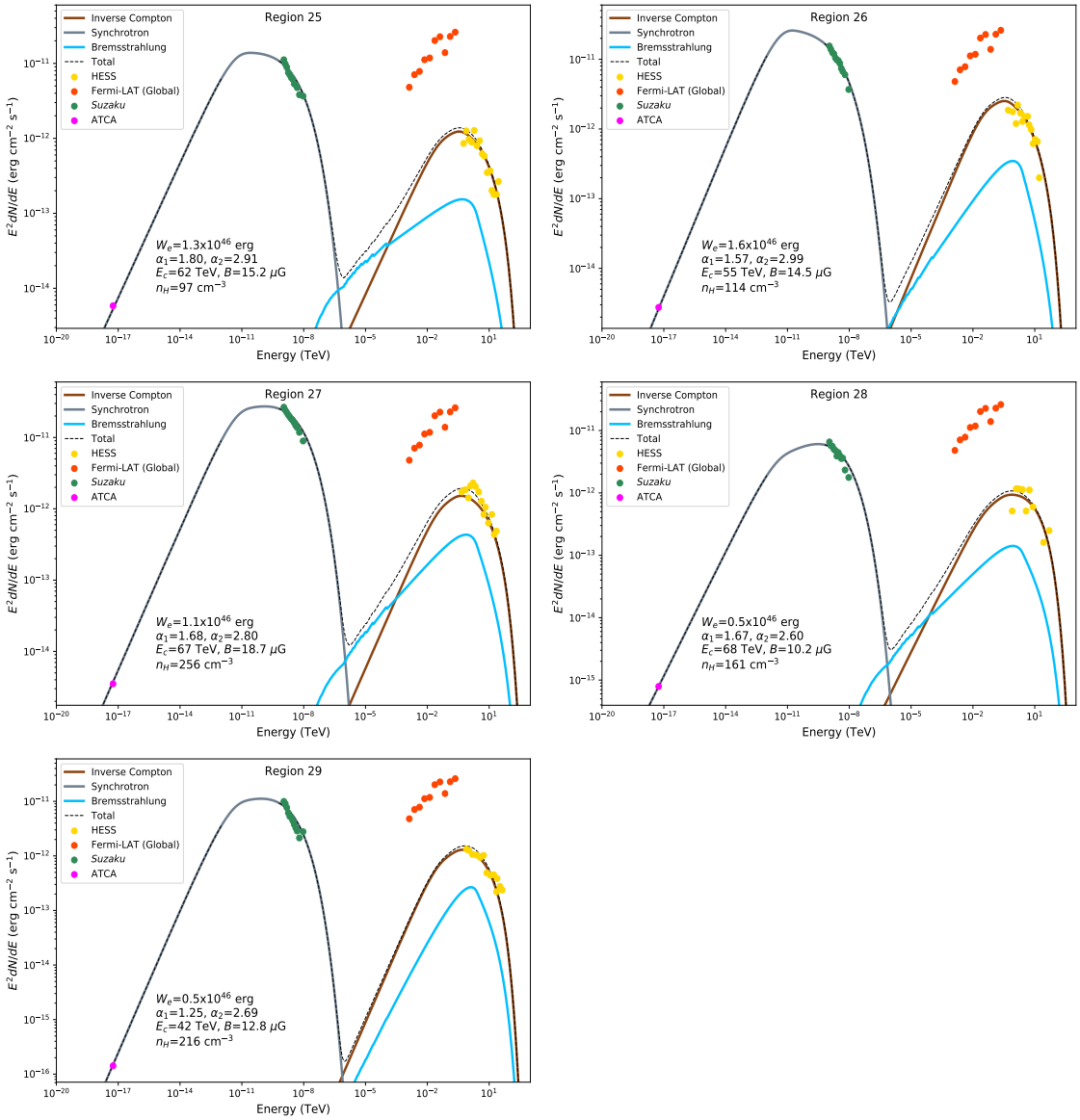

Figure D.10: Leptonic SEDs for regions 25 to 29 within RX J1713.7-3946

D.3 Leptonic Parameters from H18

Table D.1 presents the parameters derived from the pure leptonic scenario in H18. Displayed here for completeness and for comparison with the parameters chosen in our study subsection 4.3.1

Region	$W_e(\times 10^{46}$ erg)	$B(\mu$G)	α_1	α_2	E_c(TeV)
1	1.25	7.7	2.01	2.59	102
2*	1.41	8.3	1.92	2.78	93
3*	1.27	10.6	1.89	2.84	66
4*	3.11	10.5	2.05	2.75	100
5	0.51	8.3	1.50	2.94	170
6	1.13	11.3	1.85	2.56	100
7	1.00	11.4	1.72	2.68	112
8	1.02	13.6	1.63	2.68	64
9*	2.07	14.9	1.81	2.73	87
10*	4.88	12.9	2.07	2.60	90
11*	1.05	9.5	1.76	2.85	140
12	1.16	10.2	1.83	2.74	137
13	1.72	11.4	1.90	2.59	54
14	0.95	14.1	1.67	2.74	50
15*	2.03	18.2	1.63	3.26	83
16*	2.83	16.0	1.86	3.06	88
17	1.25	9.3	1.80	2.80	110
18	1.12	10.8	1.82	2.91	144
19	1.49	11.7	1.91	2.72	106
20	1.79	12.4	1.90	2.89	89
21*	1.45	18.4	1.63	2.94	77
22*	1.70	16.4	1.73	3.21	73
23	0.72	10.8	1.65	2.80	121
24	0.90	9.8	1.88	2.64	108
25	1.28	15.2	1.80	2.91	62
26	1.57	14.5	1.57	2.99	55
27*	1.50	16.7	1.61	2.91	75
28	0.55	10.2	1.67	2.60	68
29	0.50	12.8	1.25	2.69	42

Table D.1: Parameters used to model the pure leptonic model for each region (H18). An asterisk (*) placed next to a region number indicates that at least one of the H18 parameters is different to the derived SED parameters in subsection 4.3.1.

E ISM Gas and Gamma-ray Correlation Data

E.1 Results from Mopra CO + SGPS HI Data Set

For each region a correlation coefficient, ρ, is calculated in chapter 5. To calculate the significance of this correlation coefficient a bootstrapping technique is applied and a distribution of ρ values is obtained (section 5.2.1). The 3σ values (dashed lines) from these distributions are then compared against a random distribution of ρ values to calculate the p-value. This section presents these distributions for each region, followed by plots of the ISM column density against the HESS TeV γ-rays as presented in subsection 5.2.2. The results presented in this section used the Mopra data set to estimate the molecular component of the ISM.

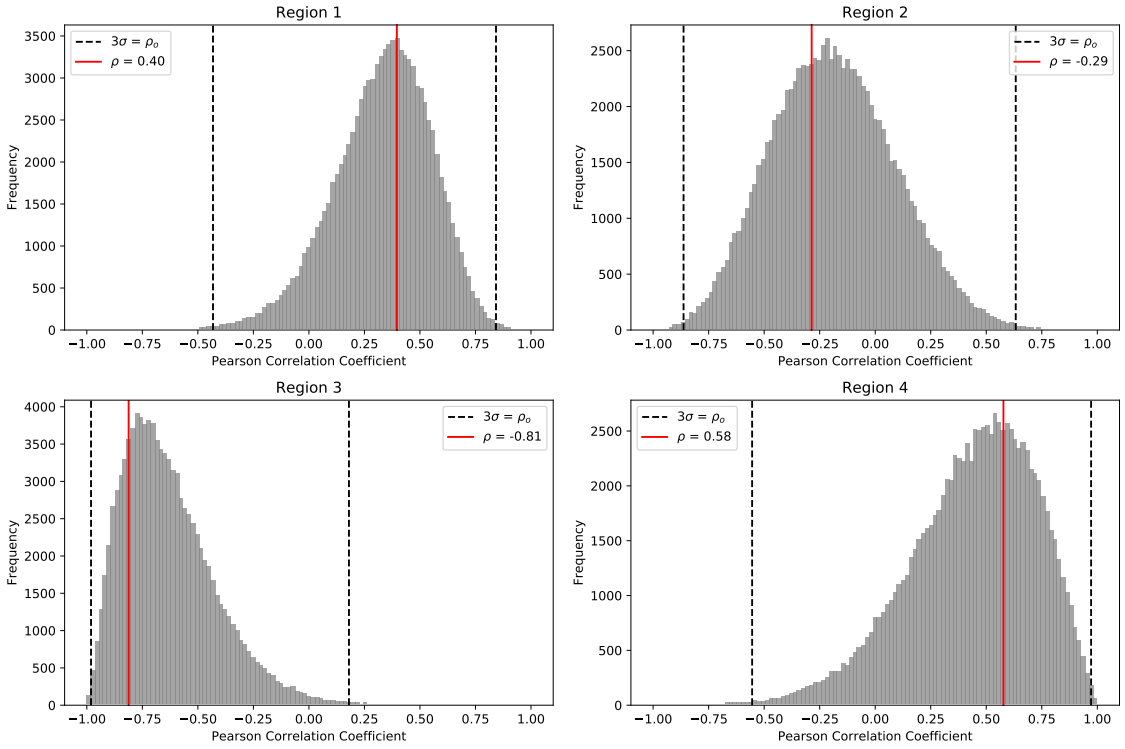

Figure E.1: The distribution of ρ values for regions 1-4, where the ISM column density has been calculated with the Mopra CO and SGPS data. Both the ISM column density and γ-ray excess counts data sets have been cleaned to ensure no noisey γ-ray data is included (see subsection 5.2.3). The red line indicates the original ρ value and the dashed lines indicate the 3σ confidence bands.

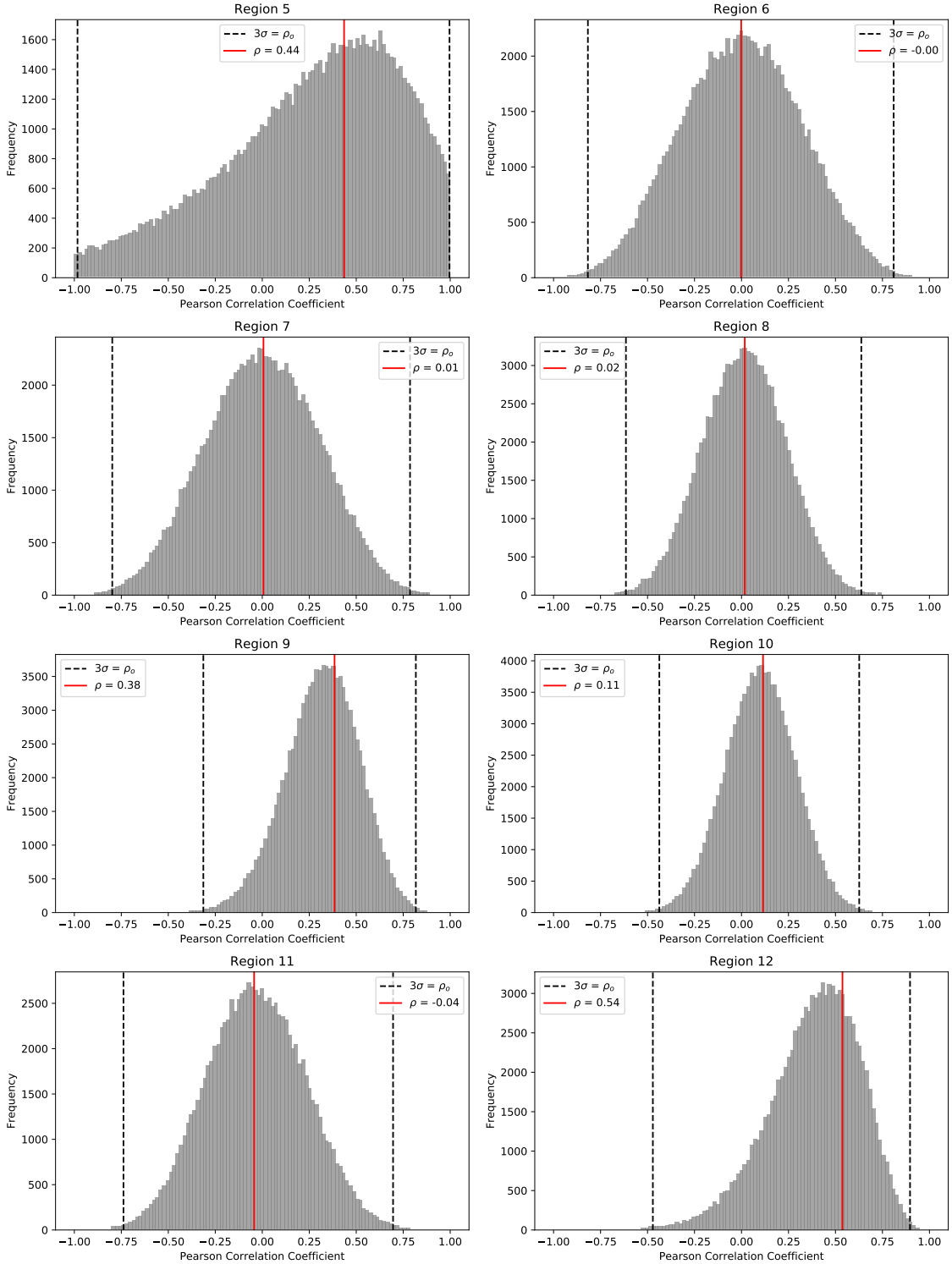

Figure E.2: Same as Figure E.1 except for regions 5-12.

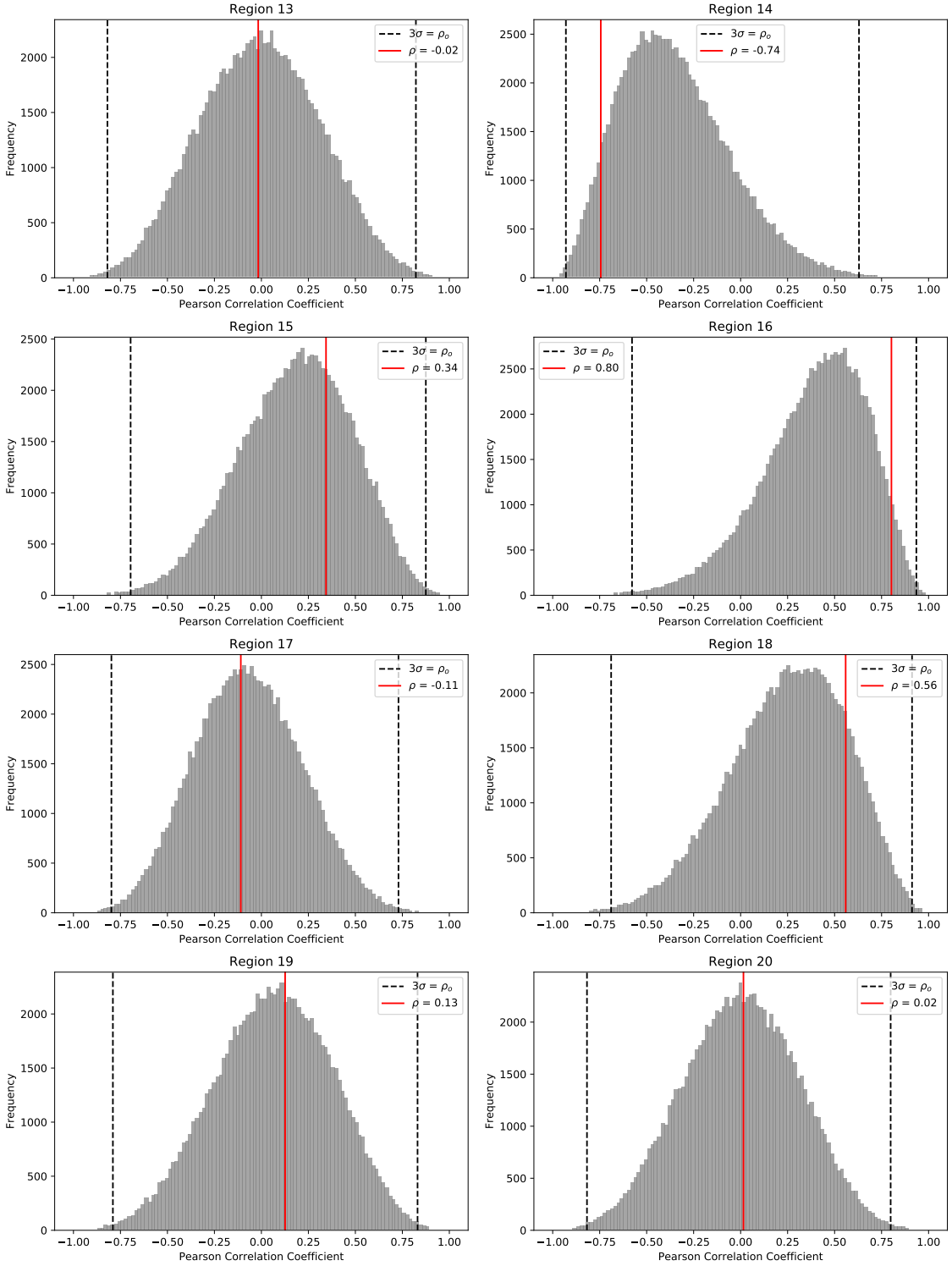

Figure E.3: Same as Figure E.1 except for regions 13-20.

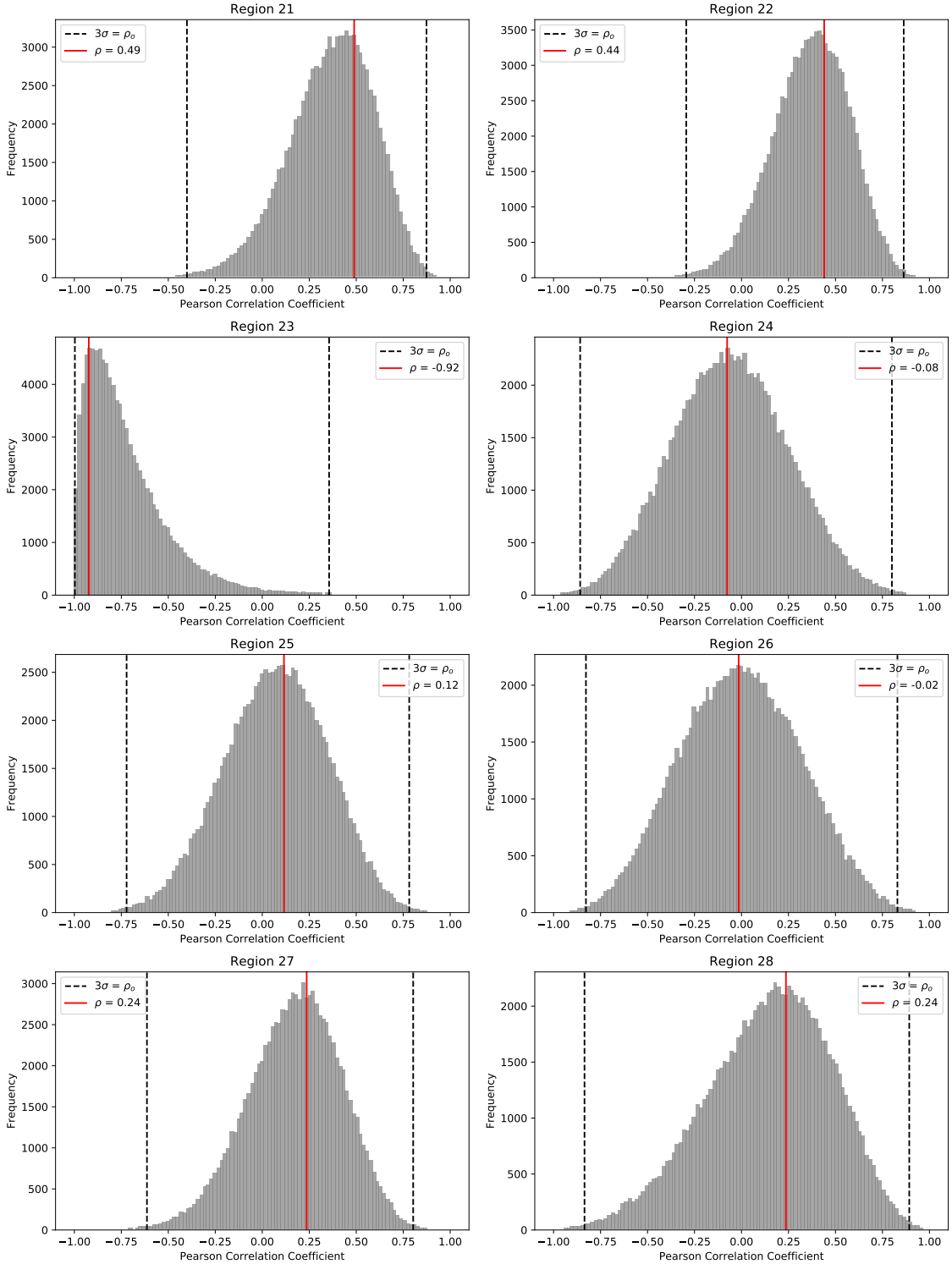

Figure E.4: Same as Figure E.1 except for regions 21-28.

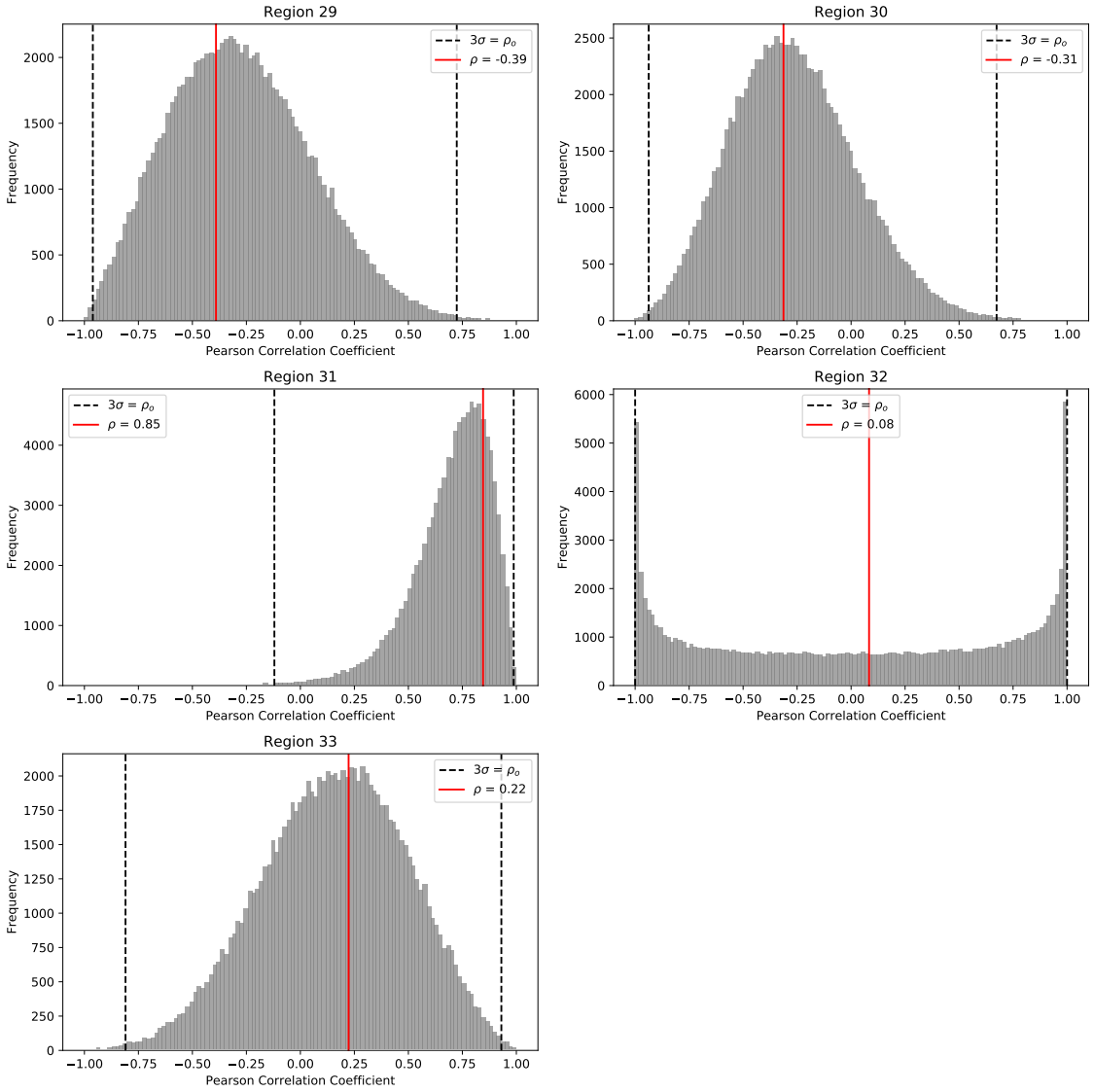

Figure E.5: Same as Figure E.1 except for regions 29-33.

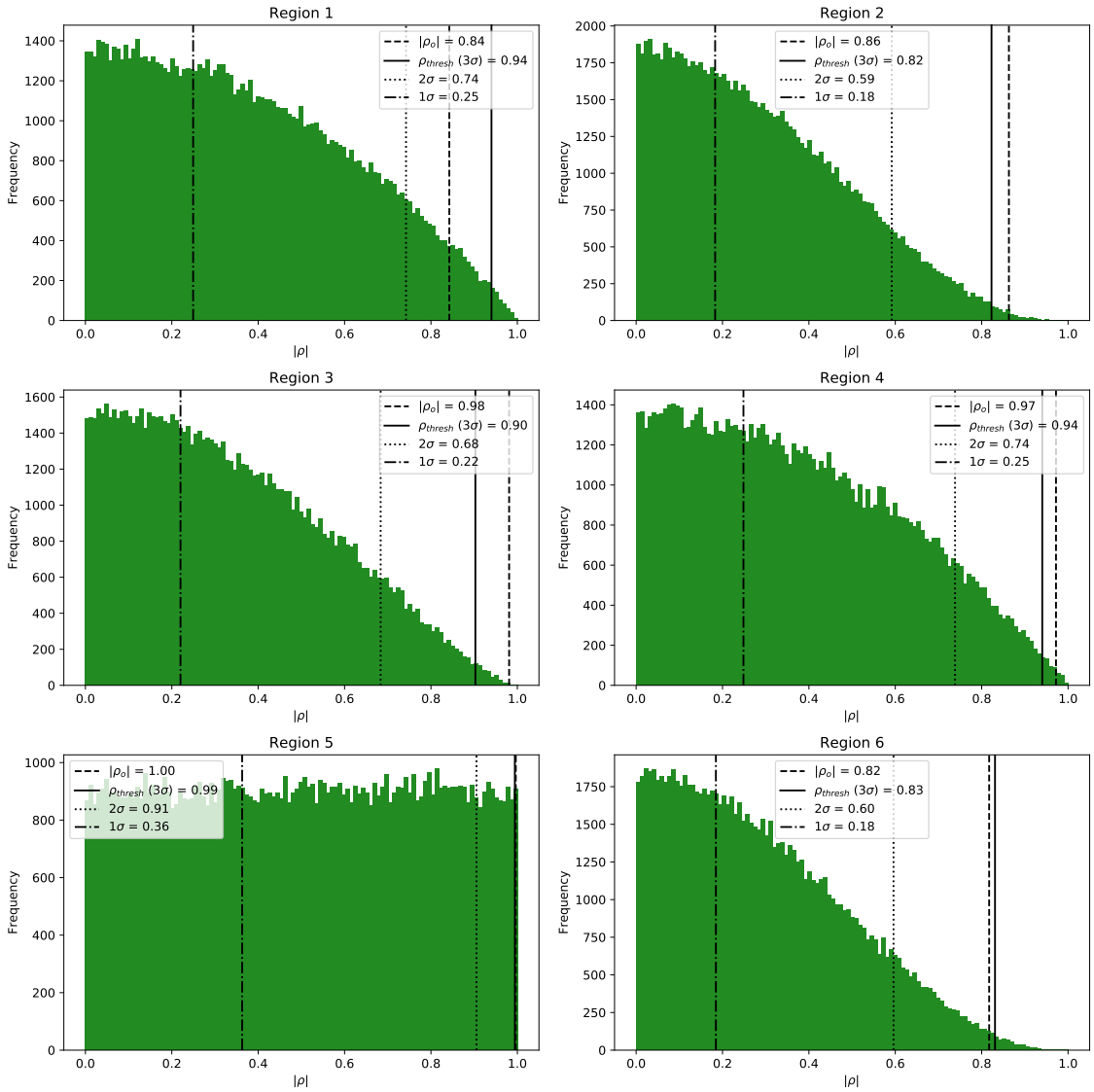

Figure E.6: The distribution of randomly distributed $|\rho|$ values, used to calculate the significance of ρ in each region. The 1σ, 2σ and 3σ values are illustrated with dot-dashed, dotted, and filled lines respectively. In being consistent with the previous plots, ρ_o is illustrated with a dashed line. The significance of ρ corresponds to the section of the distribution it falls in. See section 5.2.1 for more details.

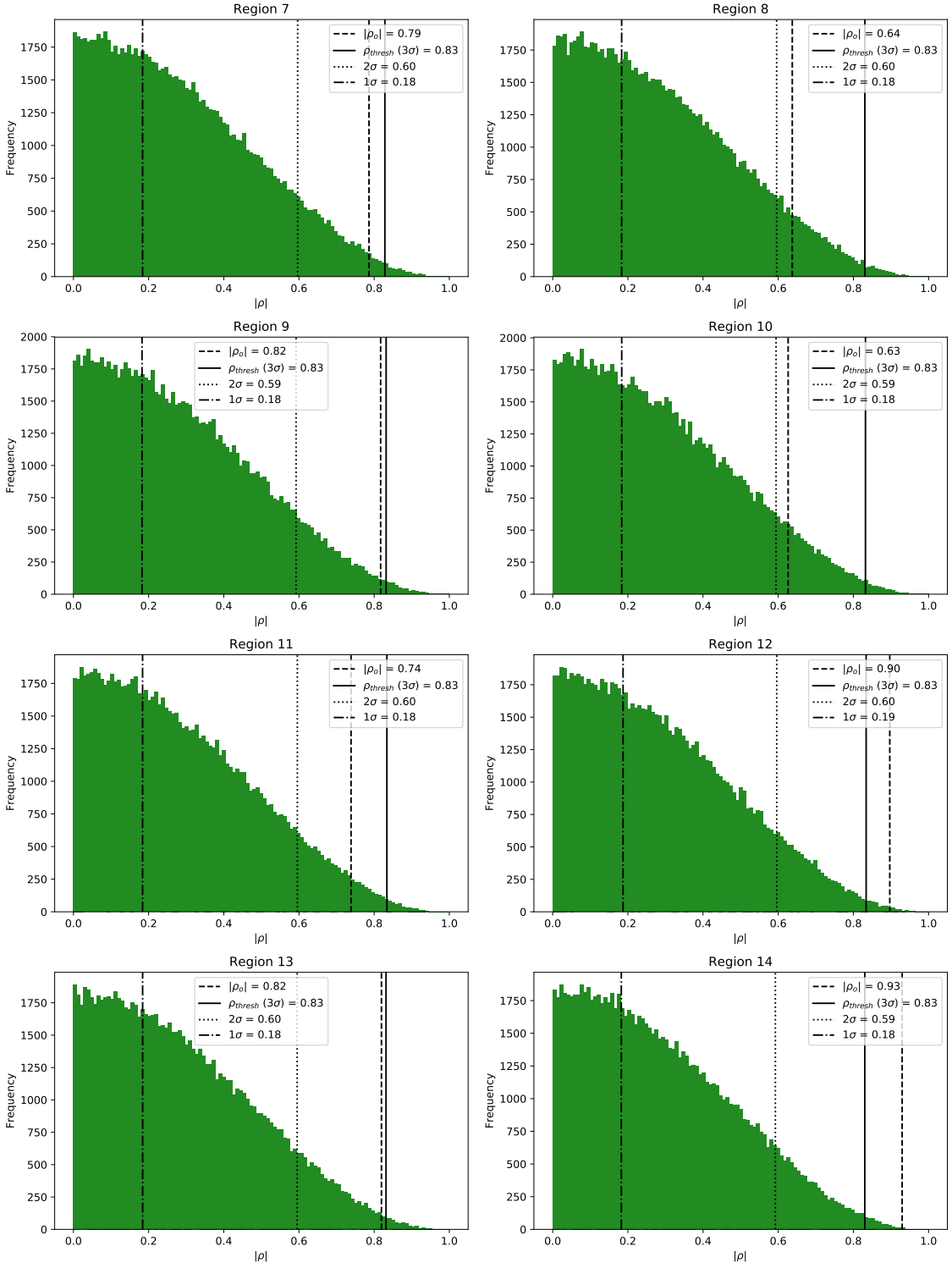

Figure E.7: Same as Figure E.6 except for regions 7-14.

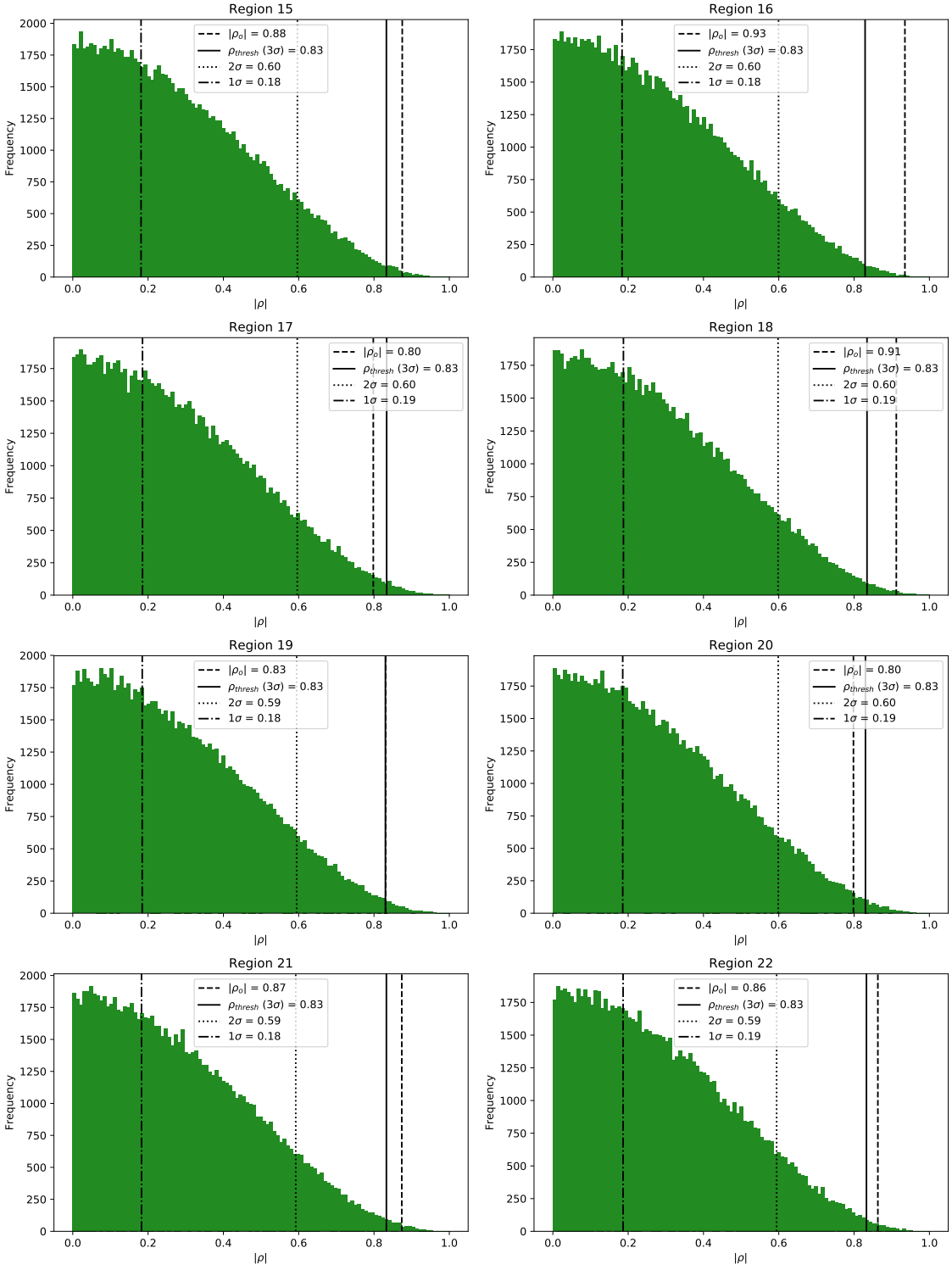

Figure E.8: Same as Figure E.6 except for regions 15-22.

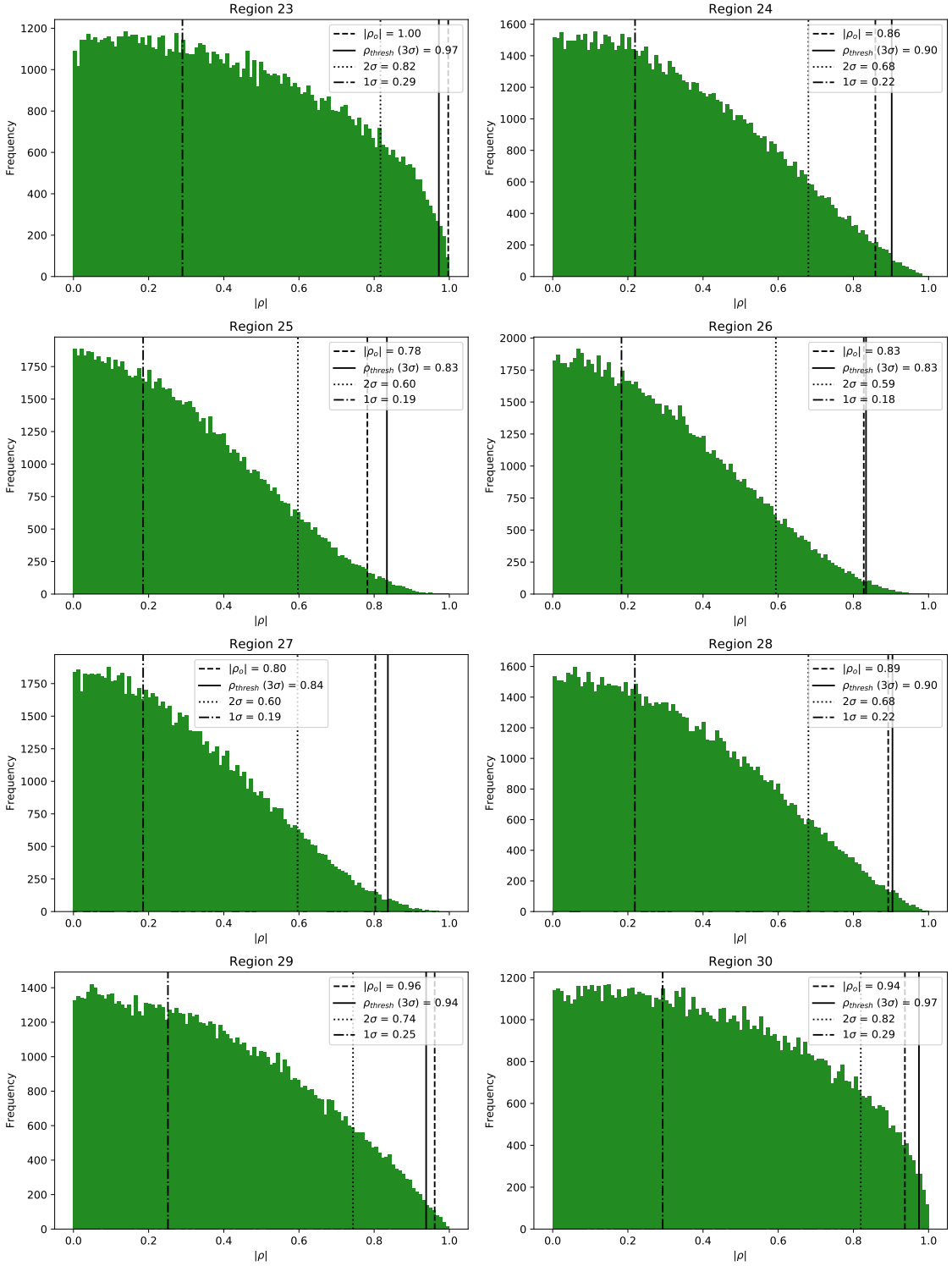

Figure E.9: Same as Figure E.6 except for regions 23-30.

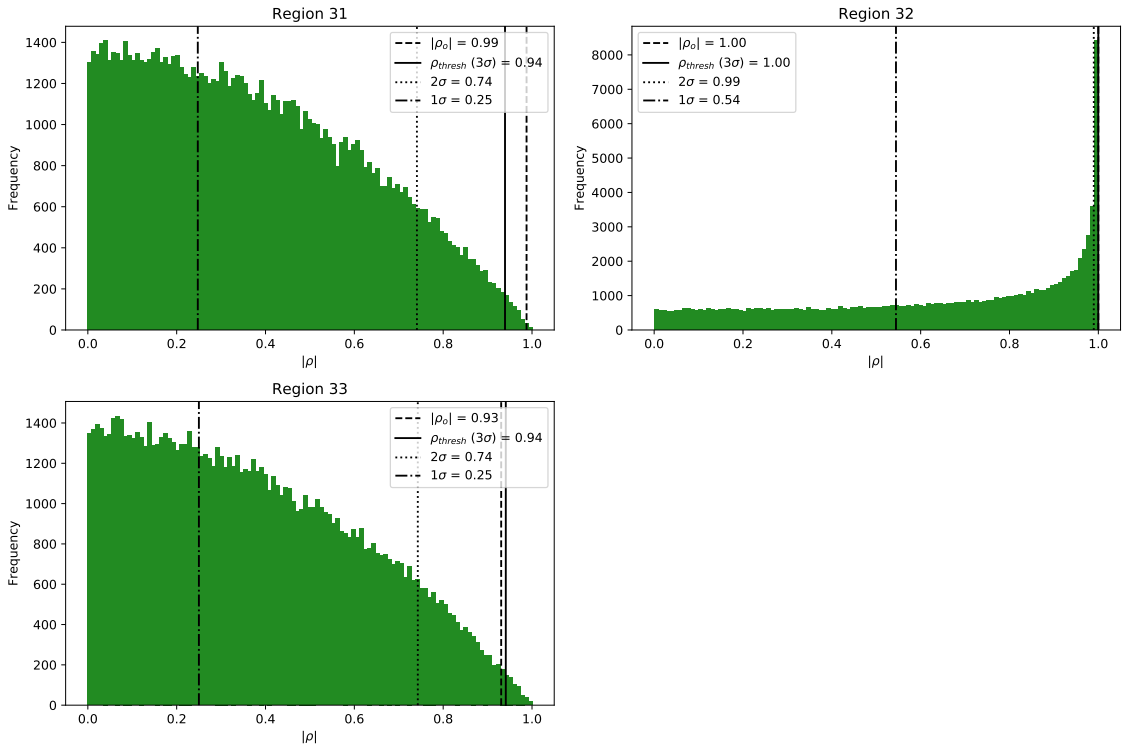

Figure E.10: Same as Figure E.6 except for regions 31-33.

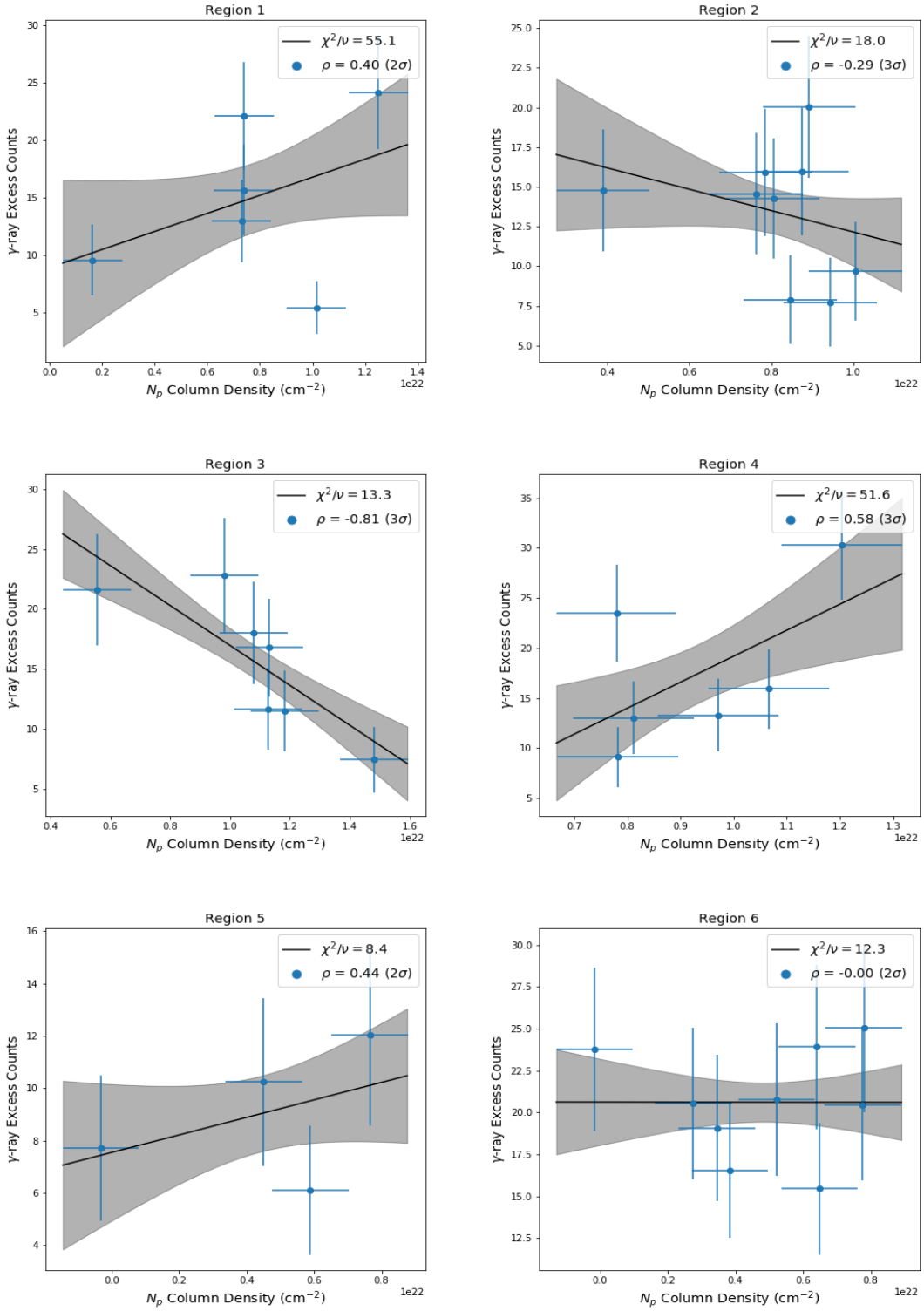

Figure E.11: The correlation scatterplots showing the relationship between the ISM gas density and the γ-rays in regions 1-6. The line of best fit is shown in black, while the grey area illustrates the 1σ confidence band.

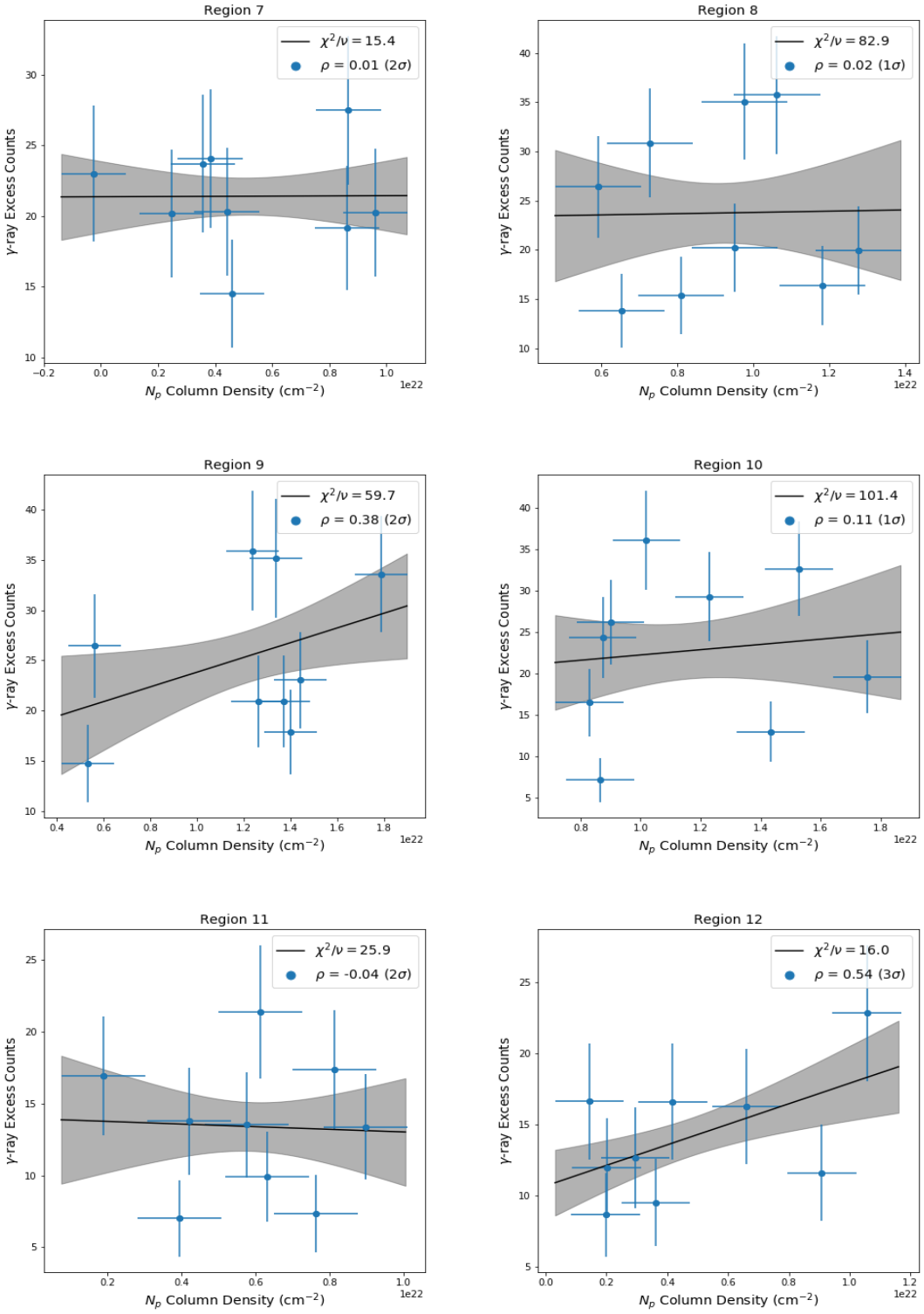

Figure E.12: Same as Figure E.11 except for regions 7-12.

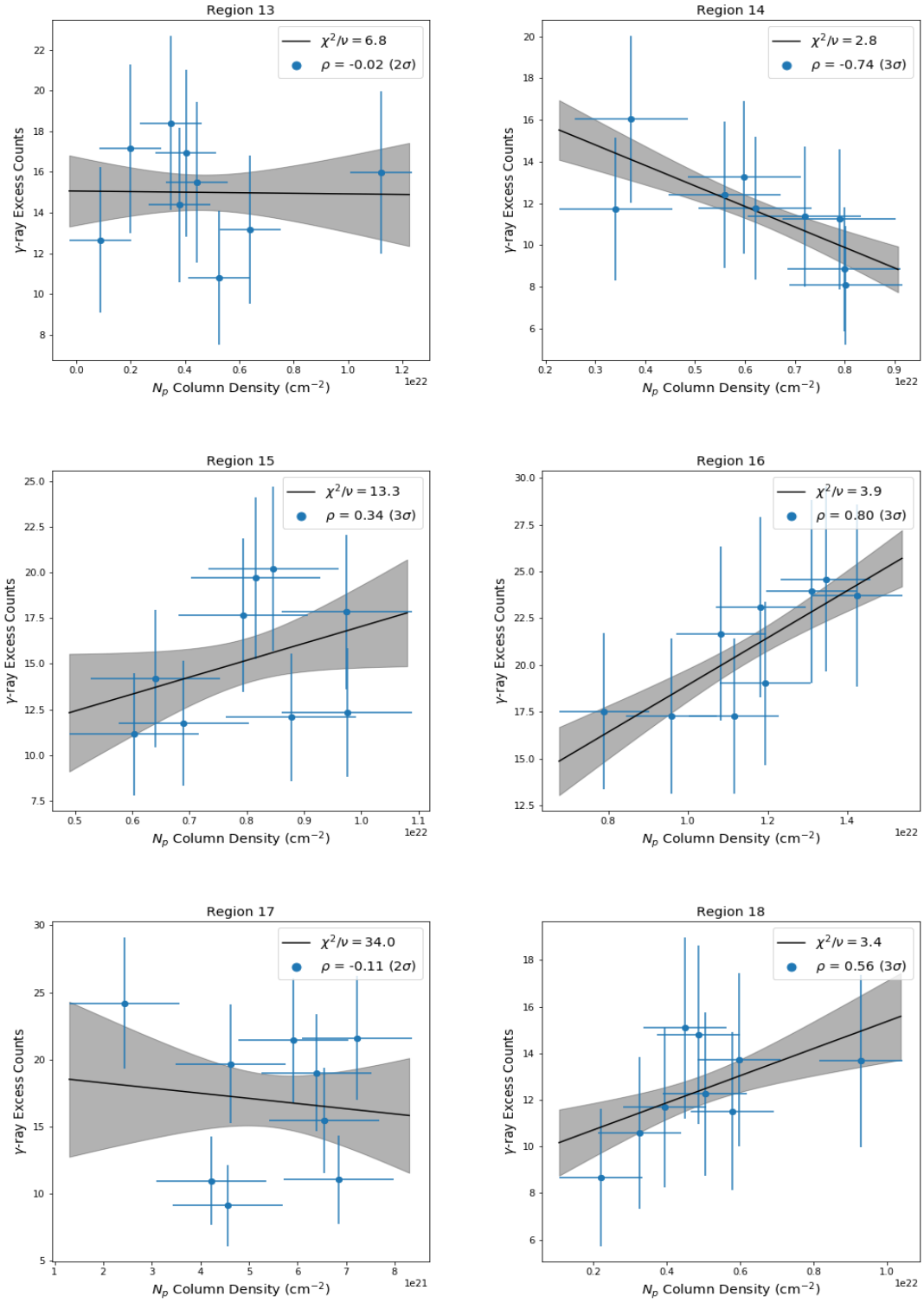

Figure E.13: Same as Figure E.11 except for regions 13-18.

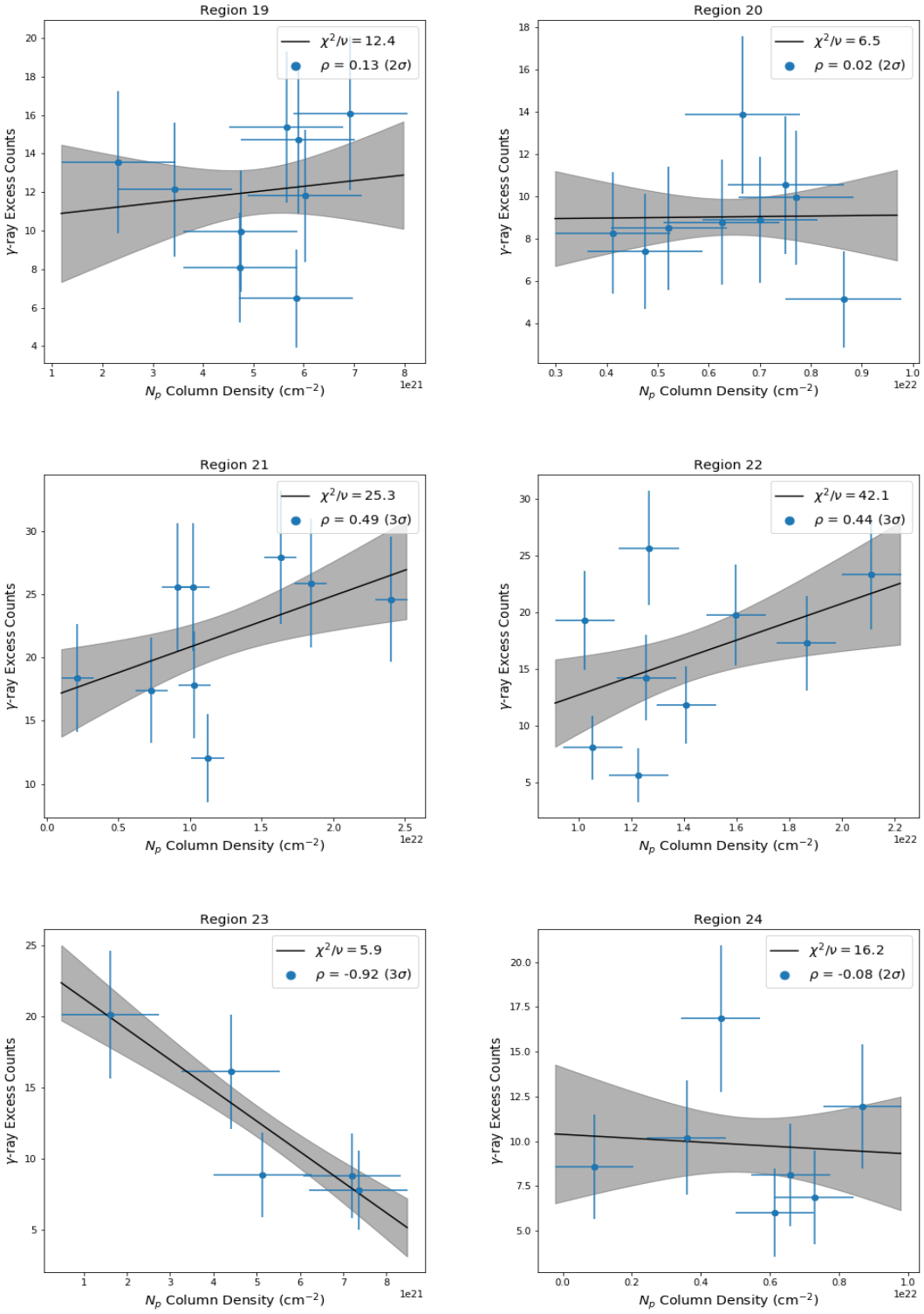

Figure E.14: Same as Figure E.11 except for regions 19-24.

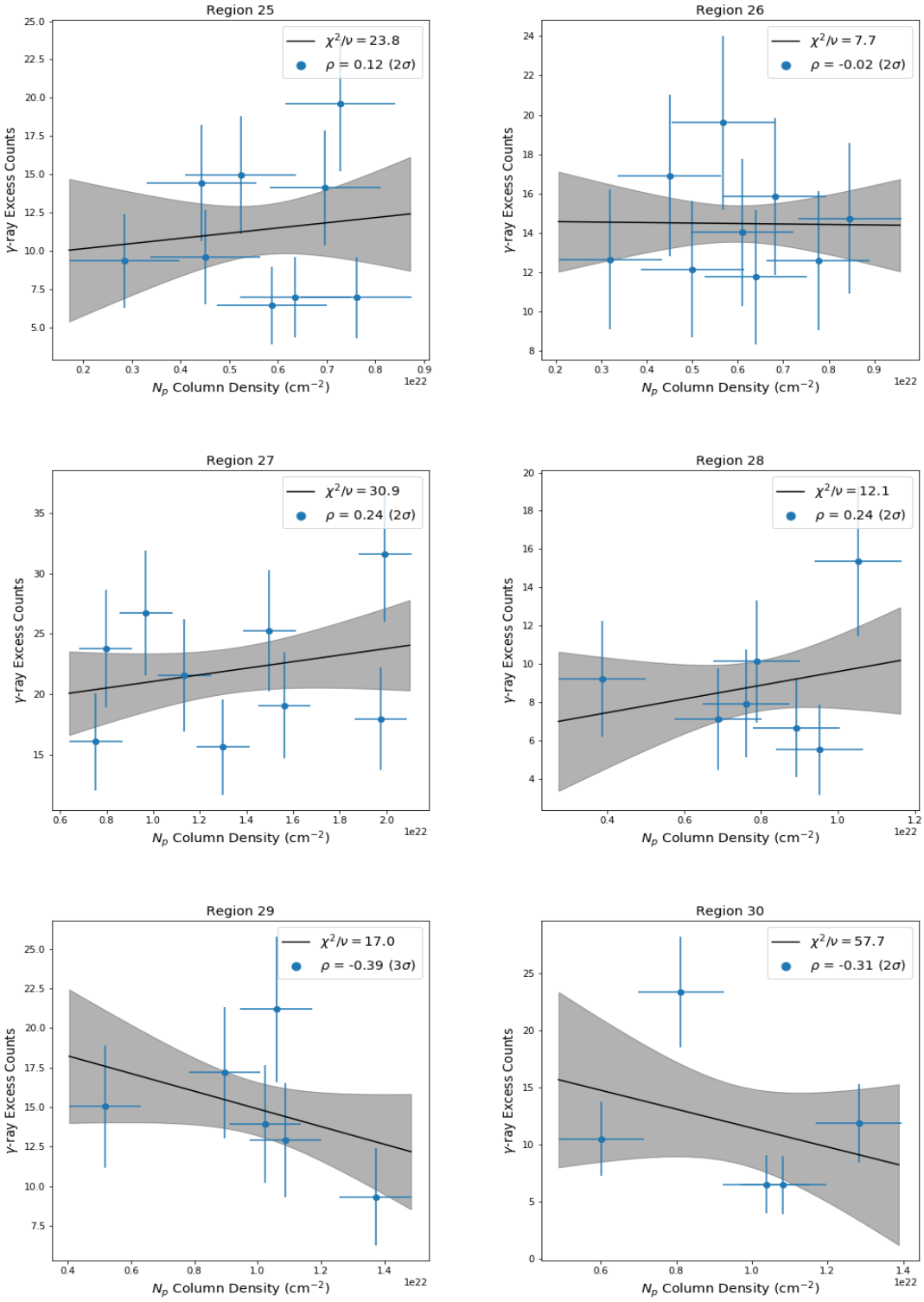

Figure E.15: Same as Figure E.11 except for regions 25-30.

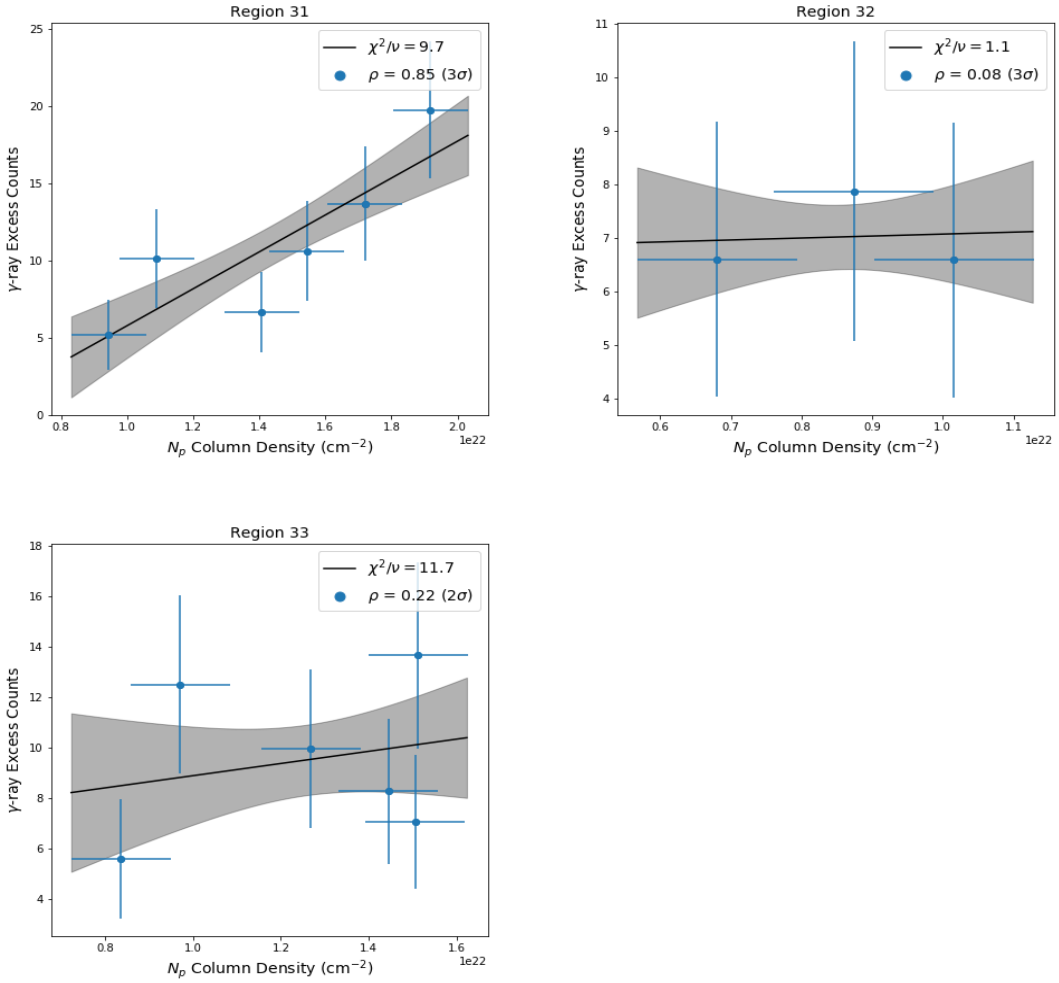

Figure E.16: Same as Figure E.11 except for regions 31-33.

E.2 Results from Nanten CO + SGPS HI Data Set

Same as the previous section except the Nanten data set is used to estimate the molecular component of the ISM.

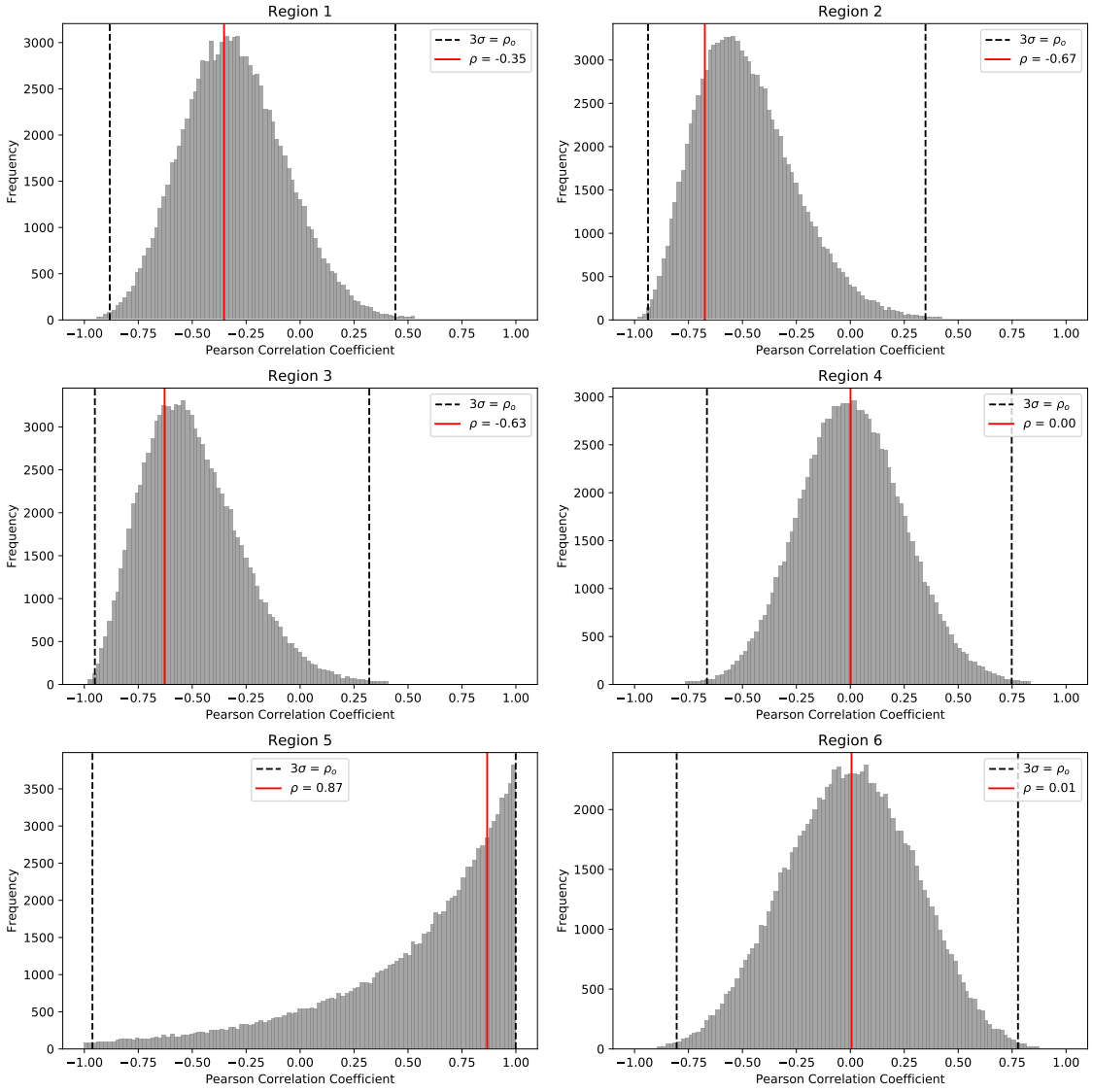

Figure E.17: The distribution of ρ values for regions 1-6, where the ISM column density has been calculated with the Nanten CO and SGPS data. Both the ISM column density and γ-ray excess counts data sets have been cleaned to ensure no noisey γ-ray data is involved (see subsection 5.2.3). The red line indicates the original ρ value and the dashed lines indicate the 3σ confidence bands.

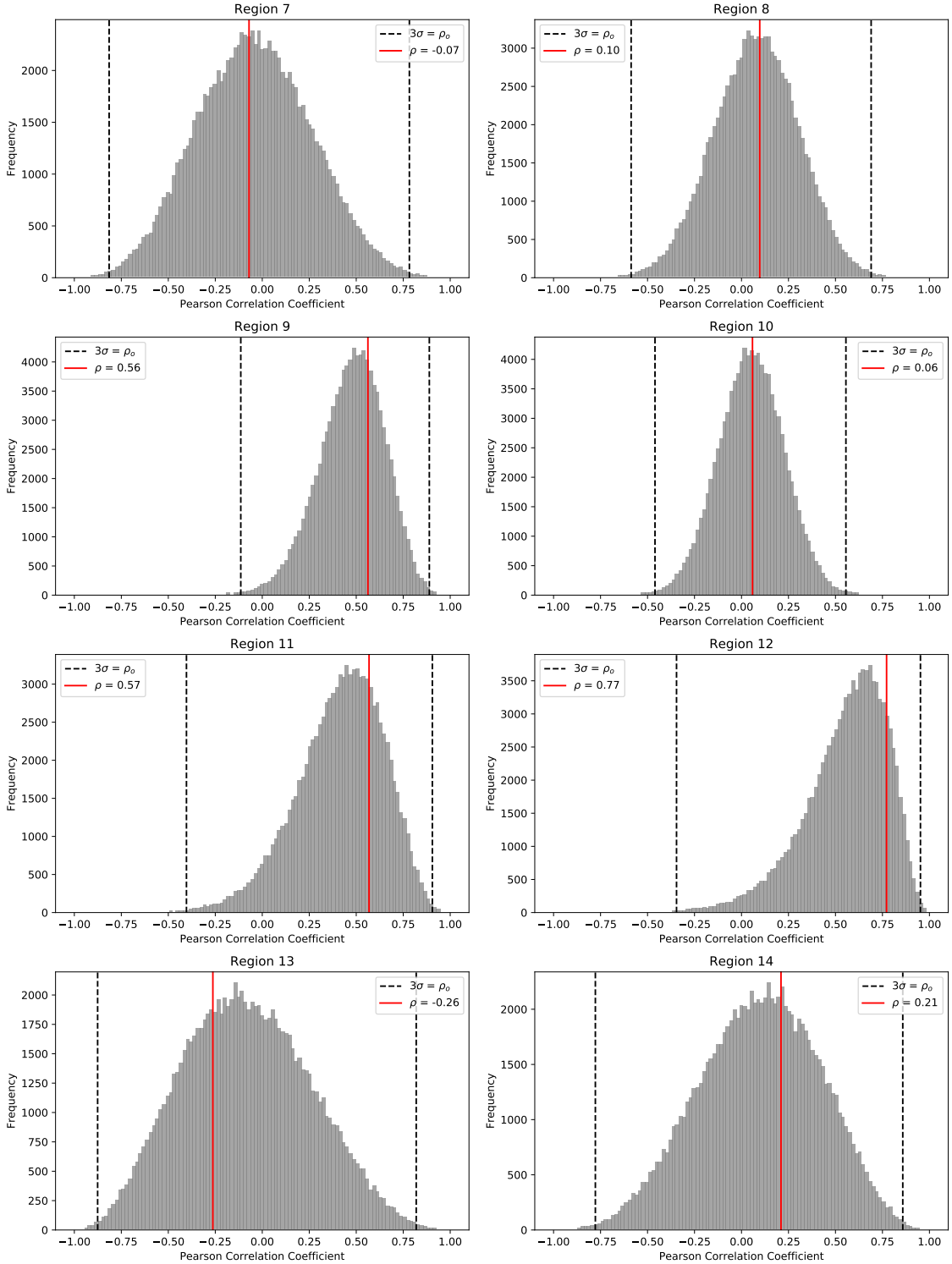

Figure E.18: Same as Figure E.17 except for regions 7-14.

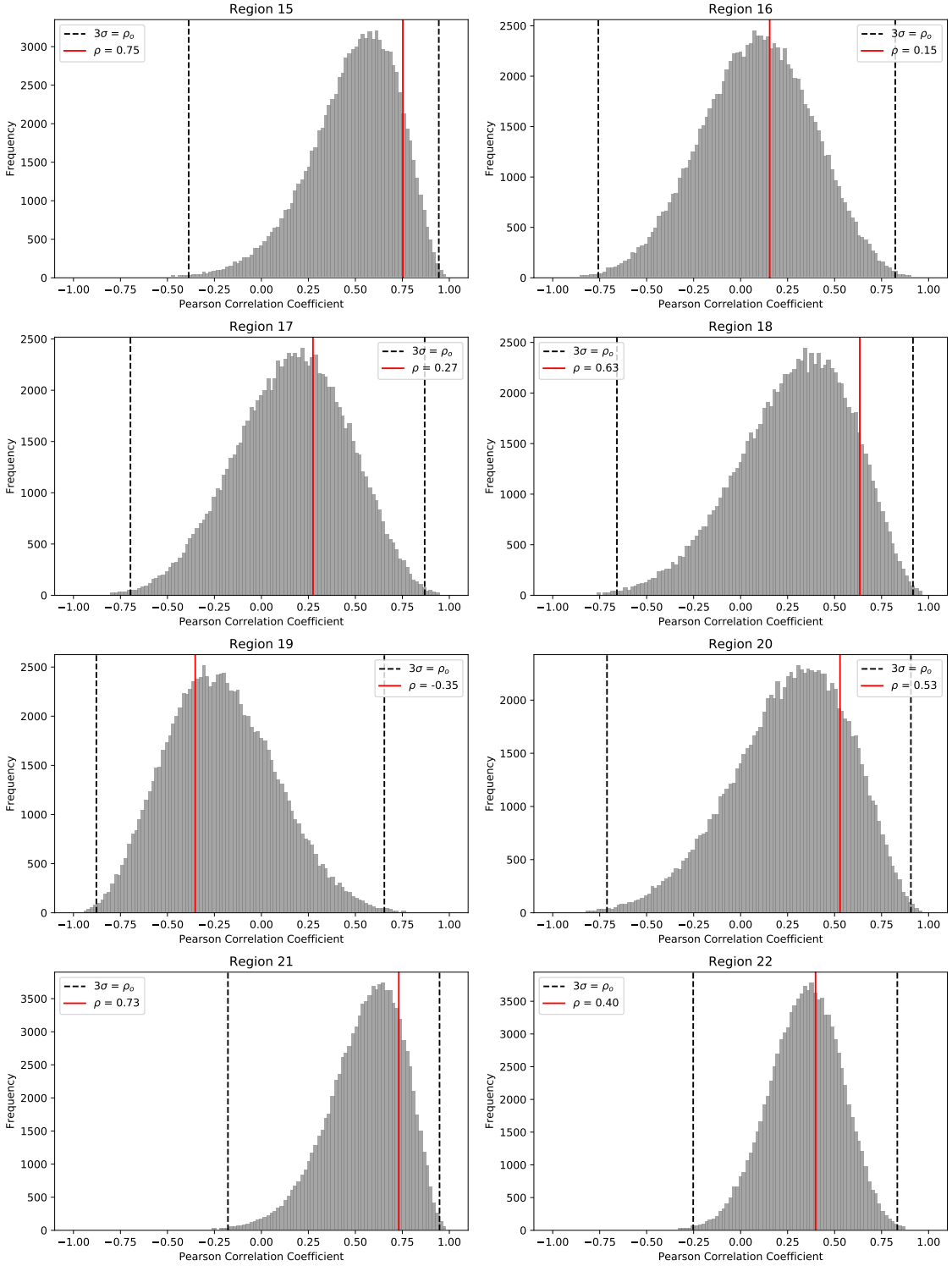

Figure E.19: Same as Figure E.17 except for regions 15-22.

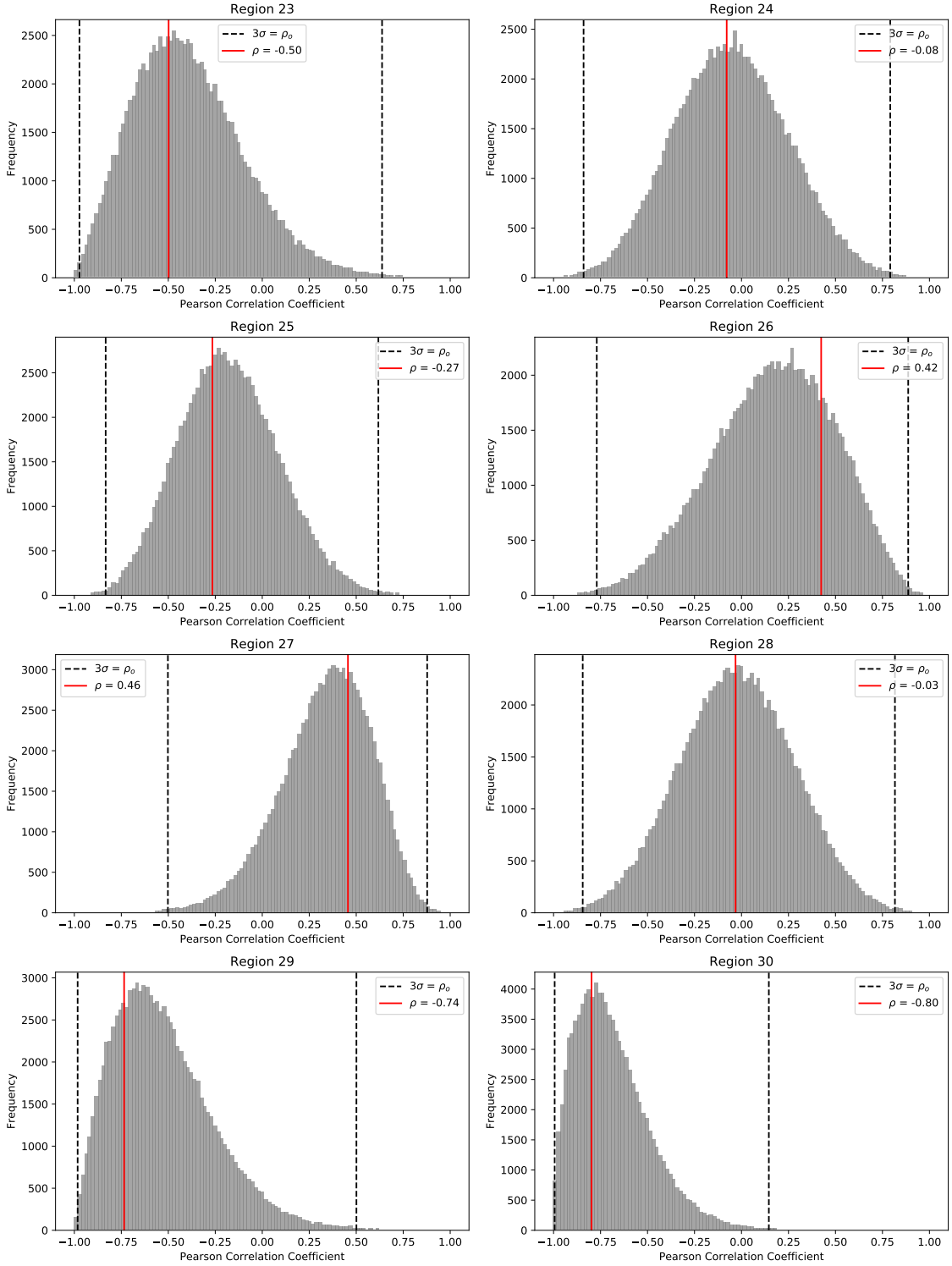

Figure E.20: Same as Figure E.17 except for regions 23-30.

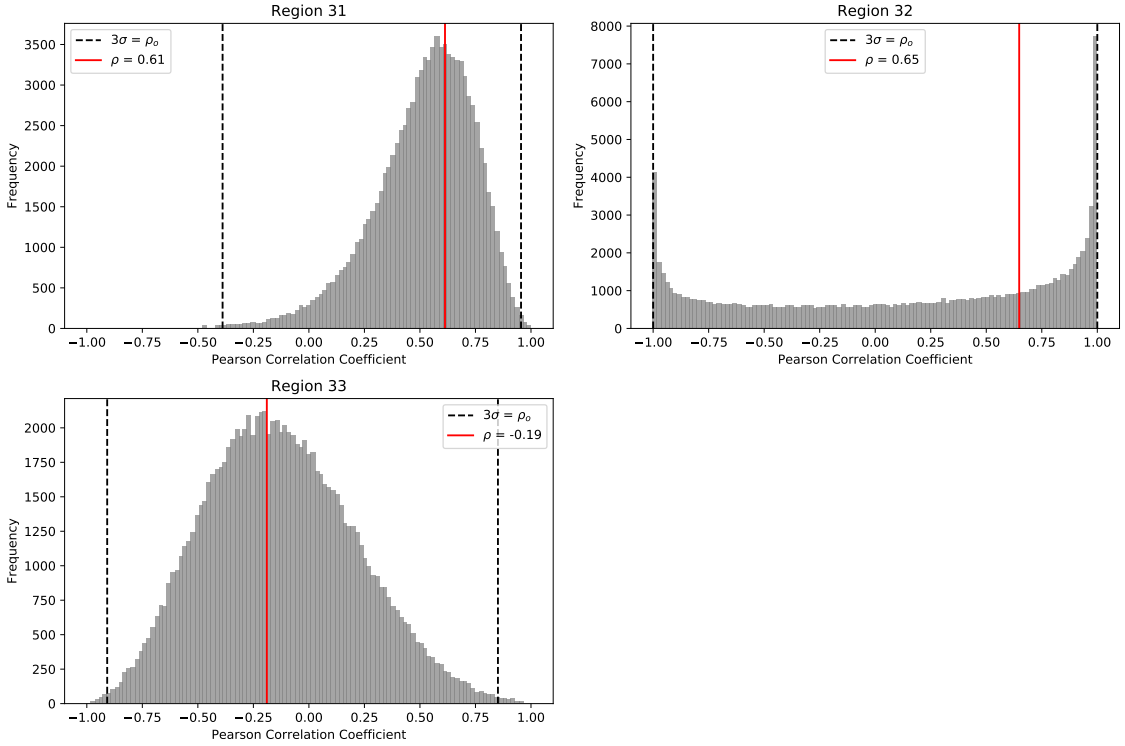

Figure E.21: Same as Figure E.17 except for regions 31-33.

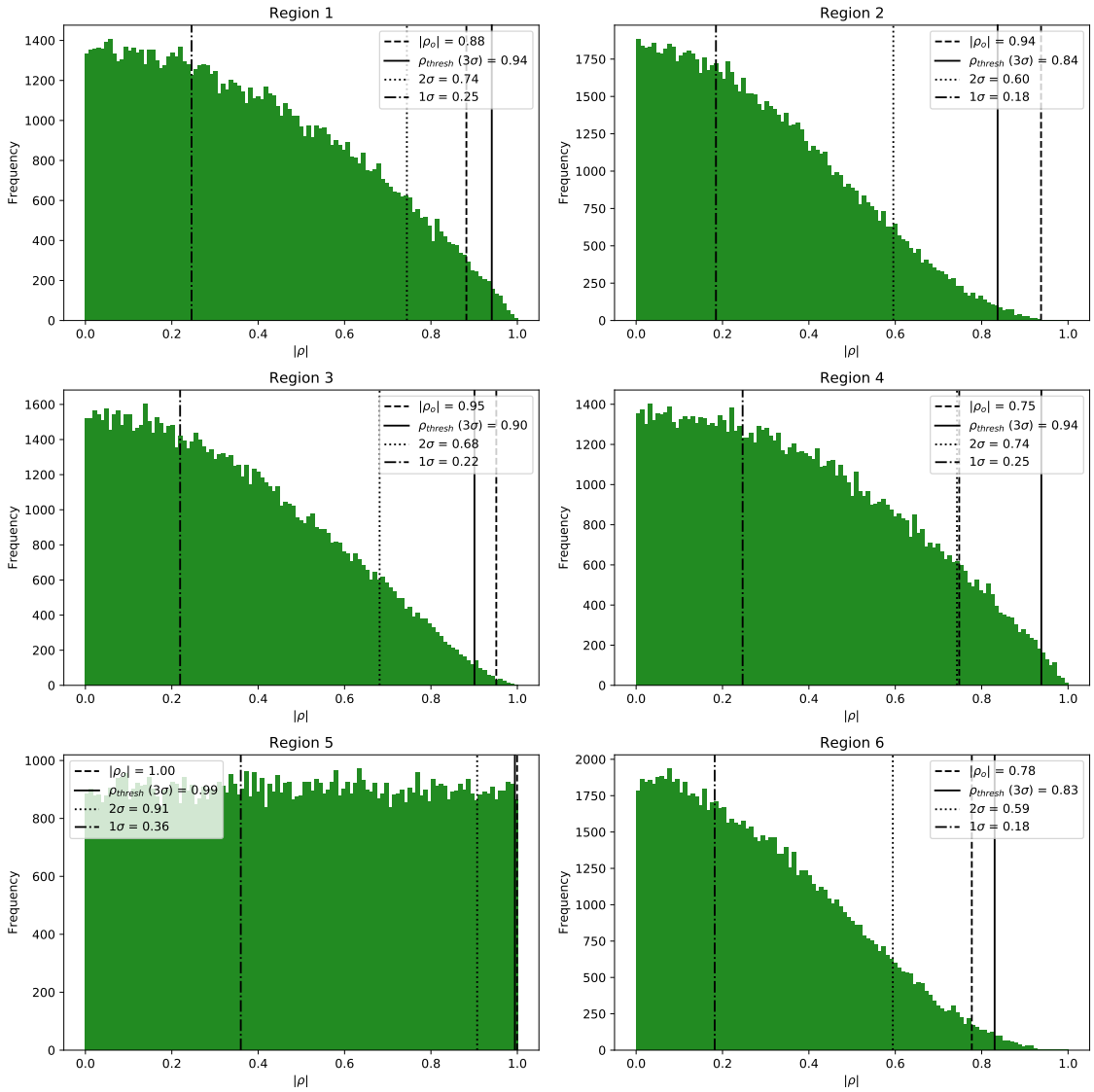

Figure E.22: The distribution of randomly distributed $|\rho|$ values, used to calculate the significance of ρ in each region. The 1σ, 2σ and 3σ values are illustrated with dot-dashed, dotted, and filled lines respectively. In being consistent with the previous plots, ρ_o is illustrated with a dashed line. The significance of ρ corresponds to the section of the distribution it falls in. See section 5.2.1 for more details.

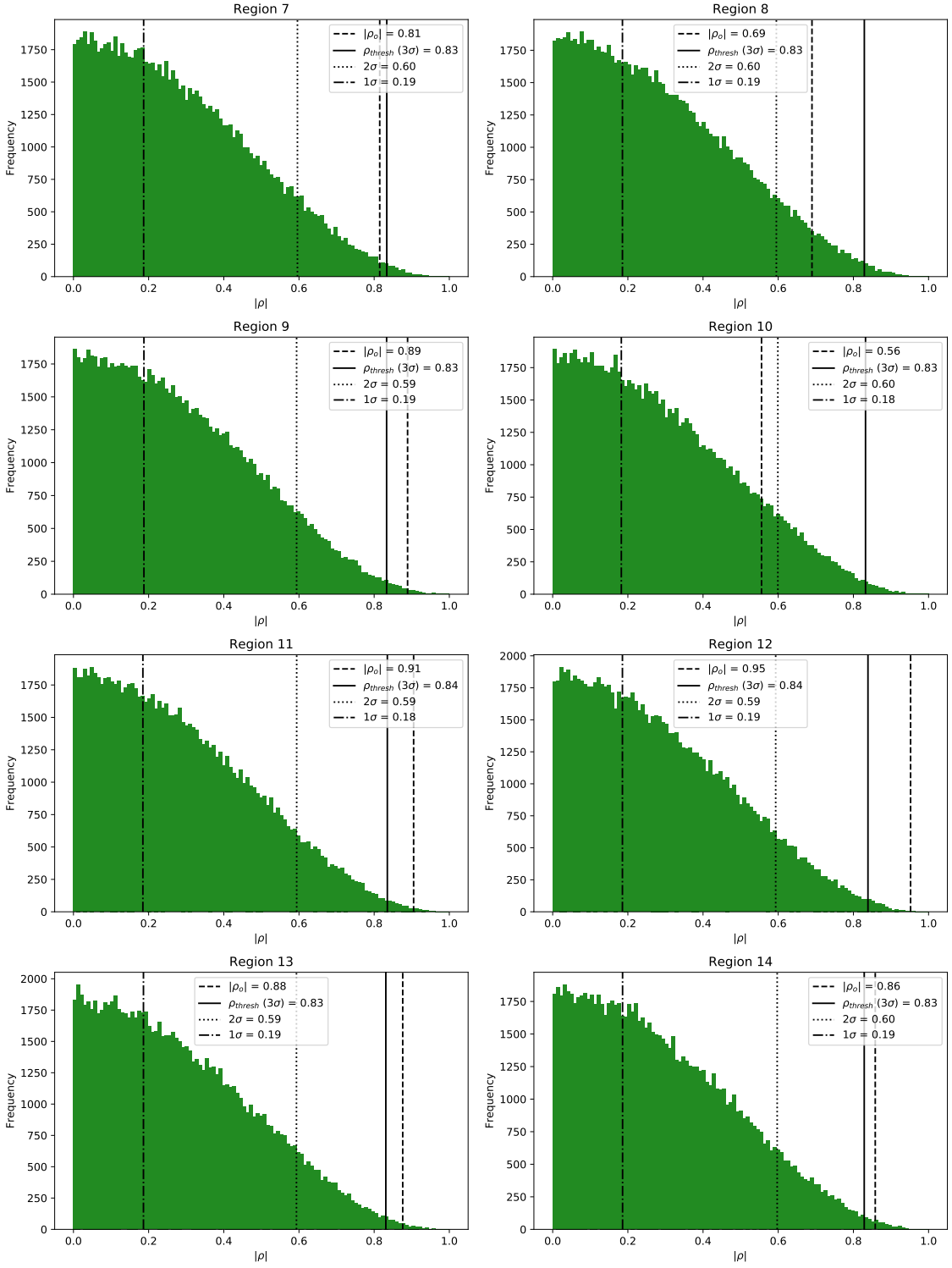

Figure E.23: Same as Figure E.6 except for regions 7-14.

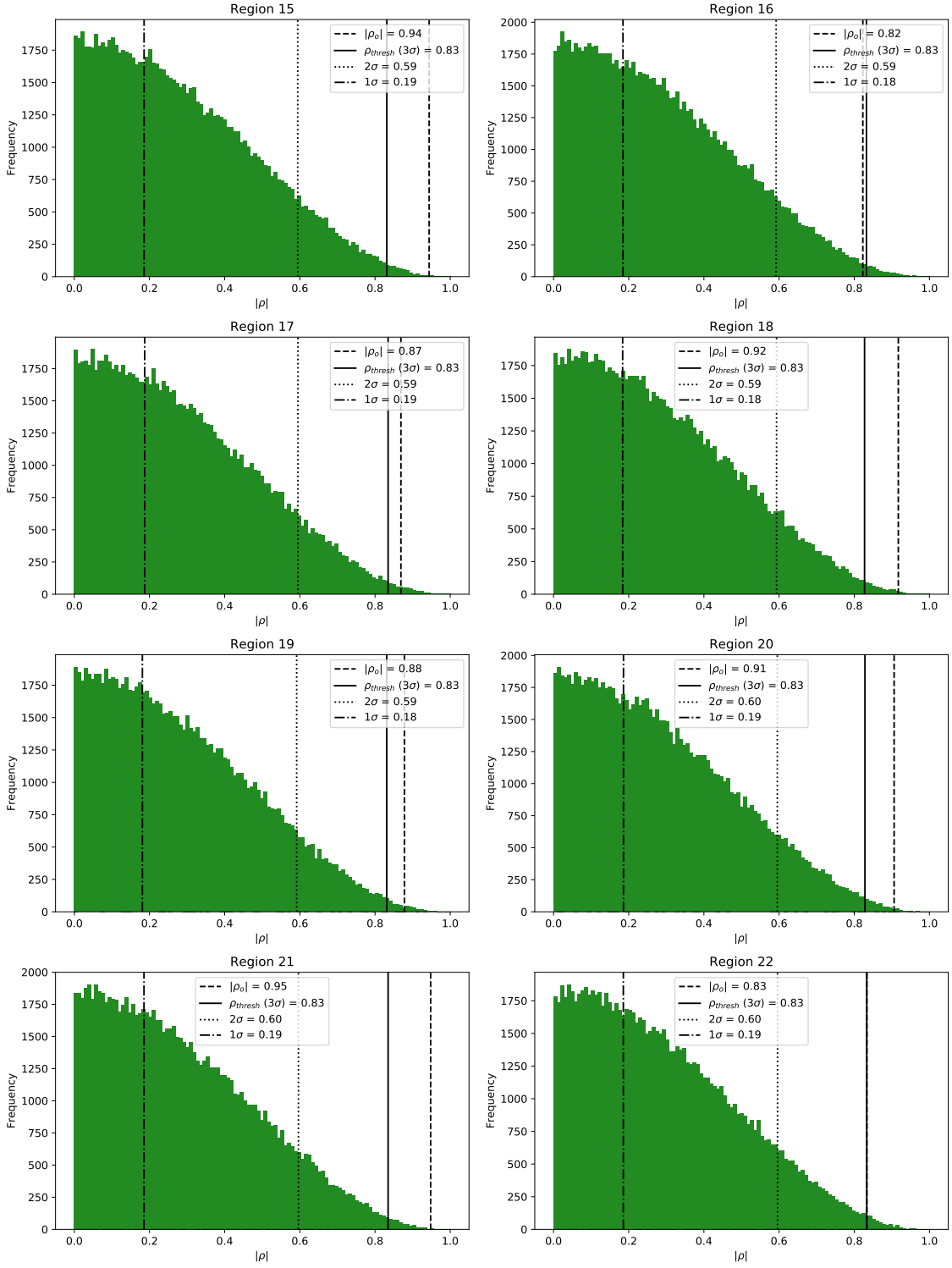

Figure E.24: Same as Figure E.6 except for regions 15-22.

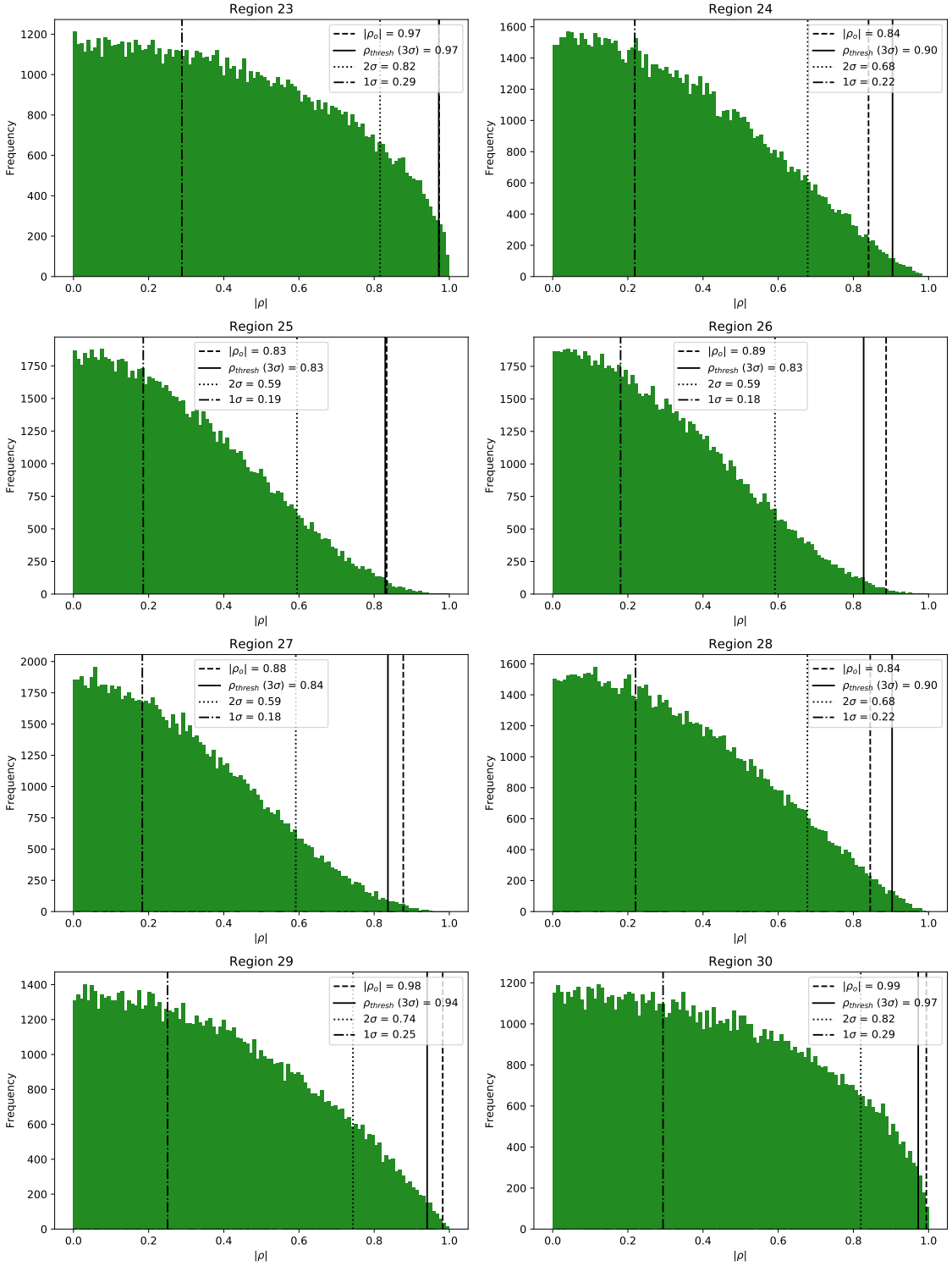

Figure E.25: Same as Figure E.6 except for regions 23-30.

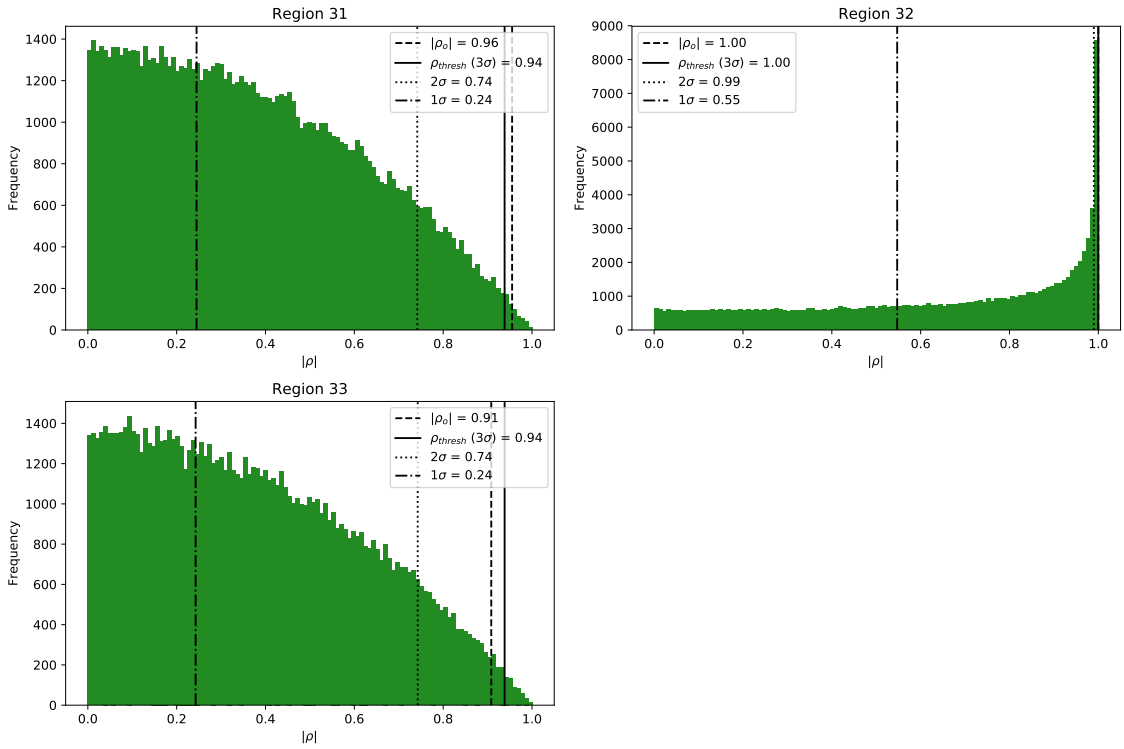

Figure E.26: Same as Figure E.22 except for regions 31-33.

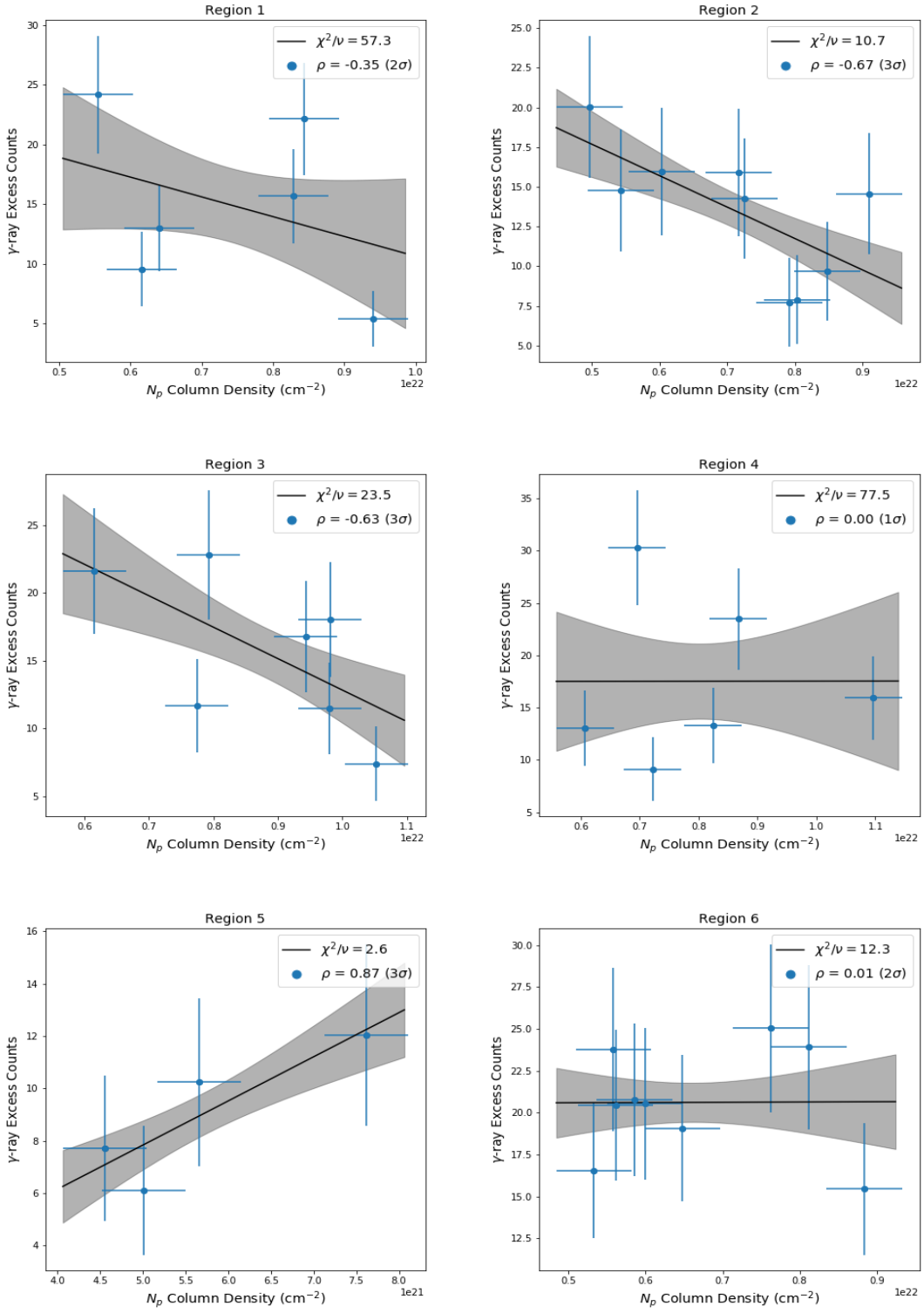

Figure E.27: The correlation scatterplots showing the relationship between the ISM gas density and the γ-rays in regions 1-6. The line of best fit is shown in black, while the grey area illustrates the 1σ confidence band.

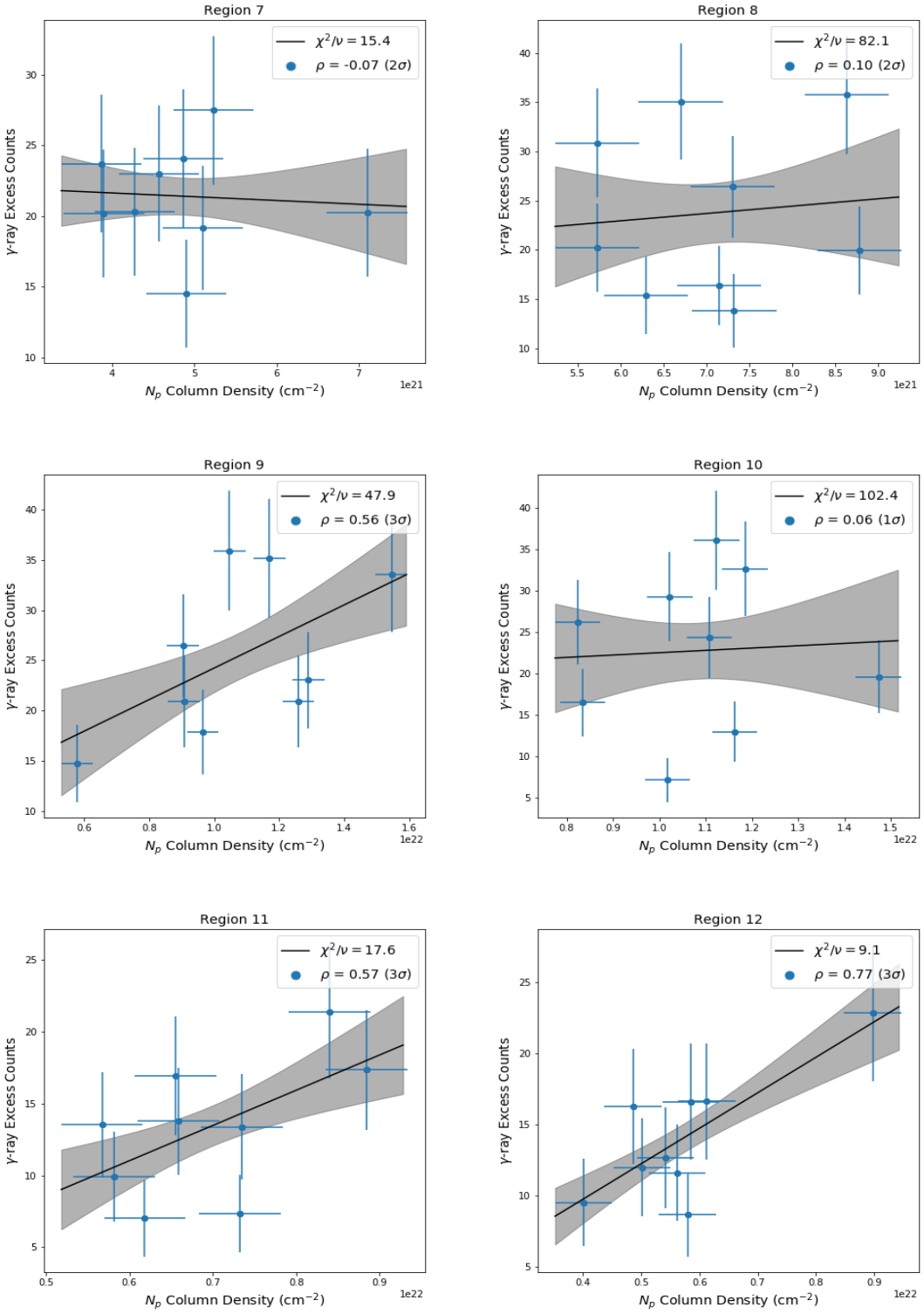

Figure E.28: Same as Figure E.27 except for regions 7-12.

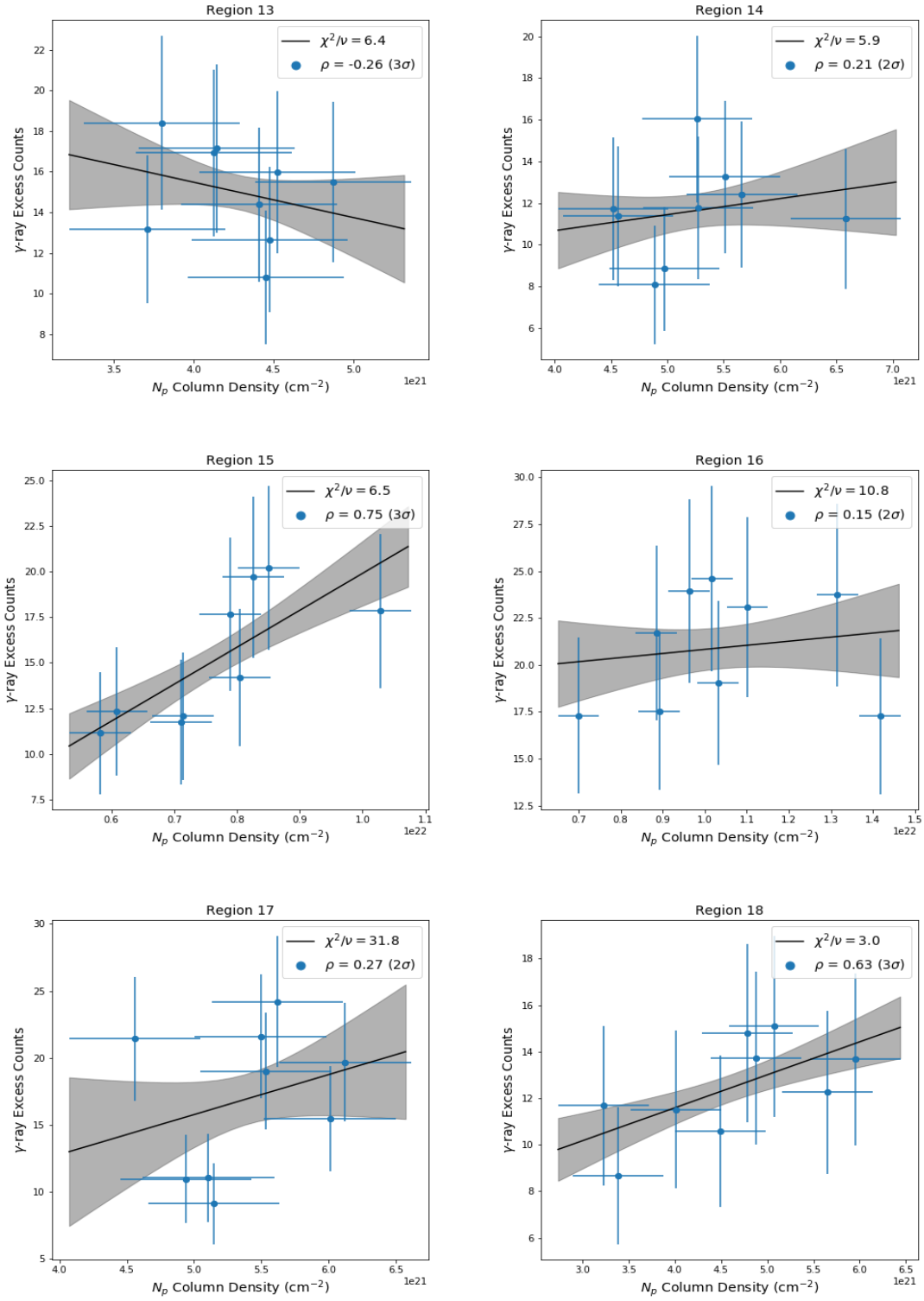

Figure E.29: Same as Figure E.27 except for regions 13-18.

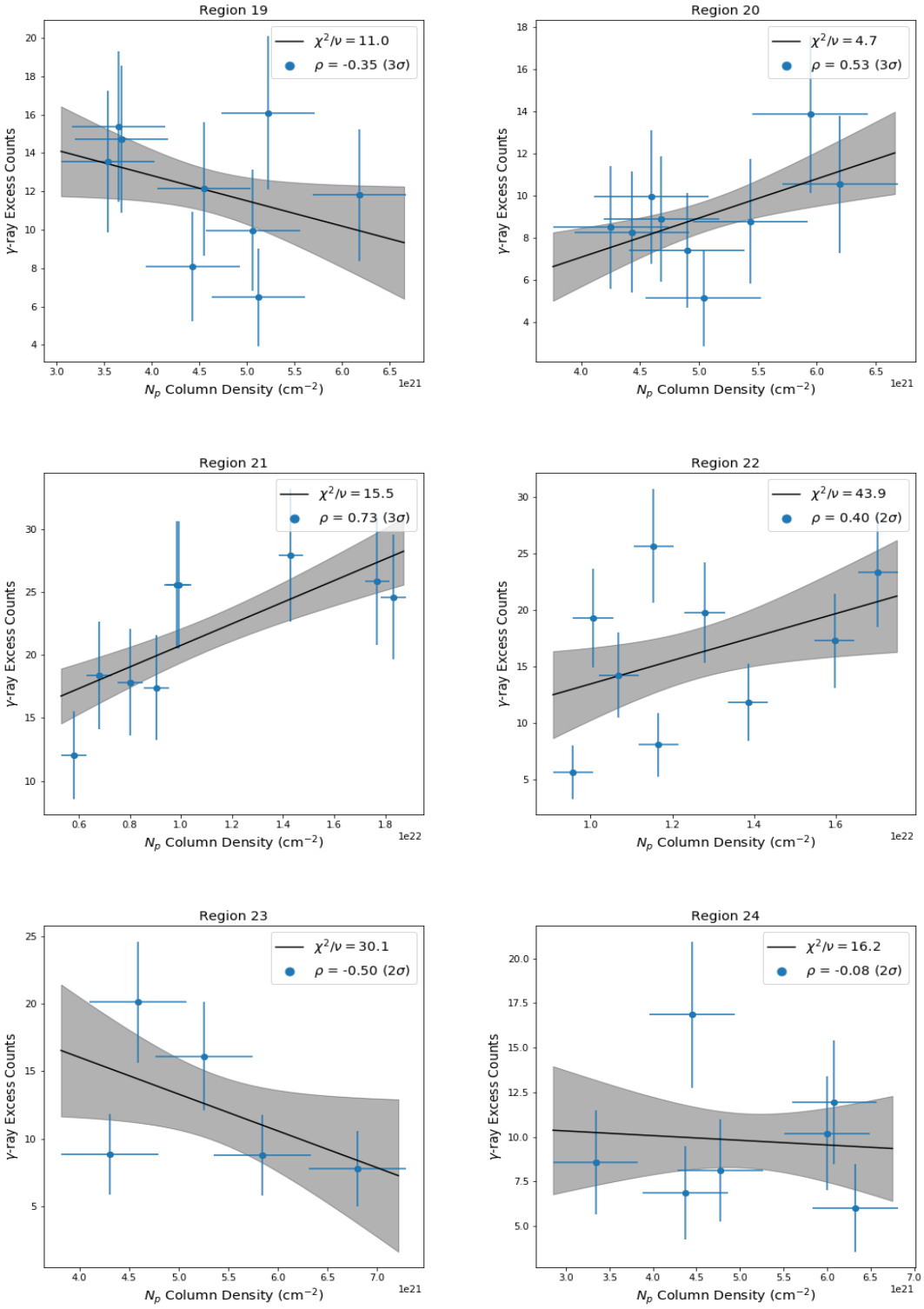

Figure E.30: Same as Figure E.27 except for regions 19-24.

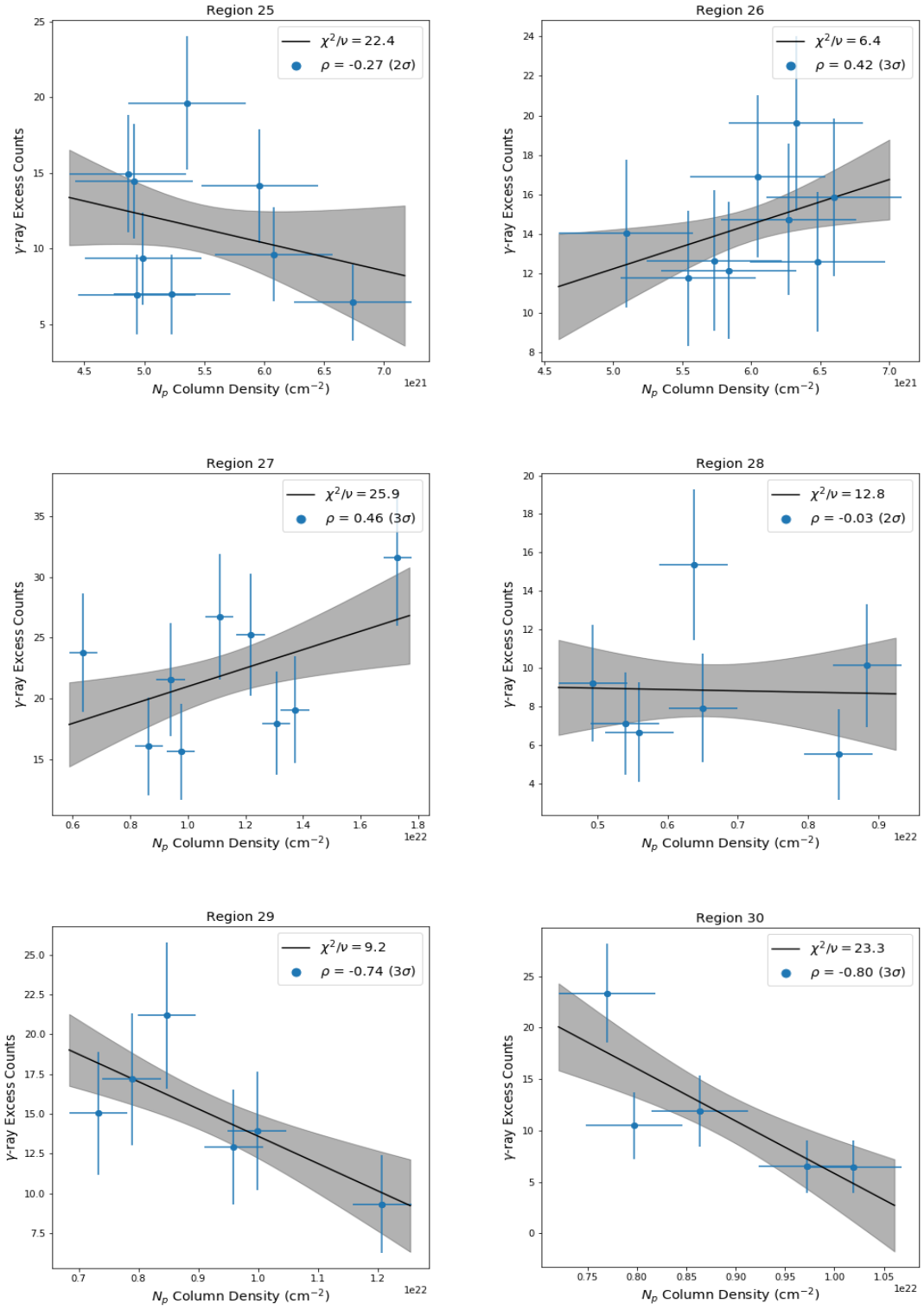

Figure E.31: Same as Figure E.27 except for regions 25-30.

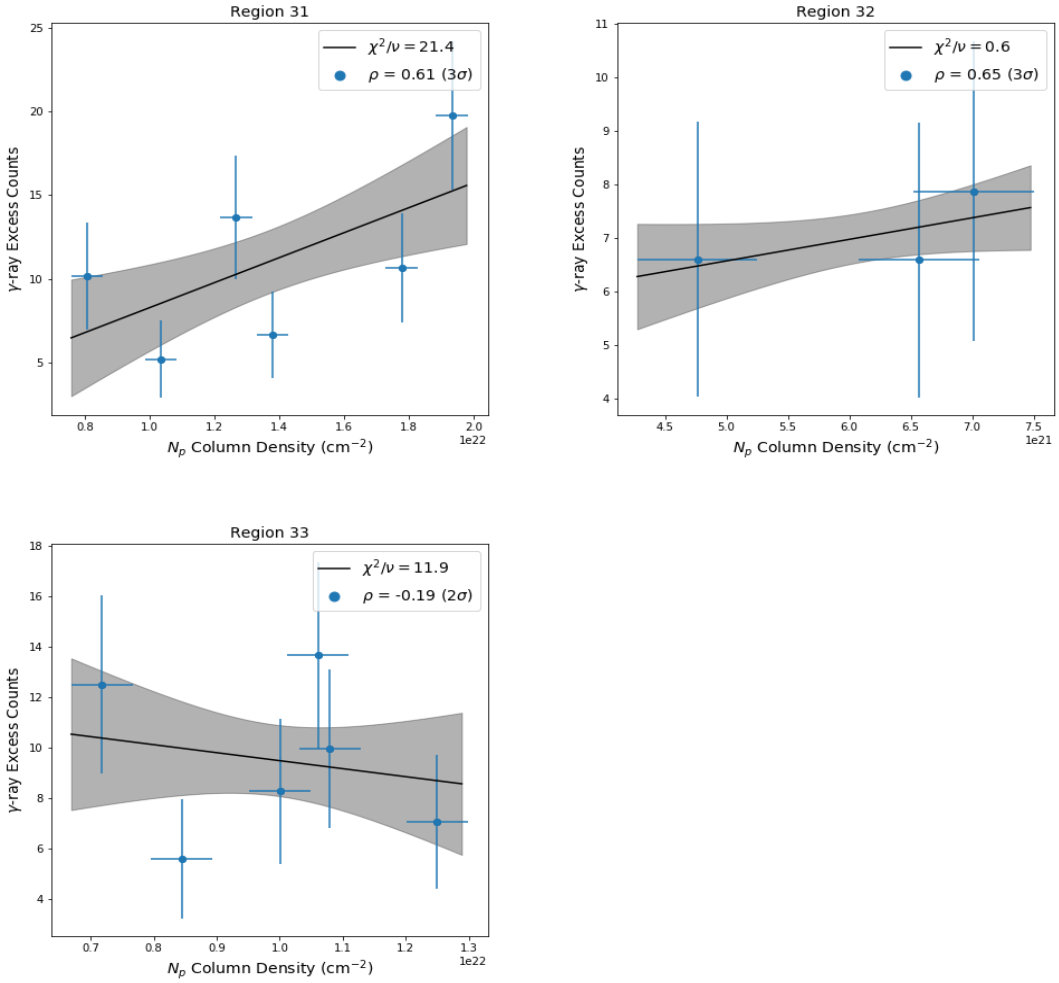

Figure E.32: Same as Figure E.27 except for regions 31-33.

F Displaying the t-Distributions for Observables and Modeled Quantities

In this appendix we present the t-distributions corresponding to the observables and modeled parameters investigated in chapter 5. The p-value, or the shaded region is required to quantify whether or not the correlated and anti-correlated regions have different observed quantities or modeled parameters.

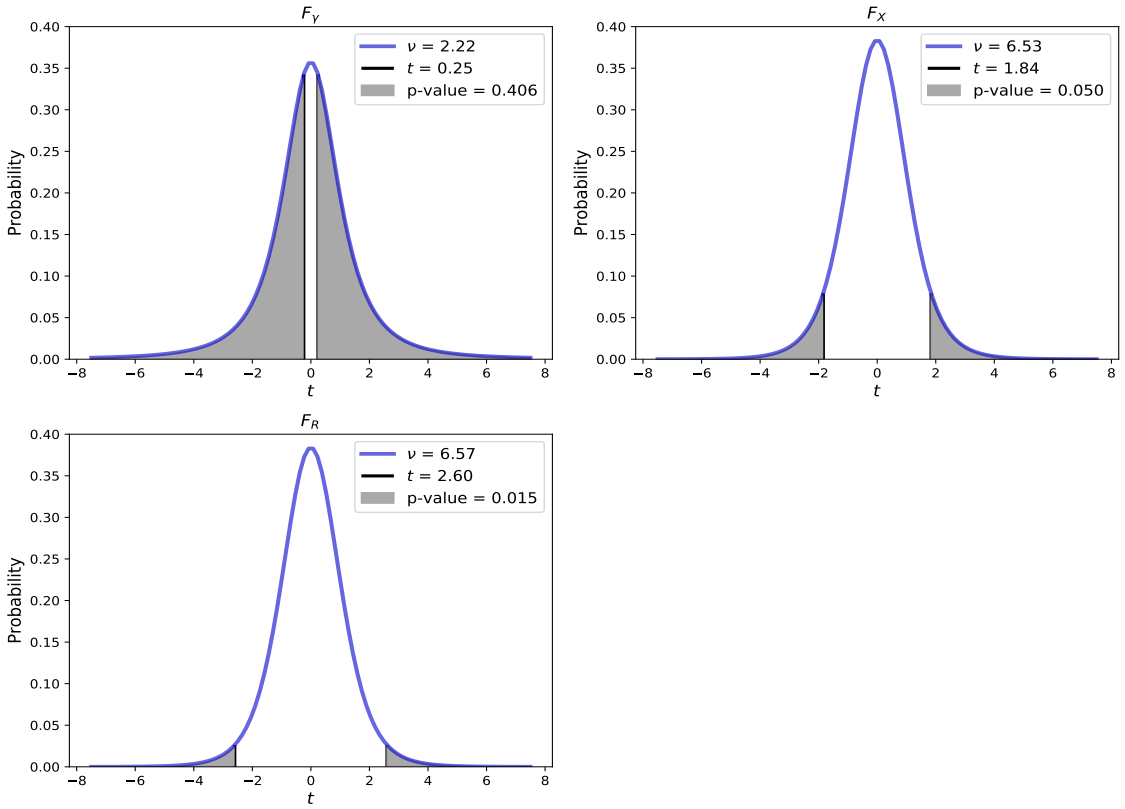

Figure F.1: Illustrations of the t-distributions for the observed γ-ray, X-ray and radio energy fluxes. The legend indicates values for the degrees of freedom, ν, the t-statistic, t, and the p-value, all characteristic of the quantity in question.

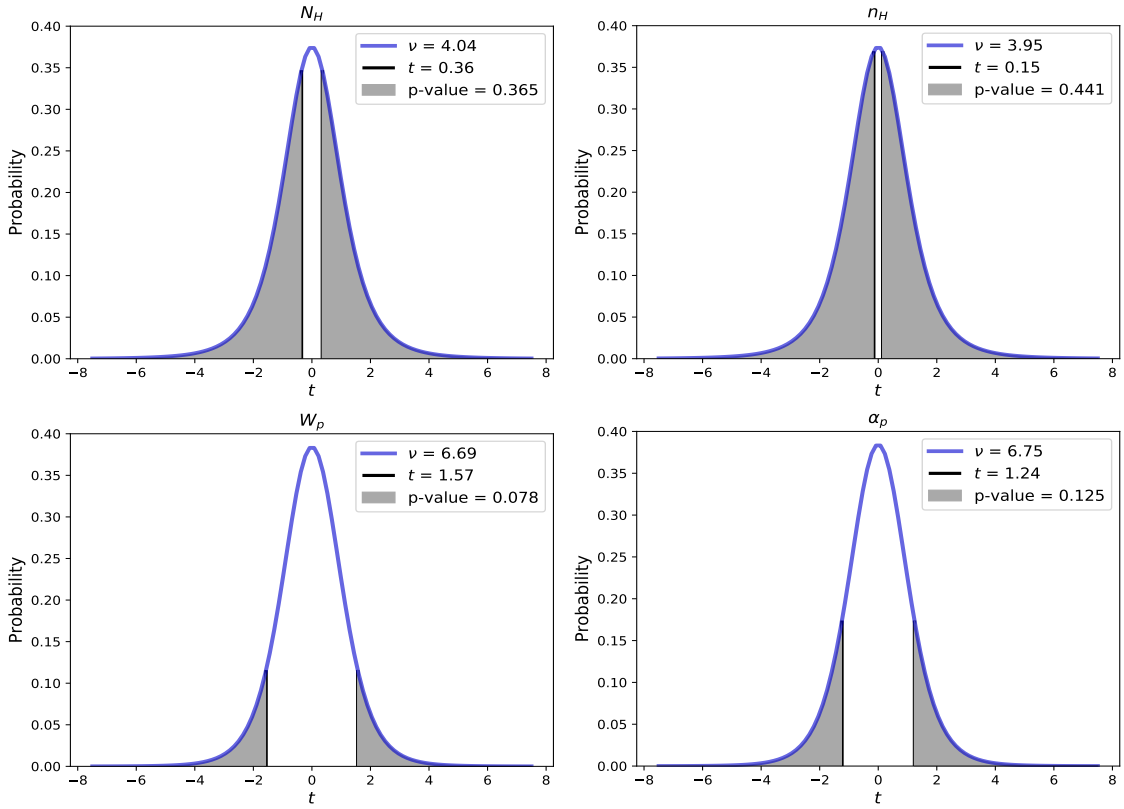

Figure F.2: Same as Figure F.1 except for the column and volume density and the hadronic SED parameters.

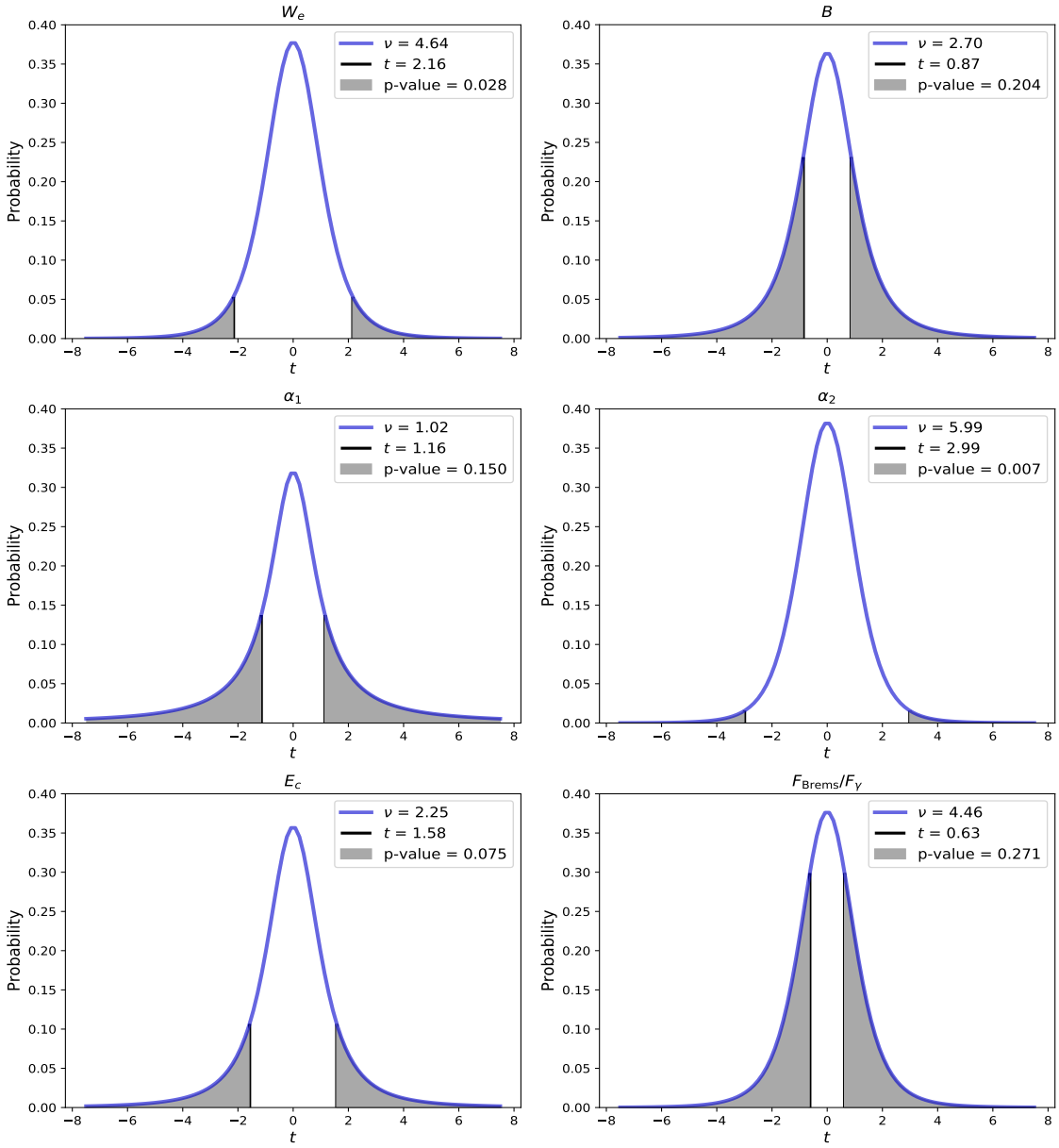

Figure F.3: Same as Figure F.1 except for the leptonic SED parameters.

Bibliography

Abdo, A. A. et al. (2010). "Fermi-LAT Study of Gamma-ray Emission in the Direction of Supernova Remnant W49B". In: *ApJ* 722, pp. 1303–1311.

Abdo, A. A. et al. (2011). "Observations of the Young Supernova Remnant RX J1713.7-3946 with the Fermi Large Area Telescope". In: *ApJ* 734, 28, p. 28.

Acero, F. et al. (2009). "A joint spectro-imaging analysis of the XMM-Newton and HESS observations of the supernova remnant RX J1713.7-3946". In: *A&A* 505, pp. 157–167.

Ackermann, M. et al. (2013). "Detection of the Characteristic Pion-Decay Signature in Supernova Remnants". In: *Science* 339, pp. 807–811.

Aharonian, F. (2013). "Gamma rays from supernova remnants". In: *Astroparticle Physics* 43, pp. 71–80.

Aharonian, F. A., A. M. Atoyan, and T. Kifune (1997). "Inverse Compton gamma radiation of faint synchrotron X-ray nebulae around pulsars". In: 291, pp. 162–176.

Aharonian, F. A. et al. (2004). "High-energy particle acceleration in the shell of a supernova remnant". In: *Nature* 432, pp. 75–77.

Aharonian, F. et al. (2006). "A detailed spectral and morphological study of the gamma-ray supernova remnant <ASTROBJ>RX J1713.7-3946</ASTROBJ> with HESS". In: *A&A* 449, pp. 223–242.

Aharonian, F. et al. (2007). "Primary particle acceleration above 100 TeV in the shell-type supernova remnant <ASTROBJ>RX J1713.7-3946</ASTROBJ> with deep HESS observations". In: *A&A* 464, pp. 235–243.

Aharonian, F. et al. (2008). "Discovery of very high energy gamma-ray emission coincident with molecular clouds in the W 28 (G6.4-0.1) field". In: *A&A* 481, pp. 401–410.

Ammosov, A. E., L. T. Ksenofontov, V. S. Nikolaev, and S. I. Petukhov (1994). "Synchrotron emission from type I supernova remnants". In: *Astronomy Letters* 20, pp. 157–162.

Atwood, W. B. et al. (2009). "The Large Area Telescope on the Fermi Gamma-Ray Space Telescope Mission". In: *ApJ* 697, pp. 1071–1102.

Baade, W. and F. Zwicky (1934). "Cosmic Rays from Super-novae". In: *Contributions from the Mount Wilson Observatory, vol. 3, pp.79-83* 3, pp. 79–83.

Bertsch, D. L. et al. (1993). "Diffuse Gamma-Ray Emission in the Galactic Plane from Cosmic-Ray, Matter, and Photon Interactions". In: *ApJ* 416, p. 587.

Blumenthal, G. R. and R. J. Gould (1970). "Bremsstrahlung, Synchrotron Radiation, and Compton Scattering of High-Energy Electrons Traversing Dilute Gases". In: *Reviews of Modern Physics* 42, pp. 237–271.

Blümer, J., R. Engel, and J. R. Hörandel (2009). "Cosmic rays from the knee to the highest energies". In: *Progress in Particle and Nuclear Physics* 63, pp. 293–338.

Braiding, C. et al. (2018). "The Mopra Southern Galactic Plane CO Survey - Data Release 3". In: *PASA* 35, e029, e029.

Burton, M. G. et al. (2013). "The Mopra Southern Galactic Plane CO Survey". In: *PASA* 30, e044, e044.

Bykov, A. M., D. C. Ellison, A. Marcowith, and S. M. Osipov (2018). "Cosmic Ray Production in Supernovae". In: *Space Sci. Rev.* 214, 41, p. 41.

Casanova, S. et al. (2010). "Modeling the Gamma-Ray Emission Produced by Runaway Cosmic Rays in the Environment of RX J1713.7-3946". In: *PASJ* 62, pp. 1127–1134.

Celli, S., G. Morlino, S. Gabici, and F. Aharonian (2018). "Supernova remnants in clumpy media: particle propagation and gamma-ray emission". In: *ArXiv e-prints*.

Dickey, J. M. and F. J. Lockman (1990). "H I in the Galaxy". In: *ARA&A* 28, pp. 215–261.

Dorfi, E. A. and L. O. Drury (1985). "Acceleration of cosmic rays in supernova-remnants". In: *International Cosmic Ray Conference* 3.

Drury, L. O. (1996). "Shell Type Supernova Remnants". In: *Space Sci. Rev.* 75, pp. 269–277.

Ellison, D. C., D. J. Patnaude, P. Slane, and J. Raymond (2010). "Efficient Cosmic Ray Acceleration, Hydrodynamics, and Self-Consistent Thermal X-Ray Emission Applied to Supernova Remnant RX J1713.7-3946". In: *ApJ* 712, pp. 287–293.

Ellison, D. C., P. Slane, and B. M. Gaensler (2001). "Broadband Observations and Modeling of the Shell-Type Supernova Remnant G347.3-0.5". In: *ApJ* 563, pp. 191–201.

Ellison, D. C., P. Slane, D. J. Patnaude, and A. M. Bykov (2012). "Core-collapse Model of Broadband Emission from SNR RX J1713.7-3946 with Thermal X-Rays and Gamma Rays from Escaping Cosmic Rays". In: *ApJ* 744, 39, p. 39.

Fermi, E. (1949). "On the Origin of the Cosmic Radiation". In: *Physical Review* 75, pp. 1169–1174.

Finke, J. D. and C. D. Dermer (2012). "Cosmic-Ray Electron Evolution in the Supernova Remnant RX J1713.7-3946". In: 751, 65, p. 65.

Fukui, Y. et al. (2003). "Discovery of Interacting Molecular Gas toward the TeV Gamma-Ray Peak of the SNR G 347.3–0.5". In: *PASJ* 55, pp. L61–L64.

Fukui, Y. et al. (2012). "A Detailed Study of the Molecular and Atomic Gas toward the γ-Ray Supernova Remnant RX J1713.7-3946: Spatial TeV γ-Ray and Interstellar Medium Gas Correspondence". In: *ApJ* 746, 82, p. 82.

Funk, S. et al. (2004). "The trigger system of the H.E.S.S. telescope array". In: *Astroparticle Physics* 22, pp. 285–296.

Gabici, S. and F. A. Aharonian (2014). "Hadronic gamma-rays from RX J1713.7-3946?" In: *MNRAS* 445, pp. L70–L73.

Gabici, S., F. A. Aharonian, and S. Casanova (2009). "Broad-band non-thermal emission from molecular clouds illuminated by cosmic rays from nearby supernova remnants". In: 396, pp. 1629–1639.

Gaisser, T. K. (1990). *Cosmic rays and particle physics*.

Ginzburg, V. L. and S. I. Syrovatskij (1967). "Cosmic rays in the Galaxy (Introductory Report)." In: *Radio Astronomy and the Galactic System*. Ed. by H. van Woerden. Vol. 31. IAU Symposium, p. 411.

Gordon, M. A. and W. B. Burton (1976). "Carbon monoxide in the Galaxy. I - The radial distribution of CO, H2, and nucleons". In: *ApJ* 208, pp. 346–353.

Gosling, J. T., J. R. Asbridge, S. J. Bame, G. Paschmann, and N. Sckopke (1978). "Observations of two distinct populations of bow shock ions in the upstream solar wind". In: *Geophys. Res. Lett.* 5, pp. 957–960.

Gould, R. J. (1969). "High-Energy Bremsstrahlung in Collisions of Electrons with One- and Two-Electron Atoms". In: *Physical Review* 185, pp. 72–79.

H. E. S. S. Collaboration et al. (2018). "H.E.S.S. observations of RX J1713.7-3946 with improved angular and spectral resolution: Evidence for gamma-ray emission extending beyond the X-ray emitting shell". In: *A&A* 612, A6, A6.

H.E.S.S. Collaboration et al. (2018). "The supernova remnant W49B as seen with H.E.S.S. and Fermi-LAT". In: *A&A* 612, A5, A5.

Hillas, A. M., ed. (1972). *Cosmic rays*. Vol. 13.

Hinton, J. A. and the HESS Collaboration (2004). "The status of the HESS project". In: *New A Rev.* 48, pp. 331–337.

Hiraga, J. S., Y. Uchiyama, T. Takahashi, and F. A. Aharonian (2005). "Spectral properties of nonthermal X-ray emission from the shell-type SNR RX J1713.7 3946 as revealed by XMM-Newton". In: *A&A* 431, pp. 953–961.

Huang, Y., Z. Li, W. Wang, and X. Zhao (2018). "Synchrotron radiation from secondary electrons in SNR shocks". In: *arXiv e-prints*.

Hwang, U., R. Petre, and J. P. Hughes (2000). "The X-Ray Line Emission from the Supernova Remnant W49B". In: *ApJ* 532, pp. 970–979.

Inoue, T., R. Yamazaki, S.-i. Inutsuka, and Y. Fukui (2012). "Toward Understanding the Cosmic-Ray Acceleration at Young Supernova Remnants Interacting with Interstellar Clouds: Possible Applications to RX J1713.7-3946". In: *ApJ* 744, 71, p. 71.

Jogler, T. and S. Funk (2016). "Revealing W51C as a Cosmic Ray Source Using Fermi-LAT Data". In: *ApJ* 816, 100, p. 100.

Kafexhiu, E., F. Aharonian, A. M. Taylor, and G. S. Vila (2014). "Parametrization of gamma-ray production cross sections for p p interactions in a broad proton energy range from the kinematic threshold to PeV energies". In: 90.12, 123014, p. 123014.

Katsuda, S. et al. (2015). "Evidence for Thermal X-Ray Line Emission from the Synchrotron-dominated Supernova Remnant RX J1713.7-3946". In: *ApJ* 814, 29, p. 29.

Koch, H. W. and J. W. Motz (1959). "Bremsstrahlung Cross-Section Formulas and Related Data". In: *Reviews of Modern Physics* 31, pp. 920–955.

Koyama, K. et al. (1995). "Evidence for shock acceleration of high-energy electrons in the supernova remnant SN1006". In: *Nature* 378, pp. 255–258.

Koyama, K. et al. (1997). "Discovery of Non-Thermal X-Rays from the Northwest Shell of the New SNR RX J1713.7-3946: The Second SN 1006?" In: *PASJ* 49, pp. L7–L11.

Krayzel, F. et al. (2013). "Improved sensitivity of H.E.S.S.-II through the fifth telescope focus system". In: *ArXiv e-prints*.

Ladd, N., C. Purcell, T. Wong, and S. Robertson (2005). "Beam Size, Shape and Efficiencies for the ATNF Mopra Radio Telescope at 86-115 GHz". In: *PASA* 22, pp. 62–72.

Lagage, P. O. and C. J. Cesarsky (1983). "The maximum energy of cosmic rays accelerated by supernova shocks". In: *A&A* 125, pp. 249–257.

Lazendic, J. S. et al. (2004). "A High-Resolution Study of Nonthermal Radio and X-Ray Emission from Supernova Remnant G347.3-0.5". In: *ApJ* 602, pp. 271–285.

Leahy, D. A. (2017). "Energetics and Birth Rates of Supernova Remnants in the Large Magellanic Cloud". In: *apj* 837, 36, p. 36.

Lee, J.-J. et al. (2008). "A 21 cm Spectral and Continuum Study of IC 443 Using the Very Large Array and the Arecibo Telescope". In: *AJ* 135, pp. 796–808.

Li, T.-P. and Y.-Q. Ma (1983). "Analysis methods for results in gamma-ray astronomy". In: *ApJ* 272, pp. 317–324.

Manolakou, K., D. Horns, and J. G. Kirk (2007). "Spectral evolution of non-thermal electron distributions in intense radiation fields". In: 474, pp. 689–700.

Maxted, N. I. et al. (2013). "Dense Gas Towards the RX J1713.7-3946 Supernova Remnant". In: *PASA* 30, e055, e055.

McClure-Griffiths, N. M. et al. (2005). "The Southern Galactic Plane Survey: H I Observations and Analysis". In: 158, pp. 178–187.

Merten, L., J. Becker Tjus, B. Eichmann, and R.-J. Dettmar (2017). "On the non-thermal electron-to-proton ratio at cosmic ray acceleration sites". In: *Astroparticle Physics* 90, pp. 75–84.

Meyer, M., D. Horns, and H.-S. Zechlin (2010). "The Crab Nebula as a standard candle in very high-energy astrophysics". In: 523, A2, A2.

Mezger, P. G., R. J. Tuffs, R. Chini, E. Kreysa, and H.-P. Gemuend (1986). "Maps of Cassiopeia A and the Crab Nebula at lambda 1.2 MM". In: *A&A* 167, pp. 145–150.

Mitsuda, K. et al. (2007). "The X-Ray Observatory Suzaku". In: *PASJ* 59, S1–S7.

Moriguchi, Y. et al. (2005). "A Detailed Study of Molecular Clouds toward the TeV Gamma-Ray Supernova Remnant G347.3-0.5". In: 631, pp. 947–963.

Muraishi, H. et al. (2000). "Evidence for TeV gamma-ray emission from the shell type SNR RX J1713.7-3946". In: *A&A* 354, pp. L57–L61.

Ohira, Y. and R. Yamazaki (2017). "Inverse Compton emission from a cosmic-ray precursor in RX J1713.7-3946". In: *Journal of High Energy Astrophysics* 13, pp. 17–21.

Pfeffermann, E. and B. Aschenbach (1996). "ROSAT observation of a new supernova remnant in the constellation Scorpius." In: *Roentgenstrahlung from the Universe*. Ed. by H. U. Zimmermann, J. Trümper, and H. Yorke, pp. 267–268.

Reynolds, Stephen P., B. M. Gaensler, and Fabrizio Bocchino (2012). "Magnetic Fields in Supernova Remnants and Pulsar-Wind Nebulae". In: *Space Sci. Rev.* 166.1-4, pp. 231–261.

Sano, H. et al. (2010). "Star-forming Dense Cloud Cores in the TeV Gamma-ray SNR RX J1713.7-3946". In: *ApJ* 724, pp. 59–68.

Sano, H. et al. (2013). "Non-thermal X-Rays and Interstellar Gas Toward the γ-Ray Supernova Remnant RX J1713.7-3946: Evidence for X-Ray Enhancement around CO and H I Clumps". In: *ApJ* 778, 59, p. 59.

Sano, H. et al. (2015). "A Detailed Study of Non-thermal X-Ray Properties and Interstellar Gas toward the γ-Ray Supernova Remnant RX J1713.7-3946". In: *ApJ* 799, 175, p. 175.

Sault, R. J., P. J. Teuben, and M. C. H. Wright (1995). "A Retrospective View of MIRIAD". In: *Astronomical Data Analysis Software and Systems IV*. Ed. by R. A. Shaw, H. E. Payne, and J. J. E. Hayes. Vol. 77. Astronomical Society of the Pacific Conference Series, p. 433.

Schlickeiser, R. (2002). *Cosmic Ray Astrophysics*.

Slane, P. et al. (1999). "Nonthermal X-Ray Emission from the Shell-Type Supernova Remnant G347.3-0.5". In: *ApJ* 525, pp. 357–367.

Stecker, F. W. (1971). "Cosmic gamma rays". In: *NASA Special Publication* 249.

Swordy, S. P. (2001). "The Energy Spectra and Anisotropies of Cosmic Rays". In: *Space Sci. Rev.* 99, pp. 85–94.

Tanaka, T. et al. (2008). "Study of Nonthermal Emission from SNR RX J1713.7-3946 with Suzaku". In: *ApJ* 685, 988-1004, pp. 988–1004.

Tanaka, T. et al. (2018). "NuSTAR Detection of Nonthermal Bremsstrahlung from the Supernova Remnant W49B". In: *ApJ* 866, L26, p. L26.

Uchiyama, Y., F. A. Aharonian, and T. Takahashi (2003). "Fine-structure in the nonthermal X-ray emission of SNR RX J1713.7-3946 revealed by Chandra". In: *A&A* 400, pp. 567–574.

Uchiyama, Y., F. A. Aharonian, T. Tanaka, T. Takahashi, and Y. Maeda (2007). "Extremely fast acceleration of cosmic rays in a supernova remnant". In: *Nature* 449, pp. 576–578.

Vink, J. (2008). "Non-thermal bremsstrahlung from supernova remnants and the effect of Coulomb losses". In: *A&A* 486, pp. 837–841.

Vink, J. et al. (2002). "Non-thermal bremsstrahlung as the dominant hard X-ray continuum emission from the supernova remnant MSH14-63 (RCW 86)". In: *arXiv Astrophysics e-prints*.

Wang, Z. R., Q.-Y. Qu, and Y. Chen (1997). "Is RX J1713.7-3946 the remnant of the AD393 guest star?" In: *A&A* 318, pp. L59–L61.

Wolszczan, A., J. M. Cordes, and R. J. Dewey (1991). "Discovery of a young, 267 millisecond pulsar in the supernova remnant W44". In: *ApJ* 372, pp. L99–L102.

Yang, R.-z., E. Kafexhiu, and F. Aharonian (2018). "Exploring the shape of the γ-ray spectrum around the "π^0-bump"". In: *A&A* 615, A108, A108.

Yuan, Q., S. Liu, Z. Fan, X. Bi, and C. L. Fryer (2011). "Modeling the Multi-Wavelength Emission of the Shell-type Supernova Remnant RX J1713.7-3946". In: *ApJ* 735, 120, p. 120.

Zabalza, V. (2015). "Naima: a Python package for inference of particle distribution properties from nonthermal spectra". In: *34th International Cosmic Ray Conference (ICRC2015)*. Ed. by A. S. Borisov et al. Vol. 34. International Cosmic Ray Conference, p. 922.

Zhang, X. and Y. Chen (2016). "The Role of the Diffusive Protons in the Gamma-ray Emission of Supernova Remnant RX J1713.7-3946–a Two-Zone Model". In: *ApJ* 821, 43, p. 43.

Zhou, X., M. Miceli, F. Bocchino, S. Orlando, and Y. Chen (2011). "Unveiling the spatial structure of the overionized plasma in the supernova remnant W49B". In: *MNRAS* 415, pp. 244–250.